

**Further Development of  
the AC<sup>2</sup> Code ATHLET for  
Evolutionary Reactors  
and Research Reactors  
(Phase A)**

## Further Development of the AC<sup>2</sup> Code ATHLET for Evolutionary Reactors and Research Reactors (Phase A)

Weiterentwicklung des  
AC<sup>2</sup>-Programms ATHLET für  
evolutionäre Reaktoren und  
Forschungsreaktoren  
(Phase A)

Final Report

Philipp Schöffel  
Anthony Di Nora  
Norman Dünne  
Volker Jacht  
Markus Junk  
Tomasz Skorek  
Daniel von der Cron  
Fabian Weyermann  
Andreas Wielenberg

August 2024

### **Remark:**

This report refers to the in-house research project RS1600 which has been funded by the German Federal Ministry for the Environment, Nature Conservation, Nuclear Safety and Consumer Protection (BMUV).

The work was conducted by the GRS.

The authors are responsible for the content of the report.

**Keywords**

AC<sup>2</sup>, CI, flow regime map, gap conductance, RBHT, software development, thermal-hydraulic system code ATHLET

## Abstract

The project RS1600, funded by BMUV, on the *Further Development of the AC<sup>2</sup> code ATHLET for Evolutionary Reactors and Research Reactors* aimed to develop and upgrade models and methods for the thermal-hydraulic system code ATHLET to support the numerous national and international code users with a powerful and reliable tool for carrying out safety analyses according to the current state of science and technology for existing reactors, advanced future reactor designs, research reactors, and SMR.

The introduction of a central flow regime map module represents a significant milestone for the ATHLET development process. In addition to the consistent use of flow pattern information and associated closure equations in the models of interphase friction, mass and energy exchange, the calculation of additional variables such as the entrainment fraction, which was previously determined on a model-specific basis, was also standardized. The central module has been expanded to allow for the use of separate flow regime maps depending on the prevailing heat transfer conditions at the wall. This development enabled the introduction of specific flow patterns and transition criteria for conditions characterized by wall condensation, which differ from adiabatic flows or heating wall conditions. Additionally, a general interpolation routine was implemented to facilitate a smooth transition between two or more flow pattern maps. The new implementation could already be verified against several application cases with satisfactory results.

By participating in the OECD/NEA project RBHT, GRS gained access to new and detailed experimental data for code validation. Evaluation of blind calculations performed in the frame of the benchmark focused on parameters relevant to quench front model validation, such as cladding temperatures at different core elevations, pressure drop along the test section, and quench front progression. Overall, the simulation results were satisfactory and generally reproduced the experimental trends. Uncertainty and sensitivity analyses were performed for two RBHT tests. Concerning the turbulence-induced precooling effect on the heater rods surface temperatures, which was observed in some tests and could not be adequately simulated by ATHLET, the forced convection to steam heat transfer and the onset of liquid entrainment were found to be the most influential parameters. The trend to underestimate pressure drops is most likely related to an overestimation of the void fraction below the swell level, which is affected by bundle interfacial shear modelling in non-dispersed flow below the quench front.

In order to simulate pipe branchings, a T-junction model was implemented to simulate the complex flow and phase distribution as well as the pressure loss in the area of such a branch-off. The new model, developed as an extension to the 2-fluid 6-equation system, also incorporates a correlation for the pressure loss and recovery in the main line. In addition, ATHLET was extended by the possibility of accounting for the Reynolds number dependency of form losses. To this end, correlations for the determination of form losses in specific geometries, such as bends and orifices, were implemented, and the option to specify tabulated data with zeta values and according Reynolds numbers was established. Furthermore, the latest version of ATHLET includes a new, dedicated model for simulating compact heat exchangers. This model comprises one- and two-phase heat transfer correlations for plate and helical heat exchangers, enhancing the code's predictive capability for passive safety systems in advanced light water reactors and SMRs.

Concerning the thermo-mechanical modelling of the reactor core, the existing fuel rod model was updated and extended with a thermo-mechanical model that is capable to reproduce the burn-up-dependent densification and swelling of the pellets, as well as the radial relocation of the fuel material. Furthermore, a new gap conductance model was implemented, which enables more detailed simulations of open and closed gaps. The validation of the new fuel rod model against the Halden BWR experiment provided satisfactory results.

The existing methods for quality assurance in program development were expanded by the introduction of new methods, and the code development process was adapted in alignment with current international standards. Two extended and quality assured, new code versions, ATHLET 3.3 and ATHLET 3.4, were released as part of the AC<sup>2</sup> program package and distributed to numerous code users.

## **Kurzfassung**

Das Rechenprogramm ATHLET (**A**nalyse der **T**hermo**H**draulik von **L**Ecks und **T**ransienten) ist ein Programm im Programmpaket AC<sup>2</sup> (**A**THLET, **A**THLET-**C**D, **C**O<sup>2</sup>**C**OSYS). AC<sup>2</sup> dient vorrangig der Simulation thermohydraulischer Prozesse in kerntechnischen Anlagen und wird von zahlreichen Organisationen im In- und Ausland als deterministisches Analysewerkzeug für Forschungsaktivitäten sowie gutachterliche Tätigkeiten zur Behördenunterstützung in kerntechnischen Genehmigungs- und Aufsichtsverfahren genutzt. Das Anwendungsspektrum von ATHLET umfasst Zustände des Normalbetriebs und des anomalen Betriebs, Störfälle wie auch Unfälle. ATHLET wird hauptsächlich von der GRS entwickelt und validiert. Unterstützung erfährt die GRS vor allem von nationalen Partnerorganisation wie bspw. HZDR, HSZG, KIT, IKE, RUB PSS, TUD und TUM.

Übergeordnetes Ziel des vorliegenden Vorhabens ist, den GRS-internen sowie externen Anwendern von ATHLET ein erweitertes, leistungsstarkes, zuverlässiges und anwenderfreundliches Werkzeug zur Verfügung zu stellen, das die Durchführung von Sicherheitsanalysen nach aktuellem Stand von Wissenschaft und Technik für bestehende Kernkraftwerke, für zukünftige, fortschrittliche Reaktoren der Generationen III und III+, für Forschungsreaktoren, sowie für SMR (Small Modular Reactors) erlaubt. Dies unterstützt die GRS auch zukünftig bei ihren Aufgaben, als wichtiger Ansprechpartner zu Fragen der nuklearen Sicherheit aufzutreten und die Bundesregierung zu diesen Fragen kompetent zu beraten. Die in diesem Vorhaben durchgeführten Programmentwicklungen tragen insbesondere dazu bei, eine realistischere Beschreibung von transienten, thermohydraulischen Vorgängen bei Auslegungsstörfällen und Unfällen zu erzielen und somit die Vorhersagegenauigkeit von ATHLET für wassermoderierte Reaktoren und evolutionäre Reaktorkonzepte im (nahen) Ausland sowie für SMR zu verbessern.

## **Einzelzielsetzungen**

Das oben formulierte, übergeordnete Gesamtziel wurde in die folgenden fünf Einzelzielsetzungen untergliedert, die von den fünf wissenschaftlich-technischen Arbeitspaketen des Projekts aufgegriffen wurden. Die Einzelziele umfassten

- den Ausbau und die Ertüchtigung der ATHLET-Modelle zur detaillierten Simulation zweiphasiger Strömungsvorgänge im Kühlsystem von Kernreaktoren. Wesentliche Aspekte betrafen die Konsolidierung und Erweiterung der programm-internen Strömungsbildkarten mit zugehörigen, strömungsbildspezifischen Schließungsgleichungen.

- die Erweiterung von Modellen zur Simulation von zweiphasigen Strömungen in komplexen Geometrien wie T-Stücken oder Abzweigungen.
- die Verbesserung der thermomechanischen Modellierung des Reaktorkerns durch Implementierung eines umfangreich erweiterten Brennstabmodells.
- die Mitarbeit in internationalen Gremien, die Unterstützung von Programmanwendern, die Begleitung und Übernahme von GRS-externen Programmweiterentwicklungen, sowie die Verbesserung der Programmhandhabung.
- die Qualitätssicherung der ATHLET-Programmentwicklung sowie die Freigabe und Verteilung aktualisierter und erweiterter ATHLET Programmversionen.

Die Relevanz dieser Einzelzielsetzungen mit Blick auf Reaktorsicherheitsanalysen sowie die hierzu durchgeführten Arbeiten und erzielten Ergebnisse werden nachfolgend knapp zusammengefasst.

### **Konsolidierung und Erweiterung der programminternen Strömungsbildkarten und Schließungsgleichungen**

Für die Simulation zweiphasiger Strömungszustände im Reaktorkühlkreislauf ist es von besonderer Bedeutung, das vorliegende Strömungsbild korrekt zu bestimmen und geeignete konstitutive Gleichungen für den Wand- und Zwischenphasenaustausch anzuwenden. Arbeitspaket 1 beschäftigte sich mit der Vereinheitlichung der bisher in ATHLET genutzten, modellspezifisch implementierten Strömungsbildkarten mit dem Ziel, dass alle Modelle ein einheitliches Strömungsbild verwenden und dementsprechend konsistente Schließungsgleichungen und Korrelationen sowohl in der Fluidodynamik als auch für den Wärmeübergang zum Einsatz kommen. Zu diesem Zweck wurde ein eigenes Strömungsbildkartenmodul in ATHLET implementiert, das in einem ersten Schritt die beiden wichtigen und detaillierten Strömungsbildkarten der Zwischenphasenreibung und des Zwischenphasenmassen- und -energieaustauschs zusammenführt. Anschließend wurde die Verwendung des zentralen Strömungsbildkartenmoduls auf die Berechnung der Wandreibung ausgedehnt. Hierbei wurde darauf geachtet, dass das vereinheitlichte Modell sich einerseits an etablierten Strömungsbildkarten aus der Literatur orientiert, andererseits aber auch die bisherige Implementierung in ATHLET aufgreift, um die in der Vergangenheit überwiegend zufriedenstellenden Ergebnisse der Programmvalidierung und -anwendung nicht zu gefährden.

Da Kondensationseffekte an Strukturen das Strömungsbild beeinflussen, wird zur Bestimmung des Strömungsbildes und der fluiddynamischen Schließungsgleichungen nun

auch das Wärmeübergangsregime herangezogen. In ATHLET werden folgende drei Wärmeübergangsregime unterschieden: kühlende Strukturen mit Wärmestrom vom Fluid zur Wand, heizende Strukturen mit Wärmestrom von der Wand zum Fluid, und Post-CHF (Critical Heat Flux)-Zustände. Für kühlende Strukturen wurde eine modifizierte Strömungsbildkarte in ATHLET implementiert, da sich Übergangskriterien im Vergleich zu beheizten Wänden unterscheiden. Um den transienten Übergang von kühlenden zu heizenden Zuständen numerisch stabil simulieren zu können, wurde ein allgemeines Interpolationsverfahren für Strömungsbildkarten entwickelt und implementiert, das eine stetige Interpolation zwischen zwei oder auch mehreren Karten erlaubt. Da sich bei Kondensation an kühlenden Wänden häufig das Strömungsbild der Ringströmung ausbildet, wurde dieses in den neuen Strömungsbildkarten berücksichtigt. Außerdem wurden für das Strömungsbild der Ringströmung spezielle Korrelationen zur Simulation von Wand- und Zwischenphasenreibung in horizontalen bzw. horizontalgeneigten Rohren sowie in vertikalen Rohren implementiert. Damit kann die Information des Strömungsbildes auch für die Berechnung des Wandwärmeübergangs Berücksichtigung finden. So werden nun bei Vorliegen einer Ringströmung und Wandkondensation automatisch dedizierte Wärmeübergangsmodelle zur Filmkondensation angesprochen. Kühlende Strukturen spielen vor allem in passiven Sicherheitssystemen wie Wärmetauschern zur Nachwärmeabfuhr und zum Druckabbau eine bedeutende Rolle, so dass die hier durchgeführte Weiterentwicklung insbesondere für die Sicherheitsbewertung von fortschrittlichen, leichtwassergekühlten Reaktoren und SMR von Relevanz ist.

### **Simulation von T-Stücken und Abzweigungen**

Arbeitspaket 2 hatte die Weiterentwicklung von Modellen zur Simulation zweiphasiger Strömungszustände in T-Stücken und Abzweigungen zum Ziel. Die hier auftretenden komplexen, mehrdimensionalen Strömungsphänomene können von einem 1D-Systemrechenprogramm nicht ohne zusätzliche, dedizierte Modelle beschrieben werden. Zu diesem Zweck wurden für das 6-Gleichungssystem von ATHLET neue Modelle zur realistischen Aufteilung der Phasenmassenströme in Abzweigungen wie auch zur adäquaten Berücksichtigung von Strömungsdruckverlusten sowohl im Abzweig als auch in Hauptströmungsrichtung implementiert. Zum Haupteinsatzbereich des neuen Modells zählen einerseits die Abbildung von Strömungsvorgängen in Rohrabzweigungen, bspw. zum Druckhalter oder zu passiven Sicherheitssystemen, sowie andererseits eine realistischere Simulation von Kühlmittelverluststörfällen mit Leckagen in Rohrwandungen oder Brüchen in Anschlussleitungen, welche in ATHLET mittels Abzweigungen modelliert werden.

## **Verbesserung der thermomechanischen Reaktorkernmodellierung**

Eine verbesserte thermomechanische Modellierung des Reaktorkerns stand im Mittelpunkt von Arbeitspaket 3. Zielsetzung der Entwicklung war eine realistischere Simulation der im Kern eingespeicherten Energie, die bspw. im Fall eines Kühlmittelverluststörfalls von zentraler Bedeutung für den Verlauf und das Maximum der Hüllrohrtemperaturen ist. Zu diesem Zweck wurde ein neues thermomechanisches Brennstabmodell in ATHLET implementiert, das verschiedene abbrand- und leistungsabhängige Effekte wie die Verdichtung, das Schwellen, und die fragmentierungsbedingte, radiale Verlagerung des Brennstoffs berücksichtigt. Darüber hinaus wurde das Wärmeübergangsmodell für den Ringspalt zwischen Brennstoff und Hüllrohr erneuert, so dass nun auch Zustände mit geschlossenem Gap und am Hüllrohr anliegendem Brennstoff realistischer simuliert werden können. Optional kann vom Anwender ein radiales Leistungsprofil im Brennstoff vorgegeben werden, um abbrandbedingte Effekte zu berücksichtigen, die zu einem Leistungsspeak im Außenbereich des Pellets führen. Außerdem wurde die Wärmeübergangsberechnung angepasst, so dass eine betrieblich bedingte Oxidationsschicht als zusätzlicher Wärmewiderstand in ATHLET Berücksichtigung findet.

## **Anwenderunterstützung, nationale und internationale Zusammenarbeit**

Arbeitspaket 4 beschäftigte sich mit der Unterstützung der Programmanwender sowie Aspekten der nationalen und internationalen Zusammenarbeit. Ein kontinuierlicher Erfahrungsrückfluss aus der Programmanwendung wurde durch regelmäßige bilaterale Kontakte sowie durch internationale AC<sup>2</sup>-Anwendertreffen sichergestellt. Im Rahmen des Austauschs wurden die Programmanwender und externe Entwickler beraten sowie durch Bereitstellung verbesserter Modelle und Ad-hoc-Entwicklungen unterstützt. Z. B. wurde ein neues Modell zur Berücksichtigung von Reynoldszahl-abhängigen Formverlusten bereitgestellt, oder das Kondensatormodell flexibilisiert. Die Schnittstellen zur Kopplung von Wärmeübergangskorrelationen wurden erweitert, um aktuelle Untersuchungen der Programmanwender bspw. für innovative Reaktorkonzepte zu unterstützen. Ein weiterer Arbeitspunkt betraf die kontinuierliche Verbesserung der Programmhandhabung, hier insbesondere mit Blick auf die Erstellung der Eingabedaten und die Anwenderinformation vor, während und nach einer Simulation. Umfangreiche Prüfungen des Eingabedatensatzes und zusätzliche Programmausgaben wurden ergänzt. Beides wirkt Fehlern bei der Datensatzerstellung entgegen und vereinfacht notwendige Korrekturen.

Darüber hinaus wurden auch außerhalb der GRS erfolgte Programmentwicklungen mit dem Ziel begleitet, diese nach erfolgreichem Abschluss in den Hauptentwicklungsweig

von ATHLET zu integrieren und damit allen Programmnutzern zugänglich zu machen. Im Rahmen dieser Arbeit konnte z. B. ein genaueres Wasser-Dampf-Stoffwertpaket, das von HSZG entwickelt wurde, übernommen werden. Außerdem wurde ein von RUB-PSS entwickeltes Modell zur Simulation helikaler Wärmeübertrager final implementiert und für alle Anwender freigegeben. Helikale Wärmetauscher sind z. B. in einigen aktuellen SMR-Konzepten vorgesehen, so dass diese Entwicklung die Aussagesicherheit von ATHLET für derartige Anwendungen stärkt.

Ein weiterer Aspekt dieses Arbeitspakets betraf die Zusammenarbeit in internationalen Arbeitsgruppen. Neben der Kooperation innerhalb des FONESYS-Netzwerks, das den Austausch mit den Entwicklern verschiedener Systemcodes wie CATHARE, SPACE, APROS oder LOCUST fördert, hat sich die GRS am OECD/NEA Rod-Bundle Heat-Transfer Projekt beteiligt. Die durchgeführten, blinden Nachrechnungen und Unsicherheitsanalysen zu Versuchen aus der RBHT-Anlage der Penn State University dienen der Programmvalidierung mit Fokus auf der Simulation des Flutens des Reaktorkerns. Insgesamt konnte ATHLET die maximalen Hüllrohrtemperaturen und den Zeitpunkt der Wiederbenetzung zufriedenstellend reproduzieren. In manchen Versuchsnachrechnungen konnte jedoch die Vorkühlung der Heizstäbe, die bspw. eine Folge erhöhter Turbulenz, induziert durch Tropfen und Abstandshalter, sein kann, nicht zuverlässig berechnet werden. Außerdem hat sich insgesamt gezeigt, dass ATHLET den Druckverlust im Bündel unterschätzt. Weitergehende Untersuchungen haben die Vermutung bestärkt, dass dies vor allem eine Folge einer nicht zufriedenstellenden Modellierung der Zwischenphasenreibung zu sein scheint.

### **Qualitätssicherung und Freigabe erweiterter ATHLET-Programmversionen**

Im Rahmen von Arbeitspaket 5 wurde die die ATHLET-Programmentwicklung begleitende, kontinuierliche Qualitätssicherung modernisiert und ausgebaut. Hierzu wurde der Softwareentwicklungsprozess unter GitLab neu aufgesetzt und um den Einsatz eines Issue-Trackers, von CMake zur Kompilierung für unterschiedliche Architekturen, sowie von Code-Reviews via Merge-Requests erweitert. Die bestehende CI-Testmatrix wurde von Jenkins nach GitLab migriert. Alle im Rahmen des Projekts durchgeführten Entwicklungen wurden (neben der Prüfung durch dedizierte Testfälle) mittels der Testmatrix der CI-Umgebung zumindest grundlegend validiert. Weitere qualitätssichernde Maßnahmen betrafen das Refactoring des Quellcodes, in dessen Zuge bspw. veraltete Fortran-Sprachkonstrukte ersetzt oder Programmteile restrukturiert wurden. Die Arbeiten dienen einer besseren Les- und Wartbarkeit des Programms und machen die ATHLET-

Entwicklung mit Blick auf neue Anwendungen und die damit verbundene Quellcodeerweiterung zukunftssicher.

Die ATHLET-Programmdokumentation, die aus User's Manual, Models and Methods Manual, Validation Manual, Programmer's Manual, und Program Updates Manual besteht, wurde entsprechend des Entwicklungsfortschritts kontinuierlich fortgeschrieben und gemeinsam mit den neuen Programmversionen an die Nutzer verteilt. Diejenigen Dokumentationsteile, die bisher noch unter der Software Quicksilver/Interleaf gepflegt wurden, wurden nach Latex oder MS Word migriert.

Innerhalb des Projektzeitraums wurden zwei neue ATHLET-Programmversionen, ATHLET 3.3.0 und 3.4.0, sowie zwei Programmpatches fertiggestellt und freigegeben. Der Freigabe gingen jeweils umfangreiche qualitätssichernde Maßnahmen und Validierungsarbeiten voraus, um die Programmzuverlässigkeit und -leistungsfähigkeit sicherzustellen. Mit den neuen Codeversionen wurden zahlreiche neue und verbesserte Modelle allen Anwendern zugänglich gemacht. Als umfangreiche Weiterentwicklungen hervorzuheben sind das neue Modell für kompakte Wärmetauscher (Platten- und helikale Wärmetauscher), das erweiterte Brennstabmodell, die Implementierung zur Berücksichtigung Reynoldszahl-abhängiger Formverluste, sowie neue und genauere Stoffwertbibliotheken zur Simulation verschiedener Arbeitsmedien wie Kalium sowie die Bereitstellung weiterer nicht-kondensierender Gase wie Xenon, Krypton und CO<sub>2</sub>. Mit dem Rechenprogramm ATHLET werden auch zahlreiche Tools zum Pre- und Postprocessing verteilt. Die Tools wurden aktualisiert und um das Python-basierte Plotprogramm batchplot ergänzt. Mit batchplot können sowohl zeit- als auch ortsabhängige Diagramme erstellt werden. Hierfür nutzt das Programm das hdf5-Ausgabedatenformat von ATHLET, das umfangreich erweitert wurde, um dem Postprocessing die benötigten Daten bereitzustellen. Zur Verteilung von ATHLET und seinen Softwarewerkzeugen als Bestandteil von AC<sup>2</sup> wurde die User Area, die als Kommunikationsplattform mit den zahlreichen nationalen und internationalen Programmanwendern dient, von der nicht mehr unterstützten Software OpenAtrium nach Sharepoint migriert.

### **Fazit und Ausblick**

Die im Projekt RS1600 zur *Weiterentwicklung des AC<sup>2</sup>-Programms ATHLET für evolutionäre Reaktoren und Forschungsreaktoren – Phase A* vorgesehenen Themen und Arbeitsschwerpunkte konnten innerhalb der Projektlaufzeit von ca. drei Jahren erfolgreich bearbeitet werden. Alle wichtigen Vorhabensziele wurden erreicht. Gleichzeitig sind nicht alle Entwicklungen abgeschlossen, einige Entwicklungen werden im Rahmen der Projektphase B weitergeführt. Im Rahmen des Projekts wurden mehrere

thermohydraulische Neuentwicklungen gestartet und Modellverbesserungen umgesetzt, um Leistungsfähigkeit und Zuverlässigkeit von ATHLET mit Blick auf ein ständig wachsendes Anwendungsspektrum zu gewährleisten. Die vorgesehenen Entwicklungen zum Brennstabmodell und T-Junction Modell konnten erfolgreich abgeschlossen werden. Die Implementierung vereinheitlichter Strömungsbildkarten wurde umgesetzt. Die Arbeiten zur Nutzung spezifischer Strömungsbildkarten und dedizierter Schließungsgleichungen für weitere Strömungsregime wie bspw. die Ringströmung konnte für kühlende Wände realisiert werden, wobei diese Arbeiten im Rahmen der Projektphase B mit Blick auf heiße Strukturen und Post-CHF-Zustände fortgeführt werden. Ebenfalls weitergeführt wird das OECD/NEA RBHT-Projekt, dessen zweite Phase in 2024 gestartet wurde. Neben der weiteren Validierung der Reflooding-Modelle in ATHLET sind in Projektphase B hierauf aufbauende Modellweiterentwicklungen geplant. Für andere Themen wurde weiterer Verbesserungsbedarf identifiziert, der in möglichen Nachfolgevorhaben weiterverfolgt werden soll.

Die intensive Zusammenarbeit und Unterstützung der Programmanwender wie auch die Kooperation in internationalen Arbeitsgruppen hat wichtige Impulse für die Weiterentwicklung von ATHLET gegeben, die im Projektverlauf aufgegriffen werden konnten und sich in zahlreichen Programmverbesserungen widerspiegeln, die im Zuge der Freigabe neuer Programmversionen bereits zu großen Teilen an alle Anwender von ATHLET verteilt wurden. Die Maßnahmen zur Qualitätssicherung der Programmentwicklung wurden durch fortschrittliche Softwarewerkzeuge, die durch die Einführung von Git als Versionsmanagementsoftware und GitLab als Projektmanagementtool verfügbar wurden, signifikant erweitert. Issue Tracker, Merge-Requests und die integrierte GitLab Continuous Integration ermöglichen effiziente Arbeitsabläufe und fördern durch Vieraugenprinzip und automatisierte Programmverifikation die Qualität der Codeentwicklung.

Insgesamt tragen die im Rahmen des Projekts erzielten Verbesserungen wesentlich dazu bei, den zahlreichen im Umgang mit ATHLET geschulten Anwendern auch zukünftig ein leistungsstarkes, zuverlässiges und anwenderfreundliches Werkzeug zur Verfügung zu stellen, das die Durchführung von Sicherheitsanalysen nach dem neuesten Stand von Wissenschaft und Technik erlaubt. Sowohl mit Blick auf den verfügbaren Modellumfang als auch bezüglich der Programmimplementierung und Dokumentation hat ATHLET einen fortgeschrittenen, qualitätsgesicherten Entwicklungsstand erreicht, wodurch das Rechenprogramm für zukünftige Anwendungen und Weiterentwicklungen auf dem Gebiet der Reaktorsicherheitsforschung gut aufgestellt ist.



# Contents

	<b>Abstract</b> .....	<b>I</b>
	<b>Kurzfassung</b> .....	<b>III</b>
	<b>Contents</b> .....	<b>XI</b>
<b>1</b>	<b>Introduction</b> .....	<b>1</b>
<b>2</b>	<b>Objectives</b> .....	<b>3</b>
2.1	Particular objectives.....	3
2.1.1	Detailed simulation of flow regimes under consideration of the prevailing heat transfer mode.....	3
2.1.2	Improved modelling for the simulation of complex two-phase flow phenomena in the cooling system of nuclear facilities.....	4
2.1.3	Improved heat transfer and thermo-mechanical modelling .....	4
2.1.4	User support and co-operation.....	5
2.1.5	Cross-cutting tasks: quality assurance, documentation and release management.....	5
<b>3</b>	<b>Detailed simulation of flow regimes</b> .....	<b>7</b>
3.1	Unification of the flow regime calculation in ATHLET .....	7
3.1.1	The situation at the start of the project .....	7
3.1.2	Implemented model developments .....	7
3.1.3	Performed test calculations.....	26
3.2	Extension of flow regime maps and closure laws for condensing horizontal flows .....	36
3.2.1	Flow regime maps for condensing flows in horizontal flow path .....	37
3.2.2	Flow regime map transition.....	40
3.2.3	Interfacial friction.....	41
3.2.4	Wall friction.....	44
3.2.5	Verification against COSMEA .....	48
3.3	Extension of closure laws for condensing vertical flows .....	54

3.3.1	Interfacial friction.....	54
3.3.2	Wall friction.....	56
3.3.3	Condensation heat transfer coefficient calculation .....	57
3.3.4	Validation against LOTUS experiment .....	58
3.3.5	Validation against PERSEO experiment .....	61
3.4	Current status in a nutshell .....	65
3.4.1	Application by the user.....	65
3.5	Residual issues and further work .....	69
<b>4</b>	<b>Improved modelling of complex two-phase flow conditions .....</b>	<b>71</b>
4.1	T-Junction Model .....	71
4.1.1	Modelling of centrifugal force term .....	71
4.1.2	Pressure evolution in the T-junction main pipe.....	74
4.1.3	Model activation.....	77
4.1.4	Validation.....	77
<b>5</b>	<b>Thermo-mechanical modelling .....</b>	<b>87</b>
5.1	Improved fuel rod model .....	87
5.2	Model description.....	88
5.2.1	Improved gap conductance model .....	88
5.2.2	Gap conductance model verification .....	95
5.2.3	Radial pellet power profile.....	108
5.2.4	Effects of oxidation layer on heat transfer .....	112
5.3	Summary and future steps.....	114
<b>6</b>	<b>User support and cooperation.....</b>	<b>117</b>
6.1	Model improvements and usability .....	117
6.1.1	Reynolds number dependent form loss calculation .....	117
6.1.2	Momentum-flux calculation .....	123
6.1.3	Wall condensation heat transfer in vertical pipes .....	126
6.1.4	Entrainment calculation in condensation model .....	128
6.1.5	Heat transfer under film boiling conditions .....	129

6.1.6	Improved condenser model .....	129
6.1.7	Further program improvements.....	130
6.1.8	Improvements related to the ATHLET start calculation .....	132
6.1.9	Input data extensions and checks.....	133
6.1.10	Extended program output .....	136
6.1.11	Improved plug-ins interfaces.....	140
6.2	National and international cooperation.....	141
6.2.1	OECD/NEA Rod-Bundle-Heat-Transfer Benchmark .....	141
6.2.2	Cooperation within FONESYS .....	167
6.2.3	Water-steam material properties library SBTL95.....	168
6.2.4	Modelling of helically coiled heat exchanger .....	169
6.2.5	Virtual international AC <sup>2</sup> user meeting 2021 .....	169
6.2.6	Hybrid international AC <sup>2</sup> user meeting 2023.....	170
<b>7</b>	<b>Cross-sectional tasks.....</b>	<b>171</b>
7.1	Quality assurance .....	171
7.1.1	Build process .....	171
7.1.2	Refactoring .....	172
7.1.3	Continuous integration (proposal for new title: Regression testing as part of continuous integration).....	174
7.2	Documentation .....	179
7.3	Release management.....	180
7.3.1	Code versions ATHLET 3.3.x.....	180
7.3.2	Code versions ATHLET 3.4.x.....	183
7.4	User area and code transfer .....	188
<b>8</b>	<b>Conclusions and outlook .....</b>	<b>189</b>
	<b>List of figures.....</b>	<b>197</b>
	<b>List of tables .....</b>	<b>203</b>
	<b>Abbreviations.....</b>	<b>205</b>

<b>Nomenclature.....</b>	<b>206</b>
<b>Literature.....</b>	<b>209</b>

# 1 Introduction

For the safety analysis of transients, incidents and severe accidents in nuclear facilities, simulation codes are applied that provide realistic, so-called best-estimate, results in accordance with the current state of science and technology. The *Federal Ministry for the environment, nature conservation, nuclear safety and consumer protection* (BMUV) promotes the development and validation of such programs within the framework of reactor safety research. On this basis, GRS is developing the AC<sup>2</sup> program package, which includes the three system codes ATHLET, ATHLET-CD and COCOSYS as well as the interactive analysis simulator ATLAS and further tools [WEY 24/]. The main purpose of the system code ATHLET (**A**nalysis of **T**hermohydraulics of **L**Eaks and **T**ransients) is the thermal-hydraulic simulation of the phenomena and processes in the pressure boundary as well as heat removal systems of nuclear facilities. The ATHLET-CD (**C**ore **D**egradation) module provides models for fission product release and for damage and displacement of the reactor core. COCOSYS (**C**ontainment **C**ode **S**ystem) is used to analyse the thermal-hydraulics and the fission product behaviour in the containment.

AC<sup>2</sup> or individual programs of AC<sup>2</sup> are used as a deterministic analysis tool both in Germany and abroad by around 70 organisations for research activities and to support the regulatory authorities in nuclear licensing and supervisory procedures. The main objective of this project was the further development and improvement of the ATHLET thermal-hydraulic system code to keep pace with the evolving state of science and technology in nuclear safety. This allows to provide the numerous national and international code users with a powerful and reliable tool for carrying out safety analyses for a wide range of postulated incidents and nuclear facilities, including current and future (advanced) reactor designs, SMRs, and research reactors. In addition, the robustness of safety assessments made on the basis of simulation results achieved with ATHLET is reinforced.

The project *Further Development of the AC<sup>2</sup> code ATHLET for Evolutionary Reactors and Research Reactors* has been split into two project phases, where phase A is dealt with in RS1600 and phase B in UMRS1615. The report at hand summarizes the results and findings achieved in project phase A.



## **2 Objectives**

ATHLET focuses on the thermal-hydraulic modelling of the cooling systems and heat removal systems of nuclear power plants and research reactors and additionally includes methods for the simulation of neutron kinetic power generation and reactor control systems. It is developed, validated, and applied for the analysis of conditions of normal operation, operational occurrences, design basis accidents and severe accidents in diverse nuclear facility designs. As component of the program package AC<sup>2</sup>, ATHLET is distributed to and used by many organizations, TSOs, research centers and universities in Germany and abroad. As a deterministic analysis tool, the code is employed for research activities as well as for supporting nuclear licensing and supervisory procedures.

The overarching goal of this project was to provide the GRS and its national and international partner organizations a powerful, reliable, and user-friendly simulation tool that permits safety analyses according to the current state of science and technology for existing reactors and nuclear facilities, for advanced Gen III+ generation reactors, for SMR (Small Modular Reactors), and for research reactors. Associated with this, the further development of ATHLET enables the assessment and extension of international safety standards and contributes to the maintenance of competence in the field of nuclear safety in Germany.

### **2.1 Particular objectives**

The aforementioned overarching goal was subdivided into five particular objectives, which were assigned to five scientific working packages. In the following, these particular objectives and the related subjects investigated in project phase A are briefly summarized.

#### **2.1.1 Detailed simulation of flow regimes under consideration of the prevailing heat transfer mode**

For the simulation of two-phase flow conditions in the reactor cooling circuit, it is of particular importance to determine the flow pattern for the flow channel correctly and consistently apply appropriate constitutive equations for wall and interphase transfer. Therefore, the previously model-specific flow regime maps and closing equations should be standardized and expanded with regard to their level of detail. Furthermore, the heat transfer regime should also be considered when determining the flow pattern and the

respective fluid dynamic closure equations. For cooling surfaces, characteristics of dedicated flow maps should be taken into account in ATHLET, since transition criteria may significantly differ when compared to adiabatic or heated walls. Cooling structures, e.g., play an important role in passive safety systems such as heat exchangers for residual heat removal and depressurization. Thus, the detailed determination of flow patterns and their transition criteria for cooling structures is of particular interest for the safety assessment of advanced light water-cooled reactors and SMR and increases the predictive capability of ATHLET for these applications.

### **2.1.2 Improved modelling for the simulation of complex two-phase flow phenomena in the cooling system of nuclear facilities**

The simulation of branchings and tees within a piping network is a challenging task for a computer program, since very complex two-phase flow phenomena are involved that cannot be correctly described by a pure 1D code without a dedicated model. Important processes that can have a decisive influence on the course of a transient or LOCA and, thus, need to be adequately considered are the splitting of the phase mass flows as well as the calculation of the flow losses. In order to properly capture these phenomena, the 6-equation model of ATHLET should be extended by a suitable T-junction model. The main area of application of the T-junction model will be branchings in the coolant network like the surge line, connecting pipes to passive heat removal systems, or the simulation of breaks, e.g., in the wall of a pipe, which are thus perpendicular to the main flow direction.

### **2.1.3 Improved heat transfer and thermo-mechanical modelling**

Main aim of this work package was the improved predictive capability of ATHLET with regard to processes inside the reactor core. Given that in the past safety analyses conducted with ATHLET have occasionally yielded an unreasonable overprediction of the cladding temperatures, it became necessary to considerably enhance the code's thermo-mechanical fuel rod model for best-estimate simulations in the context of BEPU analyses. For this purpose, additional models were implemented to more realistically describe important phenomena and processes relevant to certain design basis accidents.

In particular, the gap width between fuel and cladding, which significantly affects the heat transfer and the energy stored in the fuel, should be determined more realistically. For this purpose, both the radial relocation due to the rupture of the pellets as well as the

burn-up dependent densification and swelling of the fuel should be taken into account. In addition, high-burnup effects that influence the radial power distribution within the pellet, and the operational cladding oxidation that impacts the wall-to-fluid heat transfer should be considered.

#### **2.1.4 User support and co-operation**

In order to ensure the successful application of ATHLET, both ATHLET users as well as GRS-external code developers should be supported. This work comprises ad hoc developments, mainly to enable code application in new areas of interest or to fix program weaknesses, recommendations for input data preparation, and integration of external developments into the main ATHLET development line to provide them to all code users. A further aim of the code development is the continuous increase of the program's user friendliness to prevent potential error sources and to make it easier to fix input errors. Share of experiences should be ensured by regular bilateral contacts and biennial international user meetings held in GRS Garching. Finally, to further contribute to the international state of science and technology in the field of nuclear safety, GRS continued the cooperation within OECD/NEA benchmarks and international working groups like the FONESYS network.

#### **2.1.5 Cross-cutting tasks: quality assurance, documentation and release management**

This work package aimed at the introduction of modern methods and tools for the continuous quality assurance of the ATHLET code development, e.g., by implementing CMake for compilation, and employing code reviews via merge requests and issue trackers. The existing CI test matrix implemented on Jenkins should be migrated to Gitlab and additional tests added to ensure a broader model coverage.

According to the progress of development, the program documentation had to be continuously updated. New ATHLET (and AC<sup>2</sup>) program versions should be periodically released and distributed as installation files (for MS Windows and Linux) to all program users, so that their investigations take benefit from the latest developments and code improvements. The user area, mainly used for communication with the code users and for program distribution, should be maintained, continuously updated, and moved to a future-proof software platform.



### **3 Detailed simulation of flow regimes**

#### **3.1 Unification of the flow regime calculation in ATHLET**

##### **3.1.1 The situation at the start of the project**

As known prior to the start of the project, various ATHLET models, such as the interfacial shear model or the bulk condensation model, make use of flow pattern maps with different levels of detail and different transition criteria. All these flow pattern maps are implemented *independently* within the respective models. A review of the ATHLET source code and accompanying documentation (such as the ATHLET model description) revealed that correlations for the calculation of related physical quantities, namely the entrained liquid fraction, i.e., the fraction of the liquid flow rate that is transported as suspended droplets, as well as the local relative phase velocities, are implemented independently, too. The resulting minor issue is redundancy in the implementation, which makes maintaining the code unnecessarily harder; the major issue are inconsistencies which are introduced by the fact that the independently implemented correlations differ from each other – it can happen that the condensation rate in a control volume is calculated based on the assumption of another flow regime than the wall friction or interfacial shear in the same control volume.

Thus, one of the main objectives of the performed work was to centralize the flow regime calculation, thereby obtaining a global, unified flow pattern map which could be used consistently in various other ATHLET models.

##### **3.1.2 Implemented model developments**

Against the background described above, the following model developments were carried out:

- Unification and centralization of previously independently implemented models:
  - The calculation of the entrained liquid fraction was unified and centralized.
  - The calculation of the local relative phase velocity was unified and centralized.
  - The flow regime calculation was unified and centralized.

- The calculation of the interfacial area was adapted. The centralization is not yet complete.
- Consideration of the unified and centralized flow regime information in fluid-dynamic models:
  - The interfacial shear model was adapted so that it uses the centrally calculated flow regime information.
  - The bulk condensation and evaporation model was adapted so that it uses the centrally calculated flow regime information.
  - The wall friction model was partially adapted so that the information on the flow pattern is used where reasonable.
  - The wall heat transfer model was partially adapted so that the information on the flow pattern is used where reasonable.

The work related to the first bullet point, the unification and centralization of implemented models, is described in more detail in the following subsections.

All model developments were closely accompanied by test calculations – on the one hand to ensure that the code modifications do not compromise the general executability of ATHLET and on the other hand to detect and reduce deviations in simulation results produced by the released ATHLET version (which successfully underwent a comprehensive validation procedure) and by the development branch. Particularly the second objective is almost impossible to achieve, as it turned out that even small changes in the treated models can have significant effects on the calculated transients. Thus, the simulations were also compared to experimental results to assess whether the results became worse, were acceptable, or became better.

Regarding the programming style, emphasis was placed on separating newly implemented model routines containing correlations – e.g. for determining the flow pattern or calculating the entrained liquid fraction – from the ATHLET-specific data so that the model routines can be easily verified or used in a unit test.

### 3.1.2.1 Calculation of the entrained liquid fraction

The entrained liquid fraction affects various ATHLET models in the steady state calculation (SSC) as well as in the transient calculation (and there both in the 5- and 6-equation formulation). ATHLET contains various correlations for the calculation of the entrained liquid fraction (see /SCH 23a/) which have been implemented locally so far. Fig. 3.1 shows the entrained liquid fraction plotted against the void fraction for horizontal and vertical flow paths as calculated by various ATHLET correlations. The diagrams include no legends as the purpose of the figure is to demonstrate the diversity of the predicted entrained liquid fractions, but not to analyze the correlations in detail. Note that, especially for vertical flow paths, the evaluated correlations are applicable for certain geometries only (e.g., pipes, bundles, or annuli) and the observed variability is not necessarily a contradiction.

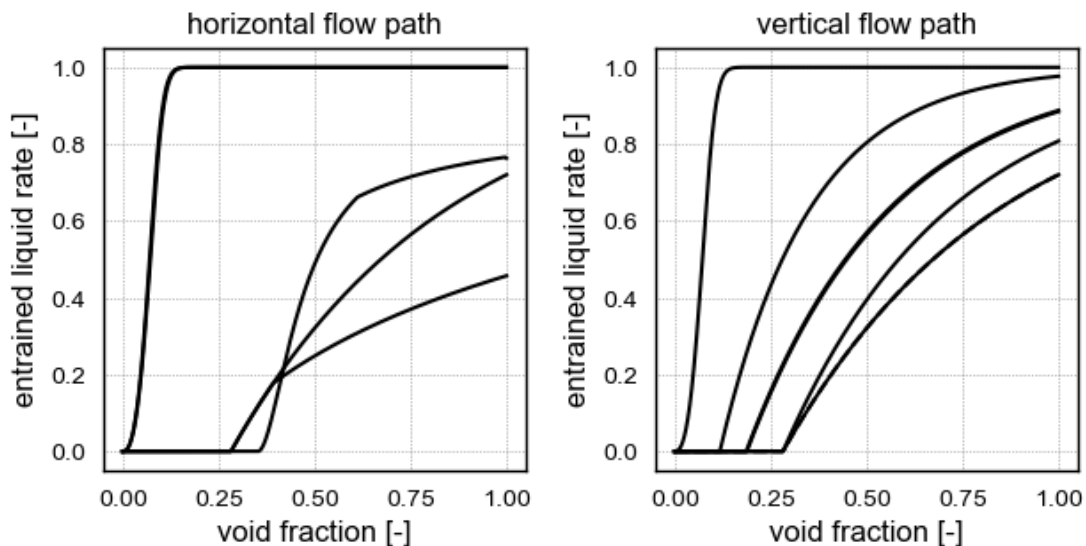


**Fig. 3.1** Entrained liquid fraction vs. void fraction for horizontal (left) and vertical (right) flow paths as calculated by various ATHLET correlations at  $p = 65 \text{ bar}$  and saturation conditions and for the assumed phase velocities  $u_l = 5 \text{ m/s}$  and  $u_v = 10 \text{ m/s}$

Within the current project, the local implementations of these correlations have now become unified and centralized so that all models which need the entrained liquid fraction as an input for further calculations – such as the condensation model or the interfacial shear model – use *the same value* now.

In test calculations accompanying the development, it was found that not all entrainment correlations in their current form are suitable for a centralized usage in ATHLET for reasons of numerical stability. Especially such correlations, which predict a rapid change of the entrained liquid fraction when the boundary conditions change, may lead to oscillating shear forces or condensation rates, which in turn enforce unacceptably small integration time steps or even lead to program crashes. In the latest program version, the correlations listed in the following subsections are applied due to their good-natured effect on the numerics. As can be seen, the shape of the correlations for horizontal and vertical flow is the same; due to the history of ATHLET as a code for the calculation of the primary circuit of nuclear reactors, the correlation for vertical flow is a bit more elaborate and distinguishes several geometry cases.

### 3.1.2.1.1 Horizontal flow

Independent of the flow path geometry, the entrained liquid fraction is calculated by the modified Pan and Hanratty correlation as described in detail in /LEE 22a/. The entrained liquid fraction  $E_d$  is calculated by evaluating

$$\frac{E_d/E_{d,max}}{1 - E_d/E_{d,max}} = 2 \times 10^{-7} \left( \frac{D(u_v - u_{v,e})^2 u_v (\rho_v \rho_l)^{1/2}}{u_T \sigma} \right) \quad (3.1)$$

where the maximum entrainment fraction  $E_{d,max}$  depends on the superficial liquid Reynolds number,  $Re_{sl}$ , and the Reynolds number of critical film flow,  $Re_{crit,F}$ :

$$E_{d,max} = 1 - \frac{Re_{crit,F}}{Re_{sl}} \quad (3.2)$$

The onset of entrainment is supposed to occur when the superficial vapor velocity  $u_{vs}$  exceeds a critical velocity  $u_{crit} = \alpha \cdot u_{v,e}$  given by

$$u_{crit} = \max(u_{crit,1}, u_{crit,2}) \quad (3.3)$$

where

$$u_{crit,1} = 0.5 \sqrt{\frac{(\rho_l - \rho_v)g\alpha A}{\rho_v d}} \quad (3.4)$$

and

$$u_{crit,2} = \begin{cases} \frac{\sigma}{\mu_l} N_\mu^{0.8} \sqrt{\frac{\rho_l}{\rho_v}} & 1635 < Re_{sl} \\ \frac{\sigma}{\mu_l} 11.78 Re_{sl}^{-1/3} N_\mu^{0.8} \sqrt{\frac{\rho_l}{\rho_v}} & Re_{sl,lim} < Re_{sl} \leq 1635 \end{cases} \quad (3.5)$$

with

$$N_\mu = \min \left[ \frac{\mu_l}{\left( \rho_l \sigma \sqrt{\frac{\sigma}{g\Delta\rho}} \right)^{1/2}}, \frac{1}{15} \right] \quad (3.6)$$

For more information on the modified Pan and Hanratty correlation, refer to /LEE 22a/ or /SCH 23a/.

### 3.1.2.1.2 Vertical flow

The entrained liquid fraction is for most flow path geometries calculated as

$$E_d = 1 - e^{-0.5 \frac{u_{crit} - u_{vs}}{u_{crit}}} \quad (3.7)$$

Only for the special case of a core inlet orifice of a BWR bundle, it is calculated as

$$E_d = 1 - e^{0.23 \cdot (u_{crit} - u_{vs})} \quad (3.8)$$

The critical velocity for onset of entrainment is given by

$$u_{crit} = f \cdot \sqrt{\frac{\rho_l}{\rho_v}} \quad (3.9)$$

with

$$f = \begin{cases} 0.25 & \text{for flow through a bundle} \\ 0.4 & \text{for annuli} \\ 0.6 & \text{in all other cases} \end{cases} \quad (3.10)$$

As for horizontal flow paths, no entrainment is assumed for void fractions below  $\alpha = 0.5$ .

### 3.1.2.2 Calculation of the local relative phase velocity

The relative velocity between the liquid and gaseous phase calculated by ATHLET is an average value for the treated junction or CV. For the calculation of interfacial shear stress however, the *local* relative velocity is decisive. In annular mist flow, for example, the velocity of the liquid in the annular film is not necessarily the same as the velocity of the liquid droplets. Consequently, the local relative phase velocities at the film and the droplet surfaces may differ from each other and from the average relative phase velocity. The local relative phase velocities are calculated in ATHLET by means of correlations which have been derived from drift-flux theory. They are described in /SCH 23a/ /SKO 01/ /SON 89/.

Analogous to the entrainment calculation, the previously independently implemented correlations for the calculation of the local relative phase velocity have been unified and centralized. Thus, inconsistencies regarding the relative velocities used in various models have been eliminated.

In the latest program version, the local relative phase velocity is calculated as a function of the phase velocities  $u_l$  and  $u_v$ , the parameter  $C_0$ , and the factor  $Z_{C_0}$ :

$$u_{r,loc} = Z_{C_0} \cdot u_v - C_0 \cdot u_l \quad (3.11)$$

$$u_{r,loc} = Z_{C_0} \cdot u_v - C_0 \cdot u_l \quad (3.12)$$

As stated above,  $C_0$  and  $Z_{C_0}$  are calculated by means of correlations which have been derived from drift-flux theory, see /SCH 23a/ for detailed information. The unified model considers:

- horizontal flow paths
- vertical flow paths
  - bundles
  - annuli
  - all other geometries

### **3.1.2.3 Flow regime calculation**

The flow regime calculation has been unified and centralized, too. As stated at the beginning of section 3.1, the various independently implemented maps exhibit different levels of detail as well as different transition criteria. Consequently, the resolution of a unified flow regime map must be as high as (or even higher than) that of the integrated flow regime map with the highest level of detail in order to capture all desired phenomena. The flow regime maps used in the latest program version are described in subsection 3.1.2.3.1.

Due to the involved physical phenomena, no one-fits-all flow regime map exists. For example, even if two pipes are perfectly similar regarding their geometry data, the flow regime transitions in these pipes will look differently if one pipe is heated from the outside while the other one is cooled. Therefore, various flow regime maps have to be implemented dedicated to various boundary conditions (see section 3.2.1). In order to avoid numerical problems, the transition from one flow regime map to another in the case of varying boundary conditions has to be smooth. To achieve this, a smoothing or blending algorithm has been implemented which is described in subsection 3.1.2.3.2.

### 3.1.2.3.1 Implemented flow regime maps

In a first step, two central flow regime maps were implemented – one for horizontal and one for vertical flow paths. Just as the “old” ATHLET maps which are the foundation for the “new”, centralized ones, both flow regime maps are oriented towards the well-known maps of Taitel and Dukler /TAI 76/ for horizontal flow and Taitel, Barnea and Dukler /TAI 80/ for vertical flow. In case that the transition criteria used in the “old” ATHLET maps contradicted those figured out by Taitel et al., preference was given to the ATHLET criteria – not because these are better at predicting flow regime transitions, but because they have proven to work numerically stably in the specific code and to produce sufficiently accurate results in the past. While this approach helps reducing the deviation of the ATHLET version with centralized flow regime maps from the latest released program version ATHLET 3.4.1, it may lead to flow regime predictions which contradict established flow regime maps or experimental observation. Presumably the most striking example is the treatment of the entrainment rate and thus of mist flow (a.k.a. droplet flow) in ATHLET: In calculations performed within the frame of a benchmark activity dedicated to the investigation of horizontal two-phase flows in Mantilla and TPTF experiments, ATHLET predicted the existence of a “stratified-mist” flow regime, which was not observed in the experiments and which is also not included in popular flow regime maps, see /LAN 22a/.

For reasons of numerical stability, the implemented flow regime maps allow for smooth flow regime transitions (e.g., from stratified flow to slug flow) during a transient. To achieve this, transition regions were introduced instead of sharp flow regime boundaries and the routines containing the flow regime maps do not return a single discrete flow regime for a given set of boundary conditions, but instead calculate a vector  $\vec{p}$  which contains the totality of the characteristics of all flow regimes, normalized to 1. This means, for example, that a flow in a transition region can be characterized as 30% annular, 10% intermittent<sup>1</sup> and 60% stratified at the same time; the corresponding vector looks like this:

---

<sup>1</sup> The term “intermittent flow” is used here and in the following as generic term comprising slug, plug, and churn flow.

$$\vec{p} = \begin{pmatrix} p_{\text{stratified}} \\ p_{\text{annular}} \\ p_{\text{bubbly}} \\ p_{\text{intermittent}} \\ p_{\text{droplet}} \\ p_{\text{pure\_liquid}} \\ p_{\text{pure\_gas}} \end{pmatrix} = \begin{pmatrix} 0.6 \\ 0.3 \\ 0 \\ 0.1 \\ 0 \\ 0 \\ 0 \end{pmatrix} \quad (3.13)$$

Below, the implemented flow regime transition criteria for horizontal and vertical flow paths are given in the form of equations. “Maps” can be created by drawing the graphs of these equations in a coordinate system with the superficial gas velocity  $u_{gs}$  on the abscissa axis and the superficial liquid velocity  $u_{ls}$  on the ordinate axis as it is done in section 3.1.3.1.

### 3.1.2.3.1.1 Horizontal flow

The implemented horizontal flow regime map is oriented towards the one presented in /TAI 76/ albeit with some differences. Fig. 3.2 shows the computation tree for the map together with the considered flow regimes. First, a criterion is evaluated to check whether the flow regime in a CV or junction can be (partially) characterized as droplet flow. The corresponding ratio is saved in  $w_{\text{droplets}}$  which equals  $p_{\text{droplets}}$ . Then, another criterion is checked whether the *remaining* flow can be (partially) characterized as stratified flow. The corresponding ratio is saved in  $w_{\text{stratified}}$ . Consequently, the overall value of the flow that can be characterized as stratified is  $p_{\text{stratified}} = (1 - w_{\text{droplets}}) \cdot w_{\text{stratified}}$ . Hereafter, a criterion for annular flow is checked and finally a distinction between bubbly and intermittent flow is made. This means that the absolute value of the flow that can be characterized as intermittent is

$$p_{\text{intermittent}} = (1 - w_{\text{droplets}}) \cdot (1 - w_{\text{stratified}}) \cdot (1 - w_{\text{annular}}) \cdot (1 - w_{\text{bubbly}}).$$

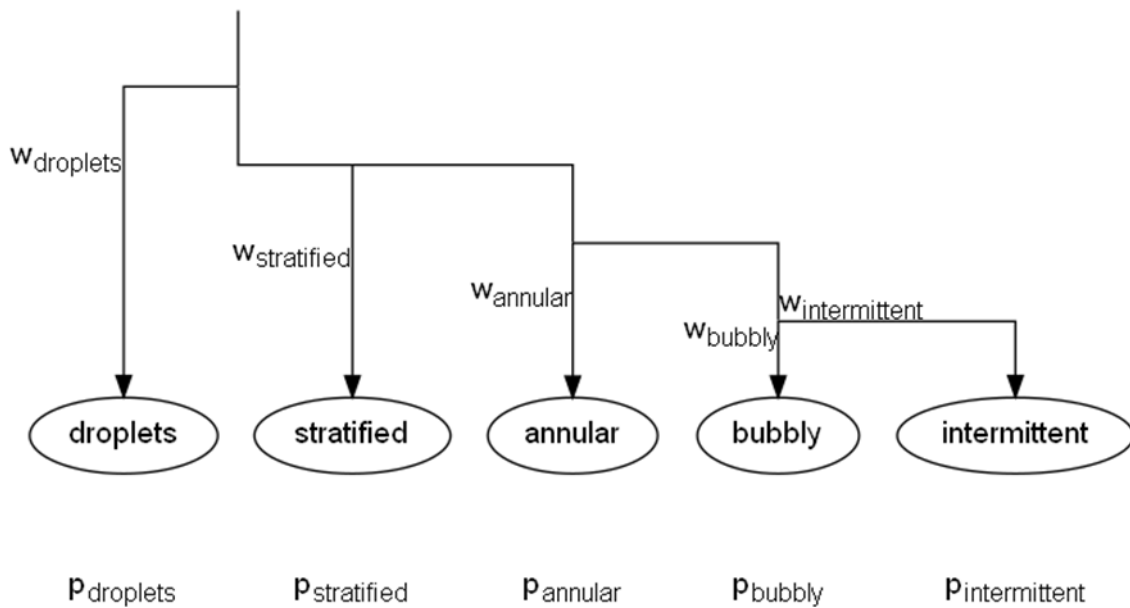


**Fig. 3.2** Decision tree with considered flow regimes for horizontal flow

The implemented transition criteria are described in the following. For a deeper insight in the reasoning behind the criteria, see /TAI 76/ and /SCH 23a/. Some variables occurring in the equations below, which represent geometric quantities, are depicted in Fig. 3.3.

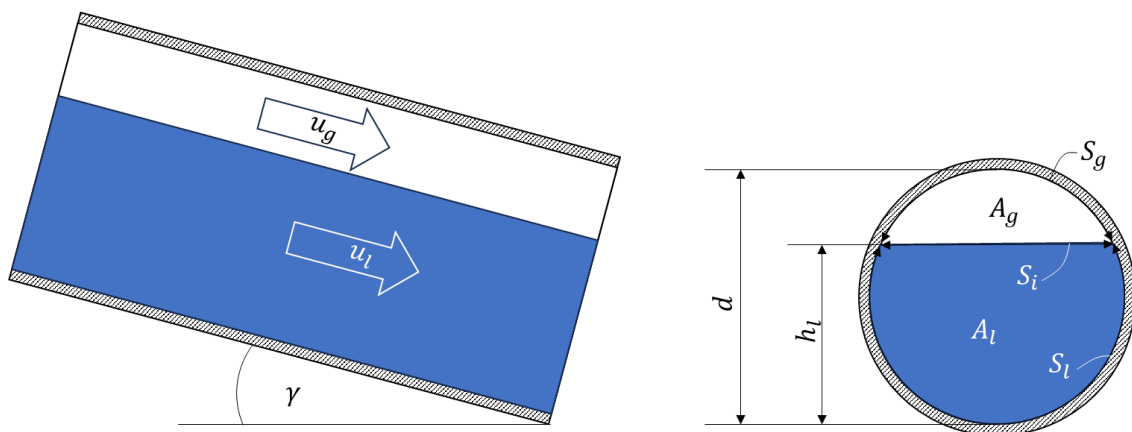


**Fig. 3.3** Variable symbols in stratified flow (graphic based on /TAI 76/)

### Droplet flow vs. non-droplet flow

The fraction of the flow pattern, which is identified as droplet flow, equals the entrained liquid fraction described in section 3.1.2.1.1. That means if the entrained liquid fraction is calculated to be 20%, it is assumed that  $p_{droplet} = 0.2$ .

### Stratified vs. non-stratified flow

For both the liquid and the gaseous phase, transition criteria are formulated in terms of critical velocities. The critical velocity for the gaseous phase is implemented as

$$u_{g,crit} = \min(u_{g,crit,1}, u_{g,crit,2}) \quad (3.14)$$

with

$$u_{g,crit,1} = \left(1 - \frac{h_l}{d}\right) \cdot \left[ \frac{(\rho_l - \rho_g) \cdot g \cdot \cos \gamma \cdot A_g}{\rho_g \cdot \frac{dA_l}{dh_l}} \right]^{\frac{1}{2}} \quad (3.15)$$

$$u_{g,crit,2} = 23.3 \cdot \left[ \frac{\sqrt{(\rho_l - \rho_g) \cdot \sigma \cdot We_{d,crit}}}{\rho_g} \right]^{\frac{1}{2}} \quad (3.16)$$

The meaning of the geometric quantities  $d$ ,  $h_l$ ,  $A_l$ ,  $A_g$ , and  $\gamma$  is explained in Fig. 3.3.  $We_d$  is the Weber number describing the ratio of the drag force and cohesion force acting on a droplet. In the code,  $We_{d,crit} = 4$  is set for the critical Weber number as this value has been used in ATHLET for many years now and proved to give acceptable results.

The critical velocity for the liquid phase is implemented as

$$u_{l,crit} = \max(10^6 \text{ m/s}, u_{l,crit}) \quad (3.17)$$

with

$$u_{l,crit} = 23.3 \cdot \left[ \frac{\sqrt{(\rho_l - \rho_g) \cdot \sigma \cdot We_{b,crit}}}{\rho_l} \right]^{\frac{1}{2}} \quad (3.18)$$

The critical Weber number of the bubble is set to  $We_{b,crit} = 7.5$ , a value which has been used in ATHLET for many years, too.

For both phases, the actual velocity is compared with its critical value. If at least one phase velocity is very low, namely

$$u_\varphi \leq u_{\varphi,crit} \quad (3.19)$$

the flow is assumed to be purely stratified, i.e.,  $w_{stratified} = 1$ . If both phase velocities are very high, namely

$$u_\varphi \geq 2 \cdot u_{\varphi,crit} \Big|_{\text{for } \varphi=l,g'} \quad (3.20)$$

the flow is defined as clearly not stratified, i.e.,  $w_{stratified} = 0$ . For the case

$$u_{\varphi,crit} < u_\varphi < 2 \cdot u_{\varphi,crit} \quad (3.21)$$

the flow is partially stratified and a smooth transition between  $w_{stratified} = 0$  and 1 is implemented. In many cases, the comparison of the liquid velocity with its critical value will yield another stratification ratio than the respective comparison for the gaseous phase (e.g.,  $w_{stratified} = 0.3$  as a result of the “liquid comparison” and  $w_{stratified} = 1$  as a result of the “gaseous comparison”). If so, the smaller value takes precedence (i.e.,  $w_{stratified} = 0.3$  in the example).

### **Annular vs. non-annular flow**

For this flow regime transition, a void fraction-dependent criterion is implemented:

For low void fractions

$$\alpha < 0.5 \quad (3.22)$$

the flow cannot be annular. For high void fractions

$$\alpha > 0.75 \quad (3.23)$$

the flow is purely annular. For values in-between both void fraction limits, a smooth interpolation is applied. The lower void fraction limit corresponds to the onset of entrainment mentioned in 3.1.2.1.1, thereby taking the fact into account that droplet flow usually occurs together with annular flow. Nevertheless, due to the structure of the decision tree depicted in Fig. 3.2, stratified-mist flow can theoretically be calculated by ATHLET if the critical velocity given by equation (3.3) is higher than that calculated by equations (3.14) and (3.17).

### Bubbly vs. intermittent flow

The transition criterion between intermittent and dispersed bubble flow is

$$u_{l,crit} = \left[ \frac{4 \cdot A_g \cdot g \cdot \cos \gamma}{S_i} \cdot \left(1 - \frac{\rho_g}{\rho_l}\right) \cdot \sqrt{\frac{\left(\frac{d_l}{v_l}\right)^n}{C_l}} \right]^{\frac{2}{2-n}} \quad (3.24)$$

The friction factor coefficient is set the constant value  $C_l = 0.046$  and the exponent to  $n = 0.2$ ; this corresponds to the assumption of turbulent flow, cf. /TAI 76/.  $d_l$  is the hydraulic diameter of the liquid phase and calculated as  $d_l = 4 \cdot (A_l/S_l)$ , see Fig. 3.3.

At liquid velocities higher than  $u_{l,crit}$ , the gas phase is dispersed into bubbles whereas at lower velocities, gas can accumulate at the top of the pipe and intermittent flow is assumed. In contrast to the other flow regime transitions, bubbly and intermittent flow are implemented to be mutually exclusive, i.e., no smooth interpolation between these two regimes is performed. This does not induce numerical problems because the

ATHLET models, since the ATHLET models care for a steady transition between bubbly and intermittent flow.

### 3.1.2.3.1.2 Vertical flow

The implemented vertical flow regime map is – with some major differences – oriented towards the one presented in /TAI 80/. The computation tree for the map including the considered flow regimes is shown in Fig. 3.4. The calculation logic is analogous to the horizontal flow regime maps. The implemented transition criteria are described in the following. For a deeper insight in the reasoning behind the criteria, see /TAI 80/ and /SCH 23a/.

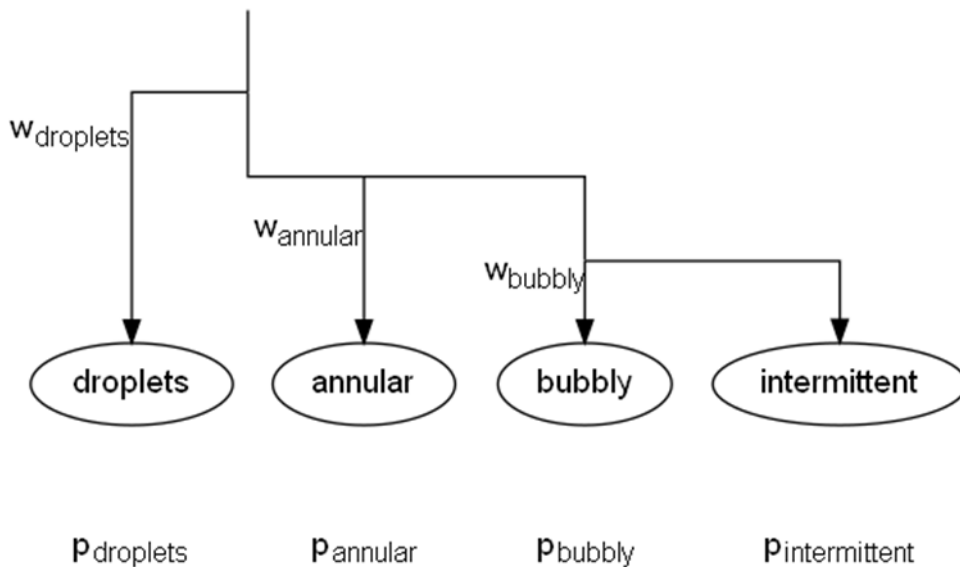


**Fig. 3.4** Decision tree with considered flow regimes for vertical flow

#### **Droplet flow vs. non-droplet flow**

The fraction of the flow pattern which is identified as droplet flow equals the entrained liquid fraction described in section 3.1.2.1.2.

#### **Annular vs. non-annular flow**

For this flow regime transition, the same void fraction-dependent criterion as reported in section 3.1.2.3.1.1.3 for horizontal flow is implemented.

## Bubbly vs. intermittent flow

For the transition between intermittent and dispersed bubble flow, two criteria are checked.

The first criterion is dependent on the flow path diameter and the void fraction: If the flow path diameter is large enough to fulfill the inequality

$$\left[ \frac{\rho_l^2 \cdot g \cdot d^2}{(\rho_l - \rho_g) \cdot \sigma} \right]^{\frac{1}{4}} > 4.36 \quad (3.25)$$

and the void fraction is

$$\alpha < 0.2, \quad (3.26)$$

it is assumed that  $w_{\text{bubbly}} = 1$ . On the other hand, if  $d$  is too small or

$$\alpha > 0.35, \quad (3.27)$$

it is assumed that  $w_{\text{bubbly}} = 0$ . For diameters large enough to fulfill (3.25), and void fractions between 0.2 and 0.35,  $w_{\text{bubbly}}$  is smoothly interpolated.

The second criterion concerns the superficial liquid velocity of the flow<sup>2</sup>. If

$$u_{ls} > \max(u_{ls,crit,1}, u_{ls,crit,2}) \quad (3.28)$$

with:

---

<sup>2</sup> Actually, equation (3.30) is a re-formulated void fraction criterion under the assumption that the phase slip velocity can be neglected for high flow rates.

$$u_{ls,crit,1} = 4 \cdot \left\{ \frac{d^{0.429} \cdot \left(\frac{\sigma}{\rho_l}\right)^{0.089}}{\nu_l^{0.072}} \cdot \left[ \frac{g \cdot (\rho_l - \rho_g)}{\rho_l} \right]^{0.446} \right\} - u_{gs} \quad (3.29)$$

$$u_{ls,crit,2} = \frac{1 - 0.52}{0.52} \cdot u_{gs} \quad (3.30)$$

$w_{bubbly}$  is always set to 1 – regardless of the outcome of the evaluation of the first criterion given with equations (3.25) to (3.27).

### 3.1.2.3.2 Blending algorithm

As has been said, in the case of varying boundary conditions, the transition from one flow regime map to another has to be smooth in order to avoid numerical problems; this is achieved by a blending algorithm. The blending algorithm is described in detail in /CRO 23/. It allows for generic blending of an arbitrary number of flow regime maps and is easily extensible to account for additional boundary conditions which might be considered in future code versions. Its correct functionality has been verified by unit test-like program runs.

The general idea may be described best by means of an example<sup>3</sup>: If we assume that dedicated flow regime maps are applied for

- horizontal flow, if the inclination angle of a pipe is less than 10°,
- vertical flow, if the inclination angle of a pipe is more than 30°,
- condensation, if the pipe wall temperature is more than 1 K below the saturation temperature of the fluid mixture,
- adiabatic walls, if the pipe wall temperature equals exactly the saturation temperature,

---

<sup>3</sup> Note that the boundary conditions given in the example do not necessarily reflect the actual implementation but are rather simplified numbers for the sake of explanation.

and the program faces a situation, in which the wall temperature is 0.6 K below the saturation temperature of the fluid mixture and the pipe inclination is 18°, ATHLET will evaluate all of the four mentioned maps, thus obtaining four different vectors  $\vec{p}$ , which are finally merged by smooth interpolation algorithms into a single resulting vector holding the ratios of each flow regime.

#### 3.1.2.4 Interfacial area calculation

As soon as the flow regime is identified, the interfacial area can be calculated. Therefore, its calculation – previously locally implemented in ATHLET’s condensation model – has been modified to take into account the global flow regime data. However, the calculation has yet to be centralized and the resulting interfacial area applied in all affected models; this might be done within the frame of a future development project.

For the interfacial area calculation, it is first pretended that only pure flow regimes are existent. For these pure flow regimes, the interfacial area is calculated and afterwards weighted by the abovementioned vector  $\vec{p}$  which holds the fractions of the contributing flow regimes.

##### 3.1.2.4.1 Bubbly flow

Under the assumption of a spherical shape, the interfacial area of a single bubble is

$$A_b = 4 \cdot \pi \cdot r_b^2. \quad (3.31)$$

If  $n_b$  bubbles are present in the treated CV, the total interfacial area is

$$A_b = 4 \cdot \pi \cdot r_b^2 \cdot n_b. \quad (3.32)$$

The volume occupied by all bubbles in a CV is

$$V_b = \frac{4}{3} \cdot \pi \cdot r_b^3 \cdot n_b = V_{CV} \cdot \alpha \quad (3.33)$$

if it is assumed that the whole vapor/gas exists in the form of bubbles, i.e., pretending that the flow regime is purely bubbly.

Solving this equation for  $n_B$  and inserting it into equation (3.32) finally yields

$$A_{\text{bubbly}} = \frac{6 \cdot V_{CV} \cdot \alpha}{d_b} \quad (3.34)$$

As in previous ATHLET versions, the bubble diameter  $d_b$  is calculated according to a correlation of uncertain origin (presumably, an in-house development based on validation).

#### 3.1.2.4.2 Droplet flow

Droplet flow is treated analogously to bubbly flow, yielding

$$A_{\text{droplet}} = \frac{6 \cdot V_{CV} \cdot (1 - \alpha)}{d_d} \quad (3.35)$$

#### 3.1.2.4.3 Stratified flow

Stratified flow occurs only in horizontal or slightly inclined pipes. The interfacial area is the product of the chord length  $S_i$  (see Fig. 3.3), which can be calculated as a function of the void fraction, the pipe diameter, and the CV length  $l_{CV}$ :

$$A_{\text{strat}} = S_i \cdot l_{CV} \quad (3.36)$$

This equation is applied for both purely stratified and stratified-wavy flow.

#### 3.1.2.4.4 Annular flow

A consideration of the water volume in a CV for purely annular flow results in the film thickness being a function of the pipe diameter  $d$  and the void fraction:

$$\delta_F = \frac{d}{2} \cdot (1 - \sqrt{\alpha}) \quad (3.37)$$

The interfacial area is

$$A_{\text{annular}} = l_{CV} \cdot \pi \cdot (d - 2 \delta_F) = l_{CV} \cdot \pi \cdot d \cdot \sqrt{\alpha} \quad (3.38)$$

However, the usage of equation (3.38) in the code led to numerical problems as the interfacial area does not approach zero when  $\alpha \rightarrow 1$ . For this reason, an alternative expression for the interfacial area has been implemented:

$$A_{\text{annular}} = \frac{V_{CV} \cdot (1 - \alpha)}{\max(\delta_F, 0.0005 \text{ m})} \quad (3.39)$$

#### 3.1.2.4.5 Intermittent flow

In the current ATHLET implementation, slug, plug, and churn flow are subsumed as “intermittent” flow. The interfacial area calculation for this flow regime is based on the following simplified consideration: When a gas plug or a liquid slug moves through the respective other phase, its front and end parts are assumed to have a spherical shape, see Fig. 3.5. Consequently, the interfacial area is estimated as

$$A_{\text{intermittent}} = \pi \cdot d^2 \quad (3.40)$$

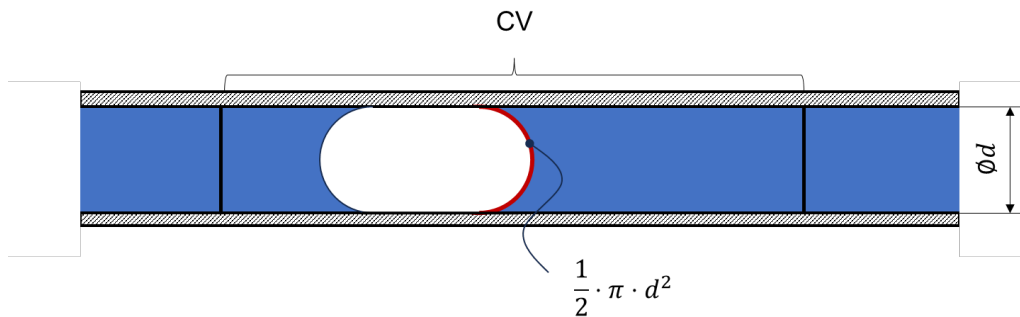


**Fig. 3.5** A gas plug moving through pipe filled with liquid

For a smooth transition to other flow regimes, the implementation considers bubbly and droplet flow as well:

$$A_{\text{intermittent}} = \min(2 \cdot \pi \cdot d^2, A_{\text{bubbly}}, A_{\text{droplet}}) \quad (3.41)$$

### 3.1.3 Performed test calculations

Two types of test calculations were performed:

- Calculations to investigate the implemented flow regime maps with regard to their flow pattern predictions; this includes stand-alone unit test-like runs of the subroutines containing the implemented flow regime transition criteria as well as ATHLET runs for simple flow path geometries, see section 3.1.3.1.
- Calculations for testing the modified ATHLET program for general operability and performance under a wide range of typical boundary conditions, see section 3.1.3.2.

#### 3.1.3.1 Investigation of the implemented maps

In the following, the implemented maps for horizontal and vertical flow paths are compared with the established maps presented from /TAI 76/ and /TAI 80/.

In stand-alone tests of the subroutines, the boundary conditions – especially the phase velocities – are fixed and given as input parameters. The void fraction, which depends on the phase slip ratio, is calculated by evaluating the shear stress correlations given in /TAI 76/ and /TAI 80/. This way, a “true” comparison of the flow regime transition criteria included in ATHLET and those given by Taitel et al. is possible.

On the downside, the results of the stand-alone tests do not represent the flow regime predictions made by ATHLET using the flow regime maps because the shear stress correlations implemented in ATHLET differ from those given by Taitel et al. A comprehensive comparison of flow regime *maps* (and not only of *transition criteria*) must include the actually used shear stress correlations since there is a feedback loop between the flow regimes and the interfacial shear stress as shown in Fig. 3.6. Therefore, very simple data sets with horizontal and vertical flow paths have been created and simulated using ATHLET. The simulation results have been compared with /TAI 76/ and /TAI 80/, too.

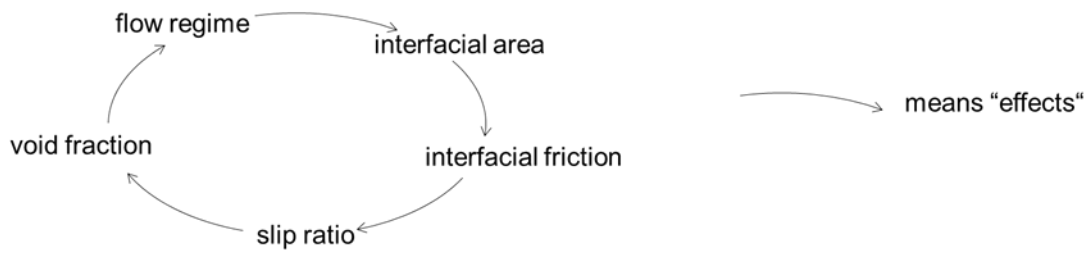


**Fig. 3.6** Feedback loop showing how the flow regime effects the interfacial friction and vice versa

### 3.1.3.1.1 Horizontal flow

#### 3.1.3.1.1.1 Stand-alone flow regime routine test

Using the superficial phase velocities  $u_{gs}$  and  $u_{ls}$  as varying input parameters, the subroutine containing ATHLET's horizontal flow regime map was called from a driver program. For each combination  $(u_{gs}, u_{ls})$ , the subroutine returned a vector  $\vec{p}$  describing the relative flow regime distribution (for an explanation of  $\vec{p}$ , see the example in equation (3.13)). If an element of  $\vec{p}$  is larger than 0.5, it indicates the flow regime, which has an absolute majority and dominates the other flow regimes. In equation (3.13), this would be the first element, meaning that the flow is predominantly stratified and can be classified accordingly.

Fig. 3.7 shows the results of mapping  $(u_{gs}, u_{ls})$  to a flow regime in comparison with the flow regime map of Taitel and Dukler for the flow of a water-air mixture in a horizontal pipe with 5 cm inner diameter at ambient conditions (25 °C and 0.1013 MPa). The diagram axes hold the superficial velocities and each marker on the diagram – i.e., each triangle, circle, and so on – represents a result of the ATHLET flow regime routine. The grey "x"-s named "not clear" in the legend describe a situation, in which none of the elements of  $\vec{p}$  has the absolute majority. One could, of course, have used another criterion for classifying the flow regimes – e.g., the relative majority of an element in  $\vec{p}$  –, but the general findings should be the same in any case.

In addition to the ATHLET results, the map contains solid black lines, which are taken from a graphic in /TAI 76/ and which represent flow regime boundaries. The corresponding flow regimes according to /TAI 76/ are put in yellow boxes. The general agreement between the /TAI 76/ flow regime map and the ATHLET map is quite good. Especially

the transitions between bubbly and intermittent flow as well as between stratified/stratified-wavy<sup>4</sup> flow and other flow regimes are well captured by the ATHLET procedure. Only intermittent vs. annular-mist flow transitions is slightly shifted to higher values of  $u_{gs}$  by ATHLET; this might be due to the chosen fluid properties at the given boundary conditions. Different to /TAI 76/, ATHLET distinguishes between purely annular and droplet (aka mist) flow; with higher superficial gas velocities, the droplet flow becomes dominant due to the increased liquid entrainment. At the boundaries of the annular and droplet flow regimes, where  $\vec{p}$  contains more than two non-zero entries, a few grey “x” markers can be found, indicating that no flow regime has the absolute majority.

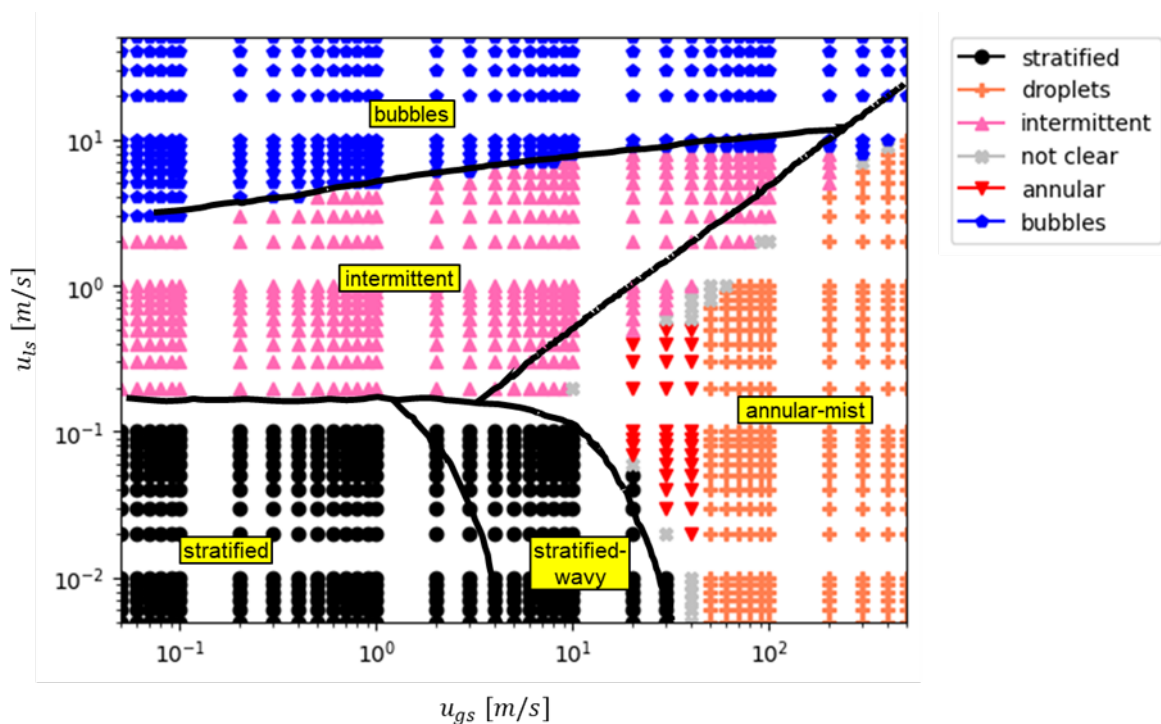


**Fig. 3.7** Stand-alone comparison of ATHLET flow regime map and /TAI 76/. Markers and legend refer to ATHLET. Black curves and yellow labels refer to /TAI 76/. Boundary cond.'s: Water-air, 25°C, 1 atm, horizontal, 5 cm diameter

### 3.1.3.1.1.2 Simple ATHLET simulation

As has been said, running ATHLET will produce flow regime predictions different to those obtained by stand-alone evaluations of the flow regime routine, because the feedback

<sup>4</sup> Note that the ATHLET map does not distinguish between stratified and stratified-wavy flow. Both flow regimes are represented by the black circles in Fig. 3.7.

exerted by various ATHLET models – especially the interfacial friction model – on the flow regime comes into play. For comparing the outcomes of ATHLET simulations with the map from /TAI 76/, a simple data set comprising a 20 m long horizontal pipe (subdivided into 40 control volumes) of 5 cm diameter and two fills – one for water and one for air – was created. The temperature (enthalpy) and pressure boundaries were set by means of a time-dependent volume. In order to populate the flow regime map with data points, numerous ATHLET simulations with varying fill mass flow rates – leading to various  $(u_{gs}, u_{ls})$  combinations – were performed. To obtain ATHLET results of a certain quality, the following procedure for simulation control and data acquisition was applied:

In order to be successfully terminated, an ATHLET run needed to fulfill the following criteria (3.42) to (3.45):

The simulation time had to be large enough so that initial transients could settle:

$$t \geq 200 \text{ s} \quad (3.42)$$

A minimum amount of gas should be present in the pipe so that a flow regime map was applicable (due to the high density, the liquid mass proved to be uncritical):

$$m_g \geq 10^{-6} \text{ kg} \quad (3.43)$$

At four different positions in the pipe (close to the entrance, close to the outlet and at two positions in-between), the time derivative of the superficial gas velocity is normalized to the current velocity. The criterion is fulfilled if, at all four positions, the modulus of this relative velocity change is below a given threshold, thereby checking the stationarity of the flow:

$$\left| \frac{\partial u_{gs}}{\partial t} \cdot \frac{1}{u_{gs}(t)} \right| \leq 10^{-5} \text{ s}^{-1} \quad (3.44)$$

The same criterion is applied for the liquid superficial velocity:

$$\left| \frac{\partial u_{ls}}{\partial t} \cdot \frac{1}{u_{ls}(t)} \right| \leq 10^{-5} s^{-1} \quad (3.45)$$

Only those runs which were successfully terminated as defined above, were considered in the further evaluation. In the next step, the control volume of the pipe was identified where the stationary pressure equaled the pressure relevant for the flow regime map (i.e., for comparison with /TAI 76/ as above 1 atm). Since it is usually hard to *exactly* meet the desired pressure in a CV, the control volume with the pressure closest to the desired value was chosen in most cases.

The flow regimes predicted by ATHLET are plotted in Fig. 3.8 in comparison with /TAI 76/, where each marker represents the result of a simulation. The picture is to be read analogously to Fig. 3.7.

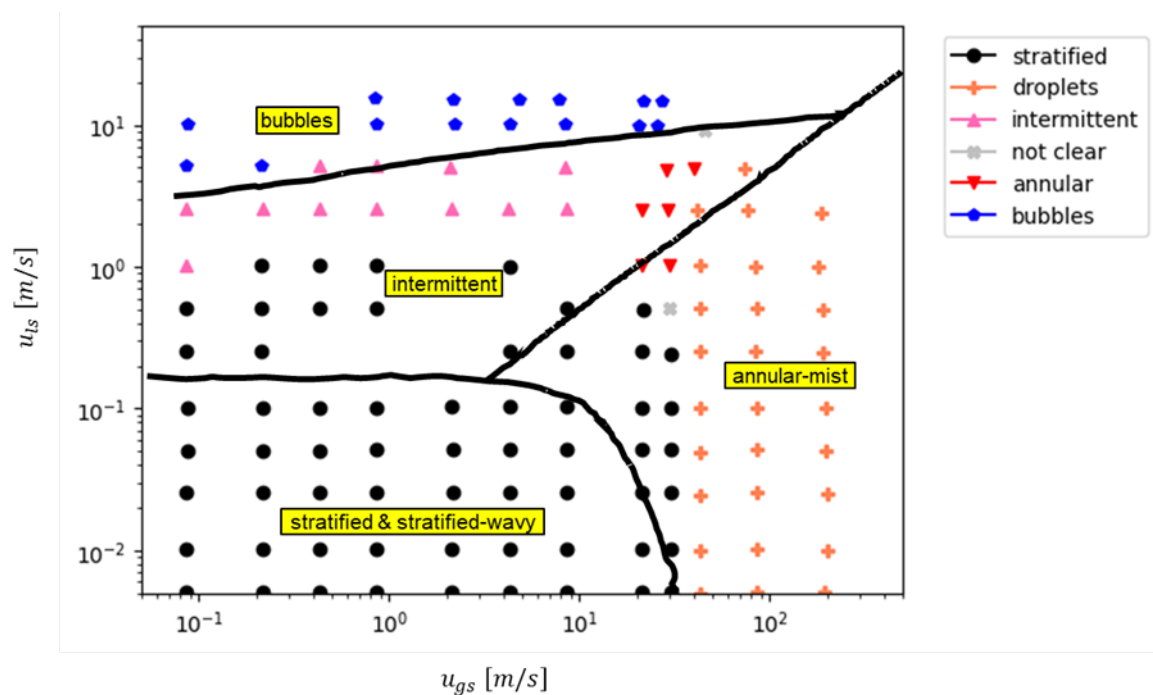


**Fig. 3.8** Comparison of ATHLET simulations and /TAI 76/.

Markers and legend refer to ATHLET.

Black curves and yellow labels refer to /TAI 76/.

Boundary cond.'s: Water-air, 25°C, 1 atm, horizontal, 5 cm diameter

As can be seen, the data points created by ATHLET do not populate the whole diagram but contain blank gaps – for very high values of  $u_{gs}$  and  $u_{ls}$  and also in-between. This is

the result of some runs not fulfilling the abovementioned criteria, in many cases because ATHLET was terminated due to very small time steps; the underlying reasons are yet to be investigated. Note that it was necessary to deactivate the limitation of the fluid velocity to sonic velocity applied in ATHLET in order to obtain at least some data points in the upper right part of the diagram because high superficial velocities for both phases mean that the real velocity of at least one phase is high, too, while the sonic velocity is (occasionally extremely) low for two-phase flow. An activated velocity limitation would lead to a de-coupling of the discharge rate and the pressure in the TDV at the outlet of the pipe so that the pressure in the pipe could no longer be controlled and became so high that no CV came even close to 1 atm.

Regarding the comparison of ATHLET simulations and /TAI 76/, the agreement is obviously much worse than that for the stand-alone routine evaluation. This can be interpreted as an indication that the interfacial friction and the wall friction models of ATHLET should be revised within the frame of future projects. Nevertheless, the general character of the /TAI 76/ map could be reproduced: Stratified flow is observed for low values of  $u_{gs}$  and  $u_{ls}$ , annular mist flow is located at the right side of the diagram, bubbly flow occurs at high liquid velocities, and intermittent flow is bordered by these other flow regimes. The bubbly/intermittent transition seems to be captured quite well, also the shape of the annular-mist flow regime is similar for ATHLET and /TAI 76/. The largest visible difference is the domination of the stratified flow regime in ATHLET compared to the literature which is presumably due to the fact that in /TAI 76/ only equation (3.15) is evaluated to distinguish between stratified and non-stratified flow, whereas ATHLET takes in addition to that equations (3.16) and (3.19) into account. It should be noted that equation (3.15) has proven successful when applied in TPTF calculations /LAN 22a/, so it is worth to consider modifying the ATHLET criterion in future code versions in order to obtain flow regime predictions closer to that found in the literature.

### **3.1.3.1.2 Vertical flow**

As for horizontal flow, results of both stand-alone routine evaluations and ATHLET simulations have been compared with a map from literature /TAI 80/. The data acquisition and diagram format are the same as described in sections 3.1.3.1.1.1 and 3.1.3.1.1.2. The only difference here is that the pipe is running vertical and that the pressure, at which the flow regimes are observed, is 1 bar (instead of 1 atm, which is a rather minor difference).

### 3.1.3.1.2.1 Stand-alone flow regime routine test

The stand-alone comparison of the ATHLET flow regime map and /TAI 80/ is shown in Fig. 3.9. While the “dispersed bubbles” region of /TAI 80/ and the bubbly flow regime predicted by ATHLET agree quite well, the other flow regime predictions are in contradiction: On the left hand side of the diagram, /TAI 80/ predicts “deformable bubbles”, which are not considered at all by ATHLET. The intermittent flow regime is located by Taitel et al. at intermediate superficial velocities whereas ATHLET calculates this flow regime for high values of both  $u_{gs}$  and  $u_{ls}$  – and for low values of  $u_{gs}$  and  $u_{ls} = 3 \text{ m/s}$ , which is just below the curve separating deformable and dispersed bubbles. While annular flow exists for high values of  $u_{gs}$  and is independent of  $u_{ls}$  in /TAI 80/, it is the dominating flow regime calculated by the ATHLET map and obviously dependent on both  $u_{gs}$  and  $u_{ls}$ . The main reason for the observed differences is that, just as for horizontal flow, the implemented flow regime criteria are a compromise between criteria from the literature and previous ATHLET implementations. Unlike horizontal flow, the implemented criteria for vertical flow differ much more from the ones found in literature.

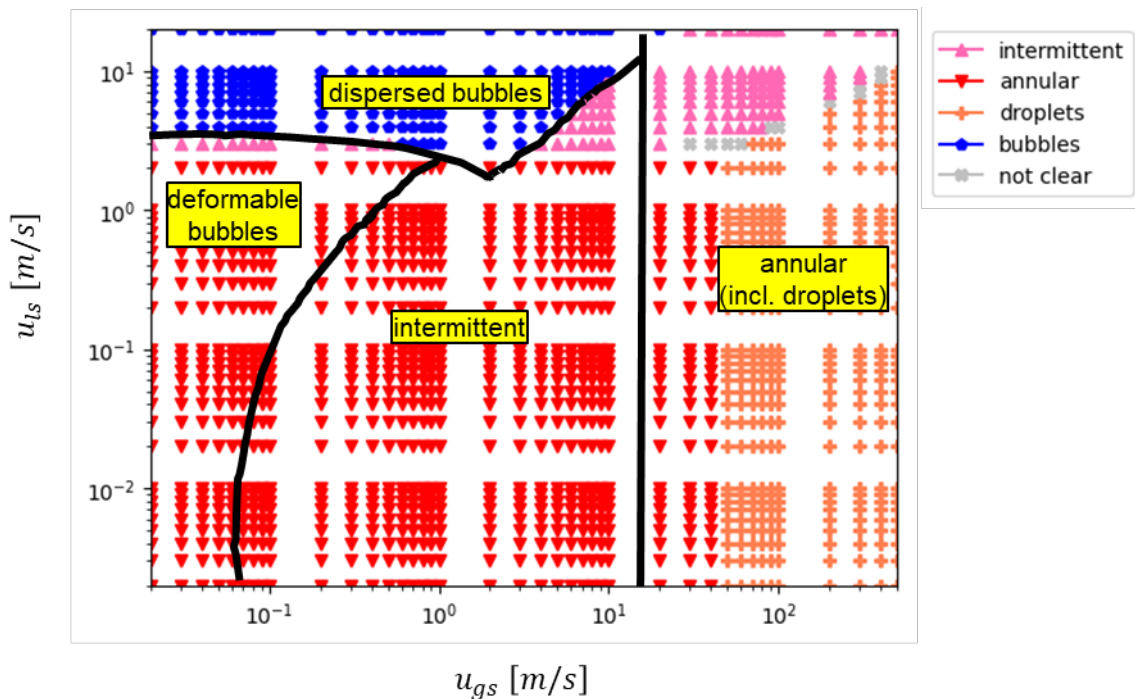


**Fig. 3.9** Stand-alone comparison of ATHLET flow regime map and /TAI 80/. Markers and legend refer to ATHLET. Black curves and yellow labels refer to /TAI 80/. Boundary cond.'s: Water-air, 25°C, 1 bar, vertical, 5 cm diameter

### 3.1.3.1.2.2 Simple ATHLET simulation

Fig. 3.10 shows the same diagram as Fig. 3.9, but with ATHLET simulation data instead of data generated by stand-alone evaluations of the flow regime routine. Unsurprisingly – apart from the “dispersed bubbles” flow regime – the agreement between ATHLET and /TAI 80/ is rather poor again, albeit qualitatively better with regard to the intermittent/annular flow transition: The intermittent flow regime is now predicted by ATHLET for  $(u_{gs}, u_{ls})$  combinations, which previously yielded annular flow in the stand-alone evaluation, so that the intermittent/annular flow transition predicted by ATHLET loosely resembles the vertical line from /TAI 80/ (shifted towards lower values of  $u_{gs}$ , though). This can be attributed to the interfacial shear and wall friction models in ATHLET, which differ from those applied in the stand-alone calculations. The deformable bubbles are now identified as intermittent flow, which can be partially justified by the fact that these bubbles – as explained in /TAI 80/ are rather large compared to the dispersed bubbles and include occasionally occurring Taylor bubbles.

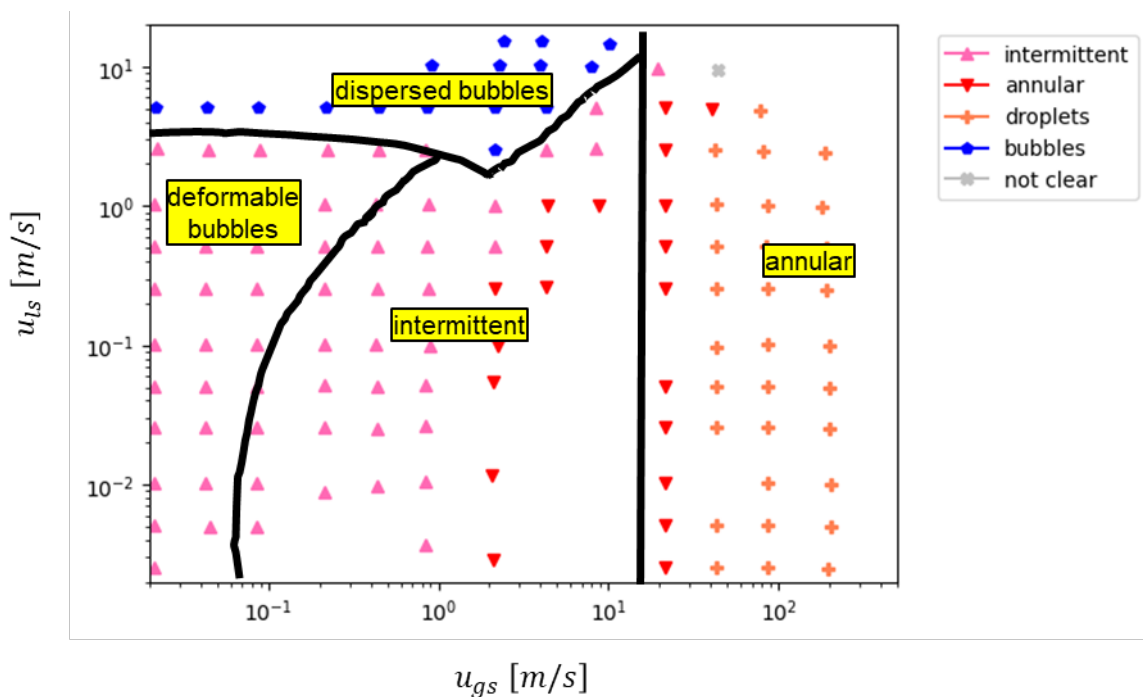


**Fig. 3.10** Comparison of ATHLET simulations and /TAI 80/.

Markers and legend refer to ATHLET.

Black curves and yellow labels refer to /TAI 80/.

Boundary cond.'s: Water-air, 25°C, 1 bar, vertical, 5 cm diameter

### 3.1.3.2 General operability tests

In addition to the simulation of simple ATHLET runs with the purpose of investigating the flow regime predictions as described above, a wide range of largely complicated data sets was simulated with the objective to check the general operability and performance of the modified ATHLET version. These test calculations were run in parallel with the code developments and proved quite useful for detecting and fixing programming errors and model weaknesses (similar to regression tests but less strict). It has to be stressed that, even though the test cases include frequently calculated ATHLET validation data sets, these calculations clearly serve no validation purposes.

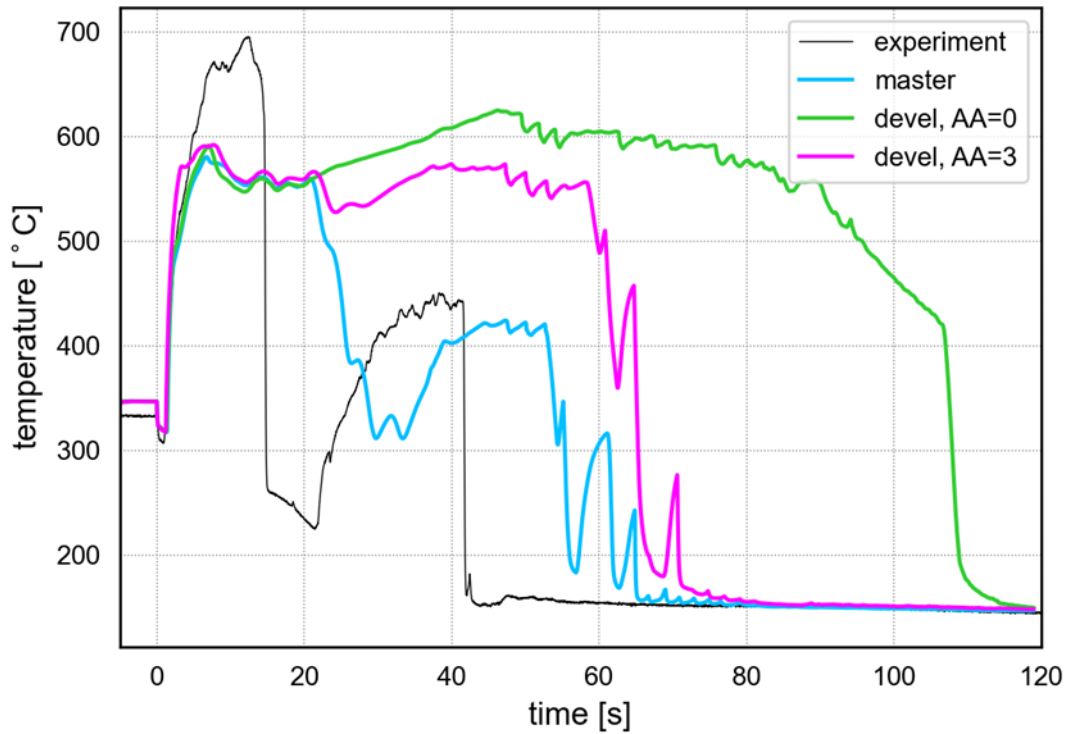
With regard to the operability, it can be said that all tested data sets run till the specified simulation end time, i.e., no premature program termination – e.g., due to small time steps or other problems – was observed. As for the performance, however, the general observation is that the ATHLET version with centralized flow regime calculation tends to need more integration time steps, and thus more run time, than the master version – at least if the feedback from the flow regimes is taken into account, i.e., if the user input<sup>5</sup> given under `CW MISCELLAN` is `AA=3`; for `AA=0`, the used number of time steps is comparable for both ATHLET versions. Nevertheless, there are also (rare) exceptions: For example, the number of time steps needed for simulating an experiment conducted at the PERSEO facility (test 7, part 1, cf. /HOL 23/) could be reduced by 20% compared to the master.

An impression regarding the effect of the developments on the simulation results, is given by Fig. 3.11 and Fig. 3.12. The first diagram shows for the LOFT LP-LB-1 experiment /HOL 23/ the development of the average cladding temperature of the central fuel assembly over time. The second diagram shows for the LSTF run SB-CL-18 /HOL 23/ the time course of the injection mass flow rate from the accumulator in the intact loop. In both diagrams, the experimental curve is drawn with a black line, the results obtained with the ATHLET master are drawn with a blue line, the results obtained with the discussed development version of ATHLET and `AA=0` are drawn with a green line, and, finally, the results of the ATHLET development version with `AA=3` are drawn in pink. In

---

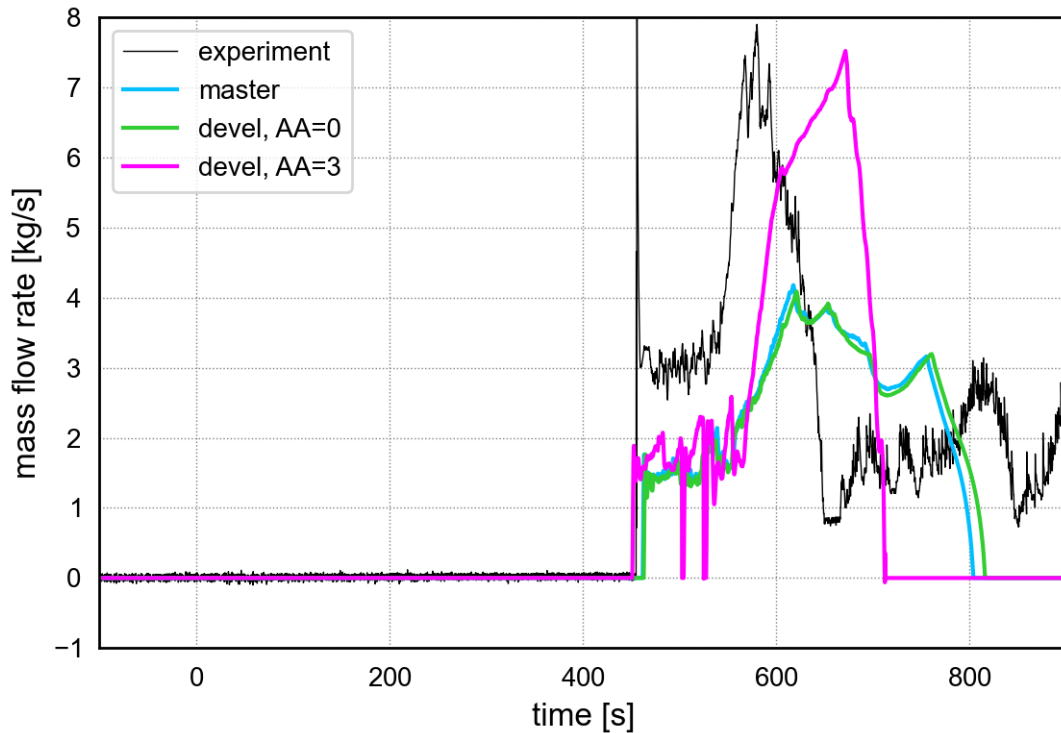
<sup>5</sup> `AA=3` means full application of the centralized flow regime maps as discussed above. `AA=0` is an intermediate development step; it means that only the entrained liquid fraction and the local relative phase velocities are centrally calculated. See section 3.3.4 for more information.

Fig. 3.11, a relatively good agreement of the master simulation with the experiment can be observed. When using the development version of ATHLET and  $\Delta A=0$ , the result clearly deteriorates. With the development version of ATHLET and  $\Delta A=3$ , i.e., full consideration of the centralized flow regime maps, the simulated cladding temperature improves again but is still worse than that calculated by the ATHLET master.



**Fig. 3.11** LOFT LP-LB-1 test: Average cladding temperature of central fuel assembly (TE-5H07-049)

In contrast to this, the accumulator injection mass flow rates predicted by the ATHLET master and the development version with  $\Delta A=0$  differ only slightly whereas setting  $\Delta A=3$  yields significantly different results which are – at least for the absolute value of the peak mass flow rate – even closer to the experimental observation.



**Fig. 3.12** LSTF run SB-CL-18: Injection mass flow rate from the accumulator in the intact loop (loop A)

As has been said, the shown figures shall only give an impression of the effect of the code modifications. A comprehensive analysis and evaluation of the physical results is pending (not only for the LOFT and LSTF simulations, but for all run test cases). This has to be done within the frame of code validation work, which can start after all major development steps concerning the flow regime simulation have been completed (see section 3.5).

### 3.2 Extension of flow regime maps and closure laws for condensing horizontal flows

In literature many investigations on flow regime maps and flow regime transition criteria can be found. The transition criteria depend on various factors. E.g., the angle of inclination or the hydraulic diameter play an important role. Concerning the diameter, “conventional” channels, for which the flow regime maps of e.g., Taitel /TAI 76/ were derived, are expected to have a hydraulic diameter larger than approx. 5 mm /KAN 03/. Other influencing factors are thermal processes. Thus, differences in the formation of flow patterns were found for condensing and evaporating flows when compared to adiabatic flows.

In general, the implemented flow regime map module enables to rather flexibly add new flow regime maps, which can be invoked depending on the current application and the defined flow channel geometry, fluid, thermal boundary conditions, etc.. However, research on flow regime transition is still a field of active development /SIK 24/. Thus, it can be expected that new flow regime maps will be developed in near future, which then can be used to improve the predictive capability of ATHLET. In the following sections condensing flows will be further investigated.

### 3.2.1 Flow regime maps for condensing flows in horizontal flow path

Various flow regime maps have been developed in the literature for condensing flows in horizontal and slightly inclined pipes. Compared to adiabatic flow, a main difference was found in the transition criteria to annular flow, for which reason a particular focus is put on the annular flow regime in the following.

The flow regime maps discussed below are based exclusively on experience with water or cooling media and pipe diameters of approx. 5 to 15 mm. The predictive capability of the various flow regime maps has often been compared in the literature, e.g., in /HAJ 03/, /TAN 82/. When comparing these maps, it must be borne in mind that the authors have defined different flow patterns and that the diagrams therefore have different levels of detail.

If the variously defined flow regimes are combined in a meaningful way (e.g., intermittent flow comprises plug, slug and elongated bubble flow), at least qualitatively, there is a reasonable agreement between the maps. If one also takes into account that the transition areas between the flow regimes do not correspond to sharp lines in reality (El Hajal estimates the lack of sharpness with respect to the mass flow density at about 50 kg/m<sup>2</sup>s) and that the inaccuracy of the measurement (especially in the case of visual determination of the flow regime) is considerable, it can be assumed that the presented maps are generally suitable with respect to their predictive quality.

Tandon et al. /TAN 82/ developed a flow regime map for condensing flows using the void fraction (in terms of  $(1 - \alpha)/\alpha$ ) and the dimensionless vapor velocity defined by Wallis ( $j_g^* = xG/[gD\rho_v(\rho_l - \rho_v)]^{1/2}$ ). With regard to the latter, it is emphasized that it is significant for flow pattern change. In principle, the Wallis parameter corresponds to a modified Froude number, which is used in a similar form by many authors to predict the onset of "slugging" and also for the transition from stratified to wavy flow. The vapour volume

fraction  $\alpha$  is a central parameter for determining the flow pattern, but as an independent coordinate it has the disadvantage that it depends on the relative velocity of the phases, which again is always a consequence of the interphase drag model. Tandon et al. give a correlation for  $\alpha$ , which they claim is valid for all flow conditions (covering different flow patterns, pressures, velocities), which is questionable. Hence the use of Tandon's flow map in ATHLET will only be possible with the same success if ATHLET provides similar vapour volume contents for the investigated flow conditions as the correlation used by Tandon. However, this is a limitation that basically applies to all available flow regime maps.

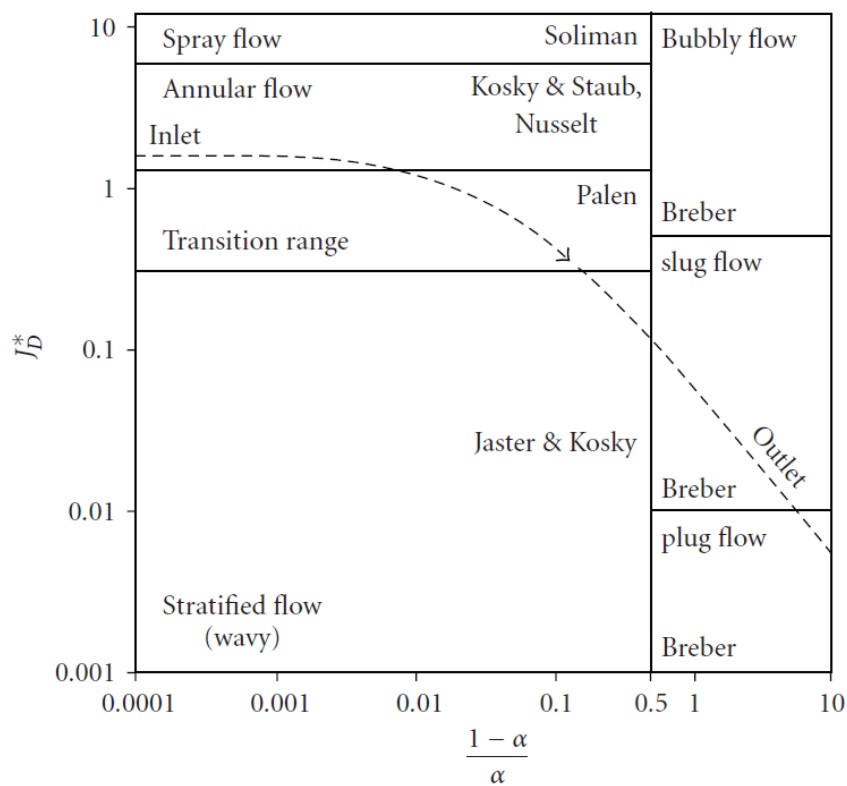


**Fig. 3.13** Modified flow regime map acc. to Tandon as given in /PAP 10/

Tandon emphasizes the excellent agreement between his transition criteria and the measured flow patterns. However, the majority of the measurements fall into the areas of wave and ring flow. Therefore, the transition criteria between these two flow patterns can be considered as particularly validated (for the present flow conditions). The measurements can be used to quantify the transition area as  $0,4 \leq j_g^* \leq 2$ . This is in good quantitative agreement with other authors, e.g., Palen /PAL 79/, who states  $0,33 \leq j_g^* \leq 1,5$ . The void limit for the annular flow regime is given as  $(1 - \alpha)/\alpha \leq 0,5$ , which

corresponds to  $\alpha \geq 2/3$ . This, again, is in good agreement with the ATHLET implementation based on /TAI 76/, where the transition region between intermittent and annular flow is defined as  $0.5 \leq \alpha \leq 0.75$ .

The flow regime map according to Tandon was implemented in ATHLET. It could be used for further investigations in the future. The direct usage of the flow regime map for ATHLET calculations is not feasible, since interpolation ranges required for a smooth transition between the flow regimes have to be defined and implemented first. However, a comparison between the flow regime determined by ATHLET and the prediction by Tandon is possible.

Another important work is the El Hajal /HAJ 03/ flow map for condensation in horizontal pipes, see Fig. 3.14. This is based on an extensively tested flow regime map developed for adiabatic and heated walls by Kattan et al. /KAT 98/, which in turn is a modification of the established flow diagram by Taitel and Dukler /TAI 76/, which is widely used in simulation programs (and in ATHLET, too).

Fig. 3.14 shows details of the El Hajal condensation flow map compared to the Kattan flow map. Depicted are the flow patterns stratified (S), stratified wavy (SW), intermittent (I), annular (A), and mist (MF). (Note: The bubble flow occurs at higher mass flow densities and is therefore not shown in the diagram.) The main difference compared to adiabatic/heated wall flow map is, that in the case of wall condensation there exists an annular flow even at a very high vapor quality. This can be explained by the fact that when a single-phase saturated vapor flow enters a cooled pipe, condensation occurs immediately on the wall and annular flow regime begins to establish.

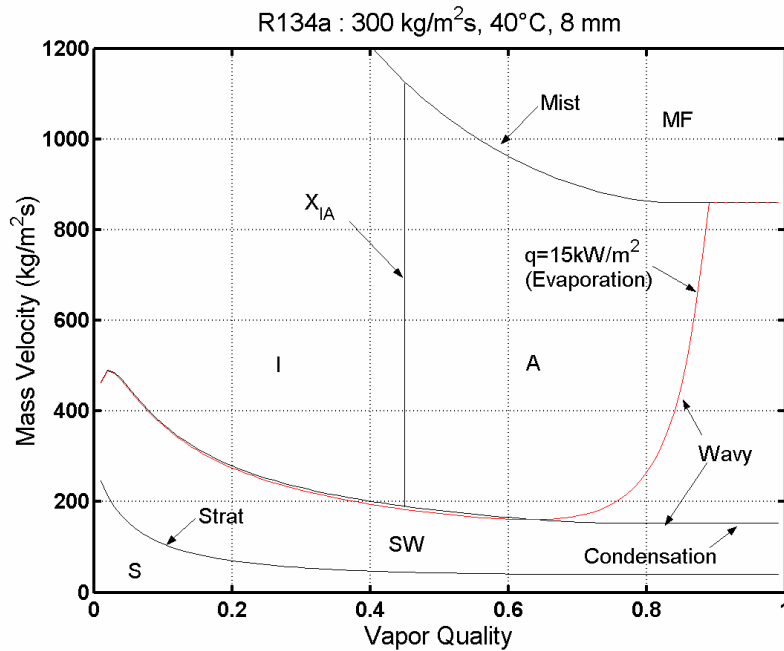


**Fig. 3.14** Flow pattern map for horizontal flow by /KAT 98/ (red line) with modification for condensation by /HAJ 03/

The former flow map of ATHLET based on /TAI 76/ was originally developed for adiabatic flows and the non-centralized, model specific implementations of the flow map did only partly distinguish the annular flow regime. Thus, in a first step, the centralized flow regime map was improved by introducing the annular flow regime, see chap. 3.1.2.3.1.1. In a second step, this flow regime map was adjusted to condensation flows by preventing the direct transition from stratified wavy flow to disperse flow and instead selecting annular flow for higher void fractions, as it is imposed by the flow regime map of /HAJ 03/ in Fig. 3.14.

### 3.2.2 Flow regime map transition

A further item concerns the implementation of transition areas between the flow maps of different heat transfer regimes (here adiabatic/heating and cooling wall). In a first step, the technical extension of the flow map module with regard to additional maps for cooling surfaces was carried out. In order to select between different flow maps, the surface temperature calculated in the HECU module of ATHLET (module for heat conduction and heat transfer) was made available in the TFD-module, where the determination of the flow regime is performed. Based on the wall subcooling (or overheating) the according flow map is selected, considering an adequate interpolation region to ensure a smooth transition between cooling and adiabatic/heating states:

$$T_w - T_{sat} = \begin{cases} < -1 & \text{condensation flow regime map} \\ > 0 & \text{evaporation flow regime map} \\ \text{else} & \text{interpolation} \end{cases} \quad (3.46)$$

Within the interpolation range, both flow regime maps are evaluated, and the combined flow regime is derived as described in chap. 3.1.2.3.2.

### 3.2.3 Interfacial friction

Prevailing flow regimes in horizontal pipe flow with condensation are annular or stratified/stratified wavy flow. Horizontal annular flow was introduced in the centralized flow regime map but wasn't separately considered in the interfacial friction model of ATHLET so far. Thus, dedicated closure laws were not available in ATHLET and had to be implemented. Similar to stratified flow, only a simplified interfacial friction correlation was implemented, which was decided to be replaced by a dedicated correlation.

In case of the 2M model, the interfacial friction is modelled as an interfacial drag force per unit volume  $F_i'''$ . Generally, it can be written as

$$F_i''' = \frac{\tau_i p_i}{A} = \frac{1}{2} \rho_c f_i \frac{p_i}{A} u_r |u_r| = C_i u_r |u_r| \quad (3.47)$$

where  $f_i$  is the interfacial friction factor and  $C_i$  the interfacial drag coefficient. Appropriate correlations for  $C_i$  were implemented in ATHLET now.

#### 3.2.3.1 Stratified and stratified wavy flow

For the interphase friction coefficient for stratified flow, a separate correlation was previously used in ATHLET, which was derived from a correlation by Wallis for the annular flow:

$$C_{i,\text{str}} = 0.005 \frac{1}{\pi D} \left( \alpha (1 - \alpha) (1 + 75 \sqrt{1 - \alpha}) \right) \rho_v \quad (3.48)$$

Due to the factor  $\alpha (1 - \alpha)$  in the numerator, the interphase friction was calculated to be very low, especially for small and large vapor volume fractions. In addition, the correlation did not explicitly differentiate (only via the vapor volume fraction) between stratified and wavy flow, while a significantly increased friction pressure loss is to be expected for the latter. Therefore, the correlation was replaced by a dedicated correlation from literature.

Taitel and Dukler /TAI 76/ proposed that the interfacial friction factor can be approximated with the wall friction factor for the horizontally stratified flow, which leads  $f_i \approx \lambda_v$ , where in ATHLET the wall friction factor is calculated according to the Colebrook model.

Based on the geometry shown in Fig. 3.15, the interfacial perimeter per flow area can be calculated as below:

$$\frac{p_i}{A} = \frac{4D_h \sin \theta}{D_h^2 \pi} = \frac{4 \sin \theta}{D_h \pi} \quad (3.49)$$

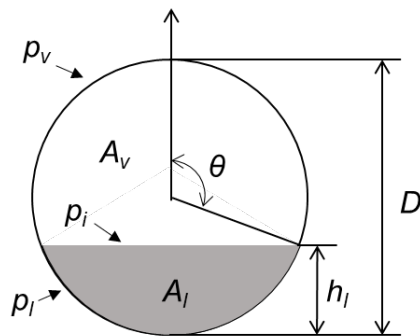


**Fig. 3.15** Schematic drawing of the horizontal stratified flow

Then, the interfacial friction coefficient of the stratified-smooth flow becomes:

$$C_{i, str} = \frac{1}{2} \rho_v \lambda_v \frac{4 \sin \theta}{D_h \pi} \quad (3.50)$$

For the wavy flow, the interfacial friction is much higher than for the stratified-smooth flow due to the existence of waves on the interface. Hence, it is necessary to define the criterion of a transition between the stratified-smooth flow and the wavy flow and how the friction will be changed in the two flow regimes. Andritsos and Hanratty /AND 87/ proposed a model that accounts for the influence of waves on both the friction factor at the

interface and the liquid wall shear stress. The empirical correlation of the interfacial friction factor is suggested as below:

$$\frac{f_i}{\lambda_v} = \begin{cases} 1 & \text{for } j_v \leq j_{v,\text{wavy}} \\ 1 + 15 \left(\frac{h_l}{D_h}\right)^{0.5} \left(\frac{j_v}{j_{v,\text{wavy}}} - 1\right) & \text{for } j_v > j_{v,\text{wavy}} \end{cases} \quad (3.51)$$

where  $\lambda_v$  is the wall friction factor of gas.  $h_l/D_h$  is the fraction of the liquid height over the total diameter in the horizontal flow as shown in Fig. 3.15, and  $j_{v,\text{wavy}}$  denotes a critical superficial velocity of gas for transition from the smooth flow to the wavy flow defined by:

$$j_{v,\text{wavy}} = 5 \text{ m/s} \left(\frac{\rho_{\text{air}}}{\rho_v}\right)^{0.5} \quad (3.52)$$

The correlation suggests that if the gas superficial velocity exceeds  $j_{v,\text{wavy}}$ , the stratified-smooth flow will turn into wavy flow and its friction factor is increased by a certain amount. Finally, the interfacial friction coefficient of the wavy flow can be written as below:

$$C_{i,\text{wavy}} = \frac{1}{2} \rho_v \lambda_v \left( 1 + 15 \left(\frac{h_l}{D_h}\right)^{0.5} \left(\frac{j_v}{j_{v,\text{wavy}}} - 1\right) \right) \frac{4 \sin \theta}{D_h \pi} \quad (3.53)$$

### 3.2.3.2 Annular flow

For the liquid film, the interfacial perimeter per flow area is calculated by:

$$\frac{p_i}{A} = \frac{4 D_{\text{film}} \pi}{D_h^2 \pi} = \frac{4 D_h \sqrt{\alpha} \pi}{D_h^2 \pi} = \frac{4 \sqrt{\alpha}}{D_h} \quad (3.54)$$

The Wallis model /WAL 70/ is used for the drag friction factor as below:

$$f_i = 0.005[1 + 75(1 - \alpha)] \quad (3.55)$$

Thus, the interfacial friction coefficient for the liquid film becomes:

$$C_{i,ann} = \frac{1}{2} \rho_v 0.005 [1 + 75(1 - \alpha)] \frac{4}{D_h} \sqrt{\alpha} \quad (3.56)$$

### 3.2.4 Wall friction

Different approaches are described in the literature for determining wall friction in two-phase flow /JU 20/. ATHLET conceptually uses a two-phase multiplier to determine the two-phase flow pressure losses. A two-phase multiplier can basically be used for all flow regimes. Due to a lack of better approaches, the two-phase multiplier is also employed for specific flow situations such as counter current flow, although the concept derived on the basis of a co-current mass flow is not proven to be valid here and may be error-prone.

For single phase flows, the friction loss by the wall is calculated as below:

$$\left(\frac{dP}{dx}\right)_{wall} = -\frac{1}{2} \frac{\lambda}{D_h} \rho u |u| \quad (3.57)$$

where  $\lambda$  is the Darcy-Weisbach friction factor. In two-phase flows, the above relation should be modified by adding the two-phase multiplication factor. Because ATHLET has two types of the governing equation for momentum, 1M model as 5-equation model and 2M model as 6-equation model, those have to be investigated individually.

In the 1M model, the total pressure drop in two-phase flows is the main concern. It is usually calculated from the pressure drop in the homogenous mixture flow and then multiplied by the two-phase flow multiplication factor to consider higher pressure drops in two-phase flows. For this, Lockhart-Martinelli /LOC 49/ and Martinelli-Nelson /MAR 48/ defined two-phase multipliers  $\phi_l^2$  and  $\phi_v^2$ . These two multipliers can be calculated as a function of the parameter  $X$  according to literature /CHI 67/.

$$\phi_{lo}^2 = \phi_l^2 (1 - x)^{1.75} = \left(1 + \frac{1}{X_{tt}^{1/a}}\right)^{1.75a} (1 - x)^{1.75} \quad (3.58)$$

$$\Phi_{vo}^2 = \Phi_v^2 x^{1.75} = \left(1 + X_{tt}^{1/a}\right)^{1.75a} x^{1.75} \quad (3.59)$$

Now, the two-phase frictional pressure gradient can be either expressed as

$$\left(\frac{dP}{dx}\right)_{2\phi,l} = -\left(1 + \frac{1}{X_{tt}^{1/a}}\right)^{1.75a} (1-x)^{1.75} \frac{\lambda_{lo} G_{tot} |G_{tot}|}{2D_h \rho_l} = -k_l G_{tot} |G_{tot}| \quad (3.60)$$

or as

$$\left(\frac{dP}{dx}\right)_{2\phi,v} = -\left(1 + X_{tt}^{1/a}\right)^{1.75a} x^{1.75} \frac{\lambda_{vo} G_{tot} |G_{tot}|}{2D_h \rho_v} = -k_v G_{tot} |G_{tot}| \quad (3.61)$$

In order to ensure a smooth transition between two frictional pressure gradients, the interpolated value over quality is used in the code:

$$\left(\frac{dP}{dx}\right)_{2\phi} = -((1-x)k_l + xk_v) G_{tot} |G_{tot}| \quad (3.62)$$

For the 1M model, the above equation can be immediately applied to obtain the two-phase frictional pressure drop. However, for the 2M model, the wall friction loss has to be calculated for each phase, vapor and liquid, separately. Therefore, when using the 6-equation model in ATHLET, the wall friction must be suitably distributed between the two phases. Up to now, this has been done according to the volume fractions of the two phases.

$$\left(\frac{dP}{dx}\right)_{w,l} = -(1-\alpha) k_{lo} \rho_l u_l |u_l| \quad (3.63)$$

$$\left(\frac{dP}{dx}\right)_{w,v} = -\alpha k_{vo} \rho_v u_v |u_v| \quad (3.64)$$

Volume weighting is a common and proven method for many flow patterns. In the case of annular flow, however, only the liquid is in contact with the wall. It is therefore more realistic to assign the wall friction to the liquid phase. On the other hand, for a stratified flow, the wall area wetted by one phase can be approximately determined on the basis of the collapsed level, so that a detailed distribution of the wall friction to both phases is also possible here.

### 3.2.4.1 Annular flow

Considering the flow regime distribution that can be expressed by the fraction that each flow regime contributes to the two-phase flow, the vapor wall friction can be given as

$$\left(\frac{dP}{dx}\right)_{w,v} = \left(\frac{dP}{dx}\right)_{w,v,ann} + \left(\frac{dP}{dx}\right)_{w,v,non-ann} \quad (3.65)$$

with

$$\left(\frac{dP}{dx}\right)_{w,v,ann} = p_{ann} \cdot \left(\frac{dP}{dx}\right)_{w,v} \quad (3.66)$$

and

$$\left(\frac{dP}{dx}\right)_{w,v,non-ann} = (1 - p_{ann}) \cdot \left(\frac{dP}{dx}\right)_{w,v} \quad (3.67)$$

Using this expression and assuming a partly annular flow, the phase wall friction can be redistributed as follows:

$$\overline{\left(\frac{dP}{dx}\right)}_{w,v} = \left(\frac{dP}{dx}\right)_{w,v} - p_{ann} \left(\frac{dP}{dx}\right)_{w,v} \quad (3.68)$$

$$\overline{\left(\frac{dP}{dx}\right)}_{w,l} = \left(\frac{dP}{dx}\right)_{w,l} + p_{ann} \left(\frac{dP}{dx}\right)_{w,v} \quad (3.69)$$

Note: This approach retains the total two-phase pressure drop calculated on the basis of a two-phase multiplier but changes the distribution of the friction loss to the phases.

### 3.2.4.2 Stratified flow

For stratified flow in a horizontal circular pipe, the wall friction can be repartitioned between the two phases depending on the relative collapsed level  $z_{cl}$  and the angle  $\theta$  as depicted in Fig. 3.15. Several ways of repartitioning of the wall friction are conceivable:

**Based on two-phase multiplier:** Similar to the above-described approach for the annular flow, the total pressure loss could be kept constant, but a redistribution of wall friction between phases according to the wetted arc length could be introduced. Then, the following expressions could be defined. Let us assume a flow situation with collapsed level in the upper half of the pipe, so that a part of the wall friction assigned to the vapor phase has to be transferred to the liquid phase friction. Using the fraction of arc length wetted by the vapor phase  $1 - \frac{\theta}{\pi}$  with  $0 < \theta < \frac{\pi}{2}$  (see Fig. 3.15), the phase wall fractions can be written as:

$$\left(\overline{\frac{dP}{dx}}\right)_{w,v} = \left(1 - p_{\text{str}} \left(1 - \frac{\theta}{\pi}\right)\right) \cdot \left(\frac{dP}{dx}\right)_{w,v} \quad (3.70)$$

$$\left(\overline{\frac{dP}{dx}}\right)_{w,l} = \left(\frac{dP}{dx}\right)_{w,l} + p_{\text{str}} \left(1 - \frac{\theta}{\pi}\right) \cdot \left(\frac{dP}{dx}\right)_{w,v} \quad (3.71)$$

Similar equations follow for a situation with collapsed level in lower half of the pipe. Adopting this approach, the total, summed-up wall fraction stays unchanged, so that the approach using a two-phase multiplier is assumed to be appropriate for the stratified flow.

**Based on single-phase pressure losses:** Assuming a stratified flow with a sharp interface between both phases, the wall friction of each phase could be calculated as single-phase pipe wall friction, reduced by the wetted arc length, and neglecting a weighting

with the void fraction as introduced in the equations (3.63) and (3.64) Then, the phase wall friction in stratified flow can be written as:

$$\left(\frac{dP}{dx}\right)_{w,l} = \frac{\tau_{wl} p_l}{A} = \frac{1}{2} \frac{\pi - \theta}{\pi} \frac{\lambda_l}{A^2 D_h} \rho_l u_l |u_l| \quad (3.72)$$

$$\left(\frac{dP}{dx}\right)_{w,v} = \frac{\tau_{wv} p_v}{A} = \frac{1}{2} \frac{\theta}{\pi} \frac{\lambda_v}{A^2 D_h} \rho_l u_v |u_v| \quad (3.73)$$

Verification has shown that the second approach based on single-phase wall friction provides better results, whereas the first approach based on two-phase pressure drop significantly underestimates the liquid friction, particularly for high void fractions with  $\alpha > 0.99$ , which causes too high liquid velocity, too low relative velocity, and consequently too high void fraction.

### 3.2.5 Verification against COSMEA

COSMEA is a test facility with a coaxial double pipe to investigate flow characteristics and heat transfer during the condensation of steam in a slightly inclined horizontal tube. It is a sub-section of the thermal-hydraulic test facility TOPFLOW (Transient two-phase flow test facility), at the Helmholtz-Zentrum Dresden-Rossendorf (HZDR). The inner pipe (tube or primary side) is a condensation pipe where hot saturated steam and water flow under high pressure, while the outer pipe (shell or secondary side) is a cooling pipe where cold water passes. The experiment was initially set up and performed in 2012. Further information can be found in /BIE 20/.

There were a few modifications to the test facility in 2020. The inclination was slightly changed from  $0.75^\circ$  to  $0.87^\circ$ . The diabatic and adiabatic lengths between the condensation pipe and cooling pipe were adjusted (Fig. 3.16). The active length for the heat transfer between the condensation pipe and cooling pipe was 2.823 m. The diameters of pipes remained unchanged from the previous facility design – the outer diameter of the condensation pipe is  $D_{\text{outer,cond}} = 48.3$  mm and the inner diameter of the cooling pipe  $D_{\text{inner,cool}} = 116$  mm. The details of the dimensions of the test section are shown in Fig. 3.16.

The COSMEA facility was selected as verification experiment, since void fraction measurements were captured at several positions along the condensation pipe. This

distinguishes COSMEA from other test facilities like TPTF or Mantilla, where void fraction was measured only at one position. However, since COSMEA was mainly devised as validation experiment for condensation models, additional uncertainties were introduced by the condensation phenomena resolved only partly by ATHLET.

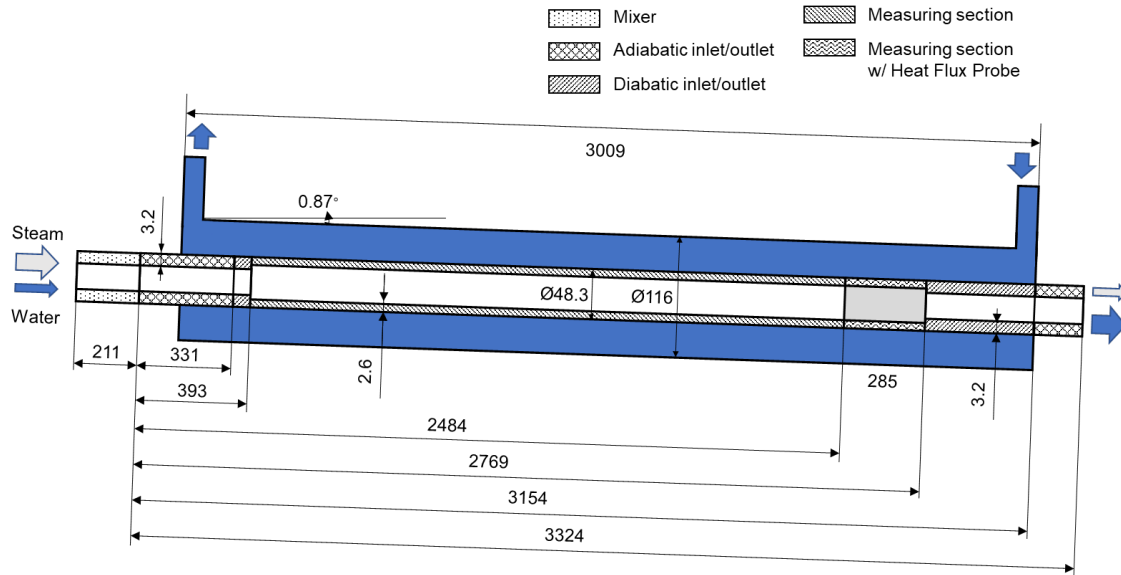


**Fig. 3.16** Schematic drawing of COSMEA test facility (2020) (not proportional to real scale)

In the experiment performed in 2020, 26 tests were carried out with changes in pressure from 5 to 65 bar, steam inlet mass flow rate from 0.02 to 1.00 kg/s, water inlet mass flow rate from 0.0 to 0.7 kg/s for the condensation pipe, and inlet water mass flow rate from 13 to 36 kg/s for the cooling pipe. The temperatures and the pressures in the cooling pipe were almost constant values at 43 °C and 3.5 bar, respectively /BOD 24/. Initial and boundary conditions are given in Tab. 3.1. In the experiment, the condensation rate in the cooling pipe, the heat flux between the condensation and cooling pipe and the temperature rise along the cooling pipe were measured when the system had reached a steady state.

**Tab. 3.1** Initial and boundary conditions of COSMEA 2020 experiment

Exp. ID	Condensation pipe				Cooling pipe		
	$P_{out}$ (bar)	$T_{L,in}$ (°C)	$\dot{m}_{L,in}$ (kg/s)	$\dot{m}_{V,in}$ (kg/s)	$P_{in}$ (bar)	$\dot{m}_{L,in}$ (kg/s)	$T_{in}$ (°C)
s51r	5.0	0.0	0.00	0.16	3.6	13.5	43.3
s53	5.0	153.6	0.37	0.02	3.5	13.1	43.5
s54	5.0	152.3	0.10	0.02	3.5	13.0	44.7
s121r	12.0	0.00	0.00	0.28	3.6	17.9	43.1

Exp. ID	Condensation pipe				Cooling pipe		
	P <sub>out</sub> (bar)	T <sub>L,in</sub> (°C)	$\dot{m}_{L,in}$ (kg/s)	$\dot{m}_{V,in}$ (kg/s)	P <sub>in</sub> (bar)	$\dot{m}_{L,in}$ (kg/s)	T <sub>in</sub> (°C)
s124	12.0	188.4	0.48	0.04	3.5	13.3	43.7
s125	12.0	188.0	0.48	0.02	3.6	13.3	43.2
s126	12.0	187.8	0.10	0.04	3.5	13.1	43.8
s126r	12.0	187.7	0.10	0.02	3.5	13.0	43.8
s251r	25.0	0.0	0.00	0.55	3.7	25.0	42.9
s254	25.0	224.6	0.70	0.08	3.6	19.0	43.1
s255	25.0	224.7	0.70	0.04	3.6	19.0	43.7
s256	25.0	224.6	0.70	0.02	3.6	15.4	42.9
s257	25.0	219.4	0.10	0.02	3.5	13.7	44.0
s451r	45.0	0.0	0.00	1.00	3.7	33.0	43.0
s454	45.0	257.9	0.70	0.15	3.6	24.0	43.7
s455	45.0	257.9	0.71	0.08	3.6	19.9	42.9
s456	45.0	257.8	0.71	0.04	3.6	18.5	43.2
s457	45.0	257.8	0.70	0.02	3.7	17.5	43.0
s458	45.0	252.8	0.10	0.02	3.6	13.1	43.8
s651r	65.0	0.0	0.00	1.00	3.6	36.3	43.0
s654	65.0	281.1	0.70	0.20	3.7	27.7	43.0
s655	65.0	281.2	0.70	0.15	3.6	26.2	43.0
s656	65.0	281.2	0.70	0.10	3.5	22.5	43.4
s657	65.0	281.2	0.70	0.05	3.6	22.2	42.9
s658	65.0	281.2	0.70	0.02	3.6	18.4	43.1
s659	65.0	274.4	0.10	0.02	3.5	13.1	41.9

The nodalisation of the test facility for the simulation is shown in Fig. 3.17. The thermo-fluid object `CONDPIPE` is the condensation pipe (primary side), which is fed with water by `LIQINLET` and steam by the junction in `VERBINJT`. `CONDPIPE` is 3.3 m long and discretized into 34 nodes, which yields approximately 0.1 m per node ( $L/D = 2.4$ ). The mixture of steam and water flows out to the time-dependent volume (TDV) `CONDOUT`, where the outlet pressure and enthalpy are assigned. The object `COOLPIPE` is the cooling pipe (outer surrounding pipe). The heat conduction objects (HCOs) shaded in red, purple, grey, and dark green connect `CONDPIPE` and `COOLPIPE` to enable the heat transfer between the two pipes. For the heat transfer calculation between inner condensation pipe and outer cooling pipe, the single-phase heat transfer coefficient on the outer side was calculated according to the Dittus-Boelter correlation /DIT 30/. As earlier investigations have shown, the single-phase heat transfer coefficient is significantly underestimated on the shell side /JOB 24/, which might be the result of turbulence introduced by the experimental setup or by wall roughness. To compensate for this effect in the

calculations presented below, the heat transfer coefficient was increased by a factor of 2.5, which is in line with the measurements and the referenced publication.

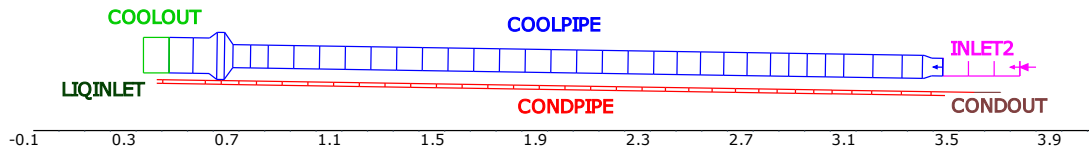


**Fig. 3.17** Nodalisation of COSMEA facility

Fig. 3.18 to Fig. 3.22 depicts the calculated and measured void fraction /BOD 24/ for COSMEA tests summarized in Tab. 3.1. To assess the newly introduced closure laws for stratified and annular flow, two simulations were compared: the reference simulation employing the standard wall and interfacial shear models of ATHLET, and the simulation invoking the dedicated models for annular and stratified flow. As can be seen from the figures, slightly improved void fraction results were found with the new implementation for many of the measuring points. Accordingly, condensate subcooling or condensation rates (Fig. 3.23) slightly improved for some tests as well, although significant discrepancies still persist, which have to be attributed (at least partly) to the heat transfer calculation.

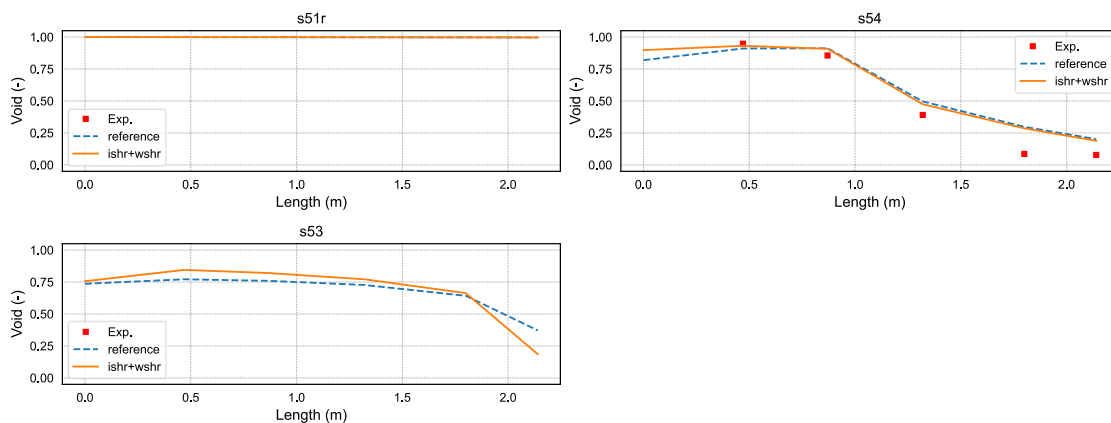


**Fig. 3.18** Void fraction along condensation pipe for COSMEA experiments at 5 bar

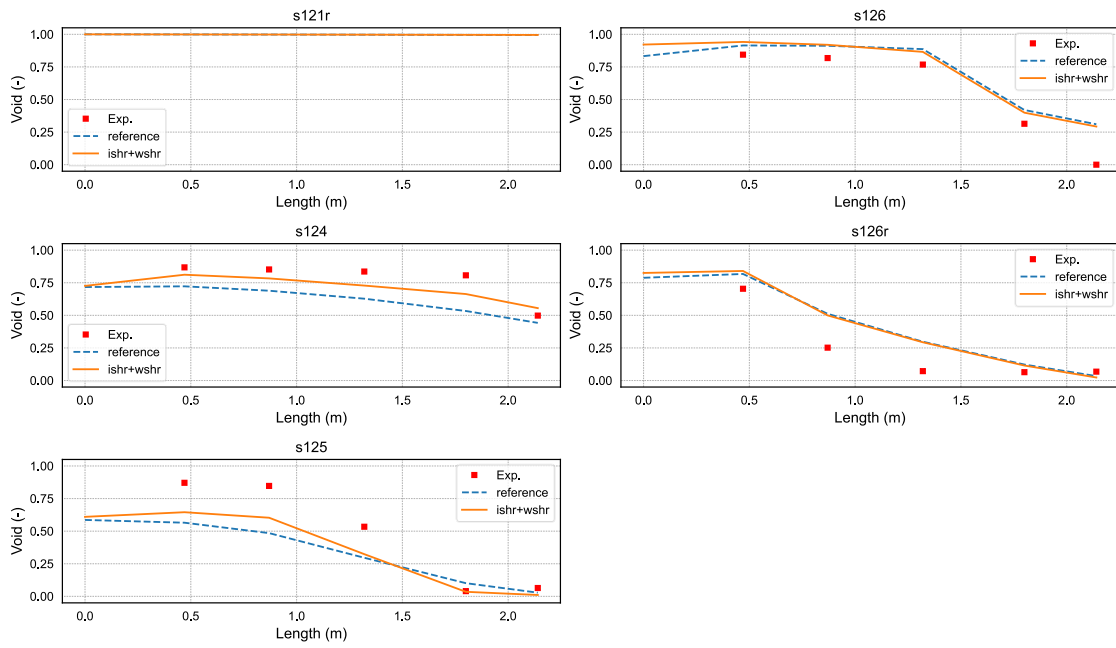


**Fig. 3.19** Void fraction along condensation pipe for COSMEA experiments at 12 bar

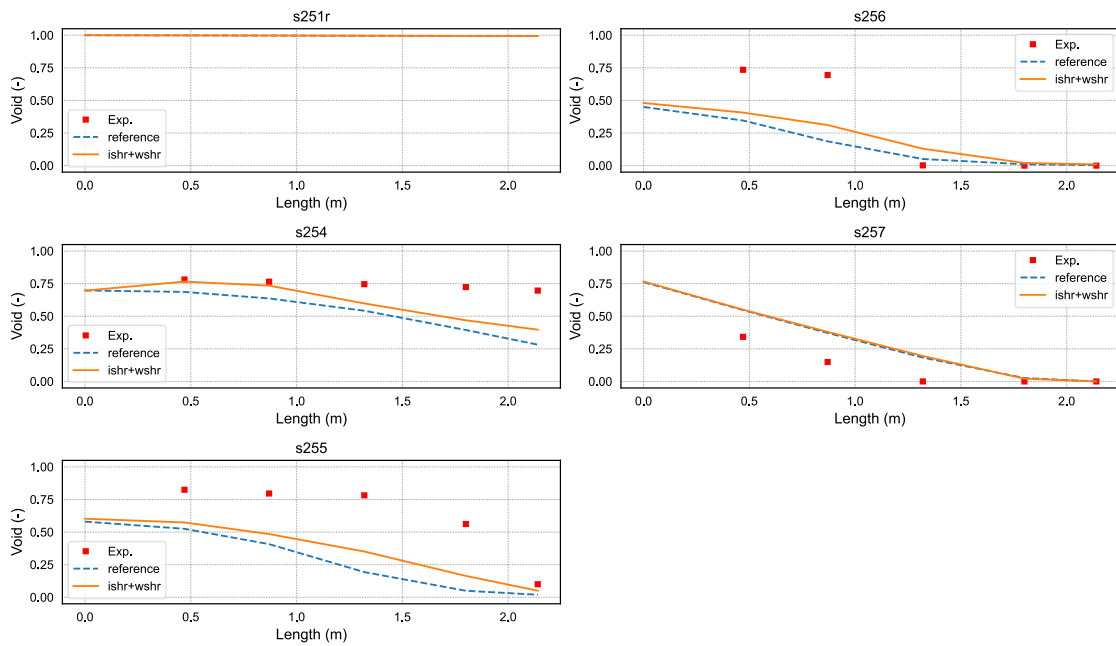


**Fig. 3.20** Void fraction along condensation pipe for COSMEA experiments at 25 bar

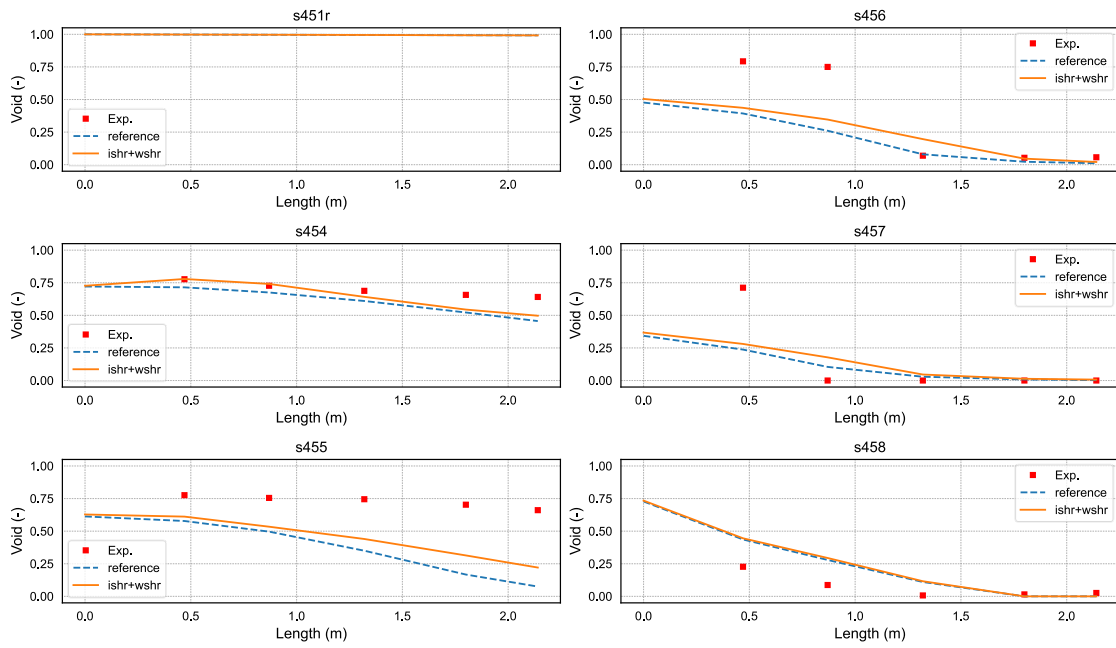


**Fig. 3.21** Void fraction along condensation pipe for COSMEA experiments at 45 bar

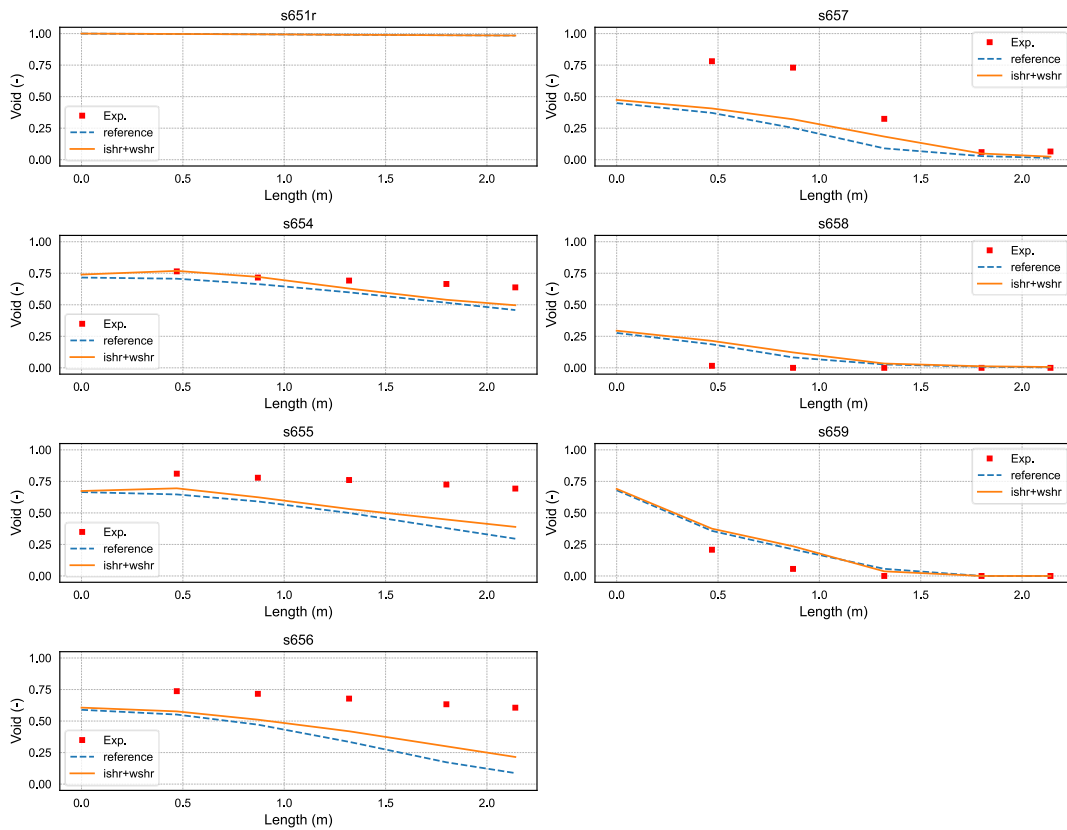


**Fig. 3.22** Void fraction along condensation pipe for COSMEA experiments at 65 bar

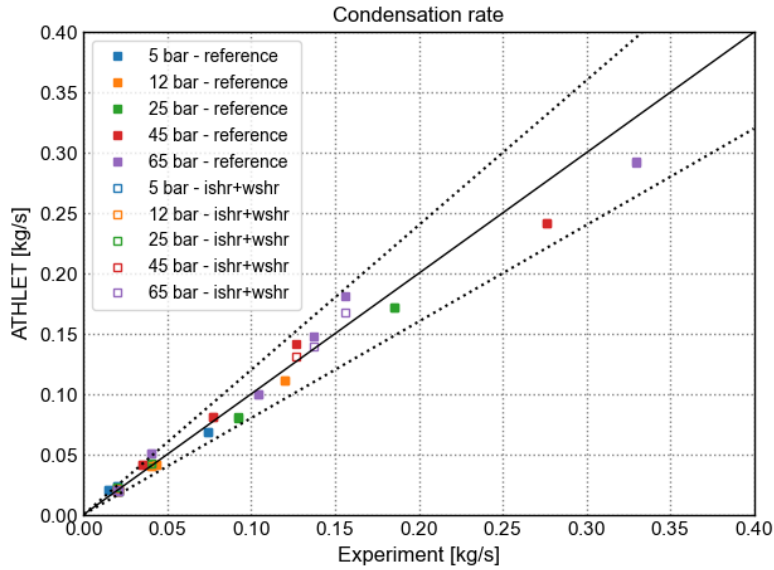


**Fig. 3.23** Measured and calculated condensation rate for COSMEA experiment

### 3.3 Extension of closure laws for condensing vertical flows

The centralized and extended ATHLET flow regime map for adiabatic and evaporation flows considers the annular flow regime as described in chap. 3.1.2.3.1.2. As a first step, this flow regime map was used for condensation flow as well. In order to treat the annular flow regime appropriately, extensions were provided to the interfacial and wall shear calculation as well as to the evaluation of the heat transfer coefficient for vertical pipe flow.

#### 3.3.1 Interfacial friction

In ATHLET (and similarly in other system codes like CATHARE /EMO 11/ or TRACE /NRC 12/), the interfacial friction calculation for vertical flow paths is based on the drift flux theory. As described in /SON 89/, /SKO 01/, starting from the drift flux equations, a formulation for the interfacial friction can be derived, so that the interfacial shear stress results from the product of an interfacial shear coefficient and the squared local relative velocity, which is the relative velocity calculated with the drift flux model. Since the ATHLET drift flux model can be understood as a full range model with general validity independent of the flow regime, the described method was previously applied without further distinction of the prevailing flow regime. However, in the past it turned out that droplet flow is not represented very accurately by the drift flux-based approach, so that interfacial friction of droplet flow was treated separately by considering the calculated entrainment fraction. In order to simulate the annular flow regime more accurately, a

dedicated approach for the calculation of the annular flow interfacial shear stress was implemented. The new model employs a specific correlation for the interfacial friction factor and is independent of the drift flux approach. For the calculation of the interfacial friction factor, different models from the literature were investigated.

In general, interfacial friction in vertical annular flow depends on the film thickness, since increasing film thickness enables the formation of disturbance waves on the film surface, which significantly impact the roughness of the phase interface and, thus, the interfacial shear. Basically, two types of interfacial friction factor correlations are available: Correlations based on the relative film thickness, e.g., derived from the void fraction, and correlations based on non-dimensional numbers to capture the effect of relevant input quantities on the wave formation, like gas velocity or liquid viscosity. For the former, the Wallis correlation /WAL 70/ (see equation (3.55)) is one example, whereas a correlation according to /JU 19/ is an example for the latter.

### 3.3.1.1 Wallis interfacial friction factor

For interfacial friction in annular flow, the well-known Wallis correlation /WAL 70/ for the interfacial friction factor was investigated:

$$f_i = 0.005(1 + 75(1 - \alpha)) \quad (3.74)$$

In order to properly derive the liquid film thickness by the liquid volume fraction  $(1 - \alpha)$ , the entrained liquid fraction  $\alpha_d$  must be considered, so that the interfacial friction factor becomes:

$$f_i = 0.005(1 + 75(1 - \alpha)(1 - \alpha_d)) \quad (3.75)$$

According to (3.47), the interfacial shear coefficient follows as:

$$C_i = \frac{\rho_g p_i}{2 A} f_i = \frac{2\rho_g}{D} \sqrt{\alpha} f_i = 0.1 \frac{\rho_g}{D} \sqrt{\alpha} (1 + 75(1 - \alpha)(1 - \alpha_d)) \quad (3.76)$$

### 3.3.1.2 Ju interfacial friction factor

Since several film thickness correlations like the previously described Wallis correlation were found to underestimate the interfacial friction factor for increasing film thickness, an additional correlation according to /JU 19/ was implemented in ATHLET:

$$f_i = 0.0028 + 4.28 \cdot We_f^{0.28} We_g^{-0.53} N_f^{0.25} \quad (3.77)$$

With the liquid Weber number  $We_f$ , the gas Weber number  $We_g$ , and the viscosity number  $N_f$ .

$$\begin{aligned} We_f &= \frac{\rho_f j_f^2 D}{\sigma} \\ We_g &= \frac{\rho_g j_g^2 D}{\sigma} \left( \frac{\Delta\rho}{\rho_g} \right)^{0.25} \\ N_f &= \frac{\mu_f}{\sqrt{\rho_f \sigma} \sqrt{\frac{\sigma}{g \Delta\rho}}} \end{aligned} \quad (3.78)$$

The range of validation of the correlation is given in terms of the relative film thickness as  $\frac{\delta}{D_h} < 0.03$ , which approximately corresponds to a film liquid fractions  $\alpha_{\text{film}} < 0.06$ . In contrast, ATHLET assumes annular flow for void fractions larger than  $\alpha > 0.75$  (with a transition range  $0.5 < \alpha < 0.75$ ). As a compromise for the calculation of the interfacial friction factor, a continuous transition between the Ju correlation for annular flow and the standard ATHLET model based on the full range drift flux approach has been implemented for void fraction between  $0.5 < \alpha < 1$ .

### 3.3.2 Wall friction

Wall friction in vertical annular flow is treated in the same way as in horizontal annular flow. As described in eqs. (3.68) to (3.69), the friction assigned to the liquid phase is a function of the share of annular flow in total flow.

### 3.3.3 Condensation heat transfer coefficient calculation

Many of the heat transfer correlations contained in ATHLET are valid for different flow patterns, or their validity, based on the literature, is not restricted to individual flow patterns. However, this does not apply to some of the heat transfer correlations for condensation on the pipe wall. These either take into account different flow patterns with their own transition criteria, which holds, e.g., for the Dobson-Chato correlation /DOB 98/. Or they are only valid for certain flow patterns, such as annular flow, and should therefore only be used for respective flow states. Since the central information on the flow pattern was not available in ATHLET so far, the correlations were used independently of the existing flow pattern.

In order to increase the predictive capability of ATHLET, the procedure for the selection of the HTC correlation under HECU was extended and now takes the flow pattern into account in case of condensing flows. If necessary or reasonable, other parameters can also be included in the selection of the HTC correlation, e.g., the duct geometry (pipe, bundle, etc.) or dimensionless parameters.

In the past, for condensation in vertical pipes, a correlation according to Carpenter-Colburn was used by default in ATHLET. In addition, a separate model according to Papini /PAP 10/ including three HTC correlations for a falling film (Nusselt (laminar), Kutateladze (laminar-turbulent), Chen (turbulent)) was implemented in ATHLET. This model has proven its applicability for simulations of vertical heat exchangers (e.g., for the PERSEO facility), but previously had to be explicitly activated by the user in the input data set for individual system domains. If the latter was done, the model was always used, regardless of whether or not condensation in annular flow was actually present.

The improved implementation harmonizes and automates the use of the Papini model with the identification of the flow pattern. To this end, the existing, centrally determined flow pattern has now also been passed on to the ATHLET heat transfer module so that it can be used there when selecting the heat transfer correlation. The Papini model is used when there predominantly exists an annular flow and condensation occurs on a cooling wall. The latter is the case when the wall temperature is below the saturation temperature of the fluid or – in the presence of NC gases – below the saturation temperature at the existing vapor partial pressure. Since the validation basis of the Papini model were pipes with a diameter of approx. 50 mm, the range for the automatic selection of

the correlation has been restricted. It is neither used for bundle geometry nor for pipes with a significantly larger diameter of more than 100 mm.

### 3.3.4 Validation against LOTUS experiment

For validation of the implemented constitutive relation for vertical annular flow an experiment performed at Long Tube System (LOTUS) test facility at Harwell Laboratory, UK, was selected [HEW 87]. The test section of the air/water test rig consisted of 31.8 mm (1.25 inch) internal diameter vertical copper tube which had a total length of 23 m. The air entered the tube at the bottom. About 2 m above the liquid is injected through porous wall section. The distance between the liquid injection and the beginning of the measurement section was approximately 18 m length (570 times the pipe diameter). This length was considered as sufficient to obtain equilibrium flow at the measurement section. The tests were performed for constant liquid mass flux of 297.1 kg/(m<sup>2</sup>s). The air mass flux varied between 2.96 and 161.69 kg/(m<sup>2</sup>s), The system pressure was kept at 239 kPa, measured at a distance of 19.5 m from the liquid injection.

The measured quantities were:

- Pressure gradient measured between purged liquid tapings spread apart at 1.26 m; the first being 18.11 m from the liquid injection point
- Liquid film flow rate measured by extracting film through a porous wall section at the top of the test tube; the entrained liquid fraction was not directly measured but it can be estimated as difference between injected liquid and measured film mass flow rate.

The experimental air-water tests were simulated by water-steam flow. Thus, the thermal-hydraulic parameters of the steam-water mixture had to be scaled. The main objective was to preserve the density ratio of water and air. Applying the original geometry and dimensions and using the experimental mass flows, the main parameters of pressure drop and entrainment correlations could be kept similar to the experiment (Tab. 3.2). To obtain comparable results, the pressure in calculations were scaled up to 5.4 bar. Simultaneously, the vapor temperature was increased to 155 °C, which is the saturation temperature for the pressure of 5.4 bar.

**Tab. 3.2** Parameter scaling for LOTUS calculations

	Experiment	Simulation
Water density	998.5 kg/m <sup>3</sup>	998.5 kg/m <sup>3</sup>
Air/steam density	2.9 kg/m <sup>3</sup>	2.9 kg/m <sup>3</sup>
Water viscosity $\eta_{w,20}$	0,001 Ns/m <sup>2</sup>	0.001 kg/m <sup>3</sup>
Air/steam viscosity $\eta_{gas}$	0.000018 Ns/m <sup>2</sup>	0.000014 Ns/m <sup>2</sup>
Viscosity ratio $\eta_{w,20}/\eta_{gas}$	55	71

It can be seen that the most important parameters for pressure drop calculations like phase densities and density ratio (approx. 344) are scaled, exactly. For the entrainment calculation, viscosity and surface tension are also important. However, viscosity and surface tension could not be scaled with the same accuracy. Surface tension is scaled exactly. The surface tension values of water for 20 °C at pressures of 2.4 bar and 5.4 bar are practically the same. The scaling of liquid and gas phase properties is satisfactory. Only the differences by gas phase viscosity could lead to an error in the calculation of entrainment rates. But since the difference is not very large, the expected error is small.

The vertical test section of the LOTUS test facility was modelled in ATHLET with 39 nodes. Wall roughness was assumed as  $10^{-6}$  m. The results of ATHLET calculations with the two fluid model and the experimental values are compared in Tab. 3.3.

**Tab. 3.3** Experimental and calculated values of LOTUS experiment

Test		Measurement			Annular flow model			
No	Air mass flux [kg/m <sup>2</sup> s]	Flow reg.	Pressure gradient [Pa/m]	Entrainment [-]	Flow reg.	pressure gradient [Pa/m]	Entrainment [-]	Void frac. [-]
1	0.00234	bub.	9489	0.0	slug	5221	0.00	0.54
4	0.052	slug	3388	0.0	slug	3847	0.00	0.71
5	0.060	slug	3217	0.0	slug	3624	0.00	0.72
10	0.072	slug	2559	0.0	ann.	3323	0.00	0.74
15	0.120	churn	2632	0.0	ann.	2345	0.00	0.81
20	0.0137	churn	2754	0.0	ann.	2113	0.00	0.83
25	0.0185	churn-ann.	2681	0.0	ann.	1657	0.00	0.87
30	0.0234	churn-ann.	2876	0.0	ann.	1365	0.00	0.90
33	0.0402	ann.	3624	0.0	ann.	1059	0.27	0.96
34	0.064	ann.	4363	0.58	disp.	1710	0.55	0.98
35	0.0686	ann.	4485	0.63	disp.	1893	0.59	0.98
37	0.0815	ann.	4631	0.76	disp.	2479	0.69	0.99
39	0.103	ann.	4702	0.88	disp.	3689	0.80	0.99
40	0.114	ann.	4972	0.91	disp.	4417	0.84	0.99
42	0.124	ann.	5363	0.92	disp.	5142	0.87	0.99

From Tab. 3.3 the following conclusions can be drawn:

- The observed and calculated flow regime partly differ due to different flow regime maps and different number of distinguished flow regimes. E.g., the experimentally determined “churn” flow regime is part of the calculated “slug” flow regime, and the experimentally determined “annular” flow regime comprises the “annular-disperse / disperse” flow regimes.

- For tests no. 1 to 4 ATHLET underestimates the pressure drop. This could be due to an overestimated interfacial friction. Since slug flow is the prevailing flow regime, the interfacial friction derived from the drift flux approach could be too high here.
- For tests no. 25 to 37 ATHLET underpredicts the pressure drop. This could be an indication that both void fraction and interfacial friction are overestimated. In that range, mainly churn and churn annular flow are experimentally observed, whereas ATHLET determined annular / annular-disperse flow. The deviatingly determined flow regime could be caused by the different transition criteria between intermittent and annular flow, as already highlighted in figure Fig. 3.9t. In ATHLET, the transition is shifted to lower superficial gas velocities, which corresponds to lower void fractions. Consequently, flow states with void fractions above approx. 0.75 are treated as annular or annular-disperse flow.
- Both the onset of entrainment as well as the entrainment fraction are quite well captured by ATHLET, although the entrainment fraction seems to be slightly underpredicted at very high void fractions. In the experiment it seems that after onset of entrainment the entrainment fraction rises rapidly with increasing gas mass flux. A less steep rise of entrainment at slightly lower velocities was predicted by the calculation. However, it can also be the case that in the experiment detection of small amounts of droplets was not successful.

Overall, the Harwell LOTUS experiment is satisfactorily reproduced by ATHLET with largest pressure drop deviations in the transition range between slug/churn and annular flow, where the simulations show significant underprediction of the pressure drops.

### **3.3.5 Validation against PERSEO experiment**

The PERSEO (in-Pool Energy Removal System for Emergency Operation) facility /BIA 03/, which is operated by SIET in Italy, was built to investigate the operational performance of a so-called isolation condenser for passive decay heat removal. The submerged condenser transfers heat to a water inventory, where steam is condensed on the inner side of the tube bundle and water is heated and finally evaporated on the outer side. Fig. 3.24 illustrates the layout of the PERSEO test facility. The secondary side consists of a heat exchanger pool (HXP), which is connected by a pipe with the Overall-Pool (OP). To activate the passive heat removal system, the valve in the connecting line is opened, so that water enters the HXP. Then steam is condensed in the vertical heat

exchanger pipes, which are connected to a steam feed line and a water drain line on the primary side.

Test 7 Part 1 performed in the PERSEO test facility aimed at the investigation of the capability and stability of the passive system to transfer heat from the primary to the secondary side. The PERSEO facility and test 7 were selected for the validation of the new annular flow model, since condensation in the vertical heat exchanger tubes caused the formation of an annular flow regime, so that the interaction of the flow regime module on the one hand with the heat transfer module and the selection of appropriate htc correlation on the other hand could be analysed.

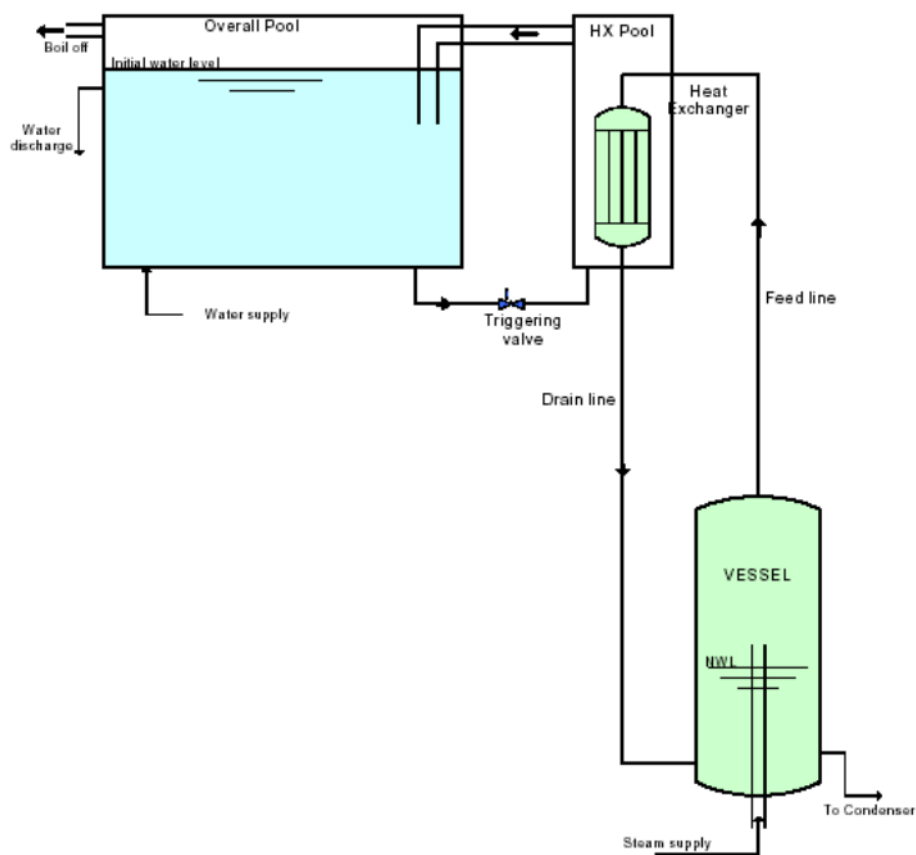


**Fig. 3.24** Schematic representation of PERSEO test facility /BIA 03/

Relevant initial and boundary conditions are presented in Tab. 3.4. The experiment was started with the opening of the trigger valve after 10475 s. During the several opening phases of the valve, water was flowing from the OP into the HXP. The isolation condenser power is depicted in Fig. 3.25. The measured power is compared to the calculated results of three different code versions and input data settings, a) the latest release version 3.4.1 with standard input settings, b) the latest release version 3.4.1 with input

settings to select specific heat transfer correlations for condensation in vertical pipes according to /PAP 10/, and c) the new code version including the centralized flow regime map module with annular flow model.

Firstly, the water entering the HXP heated up at the lower piping and the heat exchanger outlet collector. The power of the heat exchanger increased by approx. 1 MW but is underestimated in all calculations due to a too low level in the HXP (see Fig. 3.26). The power remained almost constant until the valve is opened for the last time. Then, the fill level in the HXP was increased up to the level of the upper collector, resulting in a power increase to around 20 MW. At 11260 s, the valve in the lower line is closed. The level in the HX pool then dropped due to evaporation, so that the performance of the heat exchanger started to decrease at approx. 11800 s, as its entire length was no longer submerged and wetted by water. As can be seen from the figures, the ATHLET release version with standard settings is not capable to satisfactorily represent the heat exchanger power and, consequently, the level in the HXP. The user-provided special HTC setting (label htc), where annular flow condensation correlations were employed along the whole length of the heat exchanger tubes (without consideration, and thus independent, of the currently prevailing flow regime) performed significantly better in representing the heat exchanger power. However, even slightly better results were achieved with the newly implemented flow regime map and annular flow model, noticeably without any special, user-provided settings.

**Tab. 3.4** Initial and boundary conditions for PERSEO Test 7 Part 1

<b>Vessel</b>		<b>HX Pool</b>	
Pressure	70.564 bar	Pressure	1.0061 bar
Temperature	291.5 °C	Temperature	78.3 – 230.0 °C
Level	-9.42 m	Level	0.19
<b>Trigger Valve</b>		<b>Overall Pool</b>	
1 <sup>st</sup> opening	10475 s	Pressure	1 bar
1 <sup>st</sup> closing	10608 s	Temperature	15.4 °C
2 <sup>nd</sup> opening	10621 s	Level	4.65 m
2 <sup>nd</sup> closing	10655 s		
Last opening	11039 s		
Last closing	11260 s		

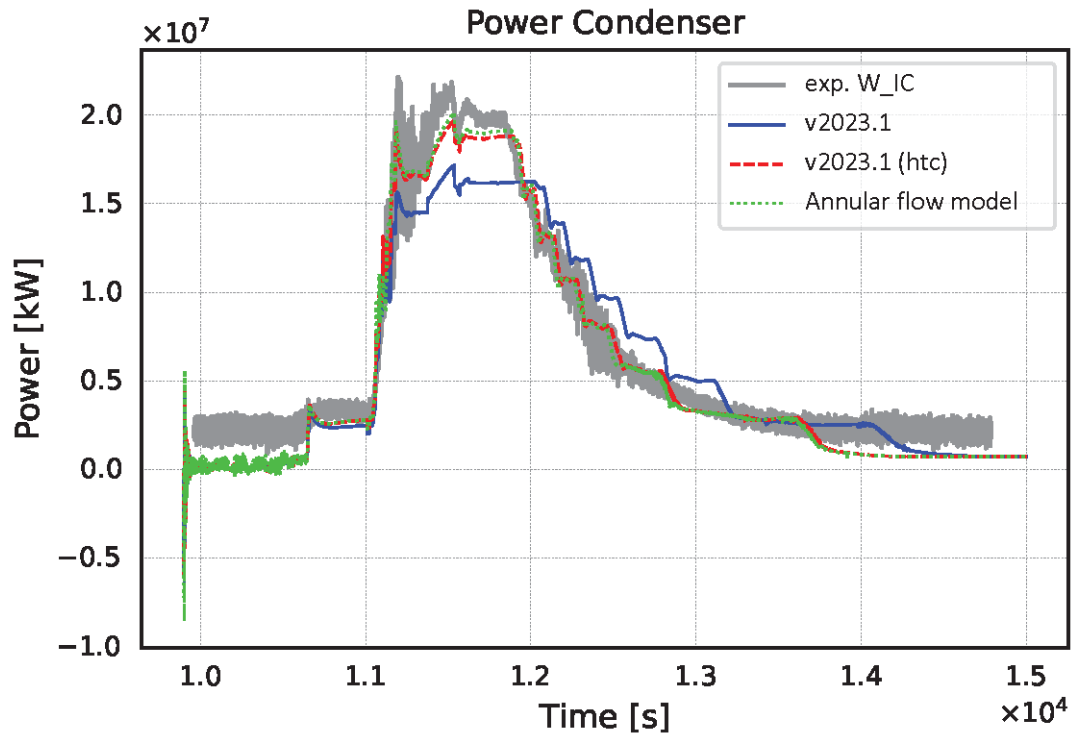


Fig. 3.25 Measured and calculated power of the PERSEO isolation condenser

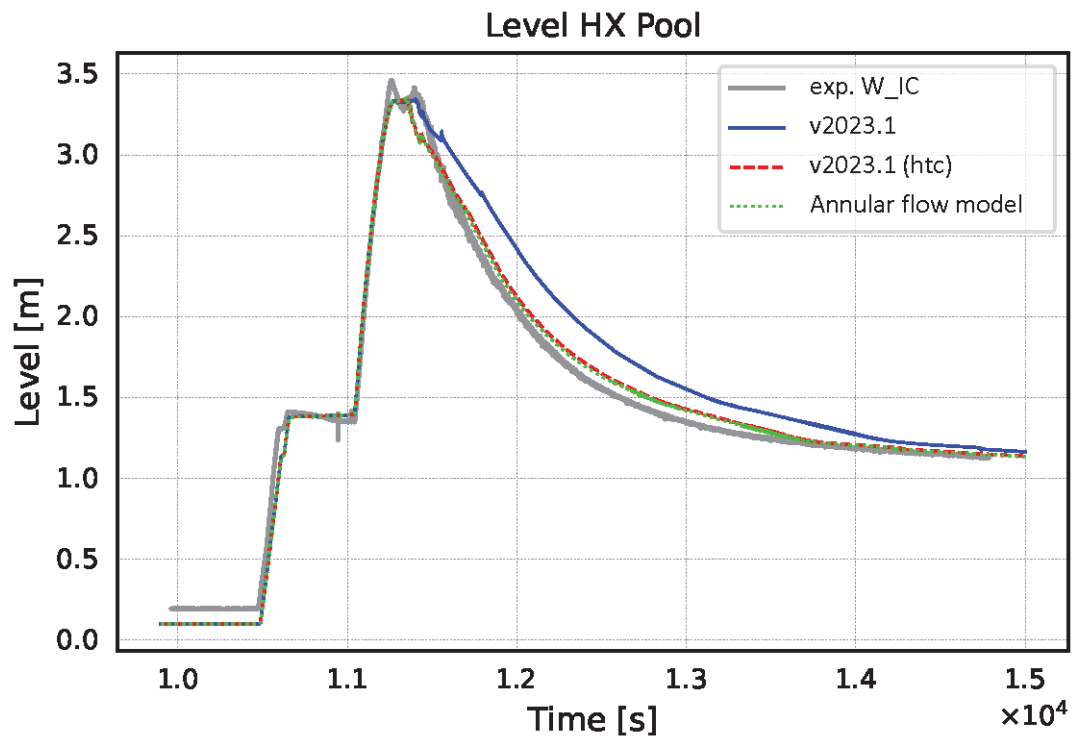


Fig. 3.26 Measured and calculated water level in PERSEO HX pool

In addition, the experiments Test 7 Part 2 and Test 9 performed in the PERSEO facility were also recalculated with the extended ATHLET modelling invoking the flow regime map module and the annular flow model. These tests considered different boundary conditions and water levels in the pools. The overall results confirmed the benefit of the expanded implementation in reproducing the measured heat exchanger power.

### **3.4 Current status in a nutshell**

As one can see from sections 3.1.2 and 3.1.3, most of the previously independently implemented correlations have become unified and centralized, whereby source code redundancy has been reduced and consistency increased. As illustrated in the sections 3.2 and 3.3, dedicated models for condensing flows in horizontal and vertical flow paths were successfully integrated. Nevertheless, it is also obvious that the application of the centralized flow regime calculation in ATHLET is still in the development and validation stage and the integration into the ATHLET main development version – although already prepared – has not been accomplished yet but is envisaged for the future.

#### **3.4.1 Application by the user**

When performing simulations with the development version, the (partial) application of the new implementation related to flow regime maps and further dependent models can be controlled via the input parameter `AA` under `CW MISCELLAN`. If `AA=0` is set, the difference to using the ATHLET master is that

- the entrainment calculation is centralized (see section 3.1.2.1),
- the calculation of the local relative phase velocities is centralized (see section 3.1.2.2),
- the flow regimes are centrally calculated, too, but not used by other ATHLET models, i.e., the predicted flow regimes are pure output quantities.

If `AA=1` is set, the flow regimes are no longer pure output quantities but considered in the wall and interfacial shear calculation (but not in other models).

If `AA=2` is set, the flow regimes considered in the bulk condensation/evaporation model (but not in other models).

If  $AA=3$  is set, the flow regimes are considered in the wall and interfacial shear model as well as in the wall friction model and the bulk condensation/evaporation model.

The options  $AA=1$  and  $AA=2$  are for testing and future validation purposes; of course, the final goal is full consideration of the centrally calculated flow regimes in all thermohydraulic models.

Independent of the chosen value for  $AA$ , the development branch produces additional print and plot output in the form of the vector  $\vec{p}$  which describes the composition of the current flow regime in a CV or junction (see equation (3.13)). Moreover, integer numbers are written out, which indicate the used flow regime map and the dominant flow regime. Below, an example print output of flow regime-related data for a horizontal pipe with 40 CVs is given. Immediately at its entrance, the pipe is filled with liquid and closely behind it – in CV No. 3, air is injected so that two-phase flow occurs. The numbers in the first column,  $FLMI$ , identify the used flow regime map;  $FLMI=10$  means that the CVs are completely filled with vapor and  $FLMI=5$  means that the flow regime map for horizontal flow paths, as presented in section 3.1.2.3.1.1 is used. The column captioned with  $FLRI$  indicates the dominant flow regime;  $FLRI=11$  means pure vapor,  $FLRI=1$  means stratified flow, and  $FLRI=8$  means droplet flow. The following columns named “ $EPFLRI...$ ” describe the percentages of the particular flow regimes – i.e., those are the elements of  $\vec{p}$ :

- $EFLRISTR$ : Stratified and stratified-wavy flow
- $EFLRIANN$ : Annular flow
- $EFLRIBUB$ : Bubbly flow
- $EFLRITAY$ : Deformable bubbles
- $EFLRISLG$ : Intermittent flow
- $EFLRICH$ : Churn flow (currently not used)
- $EFLRISTW$ : Stratified-wavy flow (currently included in stratified flow)
- $EFLRIDRP$ : Droplet flow
- $EFLRILIQ$ : Pure liquid flow
- $EFLRIVAP$ : Pure vapor flow

In all control volumes in the example, the flow regime is characterized as approximately 50% stratified and 50% droplet flow, where stratified flow prevails in the CVs closer to the pipe entrance and droplet flow from CV No. 13 to the outlet. Only in CV No. 3, another flow regime is partially existent (albeit with a negligible share) – annular flow.

Since the flow patterns are not only calculated for CVs but also for flow paths, similar output is produced for junctions (not shown here because it is analogous).

### Example print output of flow regime related data (CV-specific)

I/J	FLMI	FLRI	EFLRISTR	EFLRIANN	EFLRIBUB	EFLRITAY	EFLRISLG	EFLRICHR	EFLRISTW	EFLRIDRP	EFLRILIQ	EFLRIVAP
1		10	11 0.0000E+00	1.0000E+00								
2		10	11 0.0000E+00	1.0000E+00								
3		5	1 5.0152E-01	6.4522E-03	0.0000E+00	0.0000E+00	0.0000E+00	0.0000E+00	0.0000E+00	4.9203E-01	0.0000E+00	0.0000E+00
4		5	1 5.0629E-01	0.0000E+00	0.0000E+00	0.0000E+00	0.0000E+00	0.0000E+00	0.0000E+00	4.9371E-01	0.0000E+00	0.0000E+00
5		5	1 5.0554E-01	0.0000E+00	0.0000E+00	0.0000E+00	0.0000E+00	0.0000E+00	0.0000E+00	4.9446E-01	0.0000E+00	0.0000E+00
6		5	1 5.0481E-01	0.0000E+00	0.0000E+00	0.0000E+00	0.0000E+00	0.0000E+00	0.0000E+00	4.9519E-01	0.0000E+00	0.0000E+00
7		5	1 5.0409E-01	0.0000E+00	0.0000E+00	0.0000E+00	0.0000E+00	0.0000E+00	0.0000E+00	4.9591E-01	0.0000E+00	0.0000E+00
8		5	1 5.0337E-01	0.0000E+00	0.0000E+00	0.0000E+00	0.0000E+00	0.0000E+00	0.0000E+00	4.9663E-01	0.0000E+00	0.0000E+00
9		5	1 5.0265E-01	0.0000E+00	0.0000E+00	0.0000E+00	0.0000E+00	0.0000E+00	0.0000E+00	4.9735E-01	0.0000E+00	0.0000E+00
10		5	1 5.0194E-01	0.0000E+00	0.0000E+00	0.0000E+00	0.0000E+00	0.0000E+00	0.0000E+00	4.9806E-01	0.0000E+00	0.0000E+00
11		5	1 5.0122E-01	0.0000E+00	0.0000E+00	0.0000E+00	0.0000E+00	0.0000E+00	0.0000E+00	4.9878E-01	0.0000E+00	0.0000E+00
12		5	1 5.0051E-01	0.0000E+00	0.0000E+00	0.0000E+00	0.0000E+00	0.0000E+00	0.0000E+00	4.9949E-01	0.0000E+00	0.0000E+00
13		5	8 4.9979E-01	0.0000E+00	0.0000E+00	0.0000E+00	0.0000E+00	0.0000E+00	0.0000E+00	5.0021E-01	0.0000E+00	0.0000E+00
14		5	8 4.9907E-01	0.0000E+00	0.0000E+00	0.0000E+00	0.0000E+00	0.0000E+00	0.0000E+00	5.0093E-01	0.0000E+00	0.0000E+00
15		5	8 4.9835E-01	0.0000E+00	0.0000E+00	0.0000E+00	0.0000E+00	0.0000E+00	0.0000E+00	5.0165E-01	0.0000E+00	0.0000E+00
16		5	8 4.9763E-01	0.0000E+00	0.0000E+00	0.0000E+00	0.0000E+00	0.0000E+00	0.0000E+00	5.0237E-01	0.0000E+00	0.0000E+00
17		5	8 4.9690E-01	0.0000E+00	0.0000E+00	0.0000E+00	0.0000E+00	0.0000E+00	0.0000E+00	5.0310E-01	0.0000E+00	0.0000E+00
18		5	8 4.9617E-01	0.0000E+00	0.0000E+00	0.0000E+00	0.0000E+00	0.0000E+00	0.0000E+00	5.0383E-01	0.0000E+00	0.0000E+00
19		5	8 4.9544E-01	0.0000E+00	0.0000E+00	0.0000E+00	0.0000E+00	0.0000E+00	0.0000E+00	5.0456E-01	0.0000E+00	0.0000E+00
20		5	8 4.9471E-01	0.0000E+00	0.0000E+00	0.0000E+00	0.0000E+00	0.0000E+00	0.0000E+00	5.0529E-01	0.0000E+00	0.0000E+00
21		5	8 4.9397E-01	0.0000E+00	0.0000E+00	0.0000E+00	0.0000E+00	0.0000E+00	0.0000E+00	5.0603E-01	0.0000E+00	0.0000E+00
22		5	8 4.9323E-01	0.0000E+00	0.0000E+00	0.0000E+00	0.0000E+00	0.0000E+00	0.0000E+00	5.0677E-01	0.0000E+00	0.0000E+00
23		5	8 4.9249E-01	0.0000E+00	0.0000E+00	0.0000E+00	0.0000E+00	0.0000E+00	0.0000E+00	5.0751E-01	0.0000E+00	0.0000E+00
24		5	8 4.9174E-01	0.0000E+00	0.0000E+00	0.0000E+00	0.0000E+00	0.0000E+00	0.0000E+00	5.0826E-01	0.0000E+00	0.0000E+00
25		5	8 4.9099E-01	0.0000E+00	0.0000E+00	0.0000E+00	0.0000E+00	0.0000E+00	0.0000E+00	5.0901E-01	0.0000E+00	0.0000E+00
26		5	8 4.9024E-01	0.0000E+00	0.0000E+00	0.0000E+00	0.0000E+00	0.0000E+00	0.0000E+00	5.0976E-01	0.0000E+00	0.0000E+00
27		5	8 4.8948E-01	0.0000E+00	0.0000E+00	0.0000E+00	0.0000E+00	0.0000E+00	0.0000E+00	5.1052E-01	0.0000E+00	0.0000E+00
28		5	8 4.8873E-01	0.0000E+00	0.0000E+00	0.0000E+00	0.0000E+00	0.0000E+00	0.0000E+00	5.1127E-01	0.0000E+00	0.0000E+00
29		5	8 4.8796E-01	0.0000E+00	0.0000E+00	0.0000E+00	0.0000E+00	0.0000E+00	0.0000E+00	5.1204E-01	0.0000E+00	0.0000E+00
30		5	8 4.8720E-01	0.0000E+00	0.0000E+00	0.0000E+00	0.0000E+00	0.0000E+00	0.0000E+00	5.1280E-01	0.0000E+00	0.0000E+00
31		5	8 4.8643E-01	0.0000E+00	0.0000E+00	0.0000E+00	0.0000E+00	0.0000E+00	0.0000E+00	5.1357E-01	0.0000E+00	0.0000E+00
32		5	8 4.8566E-01	0.0000E+00	0.0000E+00	0.0000E+00	0.0000E+00	0.0000E+00	0.0000E+00	5.1434E-01	0.0000E+00	0.0000E+00
33		5	8 4.8488E-01	0.0000E+00	0.0000E+00	0.0000E+00	0.0000E+00	0.0000E+00	0.0000E+00	5.1512E-01	0.0000E+00	0.0000E+00
34		5	8 4.8410E-01	0.0000E+00	0.0000E+00	0.0000E+00	0.0000E+00	0.0000E+00	0.0000E+00	5.1590E-01	0.0000E+00	0.0000E+00
35		5	8 4.8332E-01	0.0000E+00	0.0000E+00	0.0000E+00	0.0000E+00	0.0000E+00	0.0000E+00	5.1668E-01	0.0000E+00	0.0000E+00
36		5	8 4.8253E-01	0.0000E+00	0.0000E+00	0.0000E+00	0.0000E+00	0.0000E+00	0.0000E+00	5.1747E-01	0.0000E+00	0.0000E+00
37		5	8 4.8174E-01	0.0000E+00	0.0000E+00	0.0000E+00	0.0000E+00	0.0000E+00	0.0000E+00	5.1826E-01	0.0000E+00	0.0000E+00
38		5	8 4.8095E-01	0.0000E+00	0.0000E+00	0.0000E+00	0.0000E+00	0.0000E+00	0.0000E+00	5.1905E-01	0.0000E+00	0.0000E+00
39		5	8 4.8015E-01	0.0000E+00	0.0000E+00	0.0000E+00	0.0000E+00	0.0000E+00	0.0000E+00	5.1985E-01	0.0000E+00	0.0000E+00
40		5	8 4.7934E-01	0.0000E+00	0.0000E+00	0.0000E+00	0.0000E+00	0.0000E+00	0.0000E+00	5.2066E-01	0.0000E+00	0.0000E+00

### 3.5 Residual issues and further work

The following list contains issues, which have to be resolved in subsequent work steps, as well as suggestions for further developments:

- For horizontal flow paths, it is recommended to implement a smooth transition region between bubbly and intermittent flow to avoid potential numerical problems.
- The calculation of the interfacial area should be centralized and used in all affected models.
- Currently, the models for wall friction and interfacial friction are implemented redundantly in the bulk condensation model routines in order to determine the dissipation rate of turbulent kinetic energy since this affects the condensation heat transfer. It is advisable to eliminate this redundancy and determine the turbulent kinetic energy dissipation rate directly in the wall friction and interfacial friction models.
- As test calculations revealed, computational performance seems still to be a general issue with the development branch, which holds the flow regime-related implementations. Before merging the modifications back into ATHLET's main development branch (the master), the potential for running the code more efficiently should be explored. To identify computational bottlenecks, further validation calculations are required. By introducing the abovementioned input parameter AA, the code has been prepared for this kind of investigations.
- Other flow regime maps/transition criteria as well as interfacial friction models should be included in ATHLET and tested as significant differences between the current ATHLET flow pattern map and the established map of Taitel et al. were observed especially for vertical flow paths.
- The interfacial friction calculation for vertical flow paths should be revisited, in particular for the transitional range between slug and annular flow regimes. Any changes to the interfacial friction calculation must be carefully coordinated with changes to the transition criteria given by the flow regime map, as both are interrelated and depend on each other.
- The implemented flow regime maps must be comprehensively validated.

- The presented output quantities concerning the flow regimes provide the opportunity to print or plot the spatial development of flow patterns in a pipe. It could be considered to include this as a feature in the simulation and visualization tools ATLASneo and Batchplot.

## **4 Improved modelling of complex two-phase flow conditions**

### **4.1 T-Junction Model**

When simulating flow through branches and T-junctions, the form loss and momentum flux term (convective part of the momentum equation) must generally be modelled consistently in order to achieve a realistic pressure loss or recovery. In most system codes, the user can select a special T-junction model that provides both the pressure loss and the distribution of water and vapour mass flows. So far, ATHLET provided a T-junction model for the 5-equation system. But regarding the internationally well-established 6-equation system, a dedicated model for simulating T-shaped pipe connections had not been available in the past, although in the case of a significant branching flow (and due to the resulting reduced velocity in the main flow direction) an unrealistically high pressure recovery and, thus, an incorrect system behaviour could be calculated. Hence, the development presented here aimed at closing the described modelling gap and providing an improved representation of a T-junction for the 6-equation system.

Concerning the distribution of phase mass flows between main pipe and side branch, the correlations of the 5-equation model were adopted. Details can be found in /SCH 23a/.

#### **4.1.1 Modelling of centrifugal force term**

The proposed model is based on the assumption that the three-dimensional phenomenon of two-phase flow division in a T-junction can be described as a superposition of two one-dimensional flows, in the axial direction of the main pipe and in the axial direction of the branch, i.e., radial direction of the main pipe. For the flow description in both directions one-dimensional momentum equations for liquid and gas phases are used. The multidimensional effects are considered by integration of the momentum equations in the branch direction and through introduction of special boundary conditions and closure relations for the momentum equations in the branch.

The gas and liquid phase entering the branch have different velocities. The difference is caused by different acceleration of both phases as the initial velocity (radial velocity in the main pipe) can be neglected. The acceleration depends on inertia, interfacial forces,

wall friction, gravitation, pressure forces, and due to motion along curved streamlines, the centrifugal forces acting on each phase. The terms of momentum equations with exception of centrifugal force correspond to large degree to the standard equations of ATHLET. The terms representing the centrifugal forces reflect the specific situation by flow splitting at the T-junction.

In the region of the T-junction the flow situation is very complicated, and an exact analysis of fluid motion is very difficult if not impossible at all. Nevertheless, for the purpose of the centrifugal force determination a simplified phenomenological approach has been applied. However, the flow paths of gas and liquid entering the branch have complicated geometry. For both phase flows entering the branch equivalent flow paths with constant radii of curvature have been assumed.

The radius of curvature is determined for a mean flow path of each phase entering the branch. To simplify the numerical calculation the flow paths are assumed to be circular sectors. They start at the front corner of the branch inlet in the centre of area occupied by the phase in the region of influence, tangential to the main pipe axis, and intersect the branch inlet at the centre of the branch inlet cross section, see Fig. 4.1.

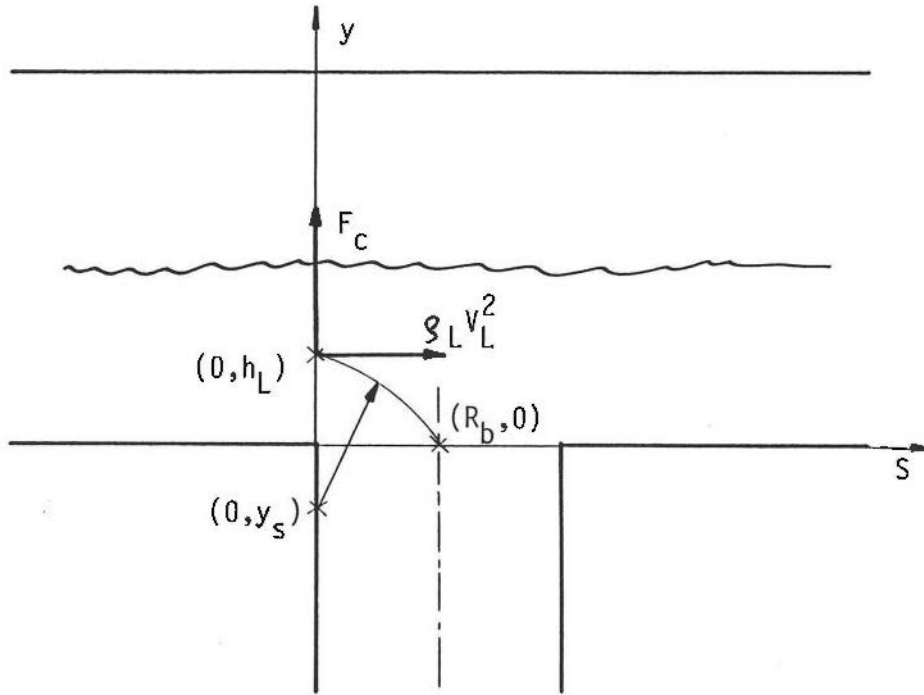


**Fig. 4.1** Scheme of determination of radius of curvature for equivalent liquid flow path for stratified flow at T-junction with downward branch

By writing for both phases the circle equation, the relation for the radius of curvature can be obtained as

$$R_i = 0.5 \left( h_i + \frac{R_b^2}{h_i} \right) \quad \text{with } i = l, v \quad (4.1)$$

The above equation is valid for both phases. The value  $h_i$  is determined taking into account the phase distribution in the region of the T-junction as it can be seen for a vertical side branch and stratified flow in Fig. 4.1. For a horizontal branch with vertical side branch the shortest distance between the centres of phase volumes in the region of influence and the inlet to the branch can be assumed as identical with the phase mean elevation in the region of influence relative to the elevation of the branch inlet.

For vertical downward and upward branches the difference between the values  $h_L$  and  $h_G$  calculated for liquid and gas phase, respectively, represents the degree of

stratification predicted by the model. In dispersed flow both phases are distributed homogeneously in the pipe cross section and the elevations of both phases, which are equivalent with flow path length, are equal.

For the horizontal side branch the radius of curvature is mainly influenced by radial phase distribution. Because the radial phase distribution at horizontal pipes is not determined in the model, it has been assumed that in this case radii of curvature of both phases are equal.

Now, the centrifugal force, projected on the side branch direction, can be written as:

$$F_{a,i} = F_{c,i} \cos \omega_i = (\cos \omega_i)^3 \rho_i \frac{(v_{1,i})^2}{R_i} \quad (4.2)$$

According to the definition of the equivalent flow path  $\cos \omega_i$  can be expressed as  $\cos \omega_i = \frac{R_i - y}{R_i}$ .

By the integral form of the balance equations, as applied in ATHLET, the momentum balance equation is integrated along the defined flow paths.

$$\int_0^{L_i} F_{a,i} dy = \frac{1}{4} \rho_i \frac{(v_{1,i})^2}{R_i^4} [R_i^4 - (R_i - h_i)^4] \quad (4.3)$$

This term is considered in the momentum equations of the 6-equation model for both phases.

#### 4.1.2 Pressure evolution in the T-junction main pipe

Pressure evolution in the diverging T-junction is related to the pressure drop at the side branch and pressure increase in the straight main pipe. The pressure drop in the side branch is caused mainly by the change of the flow direction. The change of the flow in the direction perpendicular to the initial direction of the main pipe is connected with acceleration of the branch flow from zero velocity (initial radial velocity of the flow in the

main pipe at the inlet to the T-junction) and resulting pressure drop. In addition, a significant pressure loss occurs due to building of a turbulence zone at the place of flow turning in branch direction.

Pressure increase in the straight main pipe is caused by Bernoulli effect due to flow decrease and corresponding deceleration. However, the influence of the turbulence zone and effect of pressure losses due to sudden expansion of the flow after diverging at the T-junction cause considerable pressure losses compensating partially the pressure increase due to momentum effects. Whereas the pressure drop effect in the side branch was considered in the most models of flow splitting in the T-junction, and also measured in many experiments, the effect of pressure evolution at the straight passage in the main pipe was investigated only in some works, and there are only a few experiments available where the pressure in the straight passage was measured /SAB 84/ /BUE 94/, /BAL 88/, /REI 88/. An extensive analysis of the pressure evolution at the straight passage of a T-junction could be found in the new edition of the Handbook of Hydraulic Resistance by Idelčik /IDE 08/. In this handbook the pressure drop in the main pipe and the related resistance coefficient is calculated as function of the velocity at the inlet of the T-junction, before division of the flow between side branch and the straight pipe. For the “normal” T-junction where the cross section of the main straight (st) pipe is constant, the pressure loss coefficient is described as function of relation of volumetric flows  $Q_c$  in the common duct (c) (at the T-junction inlet) and  $Q_s$  in the side branch (s).

$$\zeta_{c,st} = \frac{\Delta p_{st}}{\frac{1}{2} \rho w_c^2} = 1 - \left(1 - \frac{Q_s}{Q_c}\right)^2 - \left(1.4 - \frac{Q_s}{Q_c}\right) \cdot \left(\frac{Q_s}{Q_c}\right)^2 \quad (4.4)$$

The common flow at the T-junction inlet can be expressed as the sum of the outlet flows at side branch and straight passage. According to this the formula for pressure losses can be expressed as a function of the velocity at the straight passage.

$$\Delta p_{st} = \zeta_{st} \frac{\rho w_{st}^2}{2} \quad (4.5)$$

where  $\zeta_{st} = \zeta_{c,st} \frac{1}{\left(1 - \frac{Q_s}{Q_c}\right)^2}$

For the same reasons the volumetric flow at the T-junction inlet is expressed as sum of the side branch and straight flows:  $Q_c = Q_s + Q_{st}$

Introducing it into the above equation one gets:

$$\zeta_{st} = \zeta_{c,st} \frac{1}{\left(\frac{Q_{st}}{Q_{st} + Q_s}\right)^2} \quad (4.6)$$

According to it, also the formula of resistance coefficient should be expressed in the same way as function of outlet volumetric flows:

$$\zeta_{c,st} = 1 - \left(1 - \frac{Q_s}{Q_{st} + Q_s}\right)^2 - \left(1.4 - \frac{Q_s}{Q_{st} + Q_s}\right) \cdot \left(\frac{Q_s}{Q_{st} + Q_s}\right)^2 \quad (4.7)$$

The pressure loss at the straight passage is calculated using volumetric flow at the T-junction, expressed as a sum of volumetric flows at the branch and outlet junction of the straight pipe. Finally, the formula for determination of pressure loss in the main pipe, according to the flow splitting, is

$$\Delta p_{st} = \zeta_{st} \frac{\rho_1 \cdot (Q_{st} + Q_s)^2}{2A^2} \zeta_{c,st} \quad (4.8)$$

where  $\rho_1$  is the density of the flow at the T-junction and  $A$  the cross section of the main pipe.

Eq. (4.8) describes the pressure drop for two-phase flow mixture. For application to the equation system with separate momentum equations the total pressure loss has to be distributed between both phases. This is done proportionally to the volumetric flow of each phase. So, the pressure drop of the liquid flow is

$$\Delta p_{st} = \zeta_{st} \frac{\rho_{L,1} \cdot (Q_{st} + Q_s)^2}{2A^2} \zeta_{c,st} \cdot \frac{Q_{L,st}}{Q_{tot,st}} \quad (4.9)$$

And for the gas phase

$$\Delta p_{st} = \zeta_{st} \frac{\rho_{V,1} \cdot (Q_{st} + Q_s)^2}{2A^2} \zeta_{c,st} \cdot \frac{Q_{V,st}}{Q_{tot,st}} \quad (4.10)$$

Where:  $Q_{L,st}$  and  $Q_{V,st}$  are liquid and gas phase flows at the straight passage, respectively, and  $Q_{tot,st} = Q_{L,st} + Q_{V,st}$ .

#### 4.1.3 Model activation

The application of the 6-equation system for the T-junction can be controlled by the input parameter  $J_{TMOD}$ . The specific treatment of pressure drop in the main pipe can be optionally switched on/off. Due to not fully satisfying validation results with regard to a configuration with horizontal pipes and vertical downward branch, the 5-equation model is automatically applied for such a situation, independent of user input data. The extended T-junction model has been made available to all users with the release of code version ATHLET 3.4.0.

#### 4.1.4 Validation

For the validation of the newly developed extended T-junction model, a series of experiments done at Kernforschungszentrum Karlsruhe was used /SEE 86/, /REI 86/, /LAH 87/, /REI 88/. Phase separation and pressure differences were measured for a gas-liquid mixture flowing through the horizontal inlet pipe of a T-junction and branching pipes with different orientation (horizontally, vertically upward, and vertically downward). Experiments were done mainly using an air-water mixture, with different branch-to-inlet diameter ratios, in a pressure range between 0.4 and 1 MPa. Additionally, a few experiments were done using a steam-water mixture (only with horizontal branch, and same diameter in both pipes). The inlet void fraction and the ratio between the mass flow through the branching section and inlet mass flow,  $G_3/G_1$ , were varied in the

experiments. The outlet void fraction was measured to determine the phase separation at the T-junction, as well as the (temporally averaged) pressure at several positions both in the main channel and the branching section.

The ATHLET model of this experimental setup (Fig. 4.2) consists mainly of a horizontal pipe of 5 m length (object CHANNEL), with inner diameter 50 mm, and a branching section of 3.20 m length at position 1.85 m of the channel in different orientations (object VBRANCH resp. HBRANCH). At the start of this branching section, the T-junction model (TMODEL) is applied. At the end of the channel and the branching section, fill junctions (single junction pipes) are used to prescribe the total mass flow rates out of the system,  $G_2$  and  $G_3$ , and thus the mass withdrawal ratio (objects CHANOUT and BRANOUT). The pressure and the enthalpy of the mixture (and thus its void fraction) entering the system at mass flow rate  $G_1 = G_2 + G_3$  are set in a pressure-enthalpy boundary condition element (time-dependent volume, TDV) at the beginning of the channel (object CHANINL). Parameters are used to vary the flow conditions and the diameter of the branching section. The calculations started with single phase flow in the main channel and zero mass flow in the branching section. The inlet void fraction was adjusted to the target value right after the start of the calculation, and the mass flow ratio  $G_3/G_1$  was established after 12 s.

In the computations with this ATHLET model, the 6-equation model was generally applied for all objects, but different modelling approaches were used for the T-junction, with the 5-equation T-junction model as the base case. The computations with the 5-equation T-junction model were done using ATHLET 3.3, because in ATHLET 3.4 the improved pressure calculation in the main channel is also active for the 5-equation T-junction model when the 6-equation model is applied for the main channel. For each run, the phase separation  $X_3/X_1$  (ratio of the observed void fraction at the outlet of the branching section and the inlet void fraction) and the pressure differences  $\Delta p_{12}$  (pressure difference in the main channel between the control volumes in front of and behind the T-junction) and  $\Delta p_{13}$  (pressure drop in the T-junction) were evaluated.

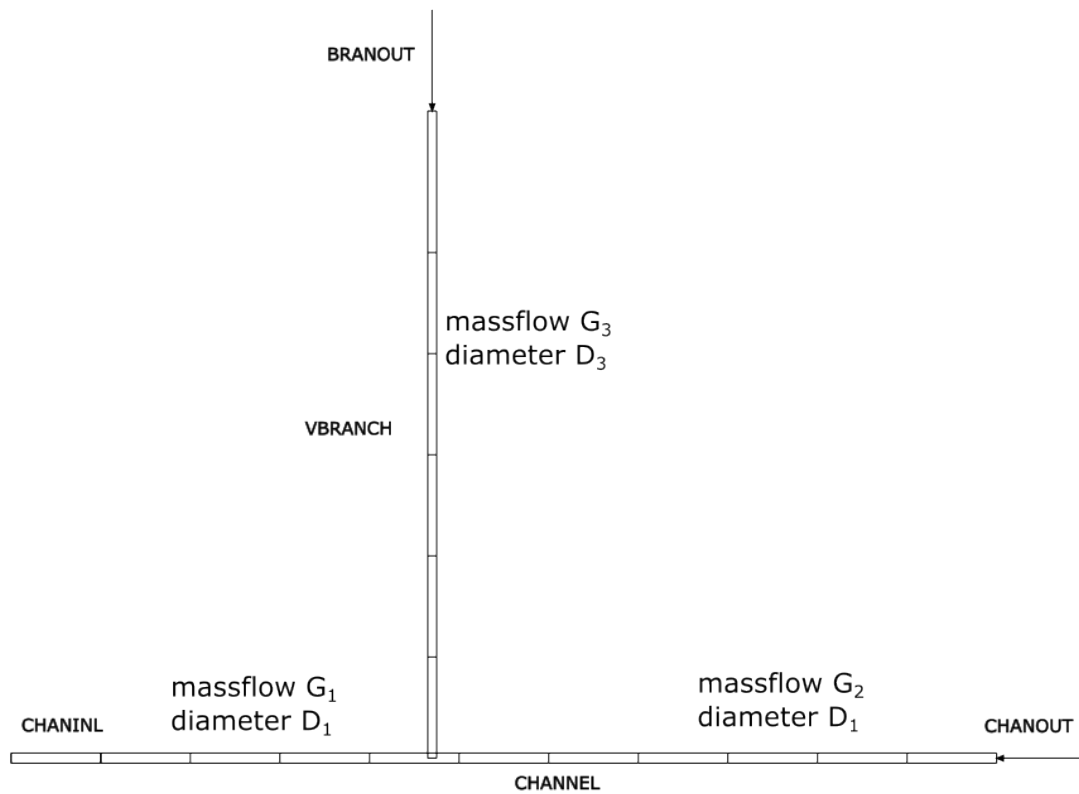


**Fig. 4.2** ATHLET representation of the experimental setup with a main pipe and a branching section (vertically upward arrangement shown here) and controlled mass flow at both outlets, as it was used for the validation of the extended T-junction model

The effect of the change of the T-junction model is shown in Fig. 4.3 and Fig. 4.4 for an arbitrarily selected test case with horizontal branching (run 19.0 in /REI 88/: diameter ratio  $D_3/D_1 = 1$ , mass flow ratio  $G_3/G_1 = 0.770$ ,  $G_3 = 4.451$  kg/s, inlet void fraction 0.038, pressure 6 bar).

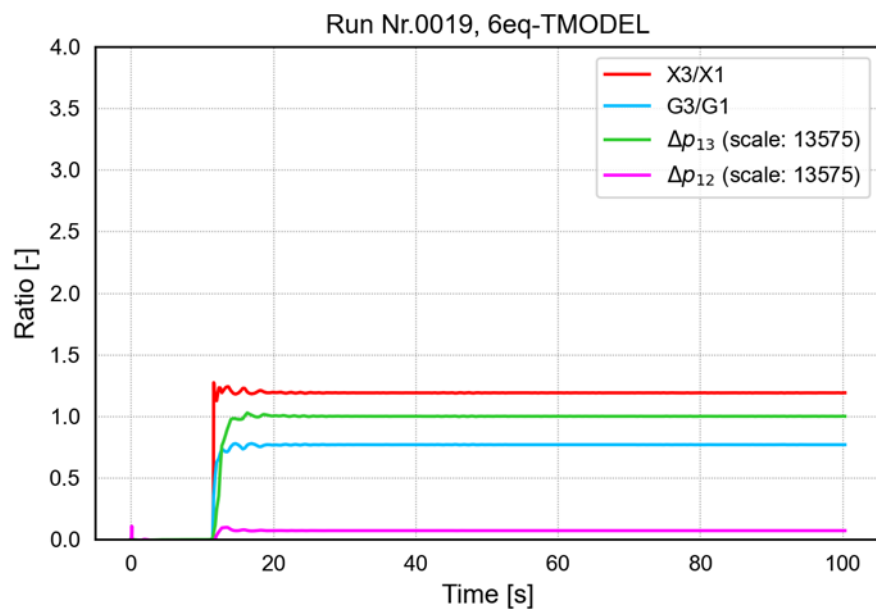
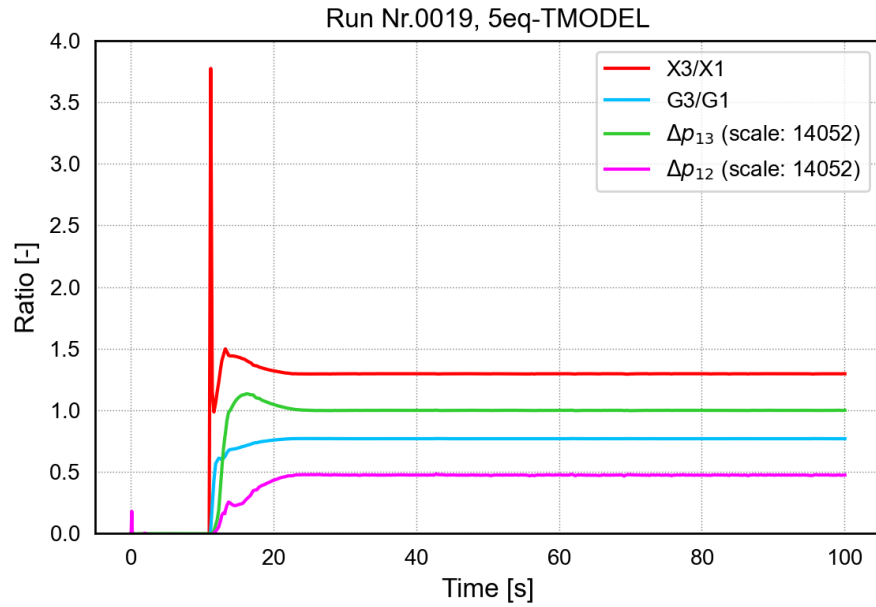


**Fig. 4.3** Effect of the change of the T-junction model for a selected test case (for flow conditions, see text). The absolute values of  $\Delta p_{12}$  and  $\Delta p_{13}$  are normalized to 1 for the graphical representation, with the maximum absolute value given in parentheses in the legend

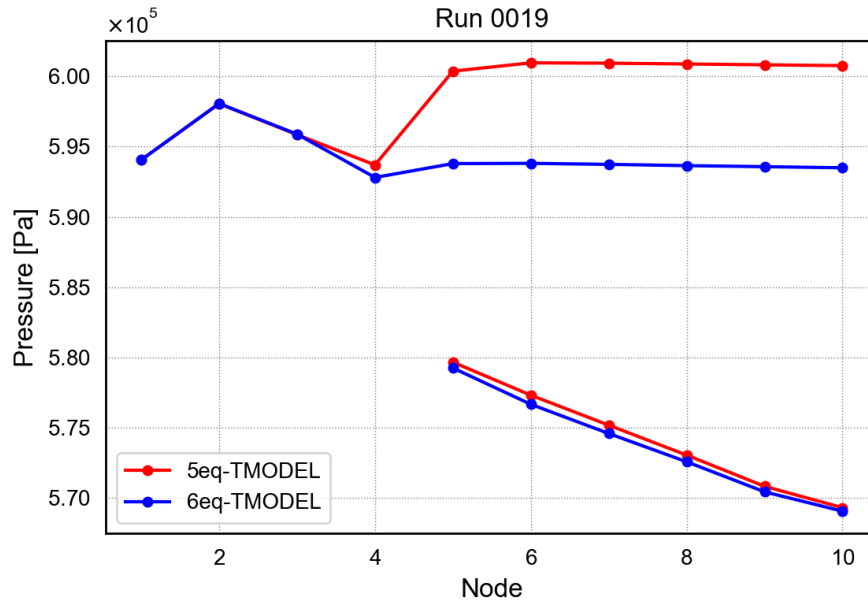


**Fig. 4.4** Pressure in the control volumes of the main channel (connected lines) and in the branching section (disconnected curves)

The change of the T-junction model has a visual effect on the separation ratio  $X_3/X_1$  (experimental value for this case: 1.249), and the pressure recovery  $\Delta p_{12}$  in the main line is strongly reduced in this test case with the 6-equation T-junction model. For a more comprehensive validation of the T-junction model options, several calculations were done for selected values of the pressure and the branching diameter with fixed inlet mass flow  $G_1$  and inlet void fraction  $X_1$ , with a slow stepwise variation of  $G_3/G_1$  from 1 to 0, such that a steady state could in principal be achieved for each step value of  $G_3/G_1$ . However, it was observed that mainly for small values of  $G_3/G_1$  (that is, low flow rate in the branching section) a steady solution could not always be achieved regardless of the applied T-junction model.

In the following, three representative cases for a horizontal branch performed at a pressure of 7 bar are investigated. Test one exhibits a high inlet mass flow at low void fraction, while test two considers low inlet mass flow at high void fraction. Finally, case three investigates different diameters of main and branching pipe at a moderate mass flow rate and average void fraction. Tab. 4.1 summarizes the boundary conditions.

**Tab. 4.1** Boundary conditions of investigated KIT T-junction experiment

Test no.	$D_3/D_1$	$G_1$	$X_1$
1	1	4.05	0.02
2	1	0.256	0.625
3	0.52	0.58	0.138

In the following, results for the three tests are presented. The phase separation figures include additional lines for equal phase separation (dashed black line) and total phase separation (dotted black line) in the T-junction. The latter prescribes the conception that the branching mass flow consists to the largest possible share of vapor (depending on the inlet quality). Experimental results from /REI 88/ with these parameters (and different values of  $G_3/G_1$ ) are included in the figures.

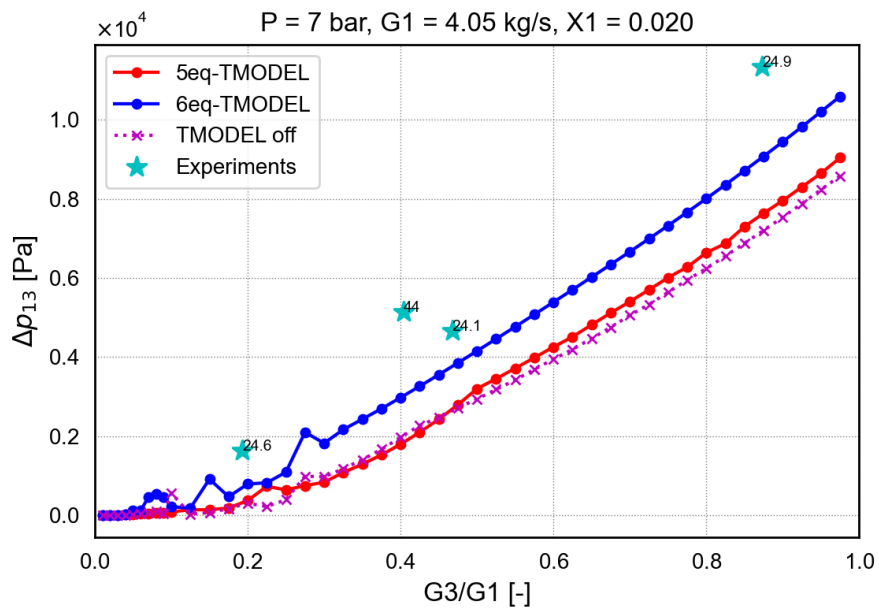


**Fig. 4.5** Pressure drop  $\Delta p_{13}$  of the flow into the horizontal side branch with same diameter as the main channel  $D_3/D_1 = 1$ , and inlet void fraction  $X_1 = 0.020$ , inlet mass flow rate  $G_1 = 4.05 \text{ kg/s}$ , at pressure 7 bar. The stars indicate experimental values (number of the experiment as in /REI 88/)

In Fig. 4.5 results of the pressure drop in the T-junction are shown and compared with experimental values (pressure 7 bar, inlet mass flow rate 4.05 kg/s, inlet void fraction

0.020). Although the stepwise variation of the applied mass flow ratio was done slowly, with sufficient time to achieve a stationary solution before the pressure drop is determined, the irregular appearance of the curve for low mass flow ratios indicates that a stationary solution could not be achieved in all cases. For this parameter set, the pressure drop is underestimated for all mass flow ratios, with better results with the application of the new 6-equation T-junction model.

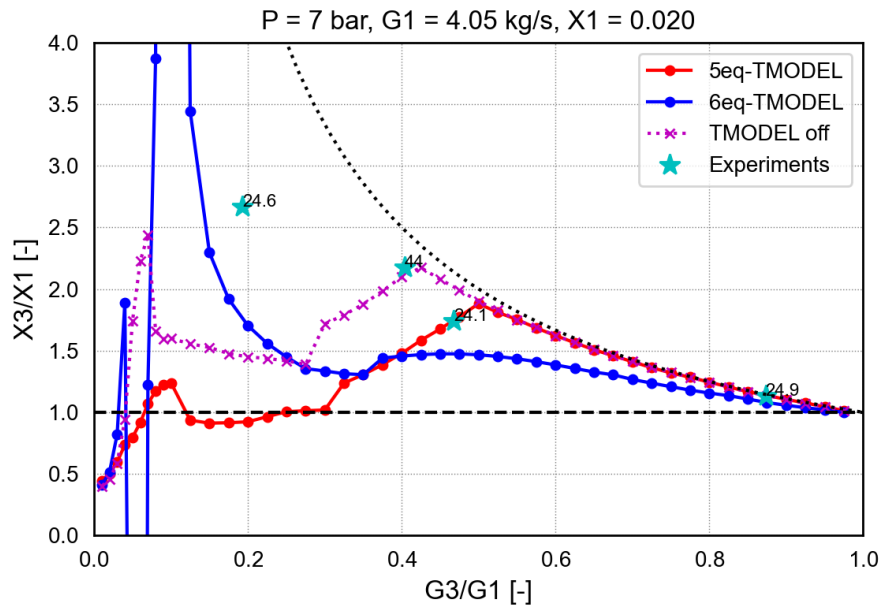


**Fig. 4.6** Phase separation  $X_3/X_1$  of the flow into the horizontal side branch with same diameter as the main channel  $D_3/D_1 = 1$ , and inlet void fraction  $X_1 = 0.020$ , inlet mass flow rate  $G_1 = 4.05$  kg/s, at pressure 7 bar

The phase separation for the same parameters is shown in Fig. 4.6. For higher values of  $G_3/G_1$ , the experimental value is reasonably reproduced in all compared modelling approaches, without an advantage for the 6-equation T-junction model. The trend for the separation is missed for low values of  $G_3/G_1$  by the 5-equation T-junction model, while the 6-equation T-junction model qualitatively reproduces the increase of the phase separation for lower mass flow ratios, however with increased stability issues for very low values of  $G_3/G_1$ .

For another set of parameters, with low inlet mass flow and high inlet void fraction (pressure 7 bar, inlet mass flow rate 0.256 kg/s, inlet void fraction 0.625), stable stationary

solutions can be achieved over the full range of  $G_3/G_1$ . The comparison of the computed phase separation with experimental values (Fig. 4.7) shows very good agreement for the 6-equation T-junction model for high values of  $G_3/G_1$ , while  $X_3/X_1$  is overestimated for lower mass flow ratios. With the 5-equation T-junction model, the phase separation is generally underestimated and not captured for this set of parameters. The pressure drop is not shown for this parameter set, because this quantity is missing in /REI 88/ for most of the experiments in this regime.

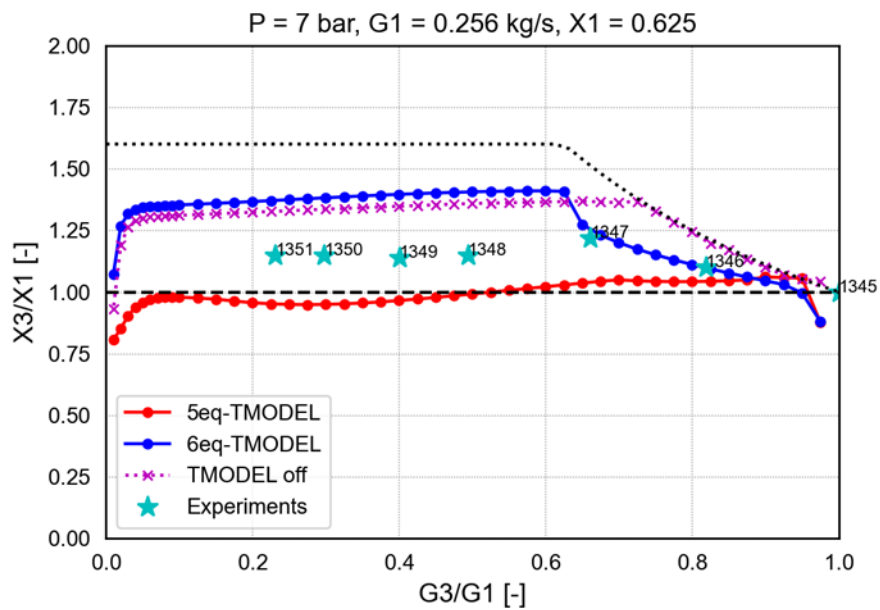


**Fig. 4.7** Phase separation  $X_3/X_1$  of the flow into the horizontal side branch with same diameter as the main channel  $D_3/D_1 = 1$ , and inlet void fraction  $X_1 = 0.625$ , inlet mass flow rate  $G_1 = 0.256 \text{ kg/s}$ , at pressure 7 bar

Finally, in Fig. 4.8 and Fig. 4.9, the results of the different modelling approaches are compared for one of the test cases with a branching section with reduced diameter ( $D_3/D_1 = 0.52$ ) compared to the main channel (pressure 7 bar, inlet mass flow rate 0.58 kg/s, inlet void fraction 0.138). Here, the phase separation is better reproduced with the 6-equation T-junction model than with the 5-equation T-junction model, which strongly overestimates the phase separation under these conditions. The pressure drop is reasonably reproduced by both models.

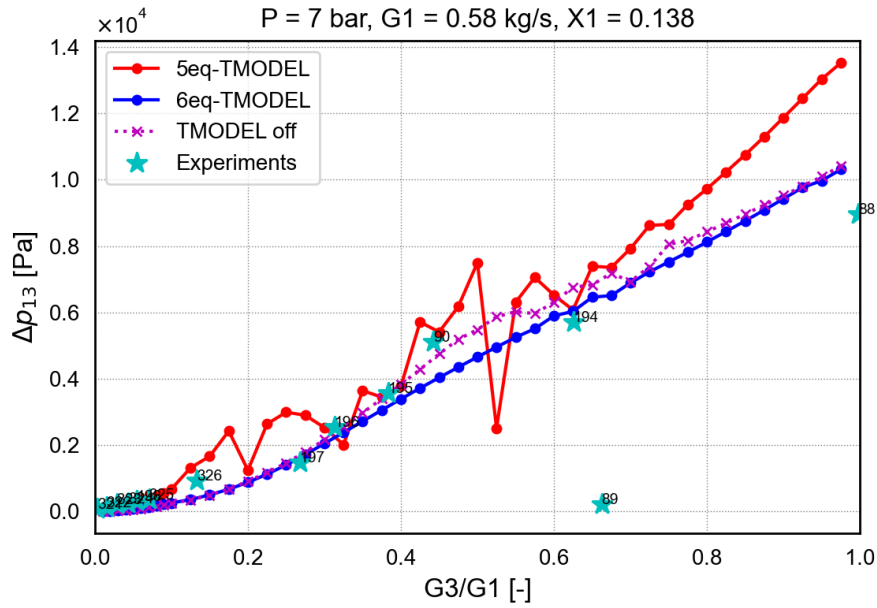


**Fig. 4.8** Pressure drop  $\Delta p_{13}$  for horizontal side branch with  $D_3/D_1 = 0.52$ , inlet void fraction  $X_1 = 0.138$ , inlet mass flow rate  $G_1 = 0.58 \text{ kg/s}$ , pressure 7 bar

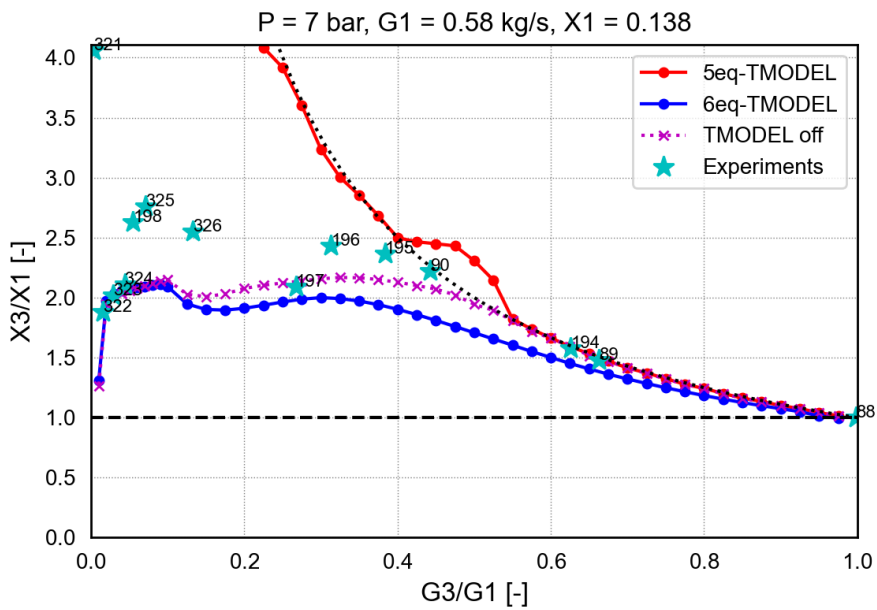


**Fig. 4.9** Phase separation  $X_3/X_1$  for horizontal side branch with  $D_3/D_1 = 0.52$ , inlet void fraction  $X_1 = 0.138$ , inlet mass flow rate  $G_1 = 0.58 \text{ kg/s}$ , pressure 7 bar

In general, it can be concluded that the newly implemented 6-equation T-junction model improves in some (though not all) parameter ranges the results for the pressure drop and for the phase separation in a horizontal T-junction, compared to the 5-equation T-junction model, except for the high mass flow ratio regime where both models perform similarly well.

On the downside, with the application of the 6-equation T-junction model, the stability of the calculation can be negatively influenced. The oscillations tend to be stronger than with the 5-equation T-junction model (or without any application of the T-junction model); high stability could only be observed when the 5-equation model is applied to the whole system, leading however to worse results. These observations reveal on the one hand the necessity to employ the more elaborate modelling of the 6-equation system but indicate on the other hand a general challenge in modelling the flow through a T-junction with the 6-equation model.

In general, it has to be stated that the oscillations observed in some calculations are not necessarily a consequence of the 5- or 6-equation T-junction model but are rather related to the imposed boundary conditions for the mass flow rates, which might not be adequate for ATHLET and correspond to a flow state unattainable by the code's two-phase flow models. The fact that the 5-equation model behaves more robust to boundary mass flow specification is to be expected and logically consistent since it uses the total mass flow as solution variable. The 6-equation model has to "translate" the total mass flow boundary condition into phase velocities (solution variables) and a corresponding phase slip, which could become inconsistent with, e.g., the two-phase pressure drop modelling.

Mainly due to the observed oscillations, further validation of the T-junction model is required in the future. For that purpose, the 6-equation T-junction model is offered as an additional input option in ATHLET, and the 5-equation T-junction model remains available. Due to its broader range of validation, the 5-equation T-junction model remains the generally recommended option so far. For T-junctions with a vertically upward branch, similar conclusions can be drawn as for the configuration with a horizontal branch.

## 5 Thermo-mechanical modelling

### 5.1 Improved fuel rod model

As a thermohydraulic system program, ATHLET is primarily, though not solely, employed for the safety analysis of water-cooled nuclear reactors. The program's capability to accurately calculate the energy stored within the reactor core during steady state and transient conditions is essential. This calculation is crucial because it influences the surface temperature of the cladding tubes and the likelihood of a boiling crisis. Such a crisis could critically impair the cooling of the cladding tubes during a postulated accident condition, posing a significant safety risk. Within this context, several factors, such as the rod gap heat transfer coefficient and the radial pellet power distribution, play a crucial role in determining the stored energy. These phenomena must be realistically modelled to ensure an adequate estimation of the energy stored in the reactor core.

To address these needs, this project has introduced several significant enhancements to ATHLET's fuel rod model. These improvements aim to refine the system's predictive accuracy and include the following key developments:

1. Extension of the existing gap conductance model with models accounting for internal fuel rod pressures and phenomena such as fuel relocation, swelling, and densification.
2. Integration of radial pellet power profiles allowing for the simulation of pellet radial distribution and "rim" effects.
3. Integration of models that simulate the thermal resistance of oxide layers potentially forming on the surface of fuel rods and their impact on the thermal exchange with the coolant.

These improvements were meticulously implemented in ATHLET's fuel rod model, significantly bolstering its capability to predict the energy stored in the fuel with higher precision. Detailed descriptions of these models and their verification activities are presented below, highlighting the rigorous validation processes that ensure their reliability and effectiveness.

## 5.2 Model description

### 5.2.1 Improved gap conductance model

The previous fuel rod model relied on a simplified gap conductance model. This model calculated the global gap heat transfer coefficient,  $HTC_{\text{gap}}$ , by considering the heat transfer mechanisms of heat conduction through the gas within the gap and fuel-to-clad radiation as shown in (5.1).

$$HTC_{\text{gap}} = HTC_{\text{cond}} + HTC_{\text{rad}} \quad (5.1)$$

In (5.1), the  $HTC_{\text{cond}}$  contribution was calculated by (5.2):

$$HTC_{\text{cond}} = \frac{\lambda_{\text{gap}}}{\max\{\delta_{\text{gap}}^{\text{eff}}, 1e^{-7}\}} \quad (5.2)$$

Where  $\lambda_{\text{gap}}$  is the thermal conductivity of the gas mixture within the gap (W/(m K)). Details of the model used to evaluate  $\lambda_{\text{gap}}$  are reported in /SCH 23a/. The effective gap width (m),  $\delta_{\text{gap}}$ , was evaluated as in shown in (5.3).

$$\delta_{\text{gap}}^{\text{eff}} = \delta_{\text{gap}}^0 + \delta u_{\text{clad}}^{\text{thermal}} - \delta u_{\text{fuel}}^{\text{thermal}} \quad (5.3)$$

Being, in particular:

- $\delta_{\text{gap}}^0$  the initial gap size at the room temperature (m);
- $\delta u_{\text{clad}}^{\text{thermal}}$  the cladding inner radius displacement due the thermal expansions (m);
- $\delta u_{\text{fuel}}^{\text{thermal}}$  the fuel outer radius displacement due the thermal expansions (m).

As per reference (5.2), it is assumed that the minimum gap size should not be less than  $10^{-7}$  m under any circumstances.

In line with advanced fuel performance models utilized in well-known codes such as FRAPCON /GEE 15a/, CTF /SAL 19/, MARS /KOR 06/, etc., models presented in (5.2) and (5.3) were further improved to account for additional modelling features, which might potentially enhance the prediction capabilities of the model.

In particular, the old gap conductance model was extended to account for:

- a better formulation of eq. (5.2) including, beyond the effective gap size, effects of fuel and clad roughness, as well as quantities, which model the imperfect heat transfer between the gas molecules and the surfaces of the fuel and clad;
- displacement of the inner radius of the cladding due to elastic mechanical effects, and
- displacement of the fuel outer radius induced by the effects of fuel radial relocation, swelling, and densification.

The extension of the model was conducted by considering models describing the cladding elastic mechanical behaviour as suggested in /SAL 19/. Models describing burnup-dependent effects of the fuel radial relocation, swelling, and densification were instead adopted from TESP-ROD, a fuel performance code developed by GRS, and implemented as suggested in /SON 02/. In addition, an updated formulation of eq. (5.2) was considered from /GEE 15a/.

According to the new model formulation, the new  $HTC_{cond}$  is described by eq. (5.4).

$$HTC_{cond} = \frac{\lambda_{gap}}{\max\{\delta_{gap}^{eff}, 0\} + A(R_f + R_c) + 1.8(g_f + g_c) - B} \quad (5.4)$$

with:

- $\lambda_{gap}$  conductivity of gap gas mixture as previously evaluated in /SCH 23a/, (W/m/K)
- $\delta_{gap}^{eff}$  as the effective gap size, m
- $A = \exp(-1.25 \cdot 10^{-3} P_{int})$ , non-dimensional coefficient depending on  $P_{int}$ , -

- $P_{int}$  fuel-cladding interfacial pressure,  $\text{kg/cm}^2$
- $R_f + R_c$  sum of fuel and clad surface roughness, m
- $g_f + g_c$  sum of extrapolation lengths in fuel and cladding, respectively, m
- $B = 1.397 \cdot 10^{-6}$ , model constant, m

In eq. (5.4), the new effective gap size,  $\delta_{gap}^{eff}$ , is determined, this time, as shown in eq. (5.5).

$$\delta_{gap}^{eff} = \delta_{gap}^0 - \delta u_{fuel} + \delta u_{clad} \quad (5.5)$$

In eq. (5.5),  $\delta_{gap}^0$  is the same initial gap size presented in (5.3) whereas  $\delta u_{fuel}$  and  $\delta u_{clad}$  are, respectively, the new total displacements of the fuel outer and cladding inner radii. The main assumption made for the evaluation of  $\delta u_{fuel}$  is that the fuel expands freely, and its expansion is not affected by either the rod inner pressure or any clad restraining force. As shown in (5.6), beyond the fuel thermal expansion,  $\delta u_{fuel}$  accounts for variations in the gap size induced by relocation, swelling, and densification of fuel. Details of the evaluation of the components of  $\delta u_{fuel}$  are summarized in Tab. 5.1, in addition, graphical representation of relocation, swelling, and densification are presented in Fig. 5.1.

$$\delta u_{fuel} = \delta u_{fuel}^{thermal} + \delta u_{fuel}^{reloc} + \delta u_{fuel}^{swel} + \delta u_{fuel}^{dens} \quad (5.6)$$

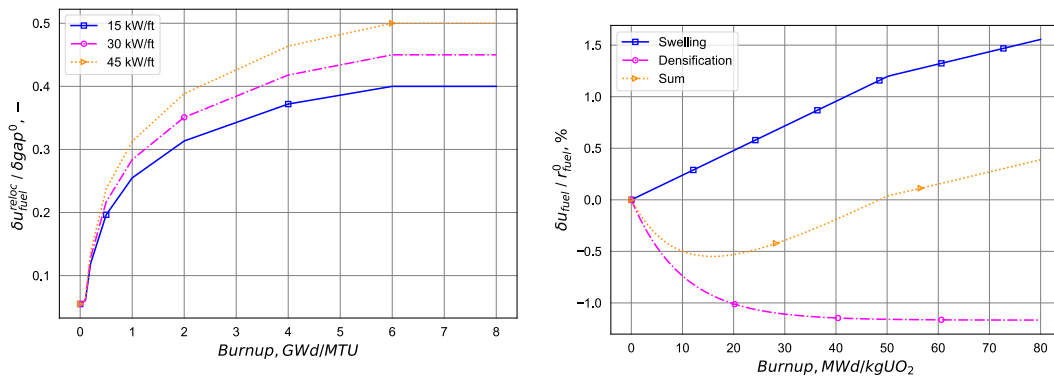


**Fig. 5.1** Fuel relocation vs. power/burnup and Fuel swelling/densification vs. burnup

The term  $\delta u_{clad}$  in eq. (5.5) is evaluated by applying eq. (5.7). The current model formulation neglects eventual plastic deformation of the clad. Details of the evaluation of the components of  $\delta u_{clad}$  are summarized in Tab. 5.1.

$$\delta u_{clad} = \delta u_{clad}^{thermal} + \delta u_{clad}^{elastic} \quad (5.7)$$

**Tab. 5.1** Components of cladding inner radius displacement:

Component	Model equations
<p>Relocation as in /GEE 15a/,  <math>\delta u_{fuel}^{reloc}</math></p>	$\delta u_{fuel}^{reloc} = \delta_{gap}^0 \cdot \begin{cases} 0.055, & bu < 0.0937 \\ 0.055 + \min\{rel, rel \cdot [0.5795 + \ln(bu)]\}, & bu \geq 0.0937 \end{cases}$ <p>Where:</p> <ul style="list-style-type: none"> <li>- <math>bu</math> burnup, MWd/kgU</li> <li>- <math>rel = \begin{cases} 0.345 &amp; , P &lt; 20 \\ 0.345 + (P - 20)/200 &amp; , 20 \leq P \leq 40 \\ 0.445 &amp; , P &gt; 40 \end{cases}</math></li> </ul> <p><math>P</math> local segment power, kW/ft</p>
<p>Swelling as in /SON 02/,  <math>\delta u_{fuel}^{swel}</math></p>	$\delta u_{fuel}^{swel} = r_{fuel}^0 \cdot \begin{cases} 0.06 \cdot bu_{FIMA}, & bu_{FIMA} < 6\% \\ (0.036 + 0.3 \cdot (bu_{FIMA} - 0.06)), & bu_{FIMA} \geq 6\% \end{cases}$ <p>Where:</p> <ul style="list-style-type: none"> <li>- <math>r_{fuel}^0</math> room temperature outer fuel radius at room temperature, m</li> <li>- <math>bu_{FIMA}</math> burnup, FIMA</li> </ul>
<p>Densification as in /SON 02/, <math>\delta u_{fuel}^{dens}</math></p>	$\delta u_{fuel}^{dens} = -r_{fuel}^0 \cdot 0.035/3 \cdot [1 - \exp(-bu/10)]$
<p>Elastic strain as in /SAL 19/,  <math>\delta u_{clad}^{elastic}</math></p>	$\delta u_{clad}^{elastic} = \varepsilon_{\theta} \cdot \bar{r}_{clad}$ <p>With:</p> <p><math>\varepsilon_{\theta}</math> as the Hoop strain, -</p> <p><math>\bar{r}_{clad}</math> as clad mean radius, m</p> <p><math>\varepsilon_{\theta}</math> is evaluated by applying the following three equations:</p> $\varepsilon_{\theta} = \frac{\sigma_{\theta} - \nu\sigma_z}{E}$ $\sigma_{\theta} = \frac{r_i P_i - r_o P_o}{r_o - r_i}$ $\sigma_z = \frac{r_i^2 P_i - r_o^2 P_o}{r_o^2 - r_i^2}$ <p>Where:</p> <ul style="list-style-type: none"> <li>- <math>\sigma_{\theta}</math> clad hoop stress, Pa</li> <li>- <math>\sigma_z</math> clad axial stress, Pa</li> <li>- <math>\nu</math> Poisson's ratio, -</li> <li>- <math>E</math> Young's modulus, Pa</li> <li>- <math>r_i, r_o</math> respectively, inner and outer clad radii at room temperature, m</li> <li>- <math>P_i</math> inner gas pressure (<math>P_{gas}</math>) or fuel-cladding contact pressure (<math>P_{int}</math>), Pa</li> <li>- <math>P_o</math> outer rod pressure, Pa</li> </ul>

Once  $\delta u_{\text{fuel}}$  and  $\delta u_{\text{clad}}$  are known,  $\delta_{\text{gap}}^{\text{eff}}$  can be evaluated. Should  $\delta_{\text{gap}}^{\text{eff}} \leq 0$ , i.e., the gap be closed, then the elastic displacement of the clad,  $\delta u_{\text{clad}}^{\text{elastic}}$ , must newly be evaluated as shown by eq. (5.8).

$$\delta u_{\text{clad}}^{\text{elastic}} = \delta u_{\text{fuel}} - \delta u_{\text{clad}}^{\text{thermal}} - \delta_{\text{gap}}^0 \quad (5.8)$$

In addition, as in this case fuel and clad are in contact, the resulting contact pressure is evaluated as presented in eq. (5.9).

$$P_{\text{int}} = \delta u_{\text{clad}}^{\text{elastic}} \frac{E(r_o - r_i)(r_o^2 - r_i^2)}{\bar{r}_{\text{clad}}[r_i(r_o^2 - r_i^2) - r_i^2(r_o - r_i)\nu]} + P_o \frac{r_o(r_o^2 - r_i^2) - r_o^2(r_o - r_i)\nu}{r_i(r_o^2 - r_i^2) - r_i^2(r_o - r_i)\nu} \quad (5.9)$$

After the evaluation of the  $\delta_{\text{gap}}^{\text{eff}}$ , eq. (5.4) requires the evaluation of the coefficient  $A$ , which multiplies the sum of fuel and clad surfaces facing each other within the gap region.  $A$  is evaluated by the expression:

$$A = \exp(-1.25 \cdot 10^{-3} P_{\text{int}}) \quad (5.10)$$

This coefficient allows simulating a flattening of the surfaces' roughness induced by an eventual contact of fuel and clad surfaces. It should be noted that for open gap configuration, that is  $\delta_{\text{gap}}^{\text{ff}} > 0$ ,  $P_{\text{int}}$  is zero and therefore  $A$  assumes the value 1, i.e., the term  $(R_f + R_c)$  is fully<sup>e</sup> accounted for in eq. (5.2).

Last but not least, the application of eq. (5.2) also requires the evaluation of extrapolation lengths in fuel and cladding, respectively, indicated as  $g_f$  and  $g_c$  /GEE 15b/. These e terms allow to consider the nonlinear heat exchange phenomena and related temperature drops due to the solid walls of fuel and clad. Such phenomena arise as gas molecules collide with the solid walls of fuel and clad and are reflected without all reaching the thermal equilibrium with the surfaces themselves. The combined effect of these two contributions is calculated as outlined in eq. (5.11). A conceptual graphical scheme of the extrapolation lengths is shown in Fig. 5.2.

$$g_f + g_c = 0.0137 \left[ \frac{\lambda_{\text{gap}} \sqrt{T_{\text{gas}}}}{P_{\text{gas}}} \right] \left[ \frac{\sum a_i f_i}{\sqrt{M_i}} \right]^{-1} \quad (5.11)$$

with:

- $P_{\text{gas}}$  gas pressure, Pa
- $T_{\text{gas}}$  gas temperature, K
- $M_i$  gram-molecular weight of  $i^{\text{th}}$  gas component, g/mol
- $f_i$  mole fraction of  $i^{\text{th}}$  gas component, -
- $a_i$  Accommodation coefficient of  $i^{\text{th}}$  gas component, -

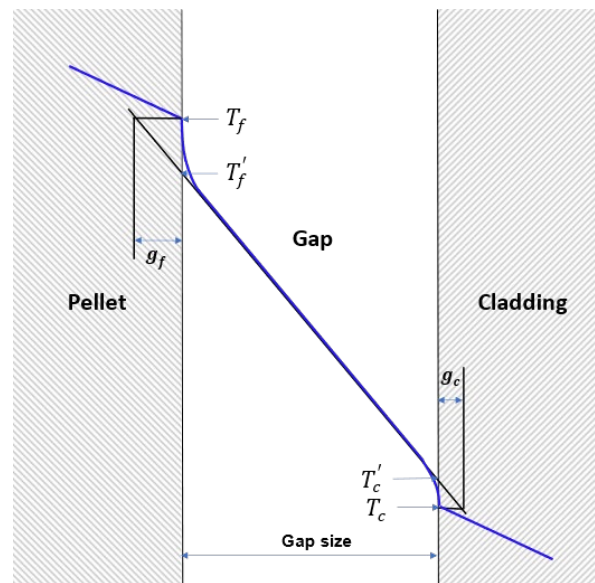


**Fig. 5.2** Conceptual scheme of fuel and cladding extrapolation lengths

It should be emphasized that  $T_f'$  and  $T_c'$  shown in Fig. 5.2 represent the temperatures at the solid walls of the fuel and cladding, respectively, when nonlinear heat exchange phenomena described earlier are neglected. By incorporating the extrapolated lengths  $g_f$  and  $g_c$  one can summarily account for nonlinear heat exchange phenomena and estimate the more realistic temperature,  $T_f$  and  $T_c$  indicated in the figure.

In eq. (5.11), the empirical constant preceding the second side of the equation allows the evaluation of extrapolation lengths in meters. Accommodation coefficients  $a_i$  are determined as shown in eq. (5.12), as reported in /GEE 15b/:

$$a_i = a_{He} + \frac{a_{Xe} - a_{He}}{M_{Xe} - M_{He}} \cdot (M_i - M_{He}) \quad (5.12)$$

with:

- $M_{Xe}$                       gram-molecular weight of Xenon gas component, g/mol
- $M_{He}$                       gram-molecular weight of Helium gas component, g/mol
- $M_i$                          gram-molecular weight of  $i^{\text{th}}$  gas component, g/mol
- $a_{He}$                         =  $0.425 - 2.3 \cdot 10^{-4} \cdot T_{\text{gas}}$
- $a_{Xe}$                         =  $0.749 - 2.5 \cdot 10^{-4} \cdot T_{\text{gas}}$

It is important to stress that the models discussed thus far are presently accessible in ATHLET only for UO<sub>2</sub> fuel and Zr clad materials, for which corresponding built-in correlations for thermophysical, mechanical, and burnup-dependent properties are available. When considering other materials, it is recommended to use the older simplified model for calculating gap conductance.

### 5.2.2 Gap conductance model verification

The model's verification and initial validation were carried out using available specification data and experimental measurements from the six-rod IFA-432 at the HBWR as referenced in /HAN 78/. The IFA-432 sample was specifically designed to gather precise experimental data that mimic the operational conditions of light-water reactors both in terms of power and burnup conditions. These data were intended for verifying fuel performance codes used by the United States Nuclear Regulatory Commission to assess stored energy in fuel. The goal was to minimize calculation uncertainties, primarily associated with changes in the gap conditions and their effects on gap conductance. The IFA-432 sample, designed to operate at a power level of roughly 15 kW/ft, reached its target burnup of 20 MWd/kg in late 1978, allowing the successful collection of the desired

experimental data. Among the provided data were histories of power and fuel (centre-line) temperatures collected at top and bottom spots of assembly rods via thermocouples, as well as measurements of clad elongation and rod internal pressure. Details of the IFA-432 test and related collected data can be found in /HAN 78/.

Considering the goal of the experiment, and the availability of data, the choice of the IFA-432 experiment as a test case for the present verification and validation purposes is suitable. In addition, as the experiment was already considered for validating the fuel performance code FRAPCON /GEE 15b/, especially with measurements from rods 1 and 3 of the assembly, the choice of the sample facilitated also the benchmarking with the U.S. code, which is more established in terms of fuel performance analysis.

In light of the above, the verification and validation of the new model were accordingly performed focusing on rods 1 and 3 samples of the IFA-432 test, the specifications of which are reported in Tab. 5.3. The specifications outlined for the power profile within the HBWR enabled the establishment of a tailored axial power profile for both rods. Such a profile ensures that the top of the rod aligns with the power peak, while the bottom operates at 70 % to 80 % of peak rod power as suggested in /HAN 78/. The power profile employed for verification and validation calculations is shown in Fig. 5.3.

**Tab. 5.2** Specifications for rods 1 and 3 of the IFA-432

<b>Specification</b>	<b>value</b>
<b>Coolant</b>	
Pressure	34.48 bar
Inlet temperature	510 K
Fuel	UO <sub>2</sub>
Active length	0.579 m
Material	UO <sub>2</sub>
Theoretical density	95.5 %
Inner diameter:	1.752 mm
Outer diameter:	
Rod 1	10.681 mm
Rod 3	10.833 mm
Roughness	2.16 μm
<b>Clad</b>	
Material	Zr-2
Outer diameter	12.789 mm
Thickness	0.94 mm
Roughness	0.64 μm
<b>Gap</b>	
Fill pressure	1 bar
Composition	Helium
Specification	value

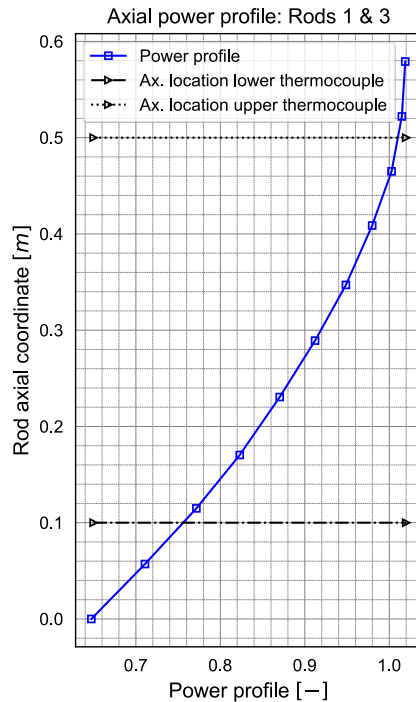


**Fig. 5.3** Axial power profile for rods 1 and 3

The verification of the new model is outlined in the following, with particular emphasis on newly incorporated features such as the elastic mechanical behaviour of the clad as well as fuel radial relocation, swelling, and densification. Considering the initial difference in gap sizes between the test cases of rods 1 and 3, which were larger in the former case and smaller in the latter (refer to fuel outer diameters in Tab. 5.3), both tests were utilized to obtain open and closed gap configurations through appropriately set power generation and burnup. This allowed for the evaluation of the model's accuracy for both modelling scenarios. The verification process involved comparing the steady-state axial profiles of gap conductance, fuel innermost (centreline), and outermost temperatures, as well as gap size against corresponding analytical solutions, which were independently derived by the authors. Naturally, the fuel centreline temperature is influenced not only by the dynamic behaviour of the gap but also by the burnup-dependent heat conductivity of  $\text{UO}_2$ .

The verification of the gap model in open gap configuration was conducted using the Rod 1 sample of the IFA-432 test, by setting a rod peak power of 35 MW/m and a burnup of 60 MWd/kg. The axial profile power depicted in Fig. 5.3 was applied to the rod.

Results

of the verification are shown in Fig. 5.4, which compares the outcomes of the new model against the 'reference' solutions obtained by employing the existing gap conductance model. Fig. 5.4.c shows an overlapping agreement between the ATHLET curves and their analytical trends for all the new models contributing to the gap size. The effects of the new (TM) model, and the models for fuel relocation, swelling, and densification on the gap size are cumulatively presented in the figure. The results indicate that the new models perform as intended. Fig. 5.4.a shows the corresponding gap conductance profiles. By itself, the introduction of the new TM module led to lower gap conductance values. Larger values of the gap conductance are obtained once the relocation effect as well as swelling and densification effects are considered. Fig. 5.4.b shows the axial temperature profiles at the fuel centreline and its outermost surface, identified in the figure, respectively, by the blue and magenta profiles. In general, the temperature profiles both at the innermost and outermost locations of the fuel approach lower values as the gap conductance increases, which is expected. Values of the gap conductance in Fig. 5.4.a are inversely correlated through equations (5.2) and (5.4) to the gap size values shown in Fig. 5.4.c. While the new TM module contributes to increasing the gap size, the effects of fuel relocation, swelling, and densification cause a significant reduction of the gap size down to roughly 25  $\mu\text{m}$ . It should be emphasized that the key component for the gap size reduction is the relocation effect. It should also be noted that the last axial fuel centreline temperature profile of Fig. 5.4.b, obtained by including the new thermal mechanical model and all burnup-effects, assumes values that are on average 100 K smaller compared to reference calculations performed with the simplified model, demonstrating thus that the new gap conductance model under the chosen operational conditions for the fuel served its purpose.

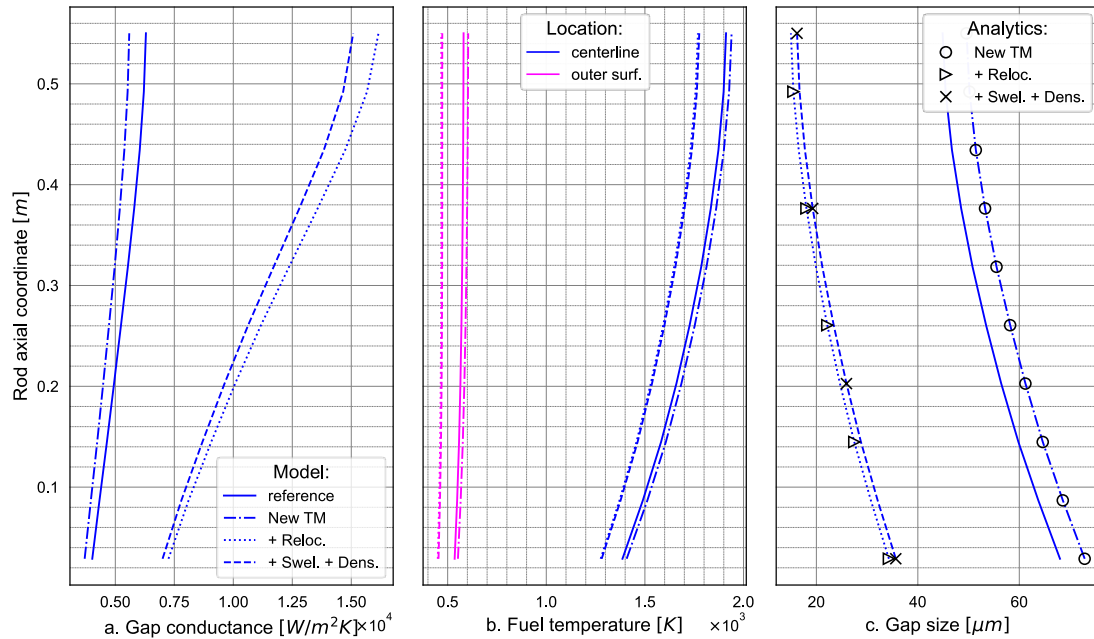
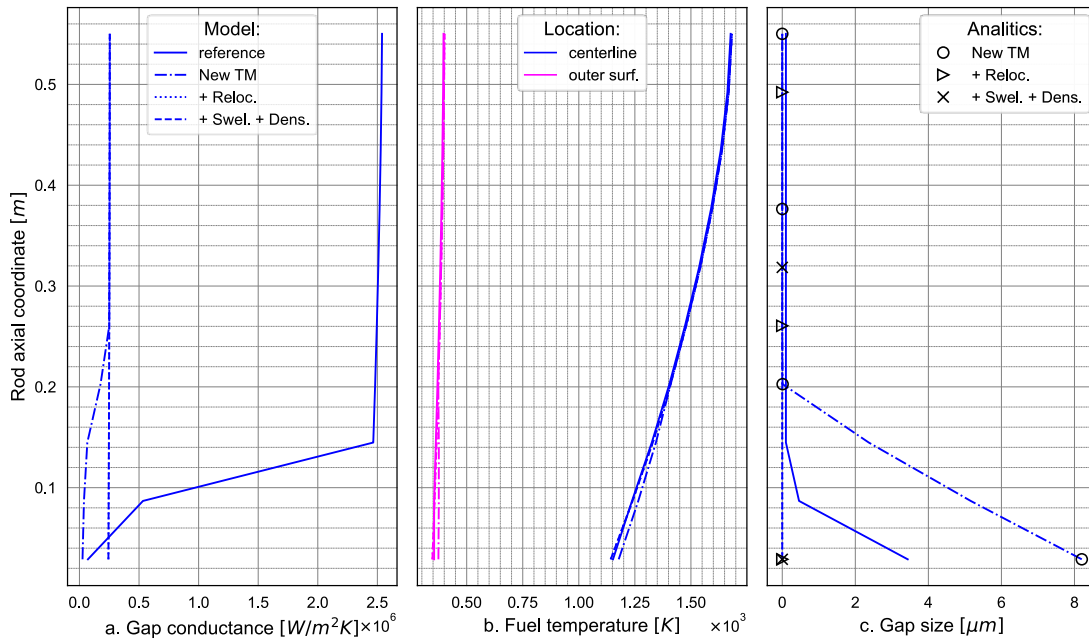


**Fig. 5.4** Verification against analytical solutions: open gap, IFA-432 rod 1 /DIN 24/

The verification of the gap model in a closed gap configuration was conducted using the Rod 3 sample of the IFA-432, by setting a rod peak power of 35 MW/m and a burnup of 60 MWd/kg as done for the previous verification case. The power axial profile presented in Fig. 5.3 was applied to the rod. Results of the verification are presented in Fig. 5.5.

Fig. 5.5c shows an overlapping agreement between the ATHLET curves and their analytic trends for all the new models contributing to the gap size. The figure shows that the closure of the gap is reached, for all solutions, almost everywhere above 0.2 m length of the rod, and completely occurred along the rod for solutions that consider relocation, swelling, and densification. Also in the closed gap case, the results of such a comparison suggest that the new model performs as intended. Fig. 5.5a presents the gap conductance profiles related to the gap size profile of Fig. 5.5c. One noticeable aspect from Fig. 5.5a is the significant discrepancy in rod gap conductance between the reference calculations and the newly evaluated gap conductance, differing by a factor of 10. This outcome is attributed to the distinct assumptions regarding the minimum gap size in the closed gap configuration between the old and new gap conductance models. Specifically, the old model assumes a minimum gap size of one-tenth of a micron once the gap is closed, whereas the new model, as described in section 5.2.1, incorporates, more realistically, the contribution of extrapolation distance and a sum of the roughness of

both fuel and clad surfaces, or at least a portion of it. Such contributions typically range within the order of microns, limiting by definition the maximum values of gap conductance.



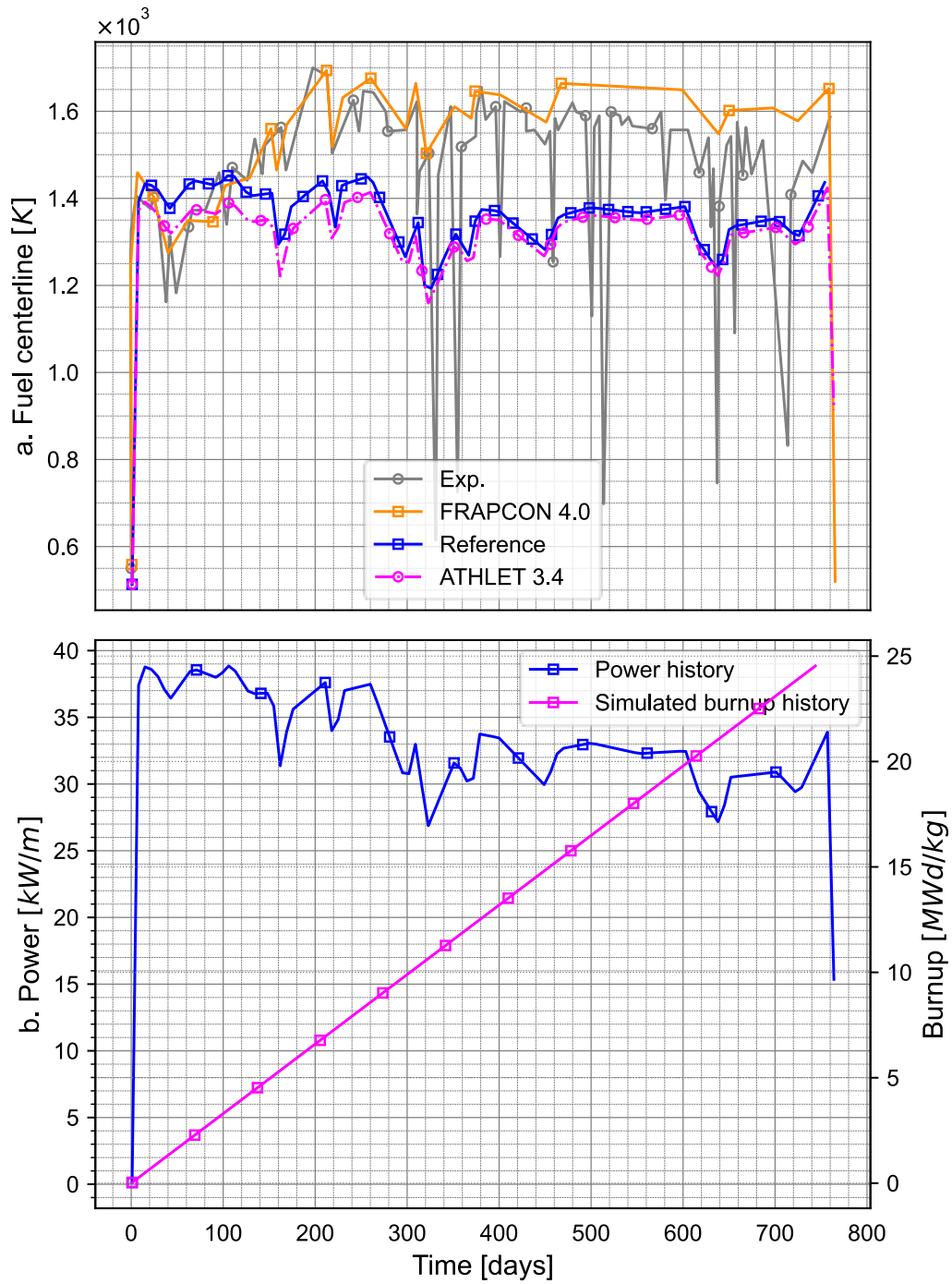
**Fig. 5.5** Verification against analytical solutions: Close gap, IFA-432 rod 3 /DIN 24/

Fig. 5.5b illustrates a nearly overlapping behaviour of the fuel temperature profiles, both at the centreline and the outermost surface, across all ATHLET solutions. Overall, aside from discrepancies related to gap size evaluation and closure, the new model does not seem to significantly affect the predictive capabilities of fuel temperature in closed gap configurations.

For validation purposes, the test cases of rods 1 and 3 from the IFA-432 were newly considered to predict the fuel centreline temperature over the duration of irradiation. Using ATHLET, steady-state calculations were conducted based on burnup and power histories available from /HAN 78/. The results of these calculations were collected along the irradiation timeline and are presented in this section. For comparison purposes, solutions were generated using both the old and new gap conductance models of ATHLET. Additionally, since the IFA-432 test case was previously utilized for the integral assessment of the established fuel performance code FRAPCON, the results were compared against FRAPCON solutions extracted from /GEE 15b/. This comparison provides insight into the quality of the ATHLET solutions in relation to the state-of-the-art fuel

performance code. Before the introduction of the actual validation results, it is important to highlight that although the imposed power and burnup levels are nearly identical for both rods 1 and 3, variations in gap sizes between the rods resulted in notable differences in the measured fuel centreline temperatures. Specifically, e.g., the fuel centreline values recorded at the lower thermocouple were on average 1500 K in Rod 1 to 1250 K in Rod 3. In the validation, this aspect played a crucial role in affecting the prediction capability of both the old and new ATHLET versions; more details are presented in the following sections. Fig. 5.6 and Fig. 5.7 show the results of the validation calculations for the Rod 1 sample of the IFA-432 test. The conditions imposed for rod peak power and burnup, extracted from /GEE 15b/, are depicted at the bottom of Fig. 5.6. There, a comparison is made between the simulation results and measurement data, for the lower thermocouple installed approximately 10 cm from the bottom of the sample.

We find that ATHLET was in general not capable of realistically predicting the fuel centreline temperature for the majority of the burnup points considered in both ATHLET versions. However, a better agreement against measurements and FRAPCON solutions can be observed during the first 100 days of irradiation when the new gap conductance model is applied. This is due to the smaller values of the gap size evaluated by the new model, which includes contributions of fuel relocation, swelling, and densification, see Fig. 5.7.a and .b. Fig. 5.7.b shows that beyond the thermal expansion effects of fuel depending on the rod power level an important contribution to the outer radial fuel displacement comes from the fuel radial relocation, which after 100 days of irradiation induces a displacement of 40  $\mu\text{m}$  in the fuel outer radius.



**Fig. 5.6** Validation against IFA-432 Rod 1: (a) Fuel centreline, and (b) power and burnup boundary conditions /DIN 24/

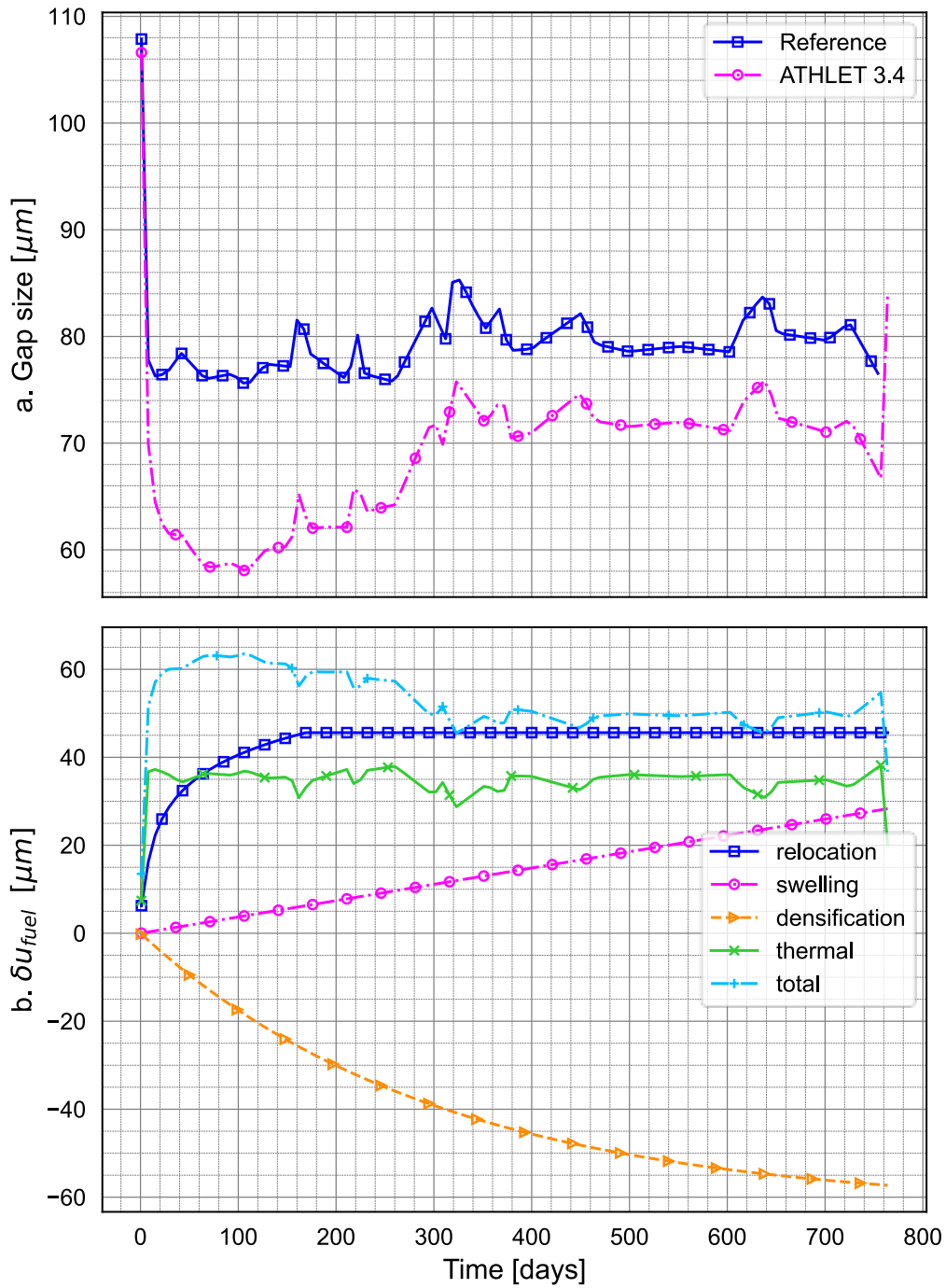


**Fig. 5.7** Validation against IFA-432 Rod 1: (a) gap size, and (b) fuel outer radial displacement and components /DIN 24/

As the burnup increases, also the negative contribution of densification to the outer fuel radius displacement becomes larger. It is only partially counterbalanced by swelling-

induced fuel pellet expansion. Overall, all burnup-dependent factors affecting the displacement of the fuel outer radius appear to be adequately captured in the new ATHLET model, aligning with expected outcomes of the models as given in Fig. 5.1.

The significant discrepancies, which are observed in comparison to measurement data and FRAPCON results, primarily stem from the absence of modelling capabilities to predict fission gas release in the current ATHLET versions, which is inherently reliant on fuel rod temperature. The release of fission gases into the gap cavity can substantially lower gas gap conductivity, consequently resulting in elevated fuel temperatures. This observation is further corroborated by /VIT 79/, which anticipated the onset of fission gas release at around 3-4 MWd/kg burnup, precisely corresponding to the observed increase in fuel centreline temperature measurements that were underestimated by ATHLET after the simulated 100 days.

Fig. 5.8, and Fig. 5.9 illustrates the outcomes of the validation calculations for Rod 3 of the IFA-432 test.

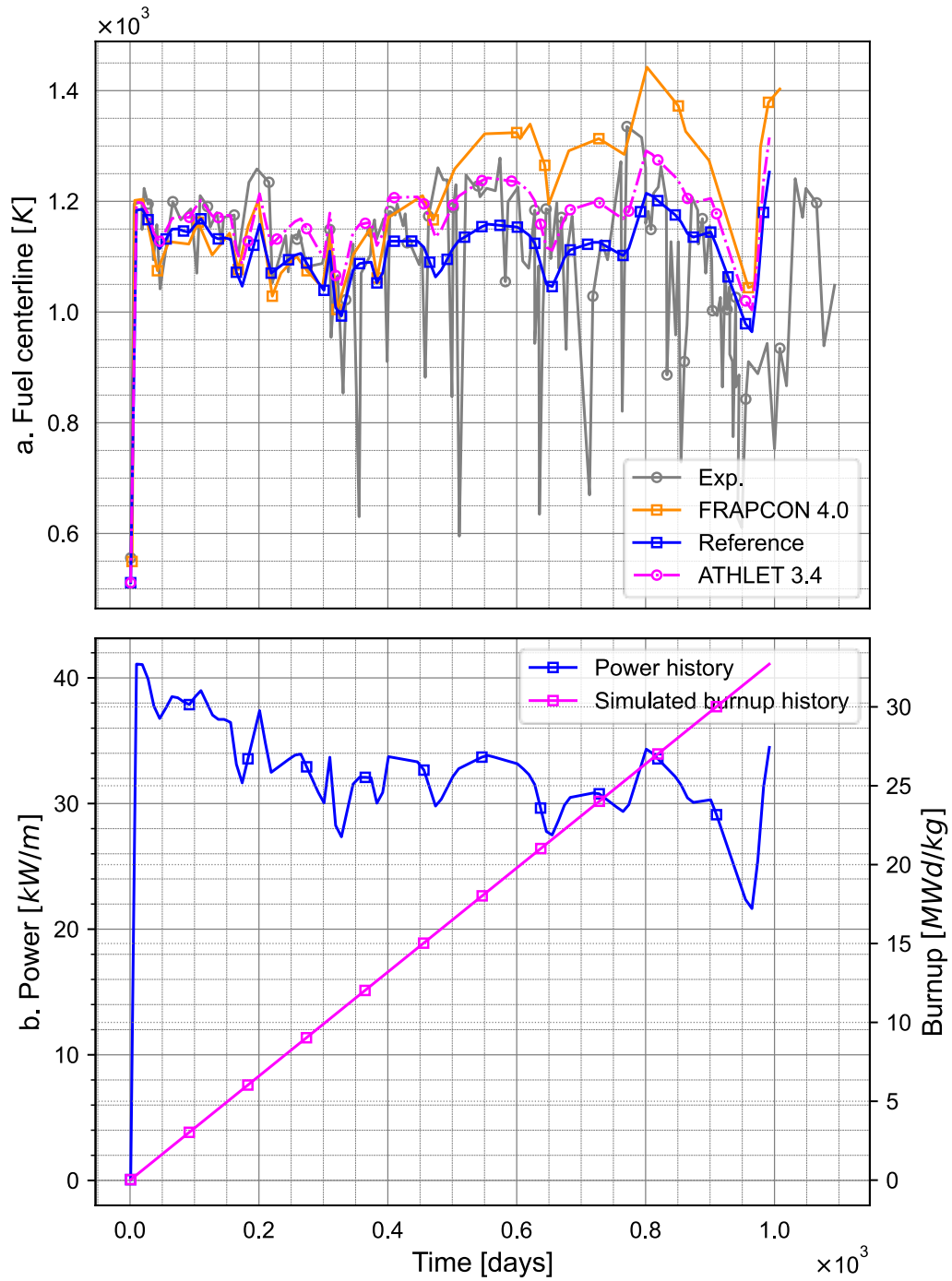


**Fig. 5.8** Validation against IFA-432 Rod 3: (a) Fuel centerline, and (b) power and burnup boundary conditions /DIN 24/

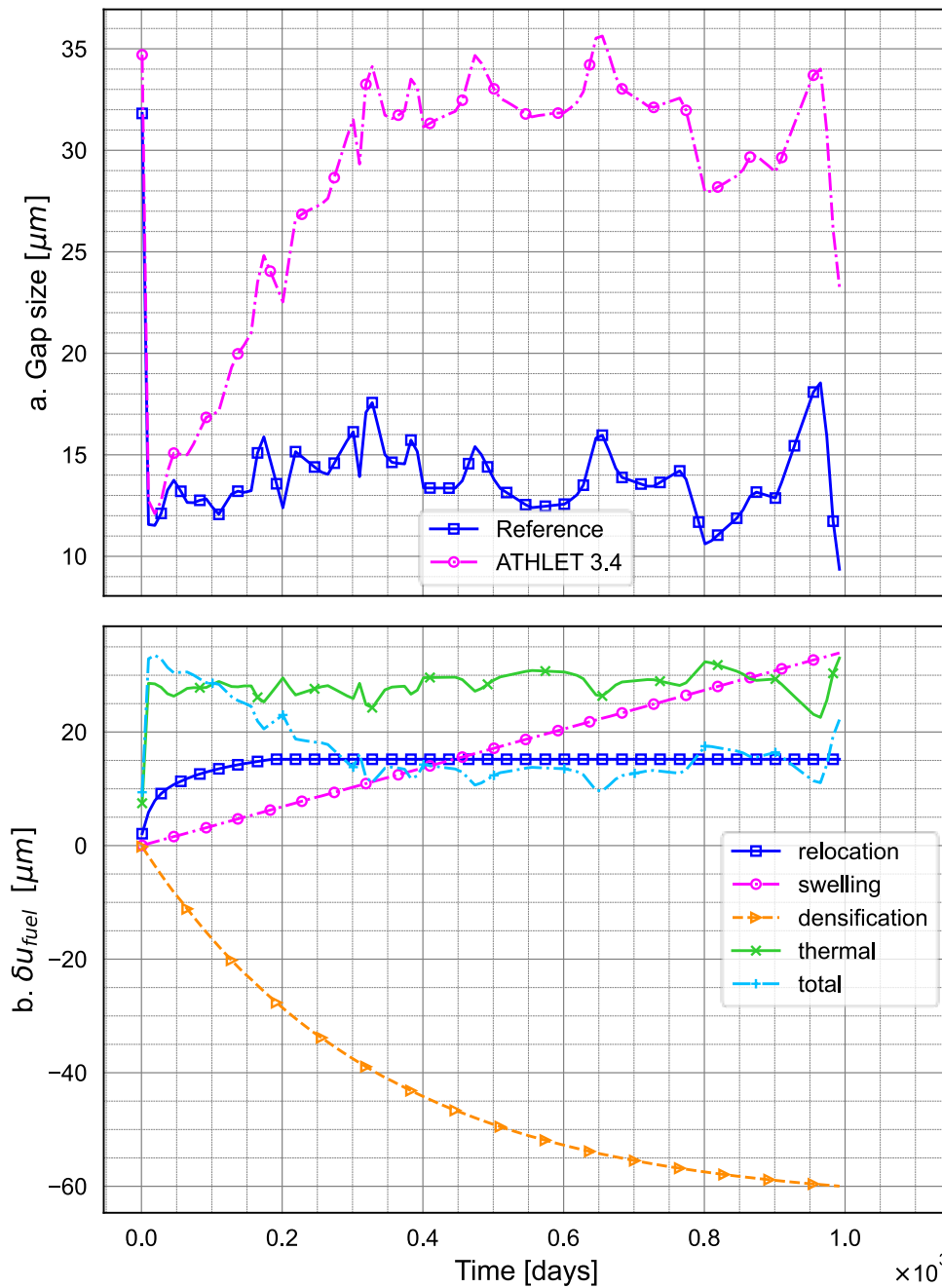


**Fig. 5.9** Validation against IFA-432 Rod 1: (a) gap size, and (b) fuel outer radial displacement and components

The imposed conditions for rod peak power and burnup, extracted from /GEE 15b/, are depicted in Fig. 5.8.b. The comparison between the simulation results and experimental data is made for the lower thermocouple installed approximately 10 cm from the bottom

of the sample. The ATHLET simulations can forecast the fuel centreline temperature for most of the analysed burnup points, especially when employing the new gap conductance model. The incorporation of fuel burnup effects, including relocation, swelling, and notably densification, as illustrated in Fig. 5.9.b, resulted in slightly improved predictions of the fuel centreline temperature. This is particularly evident in the interval between 400 and 800 days, compared to both the experiment and FRAPCON results. The latter, however, provide too high centreline temperature after about 600 s. Fig. 5.9.b illustrates the initially dominant thermal expansion effect of the fuel, followed by a modest relocation effect resulting in an outer fuel pellet radius displacement of roughly 20  $\mu\text{m}$ . As burnup increases, the negative contribution of densification becomes more pronounced, outweighing the radial relocation and swelling of the fuel. In this test case, after the initial 200 days the densification effect leads to the observed increase in gap size shown in Fig. 5.9.a. In contrast to the previous scenario, the better prediction capabilities of ATHLET are due to smaller relocation effects, resulting in a decreased release of gaseous fission products. Furthermore, the onset of this release is projected to happen around 17.5 MWd/kg burnup, as indicated in /VIT 79/.

The results indicate that, similar to FRAPCON, ATHLET with the new model more accurately predicts the fuel centreline temperature for rod 3 of the IFA-432. However, significant discrepancies were observed in the case of rod 1, both in comparison to measurements and FRAPCON results. Literature and preliminary calculations suggest that these discrepancies are due to fission gas release phenomena not accounted for in ATHLET thus far.

These effects are proportional to centreline temperature levels and are more pronounced in the case of rod 1, which experiences higher centreline temperatures. Conversely, they appear to have a negligible impact in the case of rod 3, consistent with validation results and measurements. While the reported validation was successful, further validation cases should be simulated to check the new model under a larger set of conditions.

### **5.2.3 Radial pellet power profile**

In ATHLET, power generation can be simulated using the so-called rod components, which are linked to heat structure objects that manage the heat generation within the

structures themselves. Specifically, these rod components control power generation through GCSM signals as well as through models of PK or 3D kinetics, and electrical heaters. Originally, the power generated in the axial segments of a rod's heat structures would be equally distributed across its radial layers. However, in the case of nuclear fuel rods, the energy stored in the pellet is known to be significantly influenced by the spatial power distribution within the fuel. The shielding effect of thermal neutrons by the outer fuel layer, coupled with the impact of increasing burnup, results in a higher power density at the pellet periphery compared to its centre. To accurately capture this phenomenon, a model for incorporating a radial power profile within a fuel pellet was developed and implemented in ATHLET.

The new feature allows the imposition of a radial pellet power profile for rod models controlled by a GCSM signal or neutron PK or 3D kinetics modules. It is worth noting that the radial power profile model cannot be used in combination with the electrical heater model. The pellet radial power profile can be provided by the user through a free number of tuples that describe the shape of the heat generation rate across the heat generating material zone, i.e., along the radial abscissa  $s$ . The given power profile,  $p(s)$ , is firstly linearized along  $s$  and then averaged and normalized over the fuel material layers. Such normalized layer-averaged values, hereafter called layer factors, define the average fraction of heat generated by each layer of the material and are by definition dimensionless. The evaluated layer factors are imposed over all the axial segments of the rod modelled.

The layer factors are estimated via integral averaging formulas, which take into account the geometrical configuration (e.g., cylindrical) of the modelled rod. For instance, in case of a rod model defined as a cylinder of radius  $S$ , and a number  $J$  of layers, the generic factor of layer  $j$ ,  $\langle p \rangle_j$ , located between the layer boundaries  $s_j$  and  $s_{j+1}$ , (with  $s_j < s_{j+1}$ ) is evaluated as:

$$\langle p \rangle_j = \frac{\int_0^{2\pi} d\phi \int_{s_j}^{s_{j+1}} p(s) s ds}{\int_0^{2\pi} d\phi \int_{s_j}^{s_{j+1}} s ds} = \frac{2}{s_{j+1}^2 - s_j^2} \int_{s_j}^{s_{j+1}} p(s) s ds \quad (5.13)$$

Considering that  $p(s)$  is by definition linearized along  $s$ , as the power profile is provided by tuples, the interval  $[s_j, s_{j+1}]$  can be split into  $M_j$  subintervals of boundaries  $[s_j = r_{j,m}, r_{j,m+1}, \dots, r_{j,M_j}, s_{j+1} = r_{j,M_j+1}]$  so that within each subinterval  $p(s)$  assumes the form:

$$p(s) = p_0 + \frac{p_1 - p_0}{s_1 - s_0} (s - s_0) \quad (5.14)$$

Exploiting this assumption, equation (5.13) is handled as shown in equation (5.15).

$$\begin{aligned} \langle p \rangle_j &= \frac{2}{s_{j+1}^2 - s_j^2} \int_{s_j}^{s_{j+1}} p(s) s \, ds = \frac{2}{s_{j+1} - s_j} \sum_{m=1}^{M_j} \int_{r_{j,m}}^{r_{j,m+1}} p(s) s \, ds = \\ &= \frac{1}{3(s_{j+1}^2 - s_j^2)} \sum_{m=1}^{M_j-1} p_{j,m+1} (2r_{j,m+1}^2 - r_{j,m+1}r_{j,m} - r_{j,m}^2) \\ &\quad + p_{j,m} (r_{j,m+1}^2 + r_{j,m+1}r_{j,m} - 2r_{j,m}^2) \end{aligned} \quad (5.15)$$

Finally, the normalized factors are employed to determine the heat generation of the layer  $j$  in the segment axial segment  $i$  of a fuel rod structure as shown by equation (5.16).

$$W(i, j) = Q_{tot}(t) \cdot \text{PPOW}(i) \cdot \langle p \rangle_j^{norm} \quad (5.16)$$

Where:

- $W(i, j)$  heat generation of the layer  $j$  in the axial segment  $i$
- $Q_{tot}(t)$  total power generation at time  $t$
- $\text{PPOW}(i)$  fraction of the power generated within the axial segment  $i$  of the fuel rod

It must be stressed that once evaluated during initialization calculations, the layer factors are kept constant for the whole simulation. Mathematical models were also developed

to account for non-uniform power generation in plates or spheres configurations. Further details of this model can be found in /SCH 23a/.

Fig. 5.10 illustrates ATHLET's results for a fuel rod consisting of 15 radial zones in the fuel and five radial zones in the cladding tube, situated within a core channel of a generic PWR under normal operating conditions. The three investigated power profiles in the fuel are depicted with dashed lines: constant (blue), zero burnup (0 MWd/kgHM, red), and 50 MWd/kgHM (green). For the latter profile, the power density at the pellet periphery is increased by a factor of 1.6. The corresponding steady-state radial temperature distributions in the fuel and cladding tube at the core centreline were determined and are shown as solid lines in the figure. The figure illustrates a gradual reduction in the centreline temperature, dropping from 1800 K with a flat power profile (blue) to 1600 K in the high burnup scenario (green). This underscores the significance of the model in the context of its intended application.

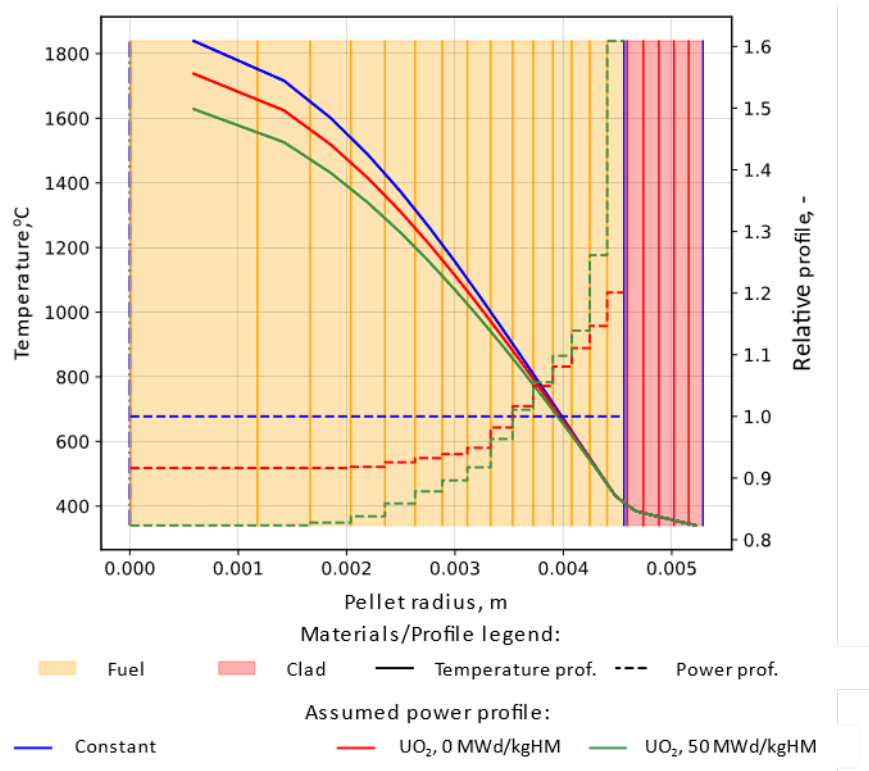


**Fig. 5.10** Temperature distribution in the fuel and cladding with different power profiles

## 5.2.4 Effects of oxidation layer on heat transfer

Before introducing the model, it is important to highlight that ATHLET already includes a fuel rod oxidation model. This model is capable of predicting the thickness of the oxidation layer that develops during the simulation, starting from a given initial oxide layer. However, the effects of the oxidation layer on the rod's surface thermal resistance had not been considered until now.

By exploiting the existing oxidation model, ATHLET can now, thanks to the current developments, determine a correction factor of the thermal resistance found across the fuel rod boundary by considering the additional thermal resistance caused by the formed oxidation layer. In particular, for a heat structure segment, the thermal resistance,  $R_{\text{oxid}}$ , used to correct the total resistance of the fuel rod is evaluated as derived by Fourier's law for heat conduction as shown in (5.17).

$$R_{\text{oxid}} = \frac{\delta u_{\text{oxid}}}{A k_{\text{oxid}}} \quad (5.17)$$

with:

- $\delta u_{\text{oxid}}$  oxide layer thickness, m
- $A$  cross sectional area of the heat structure's segment perpendicular to the heat flow, m<sup>2</sup>
- $k_{\text{oxid}}$  thermal conductivity of the oxide, W/m/K

The new model is currently only available for zirconium oxide, for which properties of thermal conductivity were implemented as function of the oxide temperature,  $T_{\text{oxid}}$ , as shown in eq. (5.18).

$$k_{\text{oxid}} = 0.835 + 1.81 \cdot 10^{-4} \cdot \min(T_{\text{oxid}}, 2973) \quad (5.18)$$

The new model was preliminary verified using a modified rod model, adapted from the IFA-432 Rod 1 model, which had previously been used to verify the extended gap

conductance model, see /HAN 78/. This adaptation postulated an additional insulation layer of oxide, assumed to be formed on the outer boundary of the rod. Two scenarios were investigated: the first with an oxidation layer thickness of 1  $\mu\text{m}$ , and the second with 50  $\mu\text{m}$ . The results are presented in Fig. 5.11. The figure illustrates the outcomes obtained from simulations run with the reference version of ATHLET (version 3.4.0) and the updated version that includes thermal resistance corrections, the outcomes of the corresponding simulations are depicted by blue and magenta lines, respectively. In the latter scenario, the temperature profile of the rod is slightly higher than in the former, although the differences are practically negligible. Larger discrepancies in the results were observed when assuming a larger initial oxide layer thickness, i.e., 50  $\mu\text{m}$ . Results of the calculation are shown in this case by the orange curve in the figure, yet these differences remain negligible.

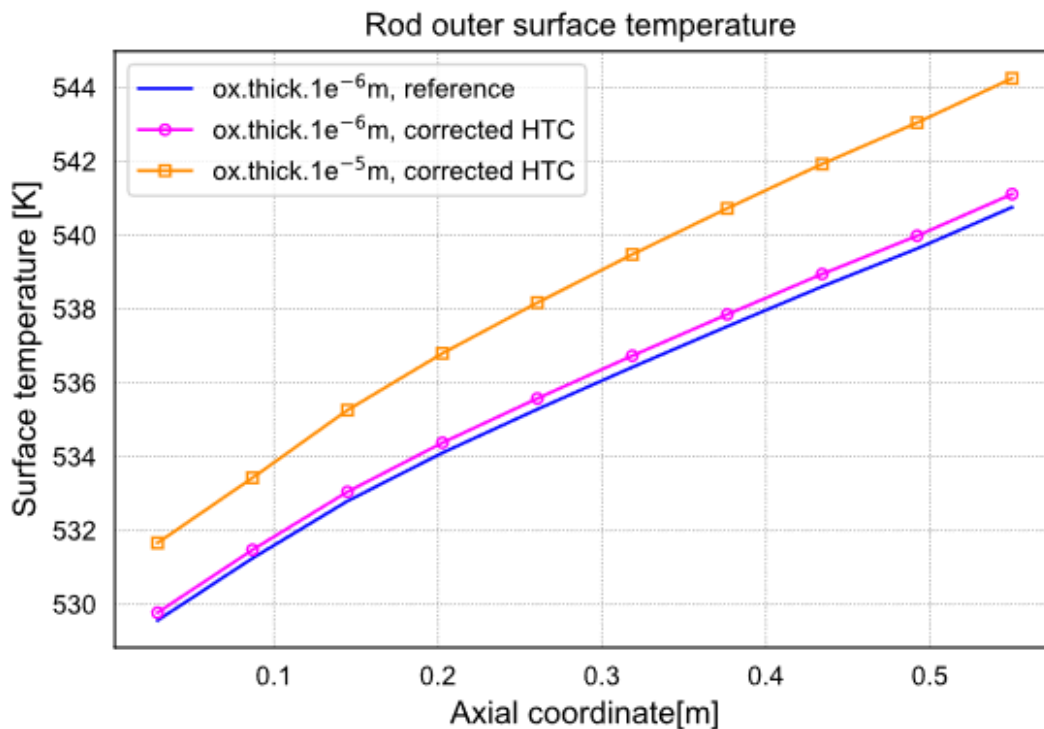


**Fig. 5.11** Axial temperature distributions at the rod outer surface

Despite the minimal variations introduced by the new model, the inclusion of an additional external oxidation layer in the determination of heat transfer from the wall to the fluid appears to provide physically grounded results. This contributes to the production of more realistic and comprehensive outcomes.

### 5.3 Summary and future steps

This chapter presented the improvements made to the existing fuel rod model of ATHLET. In particular, the improvements involved the fuel gap conductance model, incorporation of a new radial pellet power profile, and thermal resistance correction factor for wall-to-coolant heat exchange accounting for the effects of eventually formed zirconium oxide on the heat exchange process. The models were described in detail, and their preliminary verification, and possible available validation exercises, were shown. In a nutshell:

- The fuel gap conductance model has been refined to incorporate the effects of mechanical elastic deformation of the rod cladding and internal rod pressure, impacting both the cladding's mechanical behaviour and the gas conductivity properties. Additionally, the new model allows for the simulation of fuel relocation, swelling, and densification phenomena. The updated model has undergone rigorous verification through analytical comparisons and validation against experimental data from the IFA-432 experiment. Although these improvements have significantly enhanced the model's predictive accuracy, it is important to note that the absence of a fission gas release model has still hindered more precise predictions of the fuel centreline temperature during the validation activity.
- A new mathematical model to set and simulate pellets' radial power profiles, was specifically developed and implemented. The model is available for cylindrical geometry, as well as planar and spherical heat structure configurations. Preliminary applications of the model carried out during its verification were shown for a fuel pellet. The latter showed the impact of the model in reducing the fuel centreline temperature, and thus the corresponding energy stored in the fuel. In particular, considering realistic operational conditions of a LWR (fuelled with  $\text{UO}_2$ ), the results showed a decrease of the fuel centreline temperature of 100 K passing from a 'flat profile' to a more realistic fresh fuel pellet power profile, i.e., slightly higher at the fuel periphery and lower at its centre. In addition, the fuel centreline temperature was reduced further by 100 K by considering a power pellet profile at high burnup, i.e., ca 50 MWd/kgHM.
- Additionally, the new model simulating the thermal resistance of eventually formed operational oxidation layer was implemented to consider the impact of

this layer on the heat transfer phenomena occurring between fuel rods and the coolant. Despite the potential implications of the oxide layer's thickness, the model indicates that its effect on thermal exchange is minimal.

Based on the observations made during the implementation and verification of the models, it is possible to suggest further improvements to the fuel rod model for near-future implementation. For example, in relation to the gap conductance model, developing features that account for the release of fission gases from the fuel into the gap cavity could significantly enhance the accuracy of gap conductance behaviour predictions, thereby improving predictions of the fuel centreline temperature. Additionally, the evaluation of gap size could benefit from considering the plastic deformations of the cladding, which have so far been neglected. In this context, developing a more detailed TM model for the cladding that includes plastic deformation is advisable and should be considered for future developments. Lastly, it is important to note that while the current models primarily incorporate correlations for  $\text{UO}_2$  and Zircaloy materials, there is a clear need to also implement correlations for other types of fuel and, particularly, cladding materials.

Regarding the models that account for the fuel's radial profile and the effects of the oxidation layer on wall-to-fluid heat transfer, these still require validation activities. Such validation is necessary not only to confirm the results obtained during the verification activities, but also to ensure the models' robustness and predictiveness in operational scenarios.



## 6 User support and cooperation

### 6.1 Model improvements and usability

#### 6.1.1 Reynolds number dependent form loss calculation

So far, for modelling flow losses due to spatial changes in the geometry of the flow area or due to obstacles in the flow path (form losses), ATHLET allowed the specification of constant form loss coefficients  $\zeta$  (independent for each flow direction) under `PW_FRICTION` at the respective position in the TFO. The actual flow dependent form loss is then calculated by ATHLET using these constant values. This approach is sufficient for many application cases, although it neglects the Reynolds number dependence of the form loss coefficients, which depends itself on the geometry. For increased accuracy of the form loss calculation, ATHLET was extended to allow the use of Reynolds number dependent form loss coefficients. These can be either defined by the user in a table (e.g., based on measurements performed for a specific component), or, for a few generic components, by the selection of a predefined correlation.

The development is based on previous work carried out in the frame of RS1565. Now, the existing implementation was significantly extended and harmonized with other models to widen both its applicability and ease of use.

Under `PW_FRICTION`, the user can now optionally enter a string instead of a constant numerical value for the form loss coefficients `ZFFJ0` (forward flow) and `ZFBJ0` (backward flow), where the latter are defined as the dimensionless form loss coefficient divided by the square of the flow area. These strings refer to a form loss defined as a keyword under the new control word `CW_FORMLOSS`. Each form loss keyword requires several input parameters, dependent on the type of the form loss component `IFRMLTYP`. Possible types are constant value (mainly added for convenience, to switch off the Reynolds number dependence temporarily or to impose a zeta value independent of current flow area), tabulated value, bend, contraction, or orifice.

The form loss correlation must be evaluated at each time step during the transient calculation using the current Reynolds number. Therefore, efficient evaluation was one criterion for the selection of the implemented correlations.

For bends, the correlation given in /WAG 97/ was implemented. It is derived for curved sections, where the inner and outer wall have the same centre of curvature, and the ratio of the curvature radius to the pipe diameter is  $R/D \geq 1$ . The value of the form loss coefficient depends in this correlation on the friction factor  $\lambda$ , which is already computed by ATHLET.

Depending on the ratio  $R/D$ , the following relations between form loss and friction factor are used for a 90° bend:

$$\begin{aligned} \zeta_{90^\circ} &= \lambda \cdot \sqrt{(R/D)} \cdot 1.6 && \text{for } R/D \geq 8 \\ \zeta_{90^\circ} &= \lambda \cdot 12.8 / \sqrt{(R/D)} && \text{for } 2 \leq R/D < 8 \end{aligned} \quad (6.1)$$

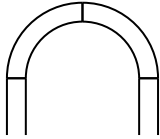
$$\zeta_{90^\circ} = \lambda \cdot 12.8 / \sqrt{(R/D)} \cdot \sqrt[4]{(2/(R/D))} \quad \text{for } 1 \leq R/D < 2$$

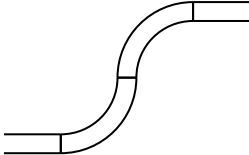
For bends with angles  $\alpha$  other than 90°, the approximation

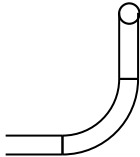
$$\zeta = \zeta_{90^\circ} \cdot \sqrt{\alpha/90^\circ} \quad (6.2)$$

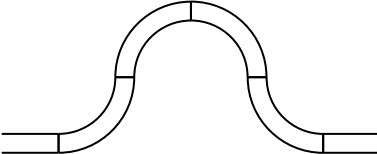
is used.

Combinations of two 90° bends leads to special components, for which the following approximate form loss relations, based on the form loss for a single 90° bend, are given:

U bend   $\zeta = 1.4 \cdot \zeta_{90^\circ}$  (6.3)

S bend   $\zeta = 2.2 \cdot \zeta_{90^\circ}$  (6.4)

3D double bend   $\zeta = 1.7 \cdot \zeta_{90^\circ}$  (6.5)

Double S bend   $\zeta = 2.4 \cdot \zeta_{90^\circ}$  (6.6)

For sudden sharp-edged contractions, a correlation for the form loss given in /IDE 08/ is used. The form loss coefficient depends on the Reynolds number  $Re$  and the geometry factor  $F$ , the ratio of the flow areas behind and in front of the contraction ( $F \leq 0.6$ ).

For very low Reynolds numbers, the following (geometry-independent) correlation is used:

$$\zeta = \frac{30}{Re} \quad \text{for } Re \leq 6 \quad (6.7)$$

For  $Re \rightarrow 0$ , the form loss coefficient is limited to  $10^6$ .

In the range  $6 < Re < 3.5 \cdot 10^4$ , the form loss coefficient is computed by linear interpolation between tabulated values given by /IDE 08/.

For high Reynolds numbers,  $Re > 3.5 \cdot 10^4$ , the form loss coefficient is given as

$$\zeta = 0.5(1 - F)^{0.75} \quad \text{for } Re \geq 3.5 \cdot 10^4 \quad (6.8)$$

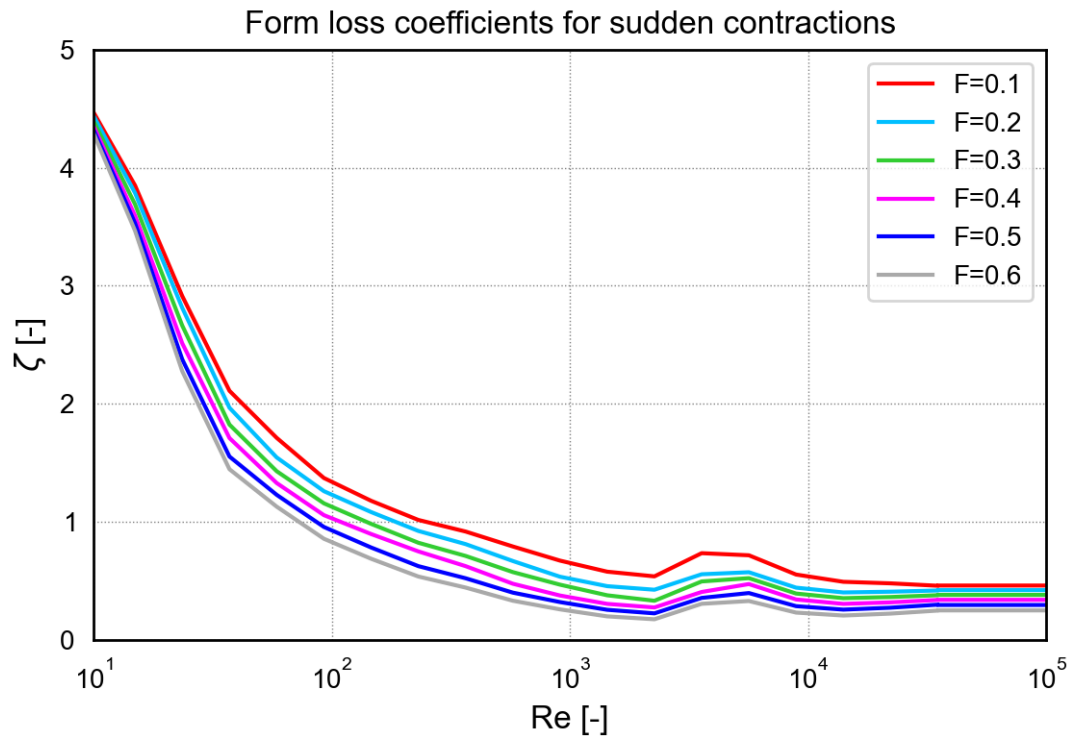


**Fig. 6.1** Form loss coefficient for sudden contractions depending on Reynolds number  $Re$  and area ratio  $F$

A correlation given in /IDE 08/ (which was slightly adapted here to ensure continuity) is applied for sharp-edged orifices, depending on the Reynolds number  $Re$  and the geometry factor  $F$ , which denotes the ratio of the orifice flow area and the pipe flow area ( $F \leq 1$ ).

For sufficiently high Reynolds numbers, a constant value is used:

$$\zeta = \zeta_1 \equiv \left( \frac{1 - F + 0.707 \cdot (1 - F)^{0.375}}{F} \right)^2 \quad \text{for } Re \geq 10^6 \quad (6.9)$$

In the range  $0 < Re \leq 33$ , the form loss is calculated using the formula (limited to  $10^6$  for  $Re \rightarrow 0$ )

$$\zeta = \frac{33}{F^2 \cdot Re} \zeta_0 + \varepsilon \cdot \zeta_1 \quad \text{for } 0 < Re \leq 33 \quad (6.10)$$

and for  $33 < Re < 10^6$ , the correlation

$$\zeta = \frac{1}{F^2} \zeta_0 + \varepsilon \cdot \zeta_1 \quad \text{for } 33 < Re \leq 10^6 \quad (6.11)$$

is applied. The parameter  $\zeta_0$  is a function of the Reynolds number and the geometry factor  $F$ , while  $\varepsilon$  is a function of the Reynolds number alone. Both  $\zeta_0$  and  $\varepsilon$  are interpolated from tabulated values given in [IDE 08]. The parameter  $\zeta_1$  is independent of the Reynolds number and equals the form loss coefficient for high Reynolds numbers given above.

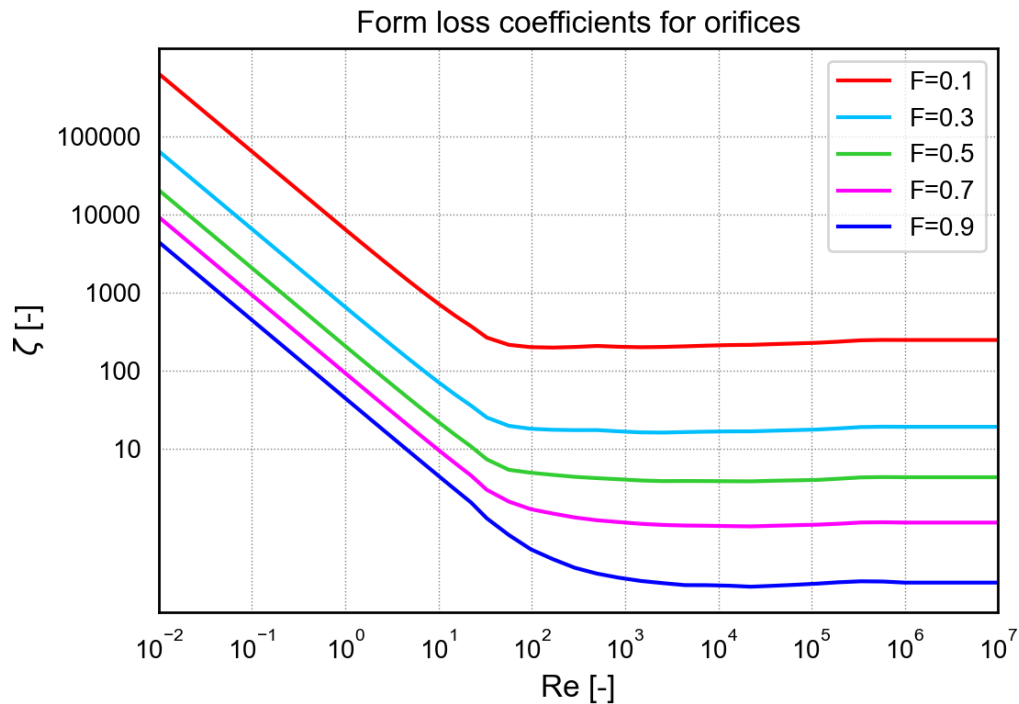


**Fig. 6.2** Form loss coefficient for sharp-edged orifices depending on Reynolds number  $Re$  and area ratio  $F$

The selected correlation is evaluated during the transient and the steady-state calculation at each time step or iteration using the current value of the Reynolds number, in case of the 6-equation model independently for liquid and vapor flow.

Form loss keywords given under  $PW_{\text{FRICTION}}$  in an object are assigned to the nearest junction in this object, in addition to an optionally given constant form loss coefficients for the same junction. Currently, up to 3 form loss keywords per flow direction can be assigned to one junction. For cross-connection objects, only 1 form loss keyword is allowed for each direction, which does not need to be applied over the full length of the object.

During the steady state calculation, friction and form losses are adapted, because the input data typically over-determine the simulation system, and the flow loss resulting from the input values does not exactly match the prescribed pressure difference along a priority chain. Thus, an adaptation factor is applied to each friction and form loss coefficient in a priority chain. The Reynolds number dependent contributions must also be multiplied with the same adaptation factor. Due to the fact that form losses have to be recalculated during the transient calculation, these factors are now stored after the steady-state calculation, and are also written to the restart file to ensure restart capability of the model. To inform the code user, the adaptation factors are also written to the print output file.

Furthermore, for junctions with an expansion of the flow area, the given constant form loss coefficient is, if necessary, increased by ATHLET to the value that corresponds to the pressure increase according to Bernoulli for a sudden flow area expansion. Thus, pressure increase caused by flow area change is usually (except for a diffuser component) compensated for and avoided by ATHLET to enhance numerical stability. With Reynolds number dependent, i.e., time dependent, form loss contributions in a junction, this compensation cannot simply be achieved by increasing the constant form loss value during the steady-state calculation and keeping this value during the whole transient calculation. Instead, the minimum form loss to compensate Bernoulli pressure recovery value is stored for this junction and compared in each time step with the computed form loss coefficient including Reynolds number dependent contributions. Finally, the larger of both is applied.

### 6.1.2 Momentum-flux calculation

During code validation against the ECTHOR experiment /BOU 85/, an erroneous behaviour of the flow simulation in a horizontal geometry was detected. The French ECTHOR experiment was a single-effect test, which investigated the phenomenon of the pump seal clearance in a PWR (scale 1:3). In the experiment, the lower (horizontal) part of the scaled pump bend was being filled with water while a forced gas mass flow through the pump seal was being imposed. Overall, eleven tests were conducted with varying gas mass flow rates. The entrained water blown out the pump seal and the amount of water remaining in the pump bend at the end of the experiment served as the main measured variables. Finally, the remaining water level in the U-tube as a function of the gas mass flow rate could be used to assess the adequacy of the interfacial friction modelling in ATHLET.

After the air mass flow had been stopped at the end of the simulation, it was noticed that the water remaining in the pump bend was not distributed evenly (corresponding to a uniform fill level) over the entire horizontal section (Fig. 6.3). An error in the momentum equation of the 6-equation model related to the momentum-flux (MF) term, which represents the convective part of the momentum equation, was identified as the root cause for this behaviour. The incorrect MF term compensated the geodetic pressure drop, which finally hindered the liquid flowing “downwards” along the horizontal pipe section (towards the left in Fig. 6.3) and produced a sharp void jump near the mid of the horizontal part of the U-tube.

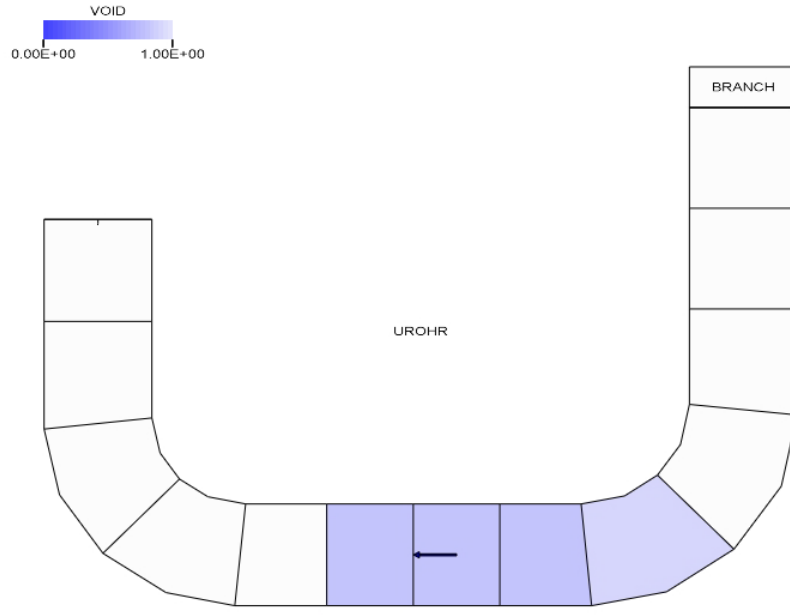


**Fig. 6.3** Incorrect phase distribution under stagnant flow conditions at the end of an ECTHOR simulation

To better understand this simulation outcome, one has to consider that, in ATHLET, the phase velocities are not necessarily reduced to zero when a phase disappears. I.e., although the liquid mass flow rate turns to zero at the end of the simulation with the vapour volume fraction being one to the left of the void jump (no liquid), the liquid phase velocity in the junctions left of the void jump do not become zero (more precisely: stays positive, i.e., directed from left to right). However, in general, this has no further influence on the simulation as long as the phase is not present. But in the special case of the MF term of the 2M model, this does not apply: The 6-equation model uses an upwind discretization for the convective part. This means that the upstream junction (with flow velocity directed towards the void jump) is also taken into account when calculating the MF term. Simplified, the MF term can be written as:

$$dp_{MF}(j_0) = \frac{\rho}{2} (WLJ_1^2 - WLJ_0^2) \quad (6.12)$$

Here, the liquid velocity  $WLJ_1$  of the upstream junction contributes to the MF-Term of junction  $j_0$  (location of void jump). But in the event of a void jump without any liquid phase

fraction, this contribution is incorrect and physically meaningless. Fig. 6.5 illustrates the flow situation and nomenclature.

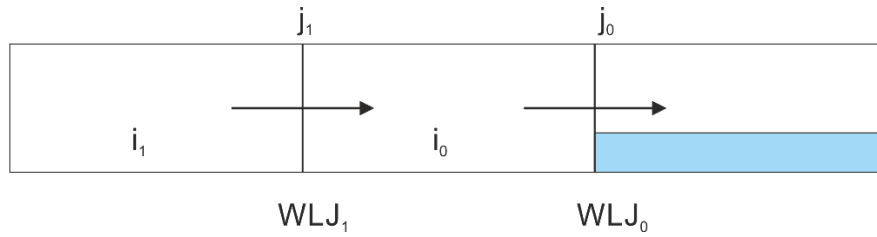


**Fig. 6.4** Momentum-flux term in the range of a void jump

Summing-up, if the respective phase is no longer present in the upstream CV and if the velocity is not equal to zero, the implementation results in an incorrect MF contribution. Consequently, the code has been modified so that an upstream junction only contributes to the MF if the corresponding phase is actually present in its upwind CV. The new formulation reads as follows:

$$dp_{MF}(j_0) = \frac{\rho}{2} \left( \frac{\alpha(i_1)}{\alpha(i_0)} WLJ_1^2 - WLJ_0^2 \right) \quad (6.13)$$

As can be seen, the momentum of junction  $j_1$  is multiplied with the void fraction ratio, whereas:

$$\frac{\alpha(i_1)}{\alpha(i_0)} = 0 \quad \text{if } \alpha(i_1) = \alpha(i_0) = 0 \quad (6.14)$$

Applying this code modification, the expected liquid distribution established inside the U-tube of the ECTHOR model. Fig. 6.6 depicts the homogenization of the fill levels along the CVs of the horizontal test section.

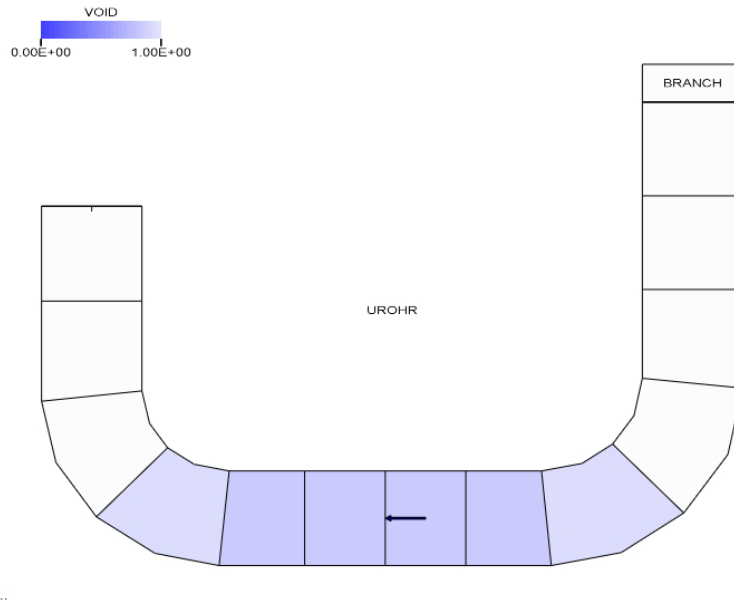


**Fig. 6.5** Phase distribution under stagnant flow conditions at the end of an ECTHOR simulation using the corrected momentum-flux term

### 6.1.3 Wall condensation heat transfer in vertical pipes

In the simulation of a vertical straight-tube condenser with flow from top to bottom and in the presence of non-condensable gases, it was observed that the condensate temperature  $T_L$  stays similar to the saturation temperature of the liquid  $T_{LS}$ , although the vapor temperature  $T_V$  (and also vapor saturation temperature  $T_{VS}$ ) is significantly lower due to the presence of non-condensable gases. This led to the phenomenon that there is no monotonously increasing temperature gradient from the pipe wall ( $T_{SL}$ ) to the inner vapour/air core of the flow. Instead, the wall is cool, the liquid condensate (film on the wall) is hot and the vapour has a temperature between the two. This is illustrated in Fig. 6.8, particularly in the active condensing phase between 700 and 900 s.

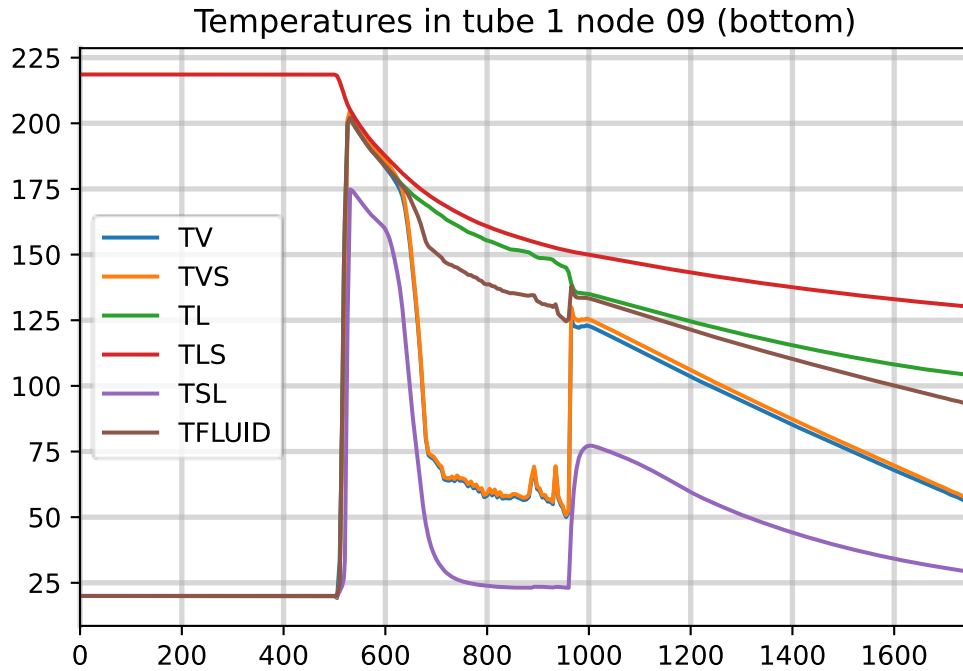


**Fig. 6.6** Temperature distribution in the lower part of the SACO

The unexpected behaviour occurred in simulations of the PKL facility that were performed as part of the PASTELS project. Here, the passive safety condenser (SACO) is introduced on the secondary side in order to condense the produced steam.

The in-depth analysis of the case was able to explain the causes of the observed behaviour and revealed various model weaknesses:

1. The significant subcooling of the vapour-gas mixture was partly caused by the fact that in the course of the transient simulation the condenser was slowly filled with cool gas from the bottom.
2. The distribution of the heat flow from the wall to the phases is achieved by ATHLET in a void fraction-weighted manner. Since in the case at hand only a very small volume of water was present in the condenser tubes, a large part of the cooling capacity was transferred to the vapour/gas phase. As the cool gas cannot condense and, thus, the bulk condensation model is basically ineffective, this approach even enlarges the strong subcooling of the vapour/gas mixture. At the same time, hardly any subcooling of the liquid is achieved.

3. In general, if the gas content in the fluid increases, the vapour condensation rate is suitably reduced in ATHLET in order to take into account the accumulation of gas in the area of the boundary layer between liquid and vapour. This procedure is applied equally to the simulation of bulk and wall condensation. In the present case, the wall condensation heat transfer from the wall to the fluid was reduced to almost zero in some simulation phases. Since the void fraction-weighted convective heat transfer to the liquid was negligible as well (see explanation above), the liquid almost didn't take part at all in the heat transfer. However, this is unrealistic, as at least a convective heat transfer to the liquid (especially to the water film in the vicinity of the wall) should remain. Now, if the standard HTC correlations had been used in ATHLET, the convective heat transfer to liquid would have been taken into account. In the present case, however, a special correlation for condensation in vertical pipes /PAP 10/ was selected by the user via the input data.

Concerning item 3 above, a model improvement was implemented so that at least a convective heat flow is taken into account. For item 2, the user was provided with a modified ATHLET version, which contains a modified distribution of the wall heat flow to the two phases. In the presence of a film flow with condensation, a larger fraction of the total wall heat flux is transferred to the liquid phase so that significant undercooling of the liquid with subsequent bulk condensation on the liquid film can be simulated. This code modification must be further analyzed and validated in future. Additional investigations related to that topic are envisaged in the project phase B working package 1.5 on wall to fluid heat flow distribution to phases.

#### **6.1.4 Entrainment calculation in condensation model**

Various models in ATHLET, like the models for interfacial friction or bulk mass and energy transfer, require an entrainment fraction to adequately calculate the interfacial transfer terms. For that purpose, e.g., a correlation according to Liles is used in ATHLET /LIL 88/, which determines an entrainment fraction as soon as a critical velocity for the onset of entrainment is exceeded. It was found that the implementation for the critical velocity, as it was implemented in the bulk condensation and evaporation model, included an error. Instead of the vapor superficial velocity, the vapor velocity was used for the determination of the onset of entrainment, which has been corrected. The corrected

implementation can cause slightly reduced entrainment rates, which again results in a decreased interfacial area and a decreased condensation rate. However, the code validation has shown that the impact on several selected validation cases is rather small.

#### **6.1.5 Heat transfer under film boiling conditions**

During the validation against reflooding tests from the RBHT, FEBA, PERICLES and FLECHT facilities, which had been performed for the release of the ATHLET 3.3 program version, a significantly increased heat transfer to the vapor phase was observed after exceeding the critical heat flux and at a (very) low liquid content. This led to a premature drop of the cladding temperatures. After changes in the calculation methodology of the heat transfer coefficient, the temperature curves significantly improved, and the quench times were generally delayed. As premature quenching was often reported for the aforementioned reflooding tests with the previous program version ATHLET 3.2.1, the changes in the new code version generally result in a better agreement with the experimental data.

#### **6.1.6 Improved condenser model**

The condenser model in ATHLET enables immediate condensation of a large amount of vapour flowing into a water reservoir, provided that the water reservoir is sufficiently subcooled. This is achieved by an artificial increase of the bulk condensation rate. The model can be used, for example, to approximate the effect of a sparger injection geometry. A sparger produces lots of very small bubbles in the vicinity of the injection location, which cannot be calculated by the standard bulk condensation model and its underlying flow regime map. The condenser model has been extended for mixtures of vapor and gas flowing into a water reservoir. In such a case, condensation is limited to saturation conditions of the vapor-gas mixture. Neglecting this measure resulted in oscillations due to too high condensation rates with subsequent evaporation required to finally achieve an equilibrium state.

### 6.1.7 Further program improvements

As part of the user support and the feedback received from the program validation, numerous insights were gained that have been incorporated into the program development and contribute, in the future, to increased code stability and an extended scope of application:

- Under CW `GCSM`, the controller type `PROP`, which can be used to determine material properties of working fluids, has been improved. Several partial derivatives of the material properties have been made available for release versions.
- Several ATHLET samples, which are distributed with the code, were improved, e.g.:
  - VVER-1000 sample: mixture level model in heat exchanger collectors activated
  - AP600 sample: drift options corrected; In addition, an example for the usage of the `GCSM` library `POSTPRO` has been added for the calculation of both the maximum fuel and the maximum cladding temperature of the reactor core.

During the application and further development of ATHLET, the following program errors were discovered and corrected:

- The visualization of a mixture level in the simulator software ATLAS was observed to be incorrect in case of components with more than eight control volumes. The root cause of the error, which was related to the ATHLET output files, was fixed.
- Two different time integration methods are available for integrator elements simulated by the `GCSM` module of ATHLET: The standard Euler-Cauchy method and the optional predictor-corrector approach. An error related to the latter was observed by a user when simulating the reactor control system. The program error could be fixed.
- During program development, test calculations with activated debug options are regularly performed to check program consistency. Now, inconsistencies were observed in the numerical calculation of the Jacobi matrix, which could cause numerical problems. The issue occurred under certain combinations of the models for mixture level, non-condensable gases, and condenser. The causes of the errors were eliminated.

- In the check valve model, an uninitialized local variable was used; the variable is now correctly initialized, allowing debug versions to run.
- Initialization of air: ATHLET provides material properties for various non-condensable gases, e.g., for hydrogen, nitrogen, oxygen, air or argon. Air can be simulated as a separate component (gas name `AIR`) or as a composition of nitrogen and oxygen (gas name `AIRN2O2`). In the latter case, which was a newly implemented option in ATHLET 3.3, both components are integrated separately so that their volume ratio is allowed to change in the course of a transient, e.g., due to cladding nitriding. As to the initialization of air, it is assumed that 79% nitrogen and 21% oxygen are present. These volume fractions were incorrectly interpreted as mass fractions in the code. The program has been corrected.
- The simulation of the NC gas component hydrogen without activation of the HECU module (i.e., without simulation of any heat conduction objects representing structures) resulted in a program runtime error, since the variable `RH2OH2` (density ratio of steam to hydrogen) had not been initialized. So far, this variable was defined in HECU, but used by the TFD-module. The variable was transferred from the HECU-module to the TFD-module.
- An error was fixed in the electrical heater model that now enables to consider the impact of the temperature dependency of the electrical resistance on local power generation.
- The process signal called `TSURFMAX`, which can be used to determine the maximum cladding temperature inside the reactor core, could previously be used without error only for input data sets with more than one rod component. This has been made more flexible.
- The model for simulating a structural moderator has been corrected. The model can be used to consider the neutron kinetic feedback of the thermal expansion of, for example, graphite in the cores of pebble-bed reactors. The old implementation only provided correct results for a core nodalisation with a single rod component. However, to account for spatial power distribution and local effects, a finer resolution with several rod components of different power is usually used in ATHLET calculations.

- The ODE solver FEBE used in ATHLET offers the possibility of solving the fluid-dynamic conservation equations both implicitly and explicitly. The user can optionally select via the input data that certain equations are to be integrated explicitly, while the rest of the equation system is to be solved implicitly. When selecting this mixed solution approach, it has been shown that under certain circumstances (e.g., explicit solution of the balance equation of the mass fraction with simultaneous simulation of non-condensable gases) a program error could occur because the matrix of the implicit part of the model equation system was constructed in an incorrect way. The error has been corrected.

#### **6.1.8 Improvements related to the ATHLET start calculation**

- The fixed-point iteration used for the pressure equation during the ATHLET start calculation (so-called steady-state calculation) has been corrected. Due to an error, the previous implementation always led to a converged value after just two iterations. However, the influence on the final results turned out to be only minimal.
- In order to debug the results of the start calculation, ATHLET offers the option of writing plot data of the complete system states after each individual iteration steps of the start calculation. However, as various variables of the valve model had not yet been initialized at this point of the calculation, this could cause a program error. The error was corrected.
- In addition, the option of writing plot data for the iterations of the start calculation was improved, so that input decks without activation of the HECU module (i.e., without definition of any HCOs) can also be processed correctly.
- In an ATHLET application, it was observed that the start calculation returned an incorrect initial pressure that was several 100 kPa higher than the pressure specified in the input data set. It turned out that if the first junction of a TFD system contains a pump (or a turbine or a compressor), the pressure in the subsequent first CV of the TFD system is increased by, for example, the nominal head of the pump. As the pressure in the first CV of a TFD system determines the pressure level of the entire system, an unexpected increase in pressure was found for the complete system. This does not meet the user's expectations of the program, since the pressure in the first CV of a TFD system is an input variable that should never be adjusted by the

code. The ATHLET start calculation was suitably extended so that the user can also use the component models for a pump, a turbine, or a compressor in the first junction of a TFD system (as well as in the last junction in case of a closed loop).

- At the beginning of the start calculation, a non-intercepted program crash occurred, which was caused by a control volume including a mixture level under non-stagnant, flowing-fluid conditions. According to the definition of the priority chains in the input deck, the control volume was to be iterated from top to bottom across the mixture level in the start calculation. Unlike control volumes with stagnant fluid, this is not possible, but was not intercepted correctly. A corresponding error check was implemented, and the related user guidelines provided in the User's Manual were clarified and expanded.
- Calculation of tables with critical flow rates (CW<sub>CDR1D</sub>): The critical discharge rates are determined once at the start of a calculation depending on the user-provided geometry data. They are stored in the form of tables, which are interpolated during the transient calculation to find the current critical flow rate depending on the current pressure, void fraction and fluid subcooling or overheating. To save calculation time, the tables are stored for subsequent calculations and only recalculated if the input data of the CDR1D model (or if the source code or the compiler version) have changed since the last calculation. Previously, a numerical change in the input data was detected by comparing the numbers considering only a limited numerical accuracy. However, it was noticed by a user that (absolutely and relatively) small changes to the geometry of a small break did not result in the recalculation of the tables. Therefore, the comparison of previous and current input data was modified. Now, it is performed on string level, so that any change to the relevant input data is reliably recognised.

## **6.1.9 Input data extensions and checks**

### **6.1.9.1 Syntax checks for the input deck**

The syntax of the input deck – including any ATHLET-CD input – is checked extensively immediately after processing of parameters. To this end, a dictionary of legal control elements (control word, pseudo-keywords, and some keywords and sub-keywords)

defined in the ATHLET Input Data Description has been build. Input under all CW is checked if

- only legal CW are present in the input deck,
- only legal KW, SW and PW are present for each CW,
- only legal control element definitions are used, e.g., a spurious non-blank character on position 6 or a spurious blank on position 5 for a PW will trigger an error,
- all PW are input only once, and are input in the order as given in the Input Data Description,
- there are no spurious input cards after the end of a fixed-length input block.

Additional syntax checks are performed under each user-input KW, where necessary. As a consequence, the legal PWs for TFO objects now depend on the TFO object type (ITYPO) and also special component models (ICMPO) .

#### **6.1.9.2 Sub-keywords under CW PARAMETERS und CW HEATCOND**

Under CW PARAMETERS, a (long) list of parameter definitions and arithmetic operations with parameters can be input. Using optional sub-keywords, this this can be structured into as many input blocks as needed. The input block defined via the SW can be activated or de-activated as needed. This facilitates configuration control of the input deck, e.g., several variants of a parameter can be defined in separate blocks, for different calculation cases in the same facility.

Under CW HEATCOND, a (potentially long) list of HCO names active in the current simulation has to be provided. This can be structured analogously via optionally input SW. This facilitates having different configurations of a facility in one input deck and activating the relevant configuration for a specific simulation case.

#### **6.1.9.3 Improvements for COPY directives**

The COPY directive, which can be applied to TFO, HCO and ROD objects in an ATHLET input deck, was evaluated as input by position in the input line. This was changed so

that a `COPY` directive is interpreted as an input of two Fortran strings. This means that the position of the string in the input line as well as additional blanks between these two strings are no longer relevant.

#### 6.1.9.4 Extension of input error and consistency checks

The consistency and input error checks for the input deck were significantly extended. For each input card, the type of the input is checked against the legal options as defined in the Input Data Description. For model option flags, each input is checked if the input options are legal. For other data, as a minimum a check if the data are sensible is performed. As an example, negative values for a pressure are rejected as are inputs larger than 1.0 for void. In some cases, a minimum value for inputs is imposed, e.g., a heat conductivity, where an input of 0.0 would risk runtime errors. In these cases, generally minimum numerical precision values at 1.0 for real numbers of single precision (in Fortran: `epsilon(1.0)`) or double precision (`epsilon(1.0D0)`) are used.

In addition, the following improvements have been implemented:

- It is now checked that the power profile for a rod, which has to be defined under `CW ROD`, is input for the complete length of the HCO representing the rod. So far, the power profile (if not completely given) was extrapolated till the end coordinate of the rod, which could result in an undesired or even unphysical power distribution. The newly implemented input check avoids such input errors.
- Expanded input data consistency checks were implemented, e.g., for the double-end break model (`CW DOUBLEND`), the fuel rod model (`PW RODCON`), and the usage of the CHF correlation according to Sudo-Kaminaga.
- The full input of multiple input levels in one TFO was modified. Now the at most two input cards for each mixture level have to be input directly after each other. As a consequence, the second input card is now optional for a collapsed level model and obligatory for a mixture level.
- For most tables input for specific models under several `CW`, it is now checked if the abscissa values are monotonously increasing during input processing. Also, the table values are checked for plausibility, if sensible. This prevents run-time errors

during the transient calculation and pinpoints the user to the specific problem in the input deck.

- Optionally, instead of using default heat transfer correlations, specific heat transfer correlations can be selected in the input data set. The user has the option of selecting certain correlations for the entire simulation domain or for individual regions (i.e., HCOs). The validity of the selected correlations is now checked centrally in the program using a new subroutine `SCHECK_HTCCOR`, which can alternatively be also used to set the default options that have proven themselves for standard applications.

#### **6.1.9.5 Extension of CW SERVICES**

Under `CW SERVICES` the optional `PW PRNT_INPUT` was added with three options. For input 0, no additional output is performed. For option 1, an effective version of the input deck is written to file with the extension “.einp” and the file name derived from the run ID. In this file, all parameter values in active objects outside of `CW PARAMETERS` are replaced by the numeric (or string) values. In order to enable comparison with the input file, after all includes have been processed, all comments are included in the “.einp”-file. However, continuation lines in the input deck are not restored but rather output on their respective first input line.

With option 2, additionally the “.ait”-file is output. This file is a dump of the significant part of the `AITEXT` array. This array includes all non-empty input cards in the input deck after all includes have been processed, all comments have been removed, and all parameters have been replaced by the respective values by `ATHLET`. It is used for the input processing in `ATHLET` and `ATHLET-CD`. The `AITEXT` array always ends with the `CW END`.

#### **6.1.10 Extended program output**

##### **6.1.10.1 Additional output quantities**

In order to thoroughly analyse an `ATHLET` calculation, integrated mass and energy balances like total working fluid and NC gas masses are very helpful. Several TFD system specific quantities have been provided already with previous `ATHLET` versions. However, the code users requested further output quantities to support their analyses. The

source code has been accordingly expanded and following additional quantities are available in both print and plot output now:

- For each TFD system:
  - Integrated energy flow from the respective TFD system into all HECU structures except those representing a rod or a heat exchanger
  - Total mass of each NC gas component in the TFD system
- For each system boundary represented by a TDV (time-dependent volume):
  - Integrated working fluid mass flow (liquid and vapour) into the TDV
  - Integrated energy flow (working fluid) into the TDV
  - Integrated gas mass flow into the TDV
  - Integrated gas energy flow into the TDV
  - Integrated hydrogen mass flow into the TDV

#### **6.1.10.2 CHF correlation related output**

If the critical heat flux is exceeded in an ATHLET simulation, the user is informed by meaningful output quantities like the DNB ratio as well as by messages in the print output. The provided information was complemented by additional data to support the user in the analysis of the simulation results:

- The specific correlation that predicted the occurrence of DNB/Dryout is printed. Depending on the setting in the input data, the minimum of various CHF correlations could be used by ATHLET, so that it is not clear to the user a priori, which correlation is limiting.
- It is checked, if the range of validity of the used CHF correlation was exceeded, and if so, this information is printed.

### 6.1.10.3 CPU time statistics

At the end of an ATHLET run, a CPU statistic is written to the output file which indicates how much of the total CPU time was consumed in the different parts of the ATHLET code. This overview supports the code development in ensuring program efficiency and detecting bottlenecks that impair code performance. The computation of CPU consumption is done using the standard Fortran subroutine *system\_clock(count, count\_rate)* and computing differences between the values of *count* at begin and end of a program section. The value of *count\_rate* depends on the platform and on the used data type. The value of *count* is reset to zero when the value of *count* exceeds the range of the variable. A too narrow integer data type (integer(4)) was used so far for the arguments of *system\_clock*; thus, resets of *count* could happen during the run of an ATHLET simulation, leading to wrong, and possibly even negative, values of the CPU time. Now, integer(8) is used which prevents this problem.

### 6.1.10.4 Control of output data amount

In response to user requests a new option has been set up to flexibly control the amount of output data provided by the mixture level model. This allows to influence the size of the print output file to keep it easier readable and manageable, particularly for long applications with many mixture level transitions and corresponding print output.

In addition, the amount of print- und plot data produced under the keywords `GENERAL`, `MONITOR` and `TFDGENERAL` can be controlled by the input settings for parameter `IOOUT0` under the `CW OBJECTCON` now.

In addition, under `PW GCSM` the new option `IOOUTG0=-1` has been added, which does not overwrite previous settings from `CW GCSM`. This allows to modify signal settings also for GCSM signals not included in the output due to a GCSM block setting of `IPRI=-1`.

### 6.1.10.5 Extended main edits

For example, by using the AC<sup>2</sup> graphical user interface, the user can interactively initiate additional print outputs (so-called main edits) in order to obtain a detailed overview of

the current simulation status. The overview output has been extended by current time derivatives of the fluid dynamic variables as well as by variables of the ATHLET-CD module SAFT.

#### **6.1.10.6 Improved minor edit output and extended time step statistics**

Previously, the time step edit did not include information about a possible time step limitation by a so-called HXX event and the consequential limitation of the following time step. For most HXX events potentially triggered in ATHLET, a statistic array that tracks occurrence of such events was added. HXX events are assigned to in total 15 classes for CVs, junctions, HCVs and rod objects. Moreover, HXX events and time step limitations from ATHLET-CD can also be tracked. If a HXX event triggers a repeat of a time step, and FEBE does not further reduce the time step subsequently, the FEBE time step statistics are replaced by the HXX event message, which is indicated by “HXX LIMIT” for DT and the HXX class name and the object index under H0N.

In addition, if a NC gas related quantity is time-step limiting, the fixed NC gas index number – if not the first gas – is output after the object index. Previously, this information was ignored, if there were more than 999 CV or junction indices, and folded as the leading digits into a combined index for less than 1000 CV or junction indices. This required some refactoring in FEBE for the computation of the respective object indices.

The minor time step edit was improved both for the console output as well as for the print output file. In the print output, the object names of TFOs, HCOs and RODs as well as the respective object-specific CV, junction, or HCV indices are provided as well.

Finally, statistics over the leading contributors to H0 time step predictions by FEBE as well as DT time step reductions by HXX events and by FEBE are computed at the end of the run. The leading contributors for limiting solution variable or HXX class as well as the associated object and its object index are printed at the end of the output file. Such information can be used to look for possible modelling issues in the input deck that limit time step size.

### 6.1.11 Improved plug-ins interfaces

On request, various universities and research institutes were provided with customised interfaces based on plug-in method for their own model developments. The MHTCEXT plug-in can be used to couple user-provided HTC correlations with ATHLET. Fig. 6.9 gives an overview on the heat transfer calculation and the selection logic for HTC correlations.

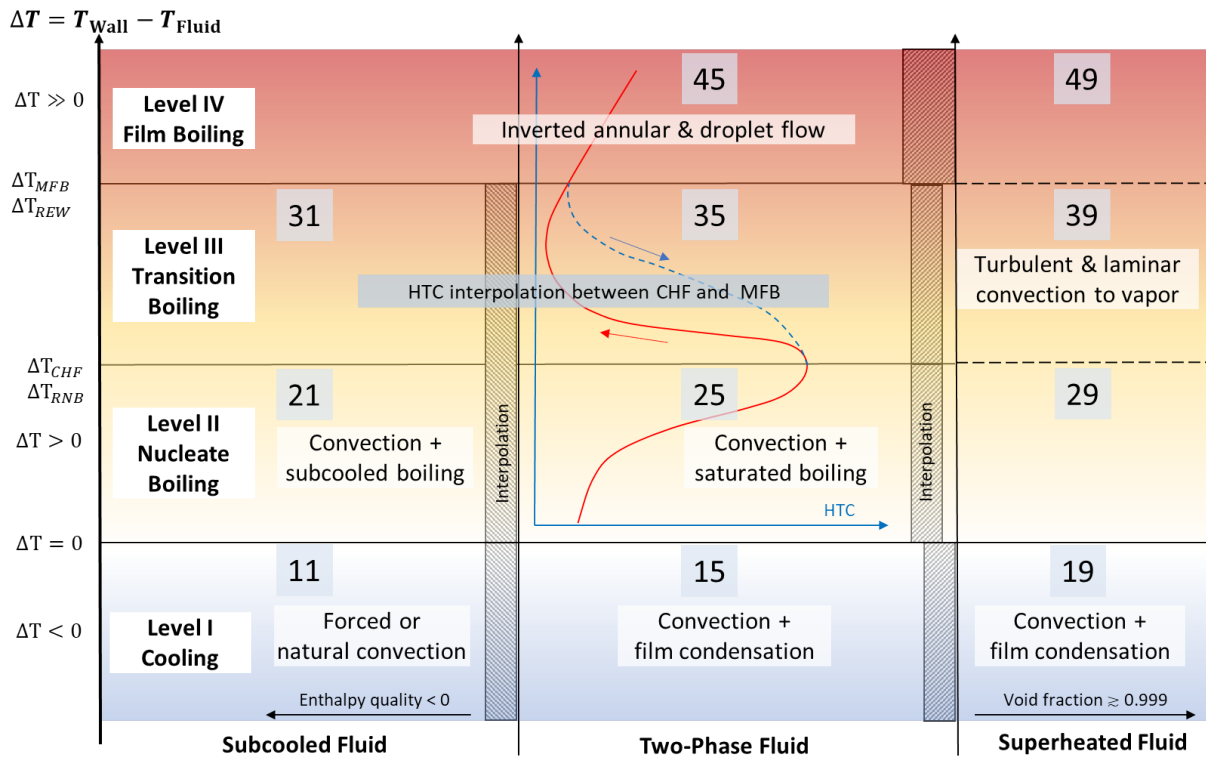


**Fig. 6.7** The HTC correlation selection logic used in ATHLET /SCH 23b/

Depending on wall subcooling or superheating, four heat transfer levels are distinguished, each of which is subdivided into three heat transfer modes. In the MHTCEXT plug-in, interfaces for following levels and modes have been added or extended in their capabilities:

- To determine the heat transfer coefficient to supercritical water, additional variables such as viscosity, specific heat capacity, and thermal conductivity of the fluid are transferred to the interface so that the user can easily calculate dimensionless

numbers such as Re or Pr number and use them in their own heat transfer correlations (regimes 21 and 25 in Fig. 6.7).

- The interface for determining the convective heat transfer to fluid could previously only be used for the working fluid water. The program has been extended so that the interface can also be used for all other working media such as liquid metals (regimes 11, 15, 21, and 25). This feature is of particular interest for the application of ATHLET to future, innovative reactor designs.
- The MHTCEXT plug-in could previously not be used with the parallelised ATHLET program version. The implementation of the plug-in has therefore been adapted (applies to all regimes).

## **6.2 National and international cooperation**

### **6.2.1 OECD/NEA Rod-Bundle-Heat-Transfer Benchmark**

#### **6.2.1.1 Introduction**

The OECD/NEA Rod Bundle Heat Transfer (RBHT) benchmark, based on experiments performed at the NRC/PSU RBHT test facility located at Pennsylvania State University, USA, was intended for the validation of system code models related to reflooding simulation. After an initial set of open tests /SCH 21a/, the next phase of the project continued with 5 blind tests. The blind phase aimed to test findings and model improvements made during the open phase. GRS participated in the RBHT project with the then current version 3.3 of the thermal-hydraulic system code ATHLET /DÜN 22a/, /DÜN 22b/.

Results of the blind tests using the 6-equation, 2-fluid model of ATHLET are presented. Evaluation focusses on parameters relevant to quench front model validation, such as cladding temperatures at different elevations, pressure drop along the test section and quench front progression. Experimental data, only available after the submission of the results, is used for comparison. The changes in ATHLET version 3.3 positively affected the quench front progression, and peak cladding temperatures are well predicted. The underestimation of the pressure drop over the bundle that was observed in the open

tests is still present in the blind results. For test B-1, heat transfer coefficients were underpredicted and the simulation failed to quench the upper section of the bundle.

The uncertainty and sensitivity analyses were performed using the GRS statistical software SUSA 4.2 /KLO 20/ based on data from the RBHT open phase as well as earlier analyses of reflooding experiments. The effect of uncertainties in the models, facility modelling, and experimental conditions is examined, and the most influential parameters are determined. Based on these results, recommendations for the future development of reflooding modelling with ATHLET are formulated.

### **6.2.1.2 Short facility and test description**

The investigated experiments were conducted at the RBHT Test Facility at the Pennsylvania State University. The test section features a 7 x 7 rod bundle with a pitch of 12.6 mm and a heated length of 3.657 m and 4 unheated support rods in the corners. The 45 electrical heater rods have a diameter of 9.5 mm and feature a skewed axial power profile, where the point of maximum power, located at 2.74 m, constitutes 1.5 times the average heating power, while the end points of the rods equal 0.5 times the average power. The bundle is contained in square housing which measures 91.3 mm x 91.3 mm.

Below the test section is a lower plenum, which is connected to the injection water line and acts as a reservoir for the coolant. Above the test section is an upper plenum, which acts as a separator with a sudden increase in flow area and a baffle, both used to de-entrain liquid from the steam, which is then collected in carryover tanks. Further details can be found in the facility description /ROS 10/.

Before the test, the steam-filled test section is heated, until the desired initial heater rod surface temperature is reached at the axial location of maximum power. At this point, the test begins, and subcooled water floods the test section from below. The test continues, until the bundle is completely quenched.

### **6.2.1.3 Facility Modelling**

The thermal-hydraulic channel of the test section is modelled as two parallel channels linked via cross-connections, enabling a quasi-2-D simulation. The channels are axially

divided into 23 control volumes (see Fig. 6.10). The central 25 heating rods are contained within the central channel while the peripheral channel contains 20 heating rods as well as the 4 unheated corner construction rods and is connected to the housing walls.

The heating rods have the same length as the thermal-hydraulic channels and are also axially divided into 23 nodes according to the thermal-hydraulic nodalisation. The rods are modelled using heat slabs with two unheated nodes at the top.

The model of the heating rod consists of three material zones: Monel 500 for the inner heated zone, boron nitride for the unheated outer zone and Inconel 600 for the cladding. The four corner rods are simulated as unheated heat slabs made of Inconel 600.

The housing of the test section is simulated considering Inconel housing and mineral wool insulation. At the inner side of the housing the heat transfer coefficients are calculated by means of correlations. At the outer side of the housing a constant heat transfer coefficient of  $3.7 \text{ W}/(\text{m}^2\text{K})$  is assumed, as stated in the facility description /ROS 10/. The housing of the test section is simulated considering Inconel housing and mineral wool insulation. At the inner side of the housing the heat transfer coefficients are calculated by means of correlations. At the outer side of the housing a constant heat transfer coefficient of  $3.7 \text{ W}/(\text{m}^2\text{K})$  is assumed, as stated in the facility description /ROS 10/.

In the thermal-hydraulic channel the grid spacer geometry is considered as decreased cross-section areas at the grid spacer levels. The cross-section areas and hydraulic diameters of the central and peripheral channels differ slightly due to housing consideration. The pressure losses at the grid spacers are considered as form loss coefficients equal to 2.0.

At the inlet and outlet of the test section respectively, a lower and upper plenum connected to both the central and peripheral channel is simulated. The lower plenum is simulated as a single control volume, while the form of the upper plenum is used as an uncertainty parameter. It consists of either two or three control volumes with a drain pipe at the top and bottom, which either connect to a common or two separate time dependent volumes.

The inlet mass flow into the test facility at the lower plenum is simulated with mass flow and enthalpy boundary condition. At the outlet of the upper plenum pressure and enthalpy boundary conditions are applied for the outlet control volume (time dependent volume in the ATHLET nomenclature). As pressure boundary condition the nominal pressure for each test has been applied.

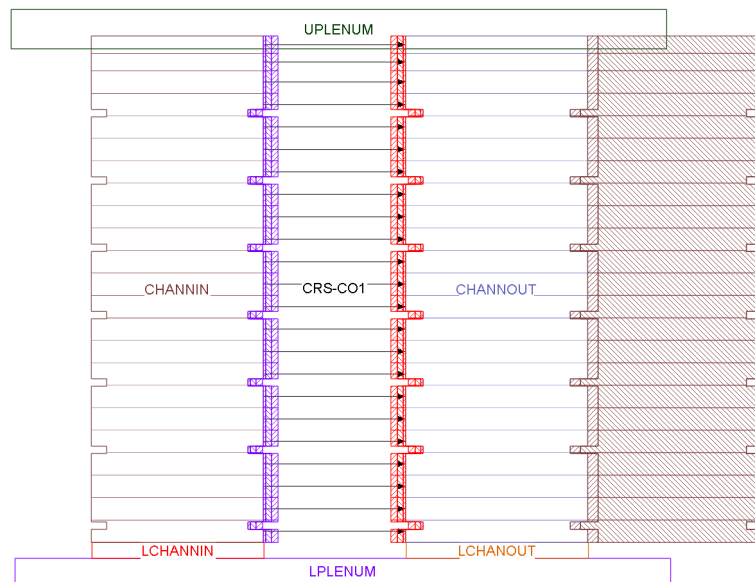


**Fig. 6.8** Nodalisation of the RBHT test section in ATHLET

The quench model parameter  $C_{QHTWB}$  which controls the enhanced heat transfer coefficient at the quench front was set near the minimum value recommended for ATHLET. To slow down the quench front progression, all the simulations used  $3 \cdot 10^4$  W/m<sup>2</sup>K instead of the default value of  $3 \cdot 10^5$ . This reduced value is based on the open RBHT simulations as well as earlier reflooding tests, which generally tended to quench early.

For the modelling of the test section thermal-hydraulics channel, a total number of 98 control volumes and 121 junctions, distributed among 9 pipe objects, 1 cross-connection object and 4 branches, was used. Heating rods are divided axially into 23 nodes and radially into 3 material zones divided into 5 layers.

#### **6.2.1.4 Initial Steady-State Conditions**

The standard procedure of initial condition definition is that ATHLET performs a steady state calculation which initializes the complete system starting from a limited number of user-supplied initial and boundary conditions by iteratively solving a set of mass, energy, and momentum balance equations for the whole system.

The temperature distribution in the heat slabs cannot be directly given as an initial condition but is calculated based on temperatures given in connected thermal-hydraulic objects/nodes solving the adequate heat transfer and heat conduction equations. To define the initial temperature distribution in the heating rods, an artificial micro-channel along the axis of the heating rods was introduced for which the axial temperature distribution was defined. The temperature was assumed to be equivalent to the measured cladding axial temperature distribution at the beginning of the tests. The initial temperature distribution in the cooling channel of the test facility was assumed to be similar to the housing temperature.

The housing as well as the insulator are divided axially into 23 nodes according to the channel nodalisation. The dimensions and materials are modelled according to the test facility description. The environment temperature was assumed as 20 °C.

#### **6.2.1.5 Sensitivity and Uncertainty Analysis Method**

GRS performed uncertainty analyses (forward uncertainty analyses) with the statistical software SUSA /KLO 19/. The applied method is an input uncertainties propagation method using Wilks' formula for determination of uncertainty limits and required number of code runs.

The input uncertainties are defined in the elicitation and quantification process. The methodology applied by the GRS is described in /SKO 04/ and the extension for application to the combined effect tests in /SKO 17/. A short overview is given below.

### 6.2.1.6 Input uncertainties quantification

Identification of potentially influential uncertain input parameters is performed in an elicitation process. No ranking of parameters is performed. Usually, all potentially important uncertainties (model parameters, initial and boundary conditions, reactor plant operating parameters, material properties, spatial discretisation, numerical parameters, scaling effects) are considered. There is no limitation to a small number of uncertain parameters, since the number of code calculations does not increase with the number of uncertain parameters.

The important steps of the elicitation process are:

- identification of important phenomena occurring during event simulation,
- identification of models corresponding to those phenomena,
- identification of potentially important uncertainties,
- compilation of the list of potentially important uncertain parameters.

For identification of the potentially important uncertain parameters each available source of information should be considered. The needed information can be obtained by:

- analyses of relevant integral experiments,
- experts' consultation,
- analysis of reference calculation of the event, and
- performing a proper variation of the reference calculation.

The usual practice is to apply the full procedure for each study. At the current stage of uncertainty and sensitivity analyses at GRS, information can be gained from numerous studies performed in the past.

The basis of model uncertainties quantification is evaluation of separate effect experiments. Other information sources for quantification of model uncertainties are experience from code validation by integral experiments, survey of the experts' state of

knowledge, comparison with published related analyses, uncertainties derived directly from the literature, and if necessary, applying theoretical physical limitations.

If a systematic error of model prediction occurs, this is usually expressed by a shift of the mean value of the subjective probability distribution function. In the methodology used at GRS each kind of input uncertainty is to be included by subjective probability distributions and no adjustment of output parameter uncertainties is applied.

The subjective probability distribution functions (SPDF) applied to quantification of uncertain input parameters depend on the state of knowledge. If information concerning the uncertainty of the input parameter has a stochastic character, e.g., it is a result of comparisons with a large number of separated effect tests, or it consists of significant number of measurements, usually the probability distribution function has the form of normal distribution. Sometimes also others statistical distributions can be used. However, in the most cases quantification of the state of knowledge is based on some selected comparisons with experimental data, frequently supported by expert judgement. In such situations usually polynomial or triangular distribution functions are applied. In the case of limited information, the uniform distribution function is adequate for the state of knowledge quantification.

#### **6.2.1.7 Sampling**

In the GRS studies, Simple Random Sampling (SRS) is used. The core of the Monte Carlo method applied for determination of output uncertainties is a sample drawn according to the joint distribution of all uncertainties. SRS is a pure random technique appropriate for the Monte Carlo method and using of Wilks' formula. The intervals of input variables variation given by normal or similar distributions are truncated according to state of knowledge or physical limitations.

The dependencies between parameters can be considered. However, in the case of two strongly dependent parameters it is preferred to consider only one of them if it is acceptable from modelling reasons. The state of knowledge dependencies can be expressed using:

- Population Measures or

- Sample Rank Correlations

In this study the conditional distribution (one of the population measures) of subjective probability distribution functions is used. The SPDF of the correction factor for an alternative model is used under the condition that this model is selected by another parameter.

#### **6.2.1.8 Uncertainty analyses**

Application of Wilks' formula enables determination of the requested probability content and confidence level only as a function of the code runs, independent on the number of defined uncertain input parameter. For the two-side tolerance interval the Wilks' formula for a coverage of  $n - 1$  is

$$1 - \alpha^n - n(1-\alpha) \alpha^{(n-1)} \geq \beta$$

where  $\beta$  is the confidence level that the code results will not be outside of the tolerance limits with the probability  $\alpha$ . Usually the 95% probability and 95% confidence level tolerance intervals are applied. For this tolerance level and the first order of formula the minimum number of 93 calculations is required.

#### **6.2.1.9 Sensitivity analyses**

The software SUSAS enables use of numerous measures of sensitivity, like Standardised Rank Regression Coefficient, Rank Correlation Coefficient and Correlation Ratio. The measures applied in SUSAS are global sensitivities. They permit the ranking of input uncertainties with respect to their relative contribution to the total uncertainty of the output parameters in the code simulation.

#### **6.2.1.10 Input uncertainties quantification**

The following models have been identified as potentially influential and considered by uncertainty analysis of RBHT experiments:

- wall heat transfer

- evaporation of droplets
- interfacial shear
- heat transfer enhancement at the quench front
- two-phase pressure drop:
  - two-phase flow multiplier
  - wall shear stress distribution between gas and liquid phase

In addition to the model uncertainties, uncertainties of the facility modelling were considered:

- form losses in the horizontal cross-connection between inner- and outer-channel
- fuel rod simulator material – boron nitride conductivity
- heat losses
- experimental uncertainties – boundary and initial conditions for the transient simulation
- spatial discretisation – axial nodalisation of the upper plenum

The quantified input uncertainties are listed in Tab. 6.1 below.

#### **6.2.1.11 Code runs**

In this study a sample of 100 input uncertainties vectors has been generated for B2 and B6, respectively, and the simulations were performed. All the code runs were successfully completed. The CPU running time was between 600 s and 1600 s per simulation, totalling slightly over a day of run time per test.

**Tab. 6.1** List of RBHT uncertain input parameters

No.	Parameter	Parameter explanation	Component/ Geometry	Ranges		Reference	Distribution	Quantification	
				min	max				
<b>Model uncertainties</b>									
Wall heat transfer									
1	OHVFC	Correction factor for single phase forced convection to steam (Mc Eligot)	All heat slabs	0.85	1.25	1.0	Uniform	Literature /GOT 85/ and expert judgement	
2	OHWFB	Correction factor for film boiling, modified Dougall-Rohsenow correlation	All heat slabs	0.65	1.3	1.0	Uniform	Literature /GOT 85/ /NIJ 80/ and KWU tests with 25-rods bundle analyses /VOJ 82/	
Evaporation									
3	ZT	Number of droplets per volume (m <sup>-3</sup> )	B-6	Whole thermal-hydraulic system	10 <sup>9</sup>	10 <sup>10</sup>	5x10 <sup>9</sup> 1/m <sup>3</sup>	Uniform 10 <sup>9</sup> - 5x10 <sup>9</sup> - 10 <sup>10</sup>	Flashing experiments, FEBA and PERICLES reflooding tests, numerous integral experiments, and user experience
			B-1/2	Whole thermal-hydraulic system	10 <sup>10</sup>	10 <sup>11</sup>	10 <sup>11</sup> 1/m <sup>3</sup>	Uniform	
Interfacial shear									
4	OIBUN	Correction factor for interfacial shear in non-dispersed vertical bundle flow	Test section	0.1	2.5	1.0	Histogram 0.1-0.84-2.5 / 50%-50%	PERICLES and THETIS boil off tests and LOFT L2-5 experiment	

No.	Parameter	Parameter explanation	Component/ Geometry	Ranges		Reference	Distribution	Quantification
				min	max			
5	OENBU	Correction factor - transition velocity from non-dispersed to dispersed droplet flow in vertical bundle	Test section	0.6	1.5	1.0	Uniform	FLECHT, FEBA and PERICLES reflooding experiments /SKO 17/ and expert judgement
6	OIVDI	Correction factor for interfacial shear in dispersed vertical droplet pipe flow	Vertical flow paths	0.5	1.5	1.0	Uniform	ANL experiments analyses /ISH 79/ and expert judgement
7	OIHPI	Correction factor for interfacial shear in horizontal flows (here cross-connections only)	Cross-connection junctions	1.0	20.0	1.0	Uniform	Expert judgement
Quench front								
8	CQHTWB	Heat transfer coefficient at lower quench front	Core	$3 \cdot 10^4$	$3 \cdot 10^5$	$3 \cdot 10^4$	Log	FEBA, FLECHT and PERICLES reflooding experiments, RBHT open tests
Two-phase pressure drop								
9	OFI2V	Multiplication factor for two-phase multiplier in vertical pipe, Martinelli-Nelson correlation	All flow paths in thermal-hydraulics system	~0.2	~2.0	1.0	Log-normal $\mu = -0.247, \sigma = 0.339$	Literature /BEA 82/ (comparison with HTFS data bank – about 3000 measured values)
10	OFRIC	Wall shear distribution liquid – vapour	Test section	-3.2	4.0	0.0	Uniform (variation between 100% wall shear to water and 80% to vapour)	Expert judgement and experience from validation

No.	Parameter	Parameter explanation	Component/ Geometry	Ranges		Reference	Distribution	Quantification
				min	max			
<b>Facility modelling uncertainties</b>								
Pressure drop, form losses								
11	ZFFJCC/ ZFBJCC	Multiplication factor for form losses	Cross-connection	0.5	3.0	1.0	Log-normal $\mu = 0.0$ , $\sigma = \ln(2)/1.96$ Truncated over [0.5 3.0]	Literature /IDE 86/ and expert judgement
Heating modelling								
12	WLF	Multiplication factor for boron nitride conductivity	Fuel rods	0.9	1.1		Normal $\mu = 1.0$ s = 0.1, truncated over [0.9; 1.1]	Literature review on accuracy of fuel rod material properties
13	HTC	Heat losses – multiplication factor	Isolation	0.65	1.5	1.0	Histogram 0.65-1.0- 1.5 / 50%-50%	Experimental test facility documentation and expert judgement
<b>Experimental uncertainties – boundary conditions</b>								
14	G-INL	Multiplication factor for inlet mass flow	Test section	0.99	1.01	1.0	Uniform	Regulation accuracy in experiment and expert judgement
15	QCOR0	Multiplication factor for heating power	Core	0.985	1.015	1.0	Normal $\mu=1.0$ , $2\sigma =0.015$ truncated over [0.985, 1.015]	Regulation accuracy in experiment and expert judgement
16	PV-P0	Additive correction term to system pressure	Test section	$-10^4$	$10^4$	0.0 Pa	Normal $\mu=0.0$ , $2\sigma = 10^4$ truncated over [- $10^4$ , $10^4$ ]	Regulation accuracy in experiment and expert judgement
17	TI-T0	Additive correction term to initial temperature in the test section	Test section	-20.0	20.0	0.0 K	Uniform	ATHLET steady-state determination accuracy and expert judgement

No.	Parameter	Parameter explanation	Component/ Geometry	Ranges		Reference	Distribution	Quantification
				min	max			
18	TINL	Additive correction term to inlet temperature	Test section	-2.0	1.5	0.0 K	Uniform	Steady-state regulation accuracy in experiment and expert judgement
19	XIT	Inlet temperature transition from saturation temp. to TINL (reflooding starts with near saturation inlet temperature)	Test section – inlet	0.0	1.0	0.0	Uniform	Regulation accuracy in experiment and expert judgement
<b>Spatial discretization</b>								
20	NO	Axial nodalisation of the upper plenum	Upper plenum	1	2	1 1 - 1 node 2 - 3 nodes	Discrete	Experience from calculation of open tests

## 6.2.1.12 Results and discussion

### 6.2.1.12.1 Results for B-1, B-3 and B-4

The results for B-1, B-3 and B-4 will be bundled, as there was no additional uncertainty analysis performed. B-1 and B-4 used a high coolant mass flow rate and heating power, but B-4's power decayed over the test and the coolant temperature was lower.

As can be seen in Fig. 6.11 and Fig. 6.12, the simulation of B-1 fails to cooldown the bundle and temperatures are consistently overestimated. With the lower coolant temperature and decaying heating power, B-4 does quench the bundle, but the entrainment related precooling is not as strong as in the experiment. B-3 shows decent agreement, results are similar to the medium coolant flow experiments from the open tests /DÜN 22b/.

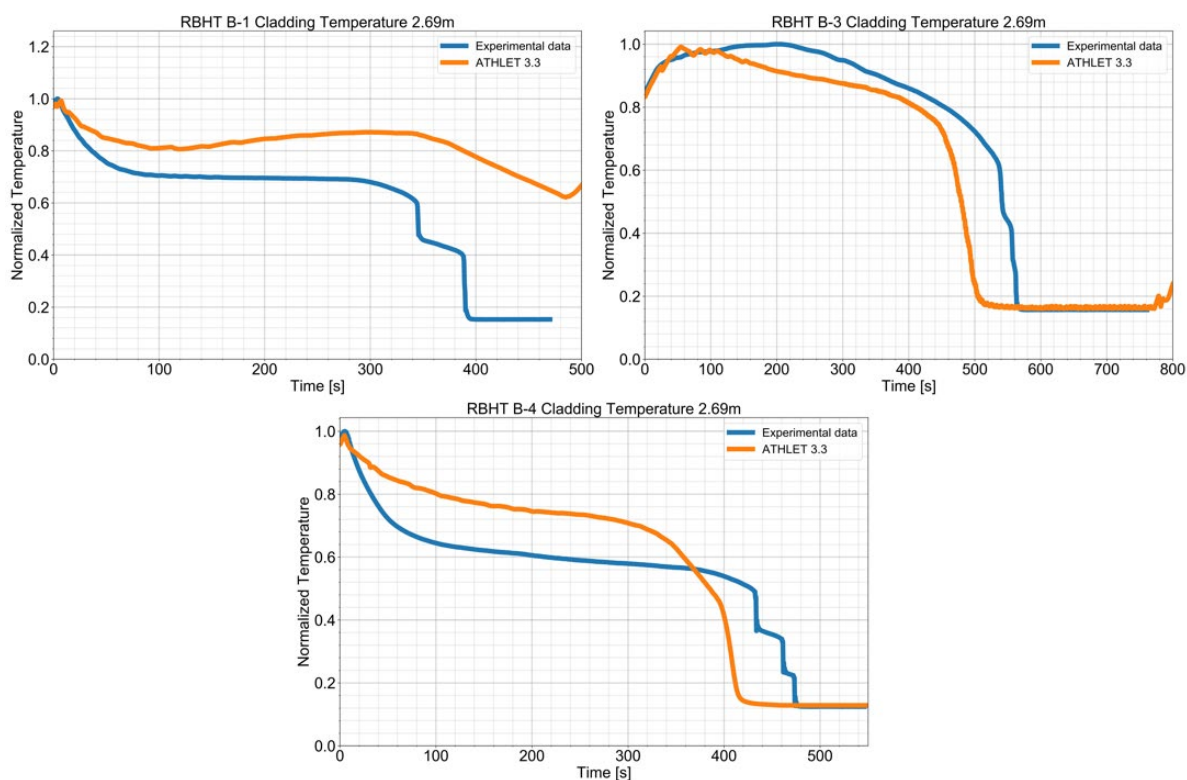


**Fig. 6.9** Cladding temperature at 2.69 m. From the upper left, B-1, B-3 and B-4 are shown

Congruent observations can be made when looking at the heat transfer coefficients at these positions in Fig. 6.13. ATHLET underestimates the heat transfer in B-1 and B-4

and the heat transfer regime change according to quenching does not occur in B-1. For B-3, calculated HTC values are higher, explaining the premature cooldown.

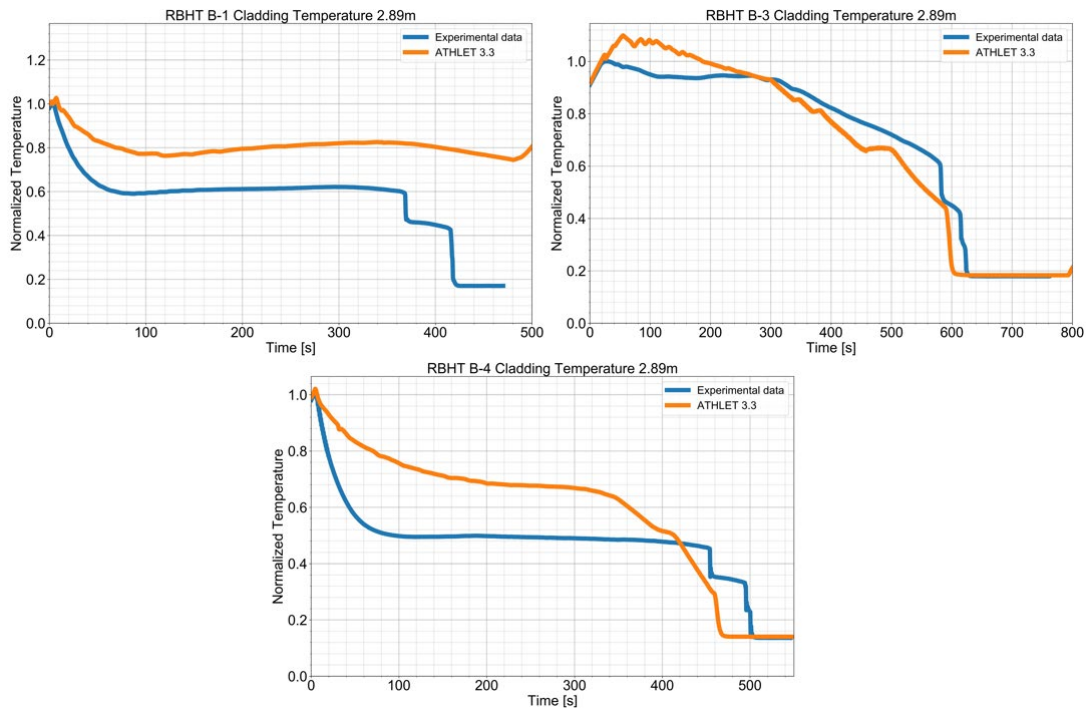


**Fig. 6.10** Cladding temperature at 2.89 m. From the upper left, B-1, B-3 and B-4 are shown

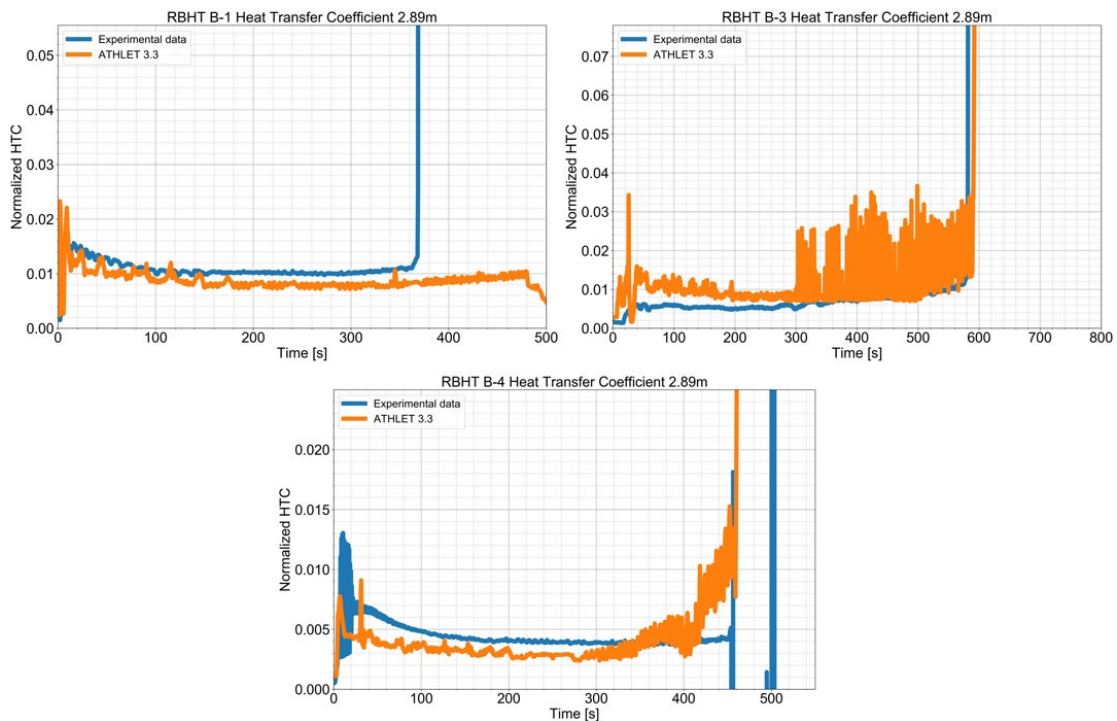


**Fig. 6.11** Heat transfer coefficient at 2.89 m. From the upper left, B-1, B-3 and B-4 are shown

For the test B-1, the quench front progresses too slowly and only reaches up below the point of maximum power. The other two tests are quenched early in the middle section of the bundle, as can be seen in Fig. 6.14.

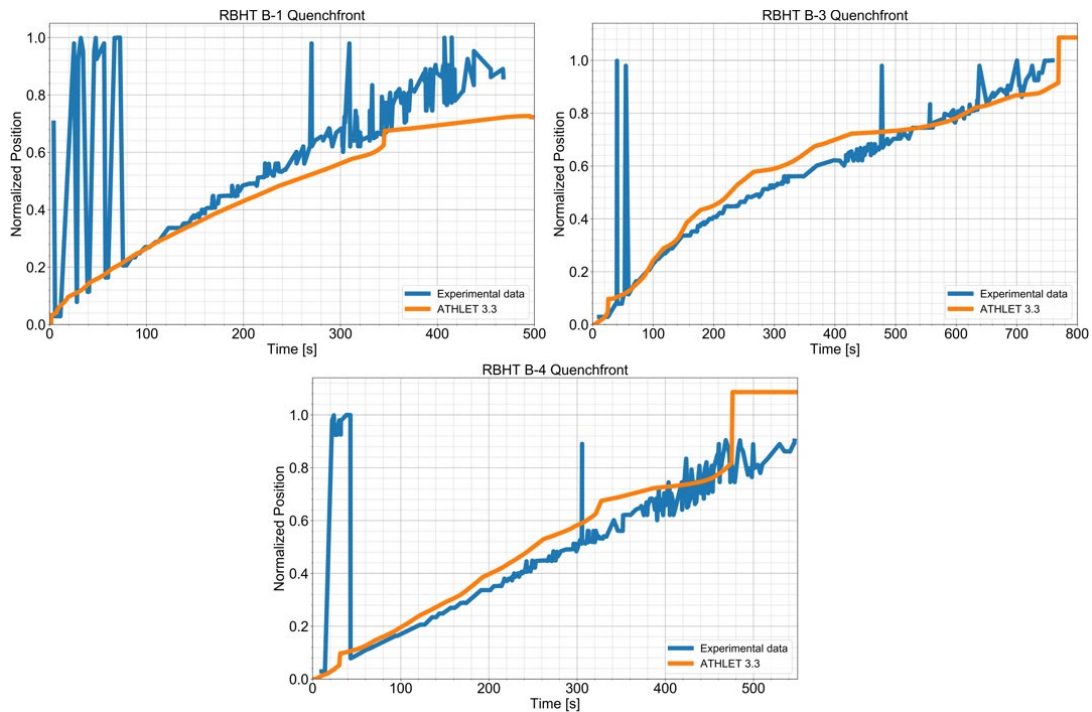


**Fig. 6.12** Quench front progression over the heated length. From the upper left, B-1, B-3 and B-4 are shown

The liquid carryover fraction behaves similarly to the open tests. The tests with higher coolant velocity show high carryover values early in the test and overestimate the amount of liquid leaving the test section over the whole reflooding process. The slower test B-3 also shows the initial overestimation, but then falls below experimental data. Near the end of the experiment, carryover values match the data for the tests B-1 and B-3, as depicted in Fig. 6.15.

In contrast, for the tests B-1 and B-3 the pressure drop over the bundle shows good agreement early in the test, then flattens fast in the simulation while the experiment shows a continuous increase, which results in a significant underestimation by the end of the test. The corresponding graphs are displayed in Fig. 6.16. This behaviour is similar to that known from the open tests. For test B-4, the discrepancy at the beginning of the transient is large. However, the physical reasons for the huge pressure drop measured at the test beginning are not clear.

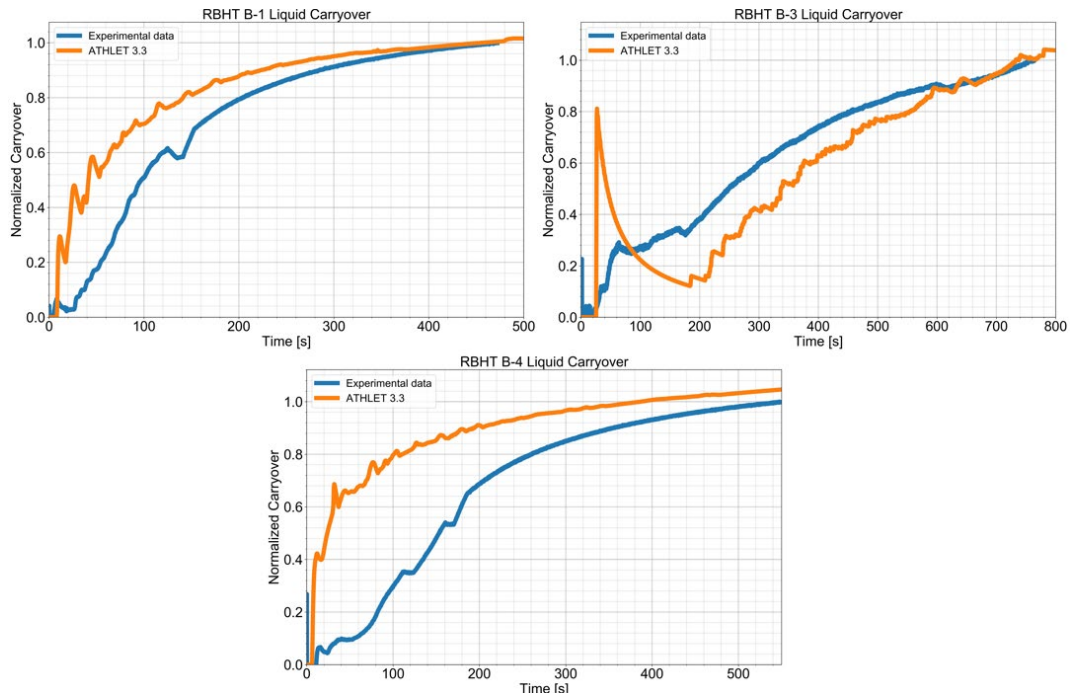


**Fig. 6.13** Liquid carryover fraction. From the upper left, B-1, B-3 and B-4 are shown

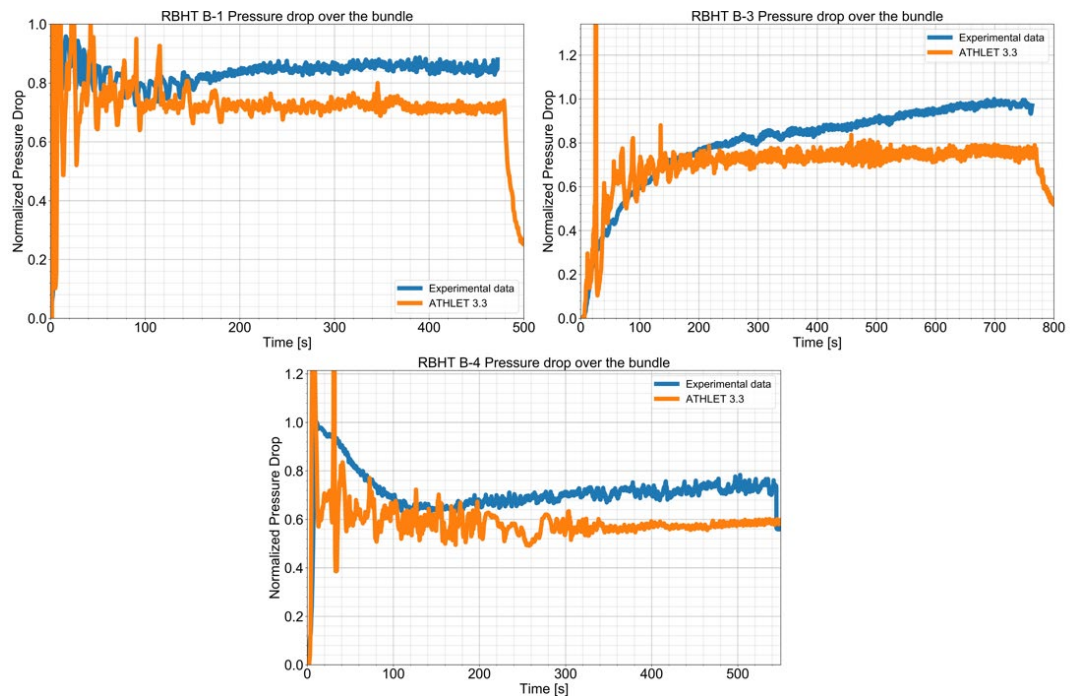


**Fig. 6.14** Pressure drop over the bundle. From the upper left, B-1, B-3 and B-4 are shown

### 6.2.1.12.2 Results for B-2 and B-6

In this section, uncertainty and sensitivity results for the tests B-2 and B-6 are presented. The plots for the uncertainty results contain the reference simulation and the

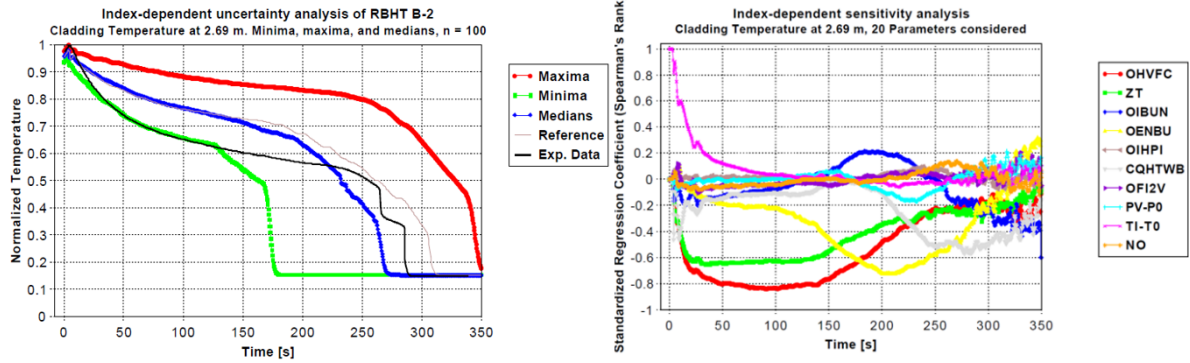
experimental data, as well as the lower uncertainty limit (minimum), upper uncertainty limit (maximum) and median results from the 100 variation simulations. The sensitivity plots show the Spearman's rank standardized regression coefficients of the ten most relevant out of the twenty uncertainty input parameters for the individual test. Positive values signify that the output parameter increases when the input increases (direct proportionality), negative values signify inverted proportionality.

Fig. 6.17 shows the cladding temperature at 2.69 m for test B-2. The experimental curve is within the uncertainty interval. For the first 120 seconds, the experimental data is near the lower uncertainty limit. The experimental curve continues to cool down slowly and then quenches between the median results and the reference calculation. The early phase of the reflooding experiment shows a strong precooling effect caused by entrained liquid, which the reference calculation could not reproduce to the extent observed in the experiment.

At the start of the test, the coolant inlet temperature is the parameter that affects the cladding temperature the most. Shortly after,  $OHVFC$ , the correction factor applied to forced convection to steam, and  $Z_T$ , the number of droplets in the vapour phase, begin to dominate. Then, at around 160 seconds,  $OENBU$ , correction factor for transition velocity for onset of entrainment, becomes more relevant. In the range of 200 to 250 seconds, the simulations reach the quench time and  $CQHTWB$ , the parameter describing the enhanced heat transfer at the quench front and controlling the velocity of the quench front propagation becomes the most influential parameter.

Similarly, Fig. 6.18 contains the results for the cladding temperature at 2.89 m. Here the precooling effect in the experiment is so strong, that the experimental data is outside of the uncertainty band. The predicted cladding temperature is significantly higher than the experimental one, though the number of droplets in the evaporation model was increased significantly according to observations from the open tests.

By looking at the sensitivities for this time span, we can infer that the forced convection to steam and the onset on liquid entrainment are the most influential parameters. Generally, the sensitivities are similar to the previous ones, except that the interfacial shear is more relevant and the effect of the quench front parameter is lessened.



**Fig. 6.15** Uncertainty and sensitivity results for the cladding temperature at 2.69 m in B-2

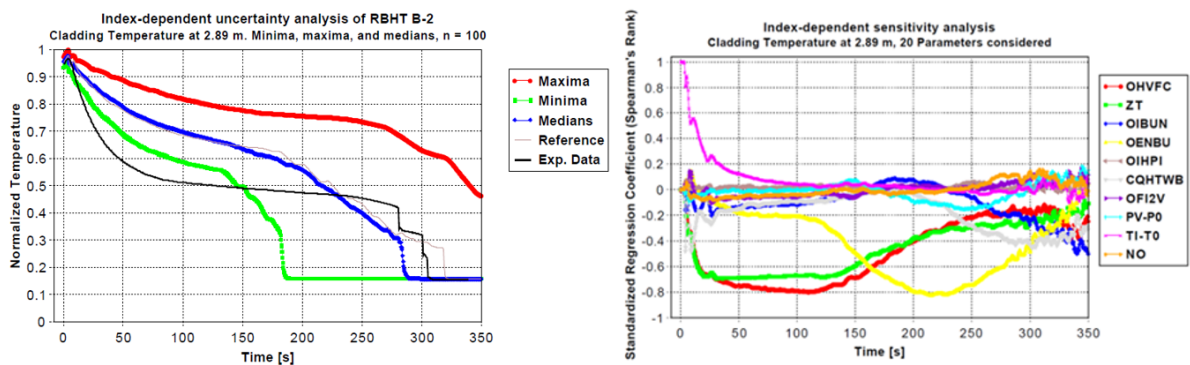


**Fig. 6.16** Uncertainty and sensitivity results for the cladding temperature at 2.89 m in B-2

Results for the pressure drop over the bundle are included in Fig. 6.19. We see that the pressure drop is underestimated by the reference calculation, as after the initial spike, the simulated value only increases slightly over the course of the test while experimental data rises significantly. A trend to underestimate pressure drops was already observed in the RBHT open tests as well as earlier simulations of reflooding tests /SKO 17/, /DÜN 22b/, /SKO 16/. The probable cause is an overestimation of the void fraction below the swell level, which is affected by interfacial shear. This assumption is supported by the strong effect of the interfacial shear represented by the correction factor  $O_{IBUN}$ . Other important parameters are the transition velocity for onset of entrainment and  $O_{FI2V}$ , the two-phase multiplier for the vertical flow. In the initial phase, the contribution of  $C_{QHTWB}$  can also be seen, strongly oscillating between high positive and negative values.

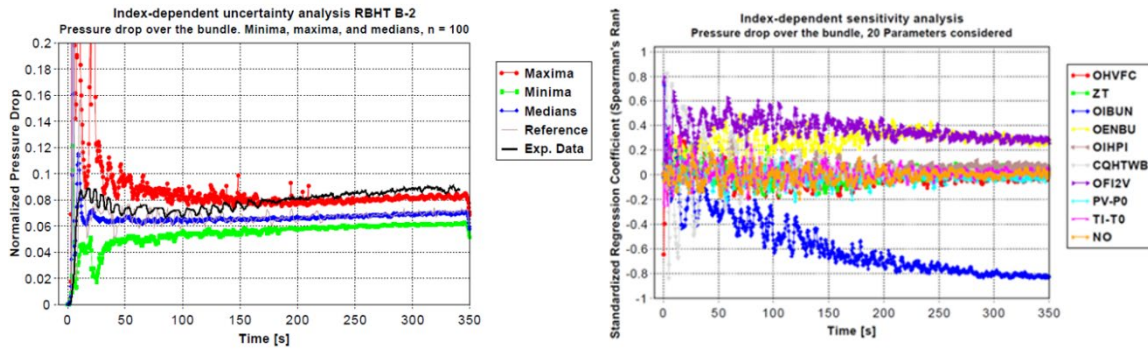


**Fig. 6.17** Uncertainty and sensitivity results for the pressure drop over the bundle in B-2

The quench front progression for test B-2 in the reference calculation is generally in good agreement with the experimental data, as can be seen in Fig. 6.20. Unsurprisingly, results are most strongly affected by the quench front parameter  $C_{QHTWB}$ . Quench front propagation is also influenced by the inlet liquid temperature at the beginning of the transient and onset of entrainment at the end of reflooding.

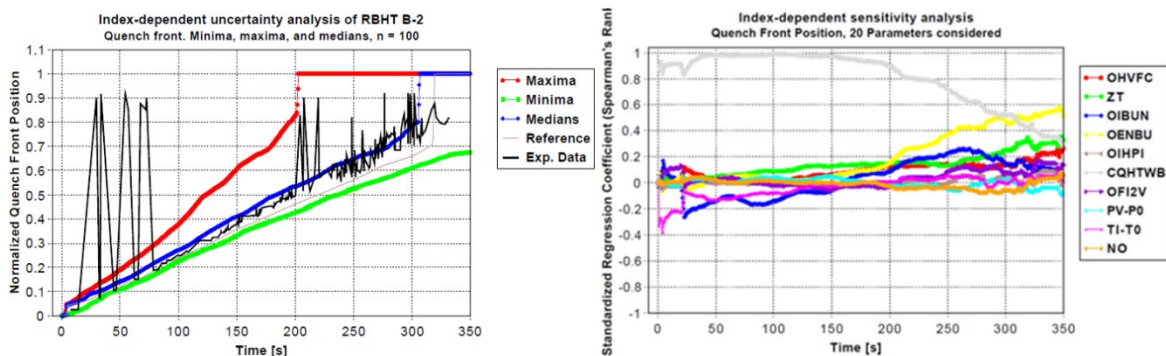


**Fig. 6.18** Uncertainty and sensitivity results for the quench front progression in B-2

Fig. 6.21 shows the liquid carryover fraction. The general trend of a strong early increase followed by a flattening as the bundle quenches is visible in the numeric data, but the experimental curve is below the uncertainty band for most of the test.

The sensitivity analysis shows that the carryover fraction is mainly affected by the nodalisation of the upper plenum and the drain system. The model of the upper plenum determines how quickly and effectively liquid is drained from the system. The parameters related to the onset of entrainment and the droplet number in the evaporation model have a relevant effect during the quenching. At the very beginning of the transient, the HTC at the quench front influences the carryover behaviour.

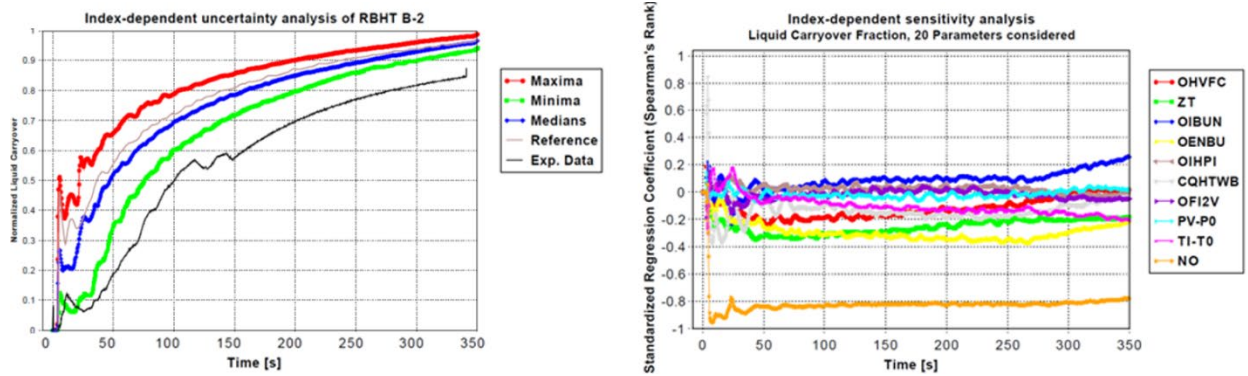


**Fig. 6.19** Uncertainty and sensitivity results for the liquid carryover fraction in B-2

Results for the test B-6 are shown in Fig. 6.22 to Fig. 6.26, beginning with the cladding temperature at 2.69 m in Fig. 6.22. In the test B-6 a lower coolant velocity than B-2 was used and as a result no strong precooling was observed. The predicted cladding temperature is in good agreement with the experimental curve. The peak cladding temperature is about the same as in the experiment but is reached about 20 seconds earlier. The reference calculation predicts quenching around 20 seconds before the experiment.

Similarly, to the B-2 sensitivities, the coolant inlet temperature is the most influential parameter at the beginning, but here it remains a relevant influence for longer. As precooling appears to be weaker in this test, the droplet number  $Z_T$  and the correction factor  $OHVFC$  to the convection to steam have a significantly lower, but still relevant influence. The most influential input uncertainties during the reflooding transient are the parameters related to the liquid entrainment,  $OIBUN$  and  $OENBU$ . It has to be noticed that the multiplication factor for the interfacial friction changes from inverted proportional to direct proportional at about 200 s.

For the cladding temperature at the higher point 2.89 m, we observe an overestimation of the peak cladding temperature in Fig. 6.23. The experimental data is outside (below) the uncertainty limit at the beginning of the transient when the PCT is reached in the simulation. In the simulation the PCT is obtained earlier than in the experiment and the temperature starts to decrease earlier. However, the quenching time agrees very well with the experiment. The most influential parameter is the liquid entrainment, and it is even more relevant than for the level 2.69 m, as the location is higher up and precooling from entrainment is more relevant. Contrary to that, the parameters related to heat transfer,  $Z_T$  and  $OHVFC$ , become less influential.

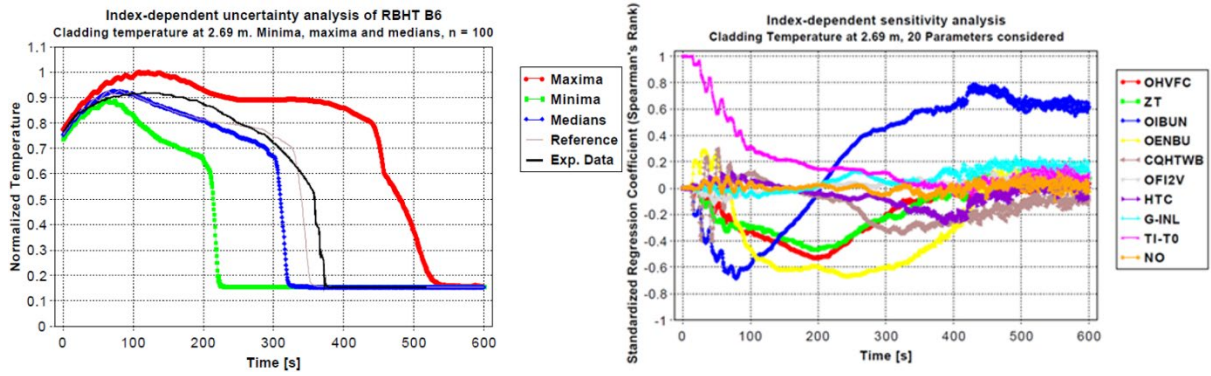


**Fig. 6.20** Uncertainty and sensitivity results for the cladding temperature at 2.69 m in B-6

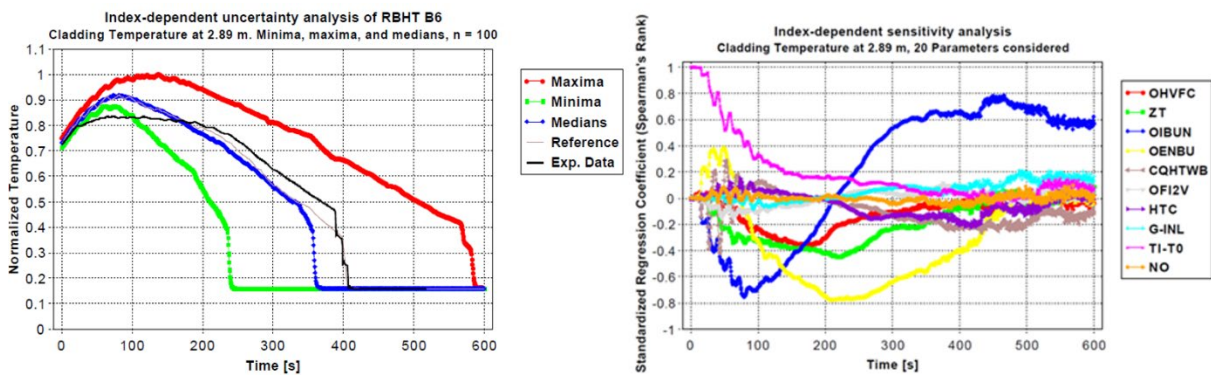


**Fig. 6.21** Uncertainty and sensitivity results for the cladding temperature at 2.89 m in B-6

Fig. 6.24 shows the pressure drop over the bundle for B-6. Except for the initial pressure spike, which is absent in B-6, the trend of the pressure drop is similar to B-2. After the first 100 s, the pressure drop basically stops to increase in the simulations, while it still rises in the experiment. The reference calculation underestimates the drop towards the end of the test, but the measured pressure drop remains within the uncertainty interval. Again, the most relevant parameter for the later phase of the transient is the interfacial shear in non-dispersed flow (below the quench front). Also, as in B-2, the inlet temperature and  $C_{QHTWB}$  have large, strongly oscillating coefficients in the early phase. Onset of entrainment,  $OENBU$ , has a significant contribution until most of the bundle is quenched.

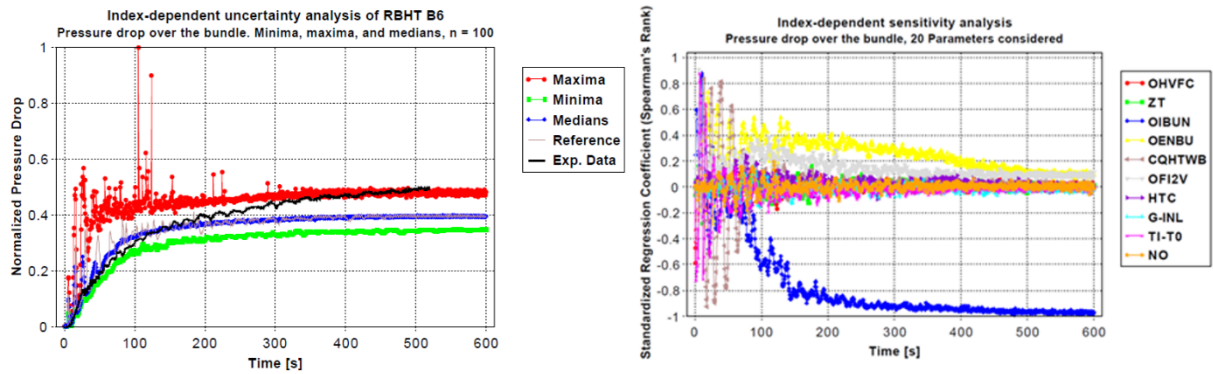


**Fig. 6.22** Uncertainty and sensitivity results for the pressure drop over the bundle in B-6

The quench front progression shows very good agreement between reference calculation and experimental data (see Fig. 6.25.). Only at the very beginning, the simulation shows a slightly faster quench front propagation than in the experiment.

For test B-6,  $CQHTWB$  is not as dominant as in the B-2 analysis. Its influence diminishes over the course of the transient whereas the parameters  $OIBUN$  and  $OENBU$  related to the liquid entrainment become more influential. Early on, variation of the coolant inlet temperature also has a strong effect on the quench front behaviour.

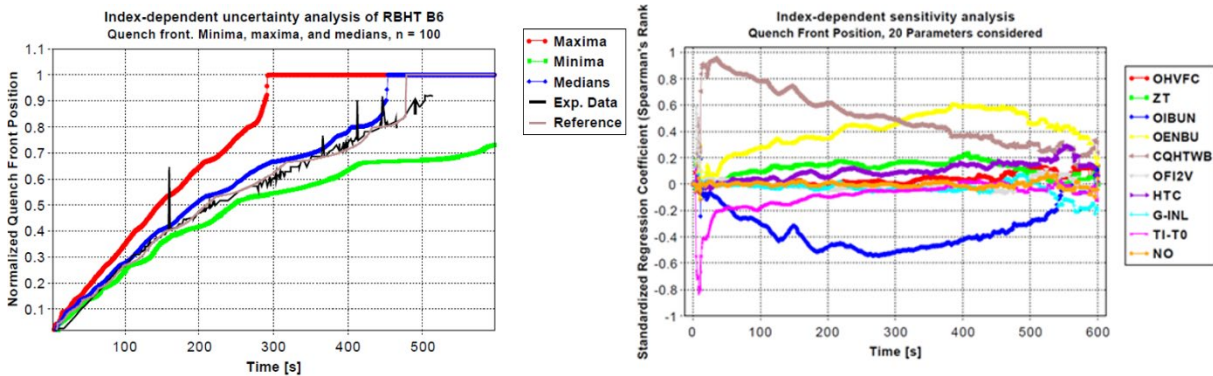


**Fig. 6.23** Uncertainty and sensitivity results for the quench front progression in B-6

Carryover data is presented in Fig. 6.26. In the early phase of the test, experimental data shows a high initial carryover spike, which is not present in the simulations and leaves the uncertainty band. This kind of behaviour is visible in the ATHLET data for B-3 and some of the open tests but did not occur for test B-6. It is not clear, why such a high carryover was measured in a test with a reflooding rate this low. For the other tests performed with similar coolant mass flows, such a large liquid carryover was not observed in the experiments.

After the spike, carryover is overpredicted by the reference calculation and the median results but remains above the lower boundary of the uncertainty band.

For most of the test, the modelling of the upper plenum is by far the most influential parameter, but especially in the early phase where carryover is underpredicted, onset on entrainment most strongly affects the simulation results. Also, the droplet number in the evaporation model influences the results during the transient to some extent. The onset of entrainment is responsible for the large amount of carried out liquid, but it is not clear, why the entrained fraction should be so large in a test this slow.

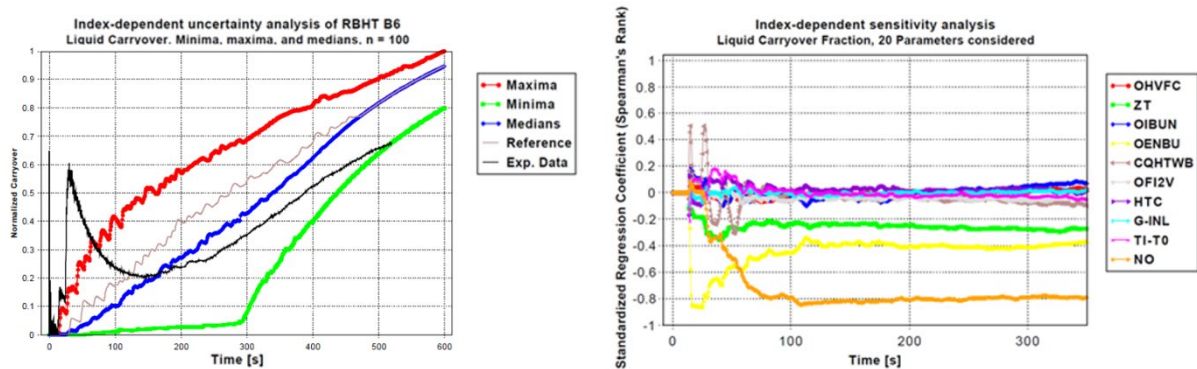


**Fig. 6.24** Uncertainty and sensitivity results for the liquid carryover fraction in B-6

### 6.2.1.13 Summary of results

Overall, the simulation results are satisfactory and generally reproduce the experimental trends. As can be seen when comparing the values of the recorded peak cladding temperatures in Fig. 6.27, all tests show good or excellent agreement. PCT for all tests occurred at the height of maximum power, which is also the case in the simulations.

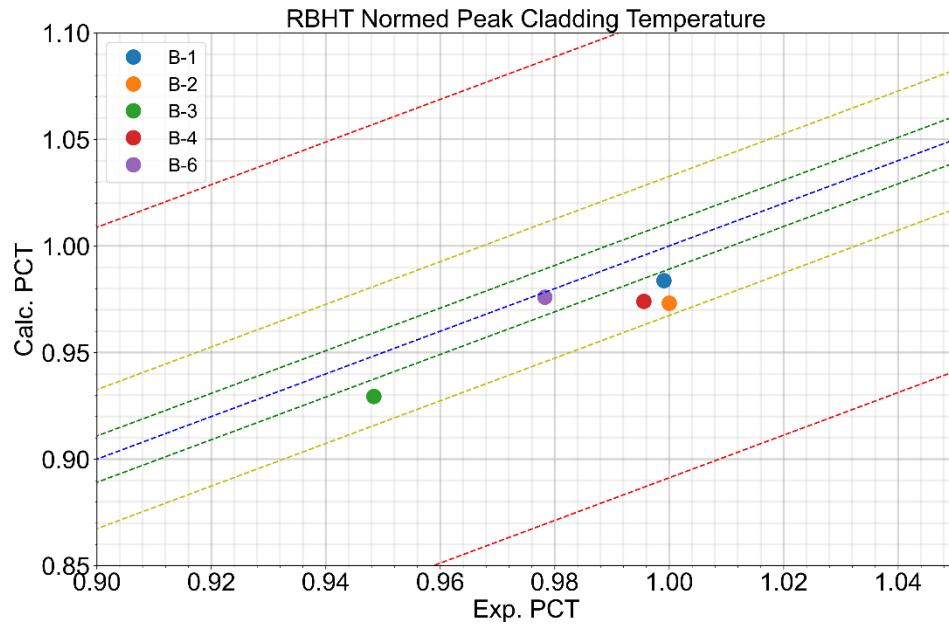


**Fig. 6.25** Comparison of simulated and experimental PCT data. From the middle to the outside, the dotted lines represent agreement rated as excellent (green), good (yellow) and fair (red)

Similarly, the quench time at the height of the PCT visible in Fig. 6.28 shows generally good to excellent agreement. B-4 is also close to good agreement. As the simulation of B-1 fails to quench at the height of the PCT, agreement is obviously poor.

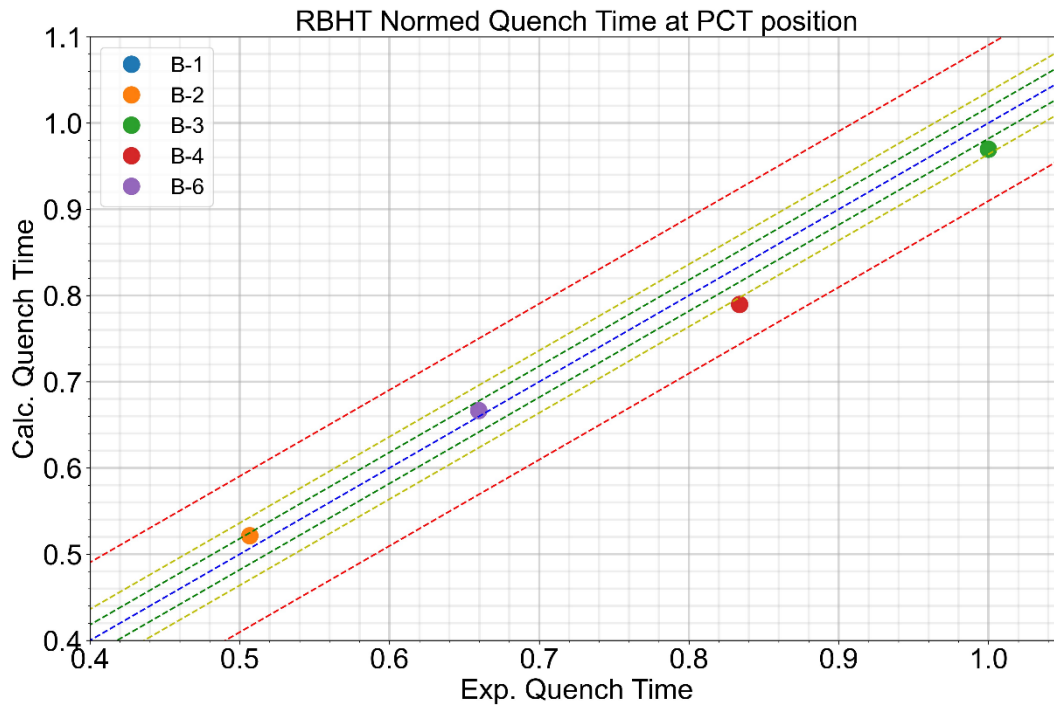


**Fig. 6.26** Comparison of simulated and experimental quench time at PCT height. From the middle to the outside, the dotted lines represent excellent, good and fair agreement

Finally, the liquid carryover at the time of the PCT quench can be seen in Fig. 6.29, where B-4 is the only test displaying excellent performance. The other three test narrowly overshoot the deviation limit of 10 %. As test B-1 fails to quench, the prediction of the carryover at quench time is considered poor. However, around the time of the experimental quench the numerical carryover value is actually in very good agreement with the experiment.

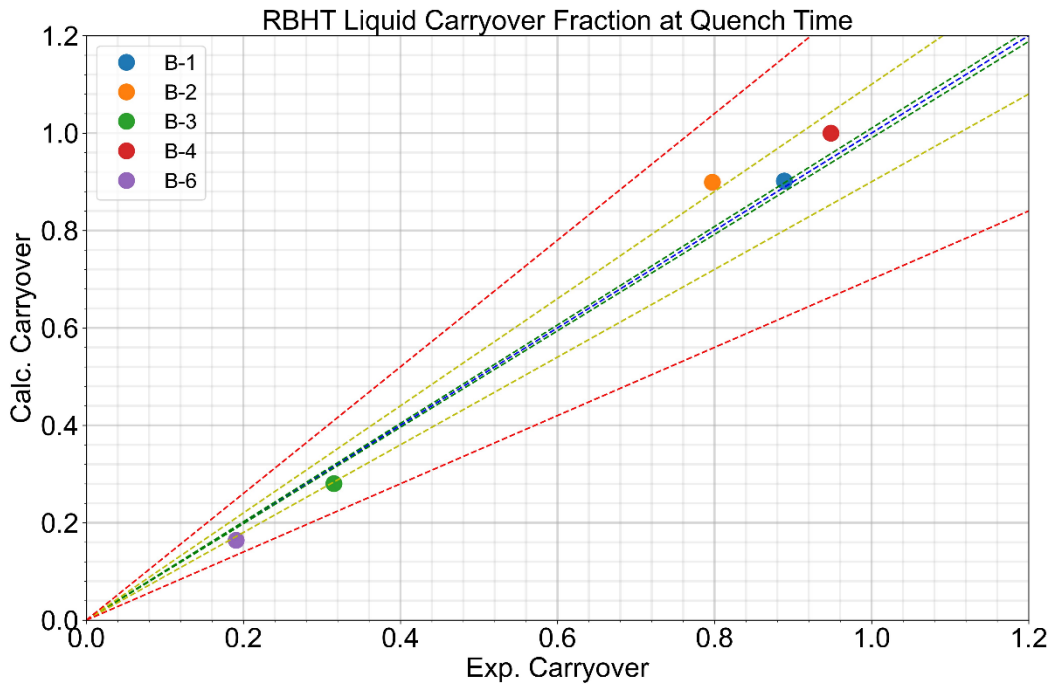


**Fig. 6.27** Comparison of simulated and experimental liquid carryover at quench time of the PCT height. From the middle to the outside, the dotted lines represent excellent, good and fair agreement

Summarizing the graphs shown in the results section, figures of merit and characteristic trends are generally well predicted. However, B-1, B-2 and B-4 showed precooling effects in the experimental data of the cladding temperatures, which were not adequately reproduced in the simulations. Temperature trends in B-3 and B-6 were generally better predicted.

Except for test B-1, which failed to quench the entire bundle, quench front behaviour was well predicted. Especially B-6 showed excellent agreement for the quench front progression over the whole bundle.

As with the open tests, the simulations of the blind tests consistently underestimate the pressure drop over the bundle in the later phase of the experiments. Sensitivity analysis supports the earlier supposition that this underestimation is strongly linked to the interfacial friction.

### 6.2.2 Cooperation within FONESYS

Another point of work concerns collaboration within the international network FONESYS (The FORum & NETwork of SYStem Thermal-Hydraulic Codes in Nuclear Reactor

Thermal-Hydraulics) /AHN 15/. Together with the FONESYS partners, several papers were submitted to the NURETH-19 conference. The publications were related to the benchmark on pressure drop and flow regime transitions in horizontal pipes using experiments from the TPTF and Mantilla test facilities /LAN 22b/, /LAN 22a/, /LAN 22c/. In addition, a separate GRS contribution was prepared for NURETH-19 that highlighted the recalculations of the TPTF and Mantilla experiments and the ATHLET model developments carried out in this context /LEE 22b/. A supplementary journal publication by GRS was included in *Nuclear Engineering and Design* /LEE 22b/.

### **6.2.3 Water-steam material properties library SBTL95**

The new material properties library for water-steam SBTL95 (developed by HSZG) was successfully integrated into the ATHLET main development line. The library, which provides more accurate material data than the ATHLET standard property package – particularly for under-pressure conditions – was implemented as a plug-in that can be optionally invoked by the user. The SBTL95 library is available since the ATHLET 3.3 program version.

GRS closely cooperated with the Hochschule Zittau-Görlitz (HSZG) to continuously improve the calculation of material properties in ATHLET. HSZG developed the SBTL95 library for ATHLET to calculate the material properties of water and steam. The library is hosted on a GitLab server operated by GRS to support joint, bilateral program development with partner institutes. With the release of AC<sup>2</sup>-2021/ATHLET 3.3.0, the SBTL95 library was made available to all users for the first time. Minor bugs that occurred in the interim application (e.g., for pressures in the range of the critical pressure) were corrected by HSZG and the improved code was made available to the users by patched ATHLET code versions.

GRS itself has extended the communication between the ATHLET code and the SBTL95 library. ATHLET now receives and interprets error codes from the SBTL95 so that any problems occurring during the SBTL95 execution can be recognized and evaluated. E.g., if the properties calculation in the SBTL95 library fails, ATHLET automatically reduces the time step size and repeats the property calculation. If this measure turns out to be not successful, ATHLET stops the calculation with a meaningful error message.

#### **6.2.4 Modelling of helically coiled heat exchanger**

Dedicated heat transfer and pressure loss correlations were investigated, implemented and verified in the course of ATHLET code development performed at PSS RUB /KRI 23/, /KRI 22/. The implementation was based on ATHLET's compact heat exchanger model approach that was introduced with the code release version 3.4.0. After comprehensive code review, refactoring, and validation, the implementation for helically coiled heat exchangers was transferred to the ATHLET main development branch, documented in the ATHLET manuals and released with ATHLET 3.4.0 /SCH 23a/. Following models were included:

- convective heat transfer to vapour for heating surface acc. to Mori-Nakayama inside helically shaped tubes /MOR 67/
- convective heat transfer to liquid for heating surface acc. to Mori-Nakayama inside helically shaped tubes /MOR 67/
- convective heat transfer to liquid for cooling surface acc. to Zukauskas outside helically shaped bundles /ŽUK 72/

Pressure drop correlations for turbulent flow inside helically shaped tubes as well as for both laminar and turbulent flow outside helically shaped bundles were also implemented. But due to persisting numerical issues, these correlations were deactivated in ATHLET 3.4.0 and, thus, are currently not invoked for the simulation of a helically coiled heat exchanger.

#### **6.2.5 Virtual international AC<sup>2</sup> user meeting 2021**

After completion and general release of the new program version AC<sup>2</sup> 2021 (contains ATHLET 3.3.0), a user meeting was held as an online event (as a consequence of the Covid pandemic) to inform users about the new features and the progress of the AC<sup>2</sup> program development. Around 70 users from various countries and organizations took part in the meeting. Among other things, innovations in ATHLET and its software tools like the newly developed, python-based Batchplot plotting tool were presented /SCH 21b/, /JAC 21/ by GRS.

### **6.2.6 Hybrid international AC<sup>2</sup> user meeting 2023**

An important aspect of the past project was the close cooperation with ATHLET users and GRS-external program developers in order to incorporate their experience into current and future program development and make it accessible to all users. To ensure an intensive exchange and effective utilisation of external findings, the three-days hybrid AC<sup>2</sup> user meeting 2023 was held at the premises of GRS Garching in November 2023. About 130 colleagues from German and international research institutions, universities, technical safety organisations and authorities participated (in person or remote) in the meeting. In about 30 presentations the recent developments, validation results and application experiences related to AC<sup>2</sup> were overviewed by GRS and external code users and developers. Several presentations were prepared to summarize new models and features included in ATHLET 3.4.0, which is part of the code release AC<sup>2</sup> 2023 /SCH 23b/, /WIE 23/, /DI 23/, /JUN 23/. Numerous bilateral contacts, particularly with German research institutions (e.g., HSZG and HZDR) were maintained and program users were advised in their application of ATHLET. Overall, the user meeting provided a comprehensive overview of the current performance and applicability of ATHLET to nuclear applications.

## **7 Cross-sectional tasks**

### **7.1 Quality assurance**

#### **7.1.1 Build process**

The CMake-based build mechanism used in ATHLET was further elaborated. Runtime libraries were automatically made available via CMake (Intel Fortran, MS VS CRT). This helped the developers and the CI to create portable builds. In addition, CMake scripts were created to compile plug-ins without usage of the ATHLET source code. This was important for users outside of GRS who use the prepared plug-ins as a basis for their own program developments. The scripts are delivered to the end users via the AC<sup>2</sup>-2023 setup file.

The source code of the ATHLET postprocessing tools was transferred from SVN to Git and the repository was cleaned up. The build process of the software tools was standardized: all utilities were converted to CMake, which enables a) clean compilation without manual intervention, and b) simple inclusion in the AC<sup>2</sup> setup for program distribution. Automated tool builds were executed in the CI. The build process for the ATHLET Input Graphic (AIG-2) was also converted to CMake so that automated builds can be generated in the CI.

Various metadata information was embedded in ATHLET and attached to the output files to improve the later traceability of performed simulation calculations. The metadata include version information such as the Git Commit SHA used, C++/Fortran compiler version, date of the last change in the source code, and information about the system on which the program was compiled. If ATHLET is created automatically in the GitLab CI, the data also contain the URL to the corresponding build job, from which further information can be obtained if required. This means that even unnamed pre-release versions can be distributed (internally) without additional maintenance effort and can still be precisely assigned and reproduced if required.

Further work was related to the maintenance of the GitLab AC<sup>2</sup> distribution project. E.g., the codes FENNECS, PEMTY and ATLASneo were included, so that they could be distributed with the AC<sup>2</sup> 2023.0 package. From the distribution project, several AC<sup>2</sup> pre-

release versions (beta, release candidate) were created for program validation, and the final package of AC<sup>2</sup> 2023 was built for distribution to all program users.

Concerning the used Fortran compiler, Intel announced that their ifort compiler will be deprecated in 2024 and should be replaced by their recently released ifx compiler as successor. As ifort is the current default Fortran compiler for AC<sup>2</sup>, it is necessary to move from ifort to ifx on occasion. In order to do so, several tests with ifx were performed, code was adapted, and feedback was shared with Intel. Currently AC<sup>2</sup> is well prepared for a smooth transition for the next major release.

### **7.1.2 Refactoring**

The ATHLET system code is continuously developed by GRS. In accordance with new demands resulting from experience of the program application, and new capabilities of the IT infrastructure, compilers, etc., adjustments are regularly made to the code design and parts of the program are modernized in terms of both implementation and content. The continuous refactoring of the source code is an important contribution to the quality assurance of the program development. In addition, since these efforts improve code readability, this work also ensures the future expandability of the program and the reduction of vulnerability to programming errors.

In this context, the ATHLET condensation model was revised and slightly corrected. A non-converging iteration loop, which was used to determine the penetration depth (a parameter required for the calculation of the condensation rate based on the surface renewal theory) was completely removed, and the code change was checked against various validation calculations. For comparison, an alternative model for the penetration depth was implemented. The new model has also been tested and can be optionally invoked via an input parameter.

Further recent measures related to refactoring:

- De-allocation of no longer used global arrays at the end of the SSC.
- A substantial part of obsolescent Fortran language features were removed from the code, e.g., "arithmetic if" or "computed goto".

- The Fortran77-specific intrinsic functions for different data types, which were still used in Fortran90), like e.g., `dmax1` or `dsqrt`, were changed to their generic intrinsic variants like *max*, *min*, or *sqrt*.
- The declaration of arguments of ATHLET procedures were extended by suitable intent attributes.
- For utilizing procedure interface checks by the compiler effectively and for avoiding programming errors, most ATHLET procedures have been integrated as sub-modules into existing or newly defined modules. They are added into procedures via use statements. Where this was not feasible for some reason, explicit interface blocks have been added wherever possible.
- Argument aliasing for dummy parameters of a procedures, which are called with the same variable as actual argument, has been removed unless explicitly allowed by current Fortran standards. Specifically, any aliasing must not involve dummy arguments that are not explicitly declared with the `intent(in)` attribute.
- ATHLET was checked for a set of input decks utilizing a range of models using the program `valgrind /VAL 20/` with regard to errors in the assignment of variables during runtime. A number of instances were identified, where unassigned variables influenced the program flow or were written into output. These cases were analysed, and the underlying errors were corrected, in most cases by explicitly initializing variables or by changing intent attributes.
- A direct access to the AITEXT array for the effective input cards or directly modifying the current array position for this array outside of the dedicated service procedures was removed from most input procedures. To this end, additional service procedures for moving in the AITEXT array have been defined.
- Refactoring for NC gas model: Previously, the values of the NC gases were stored in special, multi-dimensional data types, which caused problems in terms of access speed and, hence, numerical performance. The data types were converted into "standard" two-dimensional arrays.
- By default, ATHLET receives various command line arguments at startup, including an ID that is used as the naming prefix for the generated output files. The so-called compatibility mode for starting ATHLET, in which two IDs (problem ID and run ID) were passed as an alternative - actually a functionality of earlier ATHLET program versions that was kept for a transition period - has now been deactivated

and removed from the source code. This avoids future maintenance work and reduces vulnerability to errors when interpreting the command line arguments.

### **7.1.3 Continuous integration (proposal for new title: Regression testing as part of continuous integration)**

To ensure that ATHLET works correctly and to identify possible side effects and errors in extensions or changes to ATHLET at an early stage, regular test calculations are conducted. These have so far been automated using the Jenkins software system for execution and evaluation. Since the ATHLET source code is now hosted on a Gitlab server, which also automates the complete release process, the goal is to also perform all tests necessary for quality assurance automatically via Gitlab. For this purpose, Gitlab features its own "Continuous Integration" module called Gitlab-CI. This offers the possibility, for example, to automatically compile ATHLET and conduct initial standard tests after each change during development, or to perform and evaluate a larger number of verification and validation calculations. The latter is especially necessary for quality assurance before the release of a new program version. In the past project period, in addition to the already existing automatic compilation and setup creation, automatic testing and evaluation of the standard validation cases were added. In this regard, to tackle the needs for quality insurance discussed above, the CI capabilities of GitLab have been exploited to build an automated testing process of ATHLET, i.e., a proper and true regression testing pipeline for ATHLET. For the sake of completeness, some details on the layout of such a pipeline, as well as its conceptual scheme are introduced in the following.

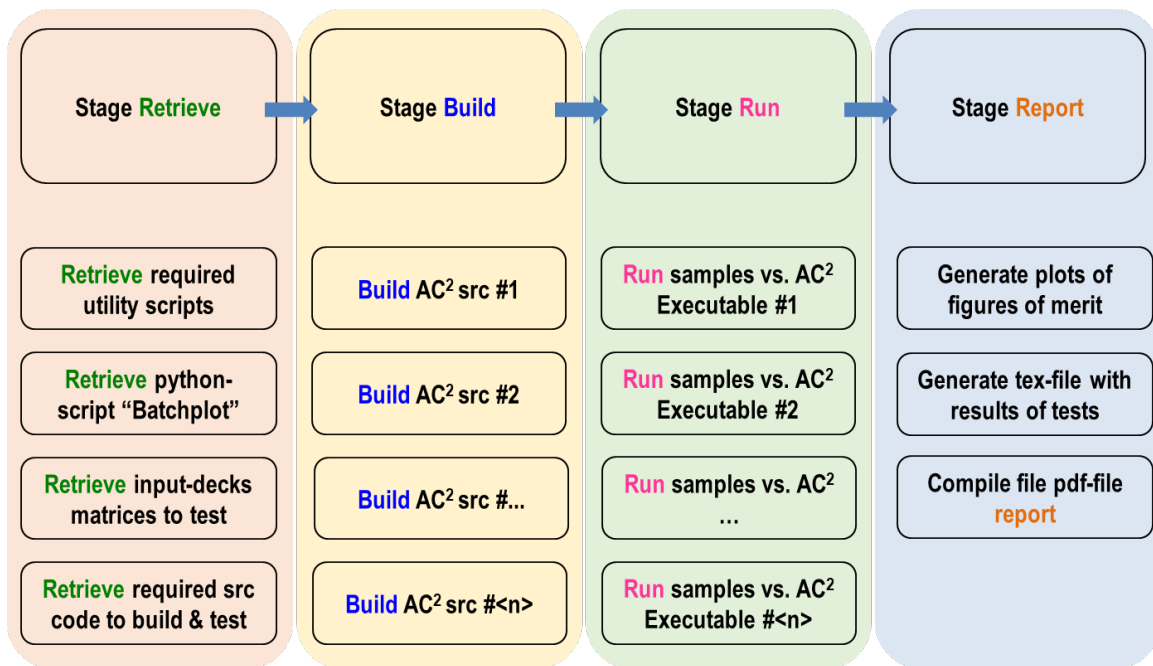


**Fig. 7.1** Conceptual scheme of Gitlab-CI pipeline

As shown in Fig. 7.1, the pipeline involves several tasks executed either sequentially or in parallel. These tasks are grouped into "stages" that determine the execution priority:

- The first stage, "Retrieve", involves retrieving all utility and plotting scripts necessary for the verification and validation activities. This stage also includes gathering the datasets making up the validation matrix for ATHLET, as well as any code sources needed for building and using ATHLET for verification and validation purposes.
- The second stage, "Build", is conditionally executed based on the need to build a user-defined version of ATHLET for testing, whether for development or release purposes. If the ATHLET versions required are already available from a previous release, the existing executables are used directly in the calculation stage (stage "Run" as referred in Fig. 7.1), and stage "Build" is skipped.
- The third stage, "Run", executes ATHLET calculations for all pre-specified executable versions against all cases in the predefined validation matrix. To minimize the total execution time of this stage, calculations are initiated in parallel by Gitlab-CI, depending on the available computing capacity.
- The fourth stage, "Report", involves processing the results from previous calculations, generating plots for the figures of merit for each case in the validation matrix, and comparing them with results from an ATHLET reference version

and/or measurement data, as available. The generated plots are automatically compiled into test reports and saved as PDF documents.

The pipeline, as outlined above, can be executed on demand on both Linux and Windows systems.

For demonstration purposes, an application of the pipeline as executed during the preparation phase of the recent 2023 release of the ATHLET is described in the following. On this occasion, the pipeline was used both for the code verification, through a code-to-code comparison with the previous 2021 version, and for the code validation against the experimental data from the ROSA-III (a scaled model of a 3500 MW BWR/6-251 reactor). As the modifications made were not intended to introduce any variations in terms of the quality of prediction for the selected test, i.e., a simulated LOCA scenario, the continuity in the predictive capability of the code was expected.

For the selected application, the ROSA-III Run 916 test was analytically replicated using the first release candidate of the 2023 AC<sup>2</sup> ATHLET code and the older official 2021 release. The test results, captured as figures of merit such as coolant temperatures at various core positions, and temperature profiles of the hottest fuel rods, see Fig. 7.2, as well as differential pressures across the recirculating pump, and other numerical indexes such as the number of time steps and Jacobian updates, see Fig. 7.3.

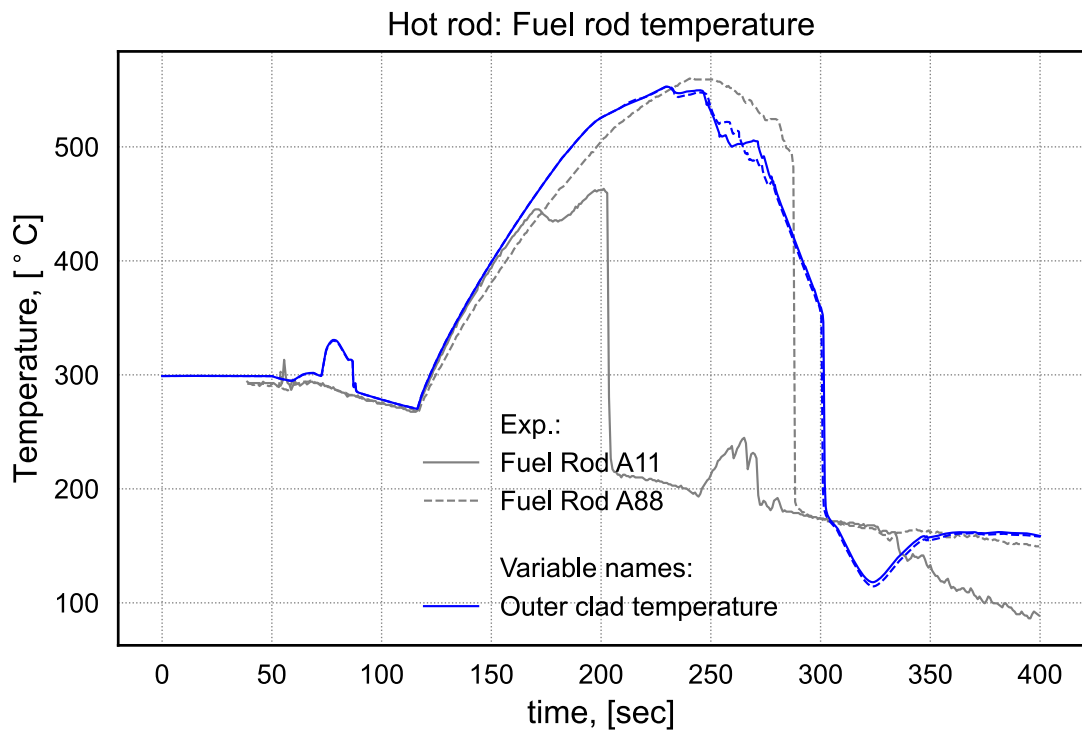
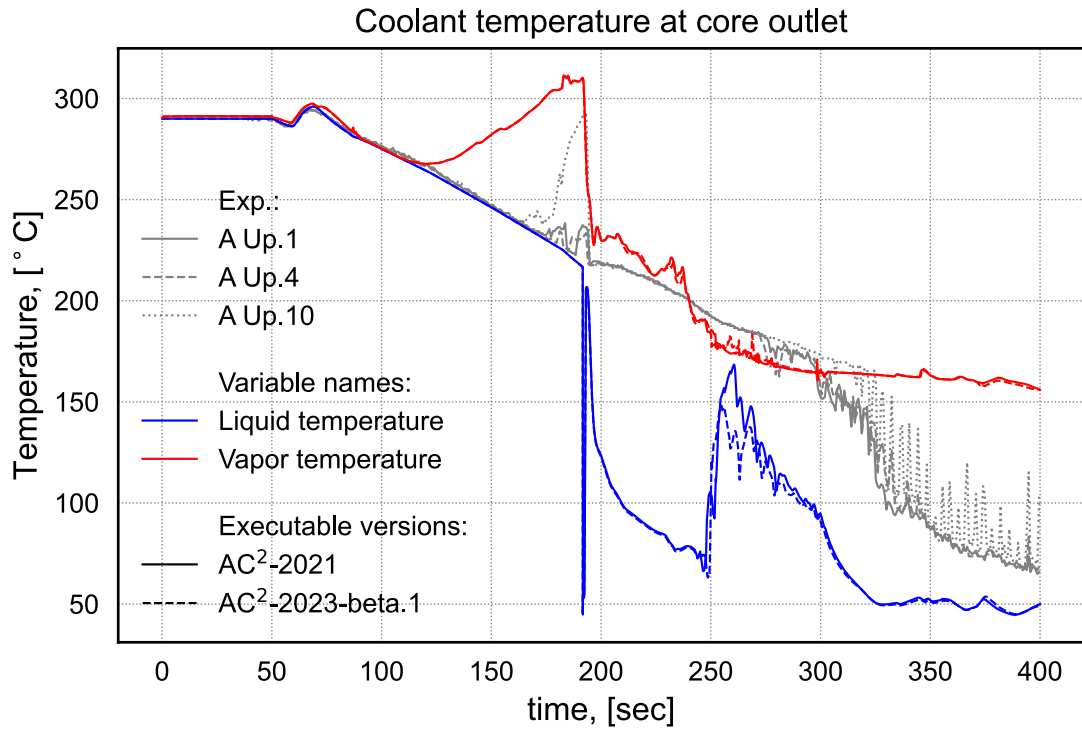


**Fig. 7.2** Pipeline application to ROSA-III test: Coolant temperature at core outlet, and hot rod fuel temperature

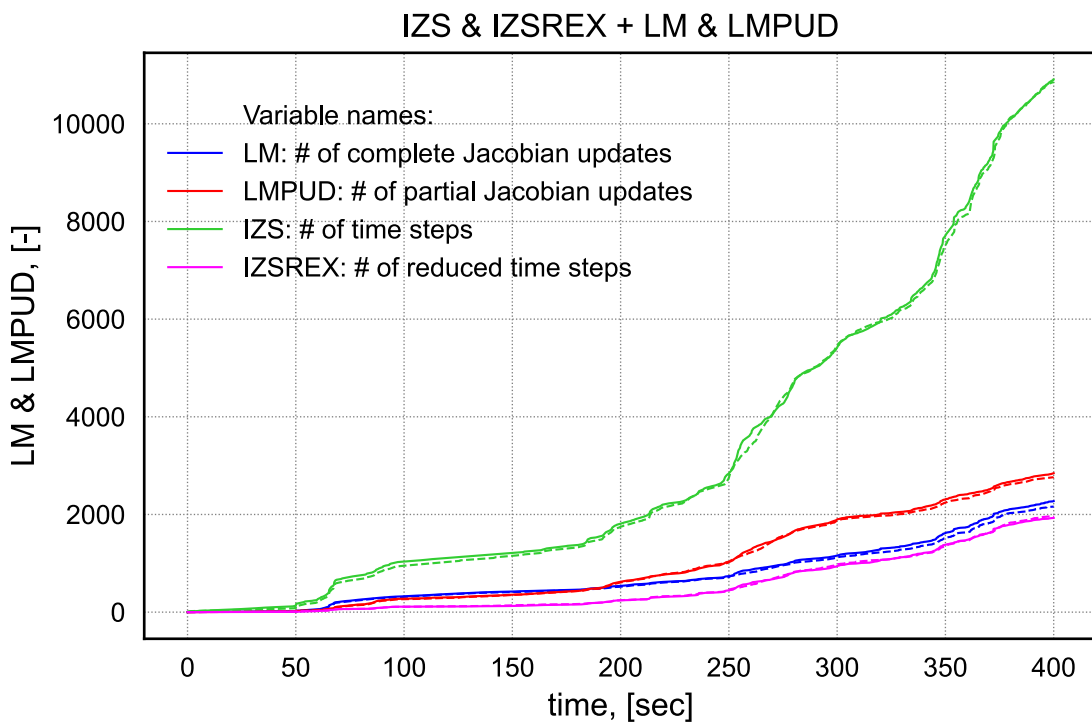
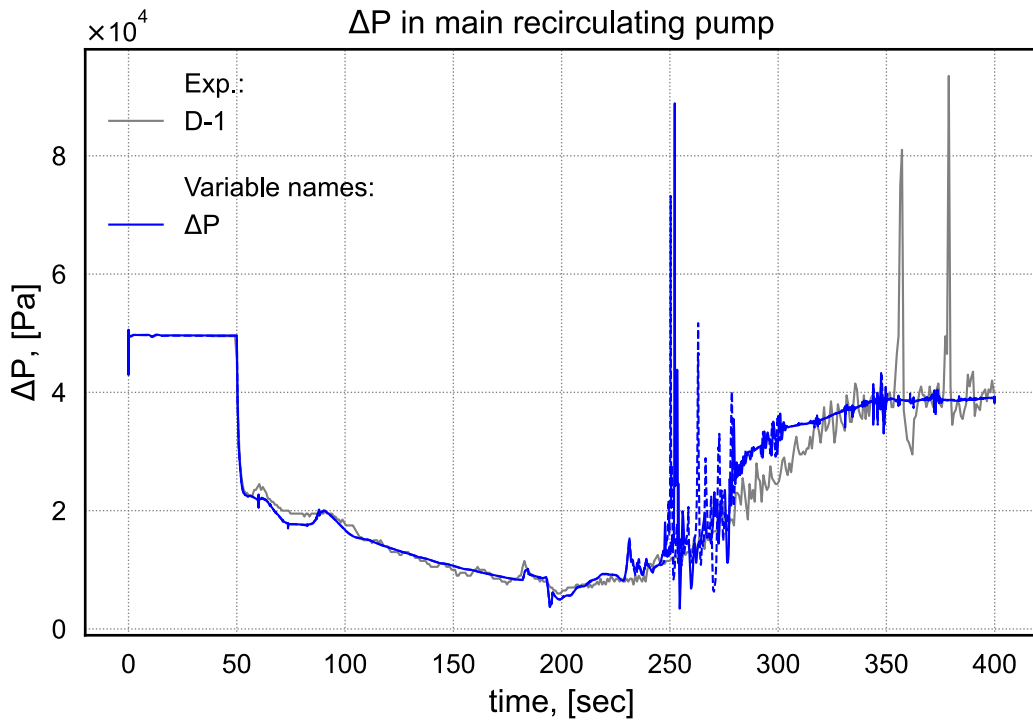


**Fig. 7.3** Pipeline application to ROSA-III test:  $\Delta P$  at recirculating pump heads, and numerical indexes, e.g., Jacobian updates and time step number

The results of the comparison automatically carried out by the pipeline showed good agreement between the simulated trends with both the older and newer versions of

ATHLET as well as against the experimental outcomes, indicating, as a matter of fact, the expected continuity in predictive capabilities.

The regression testing pipeline introduced above has proven effective in supporting the validation of ATHLET by allowing for automatic early detection of code's inconsistencies, therefore, providing important hints for eventual bug fixes to incorporate in the upcoming release. Although the current pipeline layout is effective, there is room for further enhancements. For instance:

- A key area for improvement is the expansion of graphical comparison capabilities, currently limited to time-dependent trends, introducing spatial plots for validation efforts could be particularly beneficial. Such enhancements could include generating graphical comparisons at specific time points for axial profiles of fuel rods and coolant channels, or spatial plots of key system variables in different reactor sections like the cold and hot legs of Light Water Reactors (LWRs), or in the downcomer.
- There is also a need to automate consistency checks for key system variables, particularly in restart cases, to ensure the code reliability. Systematically integrating these checks into the pipeline's configuration would enhance its consistency and effectiveness.

Overall, the ongoing efforts to continuously extend the pipeline to include more tests, verification, and validation cases, and to configure pipelines tailored for specific tasks within the AC<sup>2</sup> quality assurance process, aim to significantly enhance its utility and effectiveness.

## **7.2 Documentation**

The ATHLET program documentation package consisting of the User's Manual, Models and Methods Manual, Validation Manual, Programmer's Manual, and Program Updates Manual was updated for the releases of the new program versions ATHLET 3.3 and ATHLET 3.4. For the automatically generated documentation of the ATHLET source code, the description of the global variables has been supplemented or corrected where necessary. Parts of the manuals, which were previously edited and created using the Quicksilver Interleaf software, were transferred to MS Word. With version ATHLET 3.4, the ATHLET Input Data Description is generated from a LaTeX document.

The existing python scripts, which automatically generate the source code documentation in the Programmer's Manual including information about the module variables and the dependencies within the ATHLET source code, have been adapted and further improved.

- The classification of subroutine arguments as I (input), O (output), U (updated) or X (not used) was previously based exclusively on a separate source code analysis by the scripts. A known weakness here was that it was not tracked how such a variable might be used in a further subroutine call, so that in this case it was always assumed that it would be changed in the subroutine, which is not always the case and led to incorrect classifications. As the use of INTENT specifications for subroutine arguments is now standard in the ATHLET source code, these INTENT specifications are evaluated by the scripts with priority over their own source code analysis. This change has led to a significant reduction in incorrect classifications and therefore helps developers.
- Some of the global variables can be accessed, e.g., by plug-ins (they are referred to be “visible”) or can be used as process signals in the GCSM section of an input deck. By analyzing the source code, the information of visibility and accessibility via GCSM could be extracted and was added to the code documentation. The generated documentation supports both code developers and (experienced) code users.

### **7.3 Release management**

During the project period, several new program versions were finalized, extensively validated, generally released and distributed to program users with a valid AC<sup>2</sup> program license via the AC<sup>2</sup> User Area. Related program versions are ATHLET 3.3.0 (included in AC<sup>2</sup> 2021), the patch ATHLET 3.3.1 (AC<sup>2</sup> 2021.1), the current program version ATHLET 3.4.0 (AC<sup>2</sup> 2023), and the recent patch ATHLET 3.4.1 (AC<sup>2</sup> 2023.2).

#### **7.3.1 Code versions ATHLET 3.3.x**

The code version ATHLET 3.3.0 /AUS 21/ was released in November 2021 and included following new and improved features:

New models and features in TFD module:

- New evaporation model for mixture level with a more realistic consideration of impact of NC gases
- Modified ML condensation model
- Improved modelling of entrainment fraction (based on Pan-Hanratty) and of onset of entrainment for horizontal pipes
- Additional transport equations for solutes (mainly thought for analysis of zinc-borate issue after LOCA)
- Modelling of zinc release from internals (for gratings in containment)
- New vertical bundle drift option for small-size test facility bundle
- New gas components available: CO and CO<sub>2</sub>
- Updated thermodynamic properties of NC gases. In order to ensure consistency, specific gas constants are now calculated from molecular weights.
- Adaptation of boron transport model
- Calculation of flow losses in bulk condensation model to determine condensation rate corrected.
- Modified formulation of so-called water-level force (2M model) to consider the geometric impact of varying collapsed levels along a horizontal pipe.

New features in HECU module:

- Flow instability ratio according to Whittle-Forgan as plot quantity available (mainly for research reactors)
- Cladding oxidation model extended for FeCrAl (ATF)
- New CHF correlation according to Sudo and Kaminaga added; mainly for research reactors and fuel assemblies with narrow rectangular flow channels.
- If wall temperature exceeds Leidenfrost temperature, a modified fluid reference temperature is derived for heat transfer calculation.
- Dedicated heat transfer correlations for thermosiphons according to Gross (condensation) and Imura (evaporation) implemented (selectable via input parameters  $IHTC4L/R$  and  $HTC7L/R$ , resp.)

- Bundle factor for heat transfer in hexagonal bundles according to Inayatov added.
- Special heat transfer correlations for laminar, wavy and turbulent film condensation within vertical tubes, selectable via input parameter `IHTC4L/R`
- Slightly modified calculation of transition boiling heat transfer in order to enable earlier rewetting for those HCVs that didn't reach film boiling before

New feature in NEUKIN module:

- Additional thermal-hydraulic feedback reactivities available, mainly for liquid-metal cooled reactors: thermal cladding expansion feedback, thermal fluid or structure expansion feedback for any TFO or HCO

New feature concerning numerical solver:

- NuT – if activated – is used during SSC as well.

Improved component models:

- Condenser model with NC gases: Condensation of inflowing vapor is limited to saturation pressure at present liquid temperature.
- Separator model: For flooded separator and ML inside the dome, the distribution of carry-over steam mass flow is adjusted. Non-separated steam is directed to lowermost CV (below mixture level) of separator dome instead to separator exit branch.
- Separator model: The distribution of separated carry-under liquid mass flow below/above mixture level in separator outlet branch is corrected. Former implementation could result in (low frequency) oscillations of the mixture level in the separator outlet branch.
- Time-Dependent Volume (TDV): New optional input (`PW CORRLIMIT`) to limit or skip pressure and enthalpy adjustments after SSC

Plug-ins:

- New plug-in for water-steam material properties according to IAPWS-95 standard with increased accuracy mainly in the range of low pressure ( $\leq 1$  bar). Plugin is activated under `CW PLUGIN` writing "sbtI95" and is employed if light water is working fluid.

- Additional non-boiling model working fluids added to plug-in MPEXT.
- Coupling via HCO-surface (e.g., with COCOSYS) improved
- CFD coupling interface expanded to NC gases.

The patch ATHLET 3.3.1 /AUS 22/, which was released in October 2022, comprises various program corrections, concerning e.g.:

- Mixture gas component AIR-N2O2: Initialization of Nitrogen and Oxygen mass fractions after SSC corrected.
- GCSM predictor-corrector integration: The block-specific setting INTEK=2 resulted in an erroneous calculation of controllers of types SWITCH, TSSWITCH and INTE used in the respective GCSM block.
- Summarizing print output at the end of a run: Improved implementation to avoid negative entries for CPU time in the “CPU STATISTICS” (relevant for long running jobs only).

An important new feature provided with the patch was an additional plug-in interface that enables the user to couple own correlations for condensation heat transfer.

### 7.3.2 Code versions ATHLET 3.4.x

ATHLET 3.4.0 /SCH 23c/, the latest major code release, contains numerous program enhancements, which have been generally distributed for the first time and thus made available to all users. In particular, the following new developments are included:

New models and features in Thermo-Fluidynamics module

- Dedicated form loss correlations for bend and contraction. The correlations can be invoked using the new CW FORMLOSS.
- New CW FORMLOSS for specification of Re-number dependent flow losses via input table.
- 3D-model combined with mixture level model, e.g., for the simulation of water pools: The momentum flux calculation for horizontal flows at mixture level elevation (i.e., for junctions connected to CVs including the mixture level) has been modified, so that full acceleration loss is calculated now.

- Pressure drop correlations for plate heat exchanger geometry. The model is activated by the new PW `HTEXDEF` under CW `STEAMGEN`.
- CoolProp fluid properties library coupled via controller approach. An example python controller script is part of the AC<sup>2</sup> distribution.
- For T-junctions: pressure loss/increase in main pipe considered for 2M (6-equation) model.
- T-junction model also applicable together with 2M model (validation is on-going).
- Improved implementation of subcooled boiling at low void fraction to mitigate mass conservation error
- Initialization of arbitrary NC gas mixtures in single TFOs and complete TFD-systems enabled (new PW `INITXVNC` under CW `MULTICOMP`)
- Solute transport model considers maximum filter capacity for removal of a solute component.
- Slightly modified bulk condensation model: now, the penetration depth is non-iteratively calculated using the HTC from renewal theory; in addition, a new option `IGVK=5` has been introduced to calculate the penetration depth by the Gilliland and Sherwood correlation.

#### New models and features in HECU module:

- New heat transfer correlations for helically coiled heat exchanger: The model can be activated by the new PW `HTEXDEF` under CW `STEAMGEN`.
- Multiplication factor `OHWFC` for convective heat transfer to liquid (CW `MODELUNC` – for uncertainty and sensitivity analyses) is used for all working fluids now (was restricted to water and sodium before).
- Corrected bundle factor calculation for hexagonal bundles according to Inayatov. The correlation for hexagonal bundles is consistently used in all heat transfer levels now.
- New CHF correlation proposed by Song et al.: Can be activated by input parameters `ICH1` and `ICH6`.
- Optionally, user-defined SW may be used under CW `HEATCOND` to group the HCOs. This option can be used to easily switch on/off a group of HCOs.

- Heat transfer correlations for plate heat exchanger. The model is activated by the new PW `HTEXDEF` under CW `STEAMGEN`.
- A radial power distribution inside the power generating material zone of a rod can be optionally specified using the new PW `RADPOW`.
- New correlations for the simulation of austenitic and ferritic steels oxidation
- Extended input checks: Power profile under CW `ROD` has to be provided for the complete length of the HCO.

#### New features in GCSM:

- In addition to water, the controller `GPROP` can be applied now to other boiling working fluids (sodium, potassium) as well. The controller provides thermodynamic quantities like density, specific heat capacity, etc. for subcooled, saturated, and superheated conditions.
- The capability of the controller was extended: Additional quantities like partial derivatives of thermodynamic quantities can be calculated.

#### Plug-ins

- HDF5 writer plug-in supports SWMR (Single Writer Multiple Reader) mode now. That feature can be activated via `-swmr` command line argument or `AC2_USE_SWMR` environment variable. In general, the SWMR mode enables writing and reading an HDF5 file in parallel. By default it is false. Not supported by ATLASneo yet.
- The interface for heat transfer to supercritical water included in the `MHTCEXT` plug-in has been modified. Additional parameters are provided to the routine `MHTCEXTSC`: bulk viscosity, specific heat capacity and heat conductivity (can e.g., be used to calculate Re and Pr numbers)
- The interface for convective heat transfer to liquid included in the `MHTCEXT` plug-in is no longer limited to the working fluid water but can be used for any working fluid to employ external htc correlations.
- `MHCHFEXT` plug-in for user-provided CHF correlations extended by an interface routine for 'external fluid', invoked by the CoolProp library.

- MHTCEXT plug-in: interface `mhtcext_pdo` for user-provided film boiling htc correlation added. User-provided HTC correlation can be invoked by `IHTC1L/R<0` or `IHTC2L/R<0`.
- The MHTCEXT plug-in was corrected, so that it can be employed together with the parallel program version, too.
- Updated hdf5-writer plug-in with new CMake-file, required due to compatibility issues with ATHLET-CD and COCOSYS

#### Further general program improvements

- HDF5 file expanded by units for plot variables and TFO / HCO geometry data.
- Unit information for process signals added to key-file (used by ATLAS).
- Restart data have been extended, e.g., by data required for Reynolds number dependent form losses and by GCSM control signal parameters `IOPT`, `GAIN` and `A1` to `A4`. As a consequence of this, restart data files generated with former ATHLET versions aren't compatible and cannot be used together with ATHLET 3.4.
- Input data deviations from recommended values according to the Input Data Description are written to the `.log` file.
- Compatibility mode to start ATHLET with both arguments `problem-ID` and `run-ID` (the standard command line syntax of ATHLET 3.1 and earlier code versions) was removed.
- The names of some plot variables have been changed. Changes refer to names that included a backslash, which was mainly used for some NC gas variables. The backslash was substituted by an underscore. E.g.: `RMVMC/001` has been changed to `RMVMC_1`. As can be seen, leading zeros have been omitted as well for better readability. Please adjust existing post-processing files (`design` or `.atl` files), if one of the modified variable names is used.  
The changes became necessary, since a slash is typically used in the hdf5 format as string separator.
- Improved "Minor Time Step Edit": The print output per time step provides information on the differential equation or physical model responsible for a time step limitation and now includes information from ATHLET-CD as well.

- Input format under CW `MIXLEVEL` has changed: if more than one mixture level is defined for one TFO, the two records for the first mixture level have to be input before the two records for the second ML and so on (instead of first input record alternating for all ML before second input record alternating for all ML, as it was before).
- Recalculation of CDR1D critical discharge tables: The decision to recalculate the tables is now taken on the basis of a string-to-string comparison (instead of a numerical comparison) between the input under `CDR1DIN` and `CDR1DTAB`. This ensures the recalculation also in case of only small changes to the input values.
- Extended input checks on validity of provided `IHTC*L/R` options.
- The print output was improved, so that the name of the used CHF correlation is given now. The name was missing so far, if the correlation was employed beyond general validity bounds defined in ATHLET (print output “outside limits”).
- Extended input error checks: The syntax of the input deck has to be in accordance with the input data description. Now, the input deck is widely checked for validity and order of KW and/or PW given under the various CW available for ATHLET (and ATHLET-CD). Spurious input is detected.
- New PW `PRNT_INPUT` under CW `SERVICES` available to control the output of the input data set with parameters substituted by their values.
- Control print and plot data amount under `GENERAL`, `MONITOR` and `TFDGENERAL` by the input parameter `IOUT0` (CW `OBJECTCON`)
- Refactoring and removal of Fortran statements declared as obsolescent in Fortran 95 to prevent compiler warnings.
- Option `PLOT_SSC` enabled for datasets that don't include any HCO.
- Output at the end of the .out-file with regard to FEBE and HXX statistics expanded.
- Optional user-defined SW under CW `PARAMETERS` to structure and switch-on/off parts of the parameters section

The patch ATHLET 3.4.1 was released together with AC<sup>2</sup> 2023.2 in May 2024 and includes some minor program fixes /SCH 24/.

## 7.4 User area and code transfer

The released ATHLET program versions were distributed to all users with a corresponding program licence via the AC<sup>2</sup> user area. Since the release of ATHLET 3.3 (AC<sup>2</sup>-2021) in autumn 2021, the program has been distributed to almost 30 organizations. ATHLET 3.4 (AC<sup>2</sup>-2023) has been distributed to around 10 organizations since its program release in December 2023.

The main purpose of the user area is to facilitate the communication between the AC<sup>2</sup> development team and external code users. In addition to access-restricted sites for code transfer or file exchange, it also offers discussion forums for exchanging user experiences. The user area has been continuously maintained. This work includes continuous updates of the content and the structure of the web pages as well as the dedicated user and access rights management. The publications of ATHLET developers and users were collected and compiled in the user area in order to achieve greater transparency with regard to the program's range of applications and capabilities and to intensify the mutual exchange of experience - not least among program users. In addition, the migration of the user area from the preceding software basis Open Atrium, for which support was discontinued in 2021, to the new platform with Drupal (public part, see Fig. 7.4) and MS Sharepoint (download area with user administration) was completed.

ATHLET is composed of several basic modules for the simulation of the fundamental, multiphysical phenomena involved in the operation of a nuclear reactor, including thermo-fluid dynamics, heat conduction and heat transfer, neutron kinetics as well as control and balance-of-plant, supplemented by an implicit numerical time integration method. Other independent modules such as 3D neutron kinetic codes, Computational Fluid Dynamics (CFD) codes or the GRS containment simulator [COCOSYS](#) can be coupled by means of suitable interfaces. For the analysis of beyond design-basis accidents with core degradation, the extended code [ATHLET-CD](#) is applicable.

### Thermalhydraulics

The thermal fluid dynamic model of ATHLET is based on a six-equation two fluid model with fully separated

**Fig. 7.4** Layout of new AC<sup>2</sup> user area, based on Drupal

## 8 Conclusions and outlook

GRS develops, validates, and distributes the AC<sup>2</sup> program package, consisting of the system codes ATHLET, ATHLET-CD and COCOSYS and other tools such as the ATLAS simulator software to enable the investigation of current reactor safety issues. AC<sup>2</sup> is used to analyse states of normal and abnormal operation, incidents and accidents in reactor plants and other nuclear facilities.

The main subject of the project at hand was the improvement of AC<sup>2</sup>'s thermal-hydraulic system code ATHLET in order to keep pace with and to further develop the state of science and technology and to enable the user community to perform safety analysis for existing and future nuclear reactors in accordance with the latest state of knowledge. To this end, firstly the code's functionality was extended to cope with the increasing modelling demands of existing reactors, innovative light water reactor designs, and SMRs. Furthermore, to achieve targeted and efficient code development, sharing of experience with all program users as well as common code developments with national partners were successfully intensified, and the cooperation in international working groups like the FONESYS network or the OECD/NEA RBHT project was strengthened. Measurements to ensure the quality of the program development were expanded and new, comprehensively validated ATHLET code versions were released and distributed to the program users.

### **Unified flow regime maps and newly considered flow regimes**

The introduction of a central flow regime map module represents a significant advancement in the ATHLET development process, aiming to consolidate the existing implementation. In addition to the consistent use of flow pattern information and associated closure equations in the models of interphase friction, mass and energy exchange, the calculation of additional variables such as the entrainment fraction, which was previously determined inconsistently and on a model-specific basis, was also standardized.

In general, the software distinguishes between flow regime maps for vertical pipes, vertical bundles, and horizontal or horizontally inclined pipes. The central module has been expanded to allow for the use of separate flow regime maps depending on the prevailing heat transfer conditions at the wall. This development enabled the introduction of specific flow patterns and transition criteria for conditions characterized by wall conden-

sation, which differ from adiabatic flows. Additionally, a general interpolation routine was implemented to facilitate a smooth transition between two or more flow pattern maps.

The newly derived and implemented flow regime maps are based on both established maps from the literature as well as the previous implementation from ATHLET, which has been validated in the past and shown to be capable to produce acceptable results for many applications. However, notable discrepancies were identified between the current ATHLET flow pattern map and the well-established maps, e.g., by Taitel et al., particularly in the context of flows within vertical pipes. In connection to that, deficiencies in the modelling of the interfacial shear in vertical geometry, mainly in the transition range between slug and annular flow, were encountered in validation calculations against experiments from the Harwell LOTUS facility. It is therefore recommended that other flow regime maps and transition criteria should be included in ATHLET and investigated in the future. The centralized flow regime map module provides an optimally prepared environment for conducting such investigations.

The new implementation could already be satisfactorily verified against several applications, but a more comprehensive validation is still outstanding. The topic will be revisited in project phase B, where the implementation of flow regimes maps and closure equations for post-CHF states will be undertaken, which are characterized by inverted flow patterns that exhibit significant differences to adiabatic flows. In this context the further consolidation of the existing implementation is envisaged.

The development of the centralized flow regime map module has the potential to advance the modelling in ATHLET to a new level. On the one hand, existing flow regime maps in ATHLET can be easily extended to consider additional flow regimes that are crucial for the adequate representation of certain phenomena (like annular flow in passive heat exchanger pipes), on the other hand, further ATHLET models like, e.g., the evaporation model, which doesn't include a detailed distinction of flow regimes so far, can make use of the available flow regime information in the future to achieve more accurate predictions.

### **OECD/NEA RBHT project**

The series of reflooding experiments performed at the NRC/PSU RBHT test facility located at Pennsylvania State University, USA, were intended for the validation of system code models related to reflooding simulation. By participating in the OECD/NEA project

RBHT, the GRS gained access to new and detailed experimental data for code validation. Evaluation of blind calculations performed in the frame of the benchmark focused on parameters relevant to quench front model validation, such as cladding temperatures at different core elevations, pressure drop along the test section, and quench front progression.

Overall, the simulation results were satisfactory and generally reproduced the experimental trends. The changes to the two-phase evaporation heat transfer implemented in ATHLET 3.3 positively affected the calculated PCT, so that all tests showed good or excellent agreement. Furthermore, PCT for all tests occurred at the height of maximum power, which was also the case in the simulations. The quench time at the height of the PCT and the quench front progression were generally well predicted by ATHLET, although one calculation failed to simulate the quenching of the entire bundle.

Minor deviations between experiment and simulation were found (for some test phases) with regard to the liquid carryover, which was overestimated by ATHLET, and to the bundle precooling, which could not always be satisfactorily reproduced by the code. The underestimation of the pressure drop over the bundle that has been already observed earlier for the open tests is still present in the blind results.

Finally, uncertainty and sensitivity analyses were performed for two RBHT tests using the GRS statistical software SUSAS 4.2. The effect of uncertainties in the code models, facility modelling, and experimental conditions was examined, and the most influential parameters were determined in order to derive recommendations for the future development of reflooding modelling with ATHLET. Concerning the precooling effect that was observed in some tests and that could not adequately be simulated by ATHLET, the forced convection to steam heat transfer and the onset of liquid entrainment were found to be the most influential parameters. The latter, as well as the droplet number in the evaporation model, had also a relevant effect on the liquid carryover, which was partly overestimated in the simulations. The visible trend to underestimate pressure drops is most likely related to an overestimation of the void fraction below the swell level, which is affected by bundle interfacial shear in non-dispersed flow below the quench front.

From these findings it can be concluded that the models related to the simulation of dispers droplet flow, e.g., the entrainment calculation and the evaporation heat transfer, should be revisited, since, overall, they contribute most to the uncertainties found for cladding precooling and liquid carryover. In addition, due to the consistent

underprediction of the bundle pressure drop, the interfacial shear model should be reviewed. This also confirms the assumed shortcomings of the interfacial shear calculation for vertical flow that were derived on the basis results achieved for LOTUS test calculations above.

It is intended to revisit the RBHT experiment in phase B of the project and to use these experiences and results for an improved vertical flow modelling in heated geometries under post-CHF conditions. Furthermore, GRS will also participate in the RBHT-II project that will focus on thermal-hydraulic phenomena and conditions that, in the first project phase, proved to be difficult for the codes to simulate. To this end, re-flood tests at low and variable flow rates will be performed to obtain high-resolution droplet field and steam temperature and velocity data.

### **Thermal-hydraulic modelling**

Another area of development was the enhancement of the two-phase models of ATHLET. In order to simulate pipe branchings, a so-called T-junction model was implemented to simulate the complex flow and phase distribution as well as the pressure loss in the area of a branch-off. The flow partitioning is a multidimensional phenomenon that is challenging to predict correctly using a one-dimensional code. In the previous version of ATHLET a dedicated T-junction model for the 5-equation system has already been included. This model produced satisfactory and stable numerical results for several applications, but it also exhibited shortcomings and modelling gaps. Thus, the new model, developed as an extension to the 6-equation system, now incorporates a correlation for the pressure loss and recovery in the main line, which wasn't considered before. The new model has proven effective for both horizontal and vertical upward branchings, yielding comparable or even superior validation results to those of the previous model. However, in the case of a downward-directed branching, the older model achieved superior results, so that, consequently, the code will automatically switch to the older model for those applications. The T-junction related implementation has already been fully integrated into the current ATHLET release. However, it is expected that further model enhancements may be made based on the results of future validation.

In regard to the simulation of form losses, the user of ATHLET was previously constrained to provide constant zeta values in the input dataset. This is, in principle, a simplification that ignores the dependence of the flow losses on the Reynolds number. The degree of error increases with the magnitude of the Reynolds number variations during

the investigated transient. Accordingly, this is of particular significance for the modelling of passive systems, which exhibit a gradual start-up behavior with transition from laminar to turbulent flow, which is accompanied by a significant change of zeta values. Additionally, the start-up behavior is highly dependent on the precise modelling of the pressure losses, particularly in the absence of driving forces. In light of the aforementioned considerations, ATHLET was extended by the possibility of accounting for the Reynolds number dependency of form losses. To this end, two key elements were incorporated in the code: firstly, the correlations for the determination of form losses in specific geometries, such as bends and orifices, were implemented; and secondly, the option to specify tabulated data with zeta values versus Reynolds numbers was established.

Furthermore, the latest version of ATHLET includes a new, dedicated model for simulating compact heat exchangers. This model comprises one- and two-phase heat transfer correlations for plate and helical heat exchangers, thereby enhancing the predictive accuracy of ATHLET for passive safety systems in advanced light water reactors and SMRs.

### **Fuel rod model**

Given that in the past, safety analyses conducted with ATHLET have occasionally yielded elevated (too conservatively estimated) cladding temperatures, it became necessary to enhance ATHLET's thermo-mechanical modelling of the reactor core. To this end, the existing fuel rod model was updated and extended with a thermo-mechanical model that is capable of reproducing the burn-up-dependent densification and swelling of the pellets, as well as the radial relocation of fuel material. Furthermore, a new gap conductance model was implemented, which enables more detailed simulations of open and closed gaps. Finally, the code was complemented by a model for consideration of a radial power profile within the pellet in order to adequately represent high-burnup fuel states. The validation of the new fuel rod model against the Halden BWR experiment provided satisfactory results. The implementation is now serving as the basis for further code developments in the context of the unification of the ATHLET and ATHLET-CD rod models, which is being pursued in project UMRS1606.

### **User friendliness and cooperation**

Another key focus of the project was put on continuously enhancing the usability of ATHLET and strengthening the modelling basis according to the demands of new

applications. These developments often resulted from the regular exchange with the numerous ATHLET users. For instance, the AC<sup>2</sup> User Meetings, held every two years, provided valuable insight into users' preferences for model extensions as well as into model gaps or weaknesses. These user experiences were used to improve several models, like the condenser model and the heat transfer calculation in the post-CHF regime. Further input data error checks and expanded program outputs were also added to provide the user with more comprehensive information. All these developments ensure that ATHLET can be applied more flexibly to different types of reactor designs and make the code more robust against input data errors, also reducing the user effect.

GRS also cooperated with other system code developing organizations in the frame of the international FONESYS network. Biannual meetings were held for the purpose of exchanging information, subjecting current developments to critical reviews, and conducting joint benchmarks exercises. The latter not only provided additional experimental data for program validation but also enabled the identification of potential for further code improvement. This work will continue in phase B of the project.

The overarching objective of the project was to provide the numerous ATHLET users with extended, quality-assured program versions that allow for investigations of current safety-related issues in existing facilities and new reactor designs. For that purpose, two new code versions were released and distributed during the project period: ATHLET 3.3 in the 2021 and ATHLET 3.4 in 2023. These versions contain a significant number of new features and developments, which were subjected to comprehensive quality assurance procedures before their integration into the main development branch of ATHLET. The general release of the next AC<sup>2</sup> program version is scheduled for autumn 2025. The upcoming ATHLET version will incorporate recent developments from RS1600, thereby ensuring its availability to all program users.

### **Concluding remarks**

Overall, the main objectives of phase A of the project with regard to model improvements, quality assurance, and national and international cooperation have been successfully achieved. However, not all developments are completed, which is why further development of ATHLET will continue. This is necessary to meet new requirements from program application and to close existing model gaps related to evolutionary and innovative reactor designs. Some of the work initiated during the project's phase A will be continued in phase B. For instance, the central flow regime map module will be expanded

for post-CHF states, and the GRS participation in the RBHT project will continue in its second phase. Additionally, the work related to user support, code maintenance, and release management will be carried out continuously.

It is important to emphasize the close connection of the ATHLET code development with other projects, including those funded by the BMUV. The developments that have been conducted and approved here will directly benefit these projects and contribute to their overall progress. Conversely, several ATHLET developments performed outside GRS underwent quality assurance and could finally be integrated in the ATHLET main development branch to become available to all code users.

ATHLET is a versatile and reliable tool for analyzing thermal-hydraulic processes in nuclear power plants and research reactors. A distinctive feature of the code is its usage within numerous national and international projects and activities. Consequently, ATHLET stands for an active contribution to the maintenance of competence in the field of nuclear technology. ATHLET contains a comprehensive knowledge base on safety-relevant phenomena in nuclear reactors, including their modelling and assessment in the context of reactor safety analyses. Furthermore, the code serves as both a basis and starting point for numerous research activities as well as a software tool for training and educating young scientists. Two illustrative examples for the latter are the MISHA and ASUS projects, in which young scientists are conducting research on future reactors and SMRs, which may potentially be constructed in the vicinity of Germany. In this context, the continuous development and maintenance of ATHLET contributes to maintaining and enlarging the knowledge on reactor safety in Germany. This enables GRS to reliably inform and advise the federal government on current and future issues related to nuclear installations safety both domestically and abroad.



## List of figures

Fig. 3.1	Entrained liquid fraction vs. void fraction for horizontal (left) and vertical (right) flow paths as calculated by various ATHLET correlations at $p = 65 \text{ bar}$ and saturation conditions and for the assumed phase velocities $ul = 5 \text{ m/s}$ and $uv = 10 \text{ m/s}$ .....	9
Fig. 3.2	Decision tree with considered flow regimes for horizontal flow.....	16
Fig. 3.3	Variable symbols in stratified flow (graphic based on /TAI 76/) .....	16
Fig. 3.4	Decision tree with considered flow regimes for vertical flow.....	20
Fig. 3.5	A gas plug moving through pipe filled with liquid.....	25
Fig. 3.6	Feedback loop showing how the flow regime effects the interfacial friction and vice versa .....	27
Fig. 3.7	Stand-alone comparison of ATHLET flow regime map and /TAI 76/. Markers and legend refer to ATHLET. Black curves and yellow labels refer to /TAI 76/. Boundary cond.'s: Water-air, 25°C, 1 atm, horizontal, 5 cm diameter.....	28
Fig. 3.8	Comparison of ATHLET simulations and /TAI 76/. Markers and legend refer to ATHLET. Black curves and yellow labels refer to /TAI 76/. Boundary cond.'s: Water-air, 25°C, 1 atm, horizontal, 5 cm diameter .....	30
Fig. 3.9	Stand-alone comparison of ATHLET flow regime map and /TAI 80/. Markers and legend refer to ATHLET. Black curves and yellow labels refer to /TAI 80/. Boundary cond.'s: Water-air, 25°C, 1 bar, vertical, 5 cm diameter.....	32
Fig. 3.10	Comparison of ATHLET simulations and /TAI 80/. Markers and legend refer to ATHLET. Black curves and yellow labels refer to /TAI 80/. Boundary cond.'s: Water-air, 25°C, 1 bar, vertical, 5 cm diameter .....	33
Fig. 3.11	LOFT LP-LB-1 test: Average cladding temperature of central fuel assembly (TE-5H07-049).....	35
Fig. 3.12	LSTF run SB-CL-18: Injection mass flow rate from the accumulator in the intact loop (loop A).....	36
Fig. 3.13	Modified flow regime map acc. to Tandon as given in /PAP 10/ .....	38
Fig. 3.14	Flow pattern map for horizontal flow by /KAT 98/ (red line) with modification for condensation by /HAJ 03/ .....	40

Fig. 3.15	Schematic drawing of the horizontal stratified flow.....	42
Fig. 3.16	Schematic drawing of COSMEA test facility (2020) (not proportional to real scale).....	49
Fig. 3.17	Nodalisation of COSMEA facility.....	51
Fig. 3.18	Void fraction along condensation pipe for COSMEA experiments at 5 bar.....	51
Fig. 3.19	Void fraction along condensation pipe for COSMEA experiments at 12 bar.....	52
Fig. 3.20	Void fraction along condensation pipe for COSMEA experiments at 25 bar.....	52
Fig. 3.21	Void fraction along condensation pipe for COSMEA experiments at 45 bar.....	53
Fig. 3.22	Void fraction along condensation pipe for COSMEA experiments at 65 bar.....	53
Fig. 3.23	Measured and calculated condensation rate for COSMEA experiment.....	54
Fig. 3.24	Schematic representation of PERSEO test facility /BIA 03/.....	62
Fig. 3.25	Measured and calculated power of the PERSEO isolation condenser.....	64
Fig. 3.26	Measured and calculated water level in PERSEO HX pool.....	64
Fig. 4.1	Scheme of determination of radius of curvature for equivalent liquid flow path for stratified flow at T-junction with downward branch.....	73
Fig. 4.2	ATHLET representation of the experimental setup with a main pipe and a branching section (vertically upward arrangement shown here) and controlled mass flow at both outlets, as it was used for the validation of the extended T-junction model.....	79
Fig. 4.3	Effect of the change of the T-junction model for a selected test case (for flow conditions, see text). The absolute values of $\Delta p_{12}$ and $\Delta p_{13}$ are normalized to 1 for the graphical representation, with the maximum absolute value given in parentheses in the legend.....	80
Fig. 4.4	Pressure in the control volumes of the main channel (connected lines) and in the branching section (disconnected curves).....	81
Fig. 4.5	Pressure drop $\Delta p_{13}$ of the flow into the horizontal side branch with same diameter as the main channel $D_3/D_1 = 1$ , and inlet void fraction $X_1 = 0.020$ , inlet mass flow rate $G_1 = 4.05 \text{ kg/s}$ , at	

	pressure 7 bar. The stars indicate experimental values (number of the experiment as in /REI 88/)	82
Fig. 4.6	Phase separation $X3X1$ of the flow into the horizontal side branch with same diameter as the main channel $D3D1 = 1$ , and inlet void fraction $X1 = 0.020$ , inlet mass flow rate $G1 = 4.05 \text{ kg/s}$ , at pressure 7 bar	83
Fig. 4.7	Phase separation $X3X1$ of the flow into the horizontal side branch with same diameter as the main channel $D3D1 = 1$ , and inlet void fraction $X1 = 0.625$ , inlet mass flow rate $G1 = 0.256 \text{ kg/s}$ , at pressure 7 bar	84
Fig. 4.8	Pressure drop $\Delta p13$ for horizontal side branch with $D3D1 = 0.52$ , inlet void fraction $X1 = 0.138$ , inlet mass flow rate $G1 = 0.58 \text{ kg/s}$ , pressure 7 bar	85
Fig. 4.9	Phase separation $X3X1$ for horizontal side branch with $D3D1 = 0.52$ , inlet void fraction $X1 = 0.138$ , inlet mass flow rate $G1 = 0.58 \text{ kg/s}$ , pressure 7 bar	85
Fig. 5.1	Fuel relocation vs. power/burnup and Fuel swelling/densification vs. burnup	90
Fig. 5.2	Conceptual scheme of fuel and cladding extrapolation lengths	94
Fig. 5.3	Axial power profile for rods 1 and 3	98
Fig. 5.4	Verification against analytical solutions: open gap, IFA-432 rod 1 /DIN 24/	100
Fig. 5.5	Verification against analytical solutions: Close gap, IFA-432 rod 3 /DIN 24/	101
Fig. 5.6	Validation against IFA-432 Rod 1: (a) Fuel centreline, and (b) power and burnup boundary conditions /DIN 24/	103
Fig. 5.7	Validation against IFA-432 Rod 1: (a) gap size, and (b) fuel outer radial displacement and components /DIN 24/	104
Fig. 5.8	Validation against IFA-432 Rod 3: (a) Fuel centerline, and (b) power and burnup boundary conditions /DIN 24/	106
Fig. 5.9	Validation against IFA-432 Rod 1: (a) gap size, and (b) fuel outer radial displacement and components	107
Fig. 5.10	Temperature distribution in the fuel and cladding with different power profiles	111

Fig. 5.11	Axial temperature distributions at the rod outer surface .....	113
Fig. 6.1	Form loss coefficient for sudden contractions depending on Reynolds number $Re$ and area ratio $F$ .....	120
Fig. 6.2	Form loss coefficient for sharp-edged orifices depending on Reynolds number $Re$ and area ratio $F$ .....	121
Fig. 6.3	Incorrect phase distribution under stagnant flow conditions at the end of an ECTHOR simulation.....	124
Fig. 6.4	Momentum-flux term in the range of a void jump .....	125
Fig. 6.5	Phase distribution under stagnant flow conditions at the end of an ECTHOR simulation using the corrected momentum-flux term .....	126
Fig. 6.6	Temperature distribution in the lower part of the SACO .....	127
Fig. 6.7	The HTC correlation selection logic used in ATHLET /SCH 23b/ .....	140
Fig. 6.8	Nodalisation of the RBHT test section in ATHLET .....	144
Fig. 6.9	Cladding temperature at 2.69 m. From the upper left, B-1, B-3 and B-4 are shown .....	154
Fig. 6.10	Cladding temperature at 2.89 m. From the upper left, B-1, B-3 and B-4 are shown .....	155
Fig. 6.11	Heat transfer coefficient at 2.89 m. From the upper left, B-1, B-3 and B-4 are shown .....	155
Fig. 6.12	Quench front progression over the heated length. From the upper left, B-1, B-3 and B-4 are shown .....	156
Fig. 6.13	Liquid carryover fraction. From the upper left, B-1, B-3 and B-4 are shown .....	157
Fig. 6.14	Pressure drop over the bundle. From the upper left, B-1, B-3 and B-4 are shown.....	157
Fig. 6.15	Uncertainty and sensitivity results for the cladding temperature at 2.69 m in B-2 .....	159
Fig. 6.16	Uncertainty and sensitivity results for the cladding temperature at 2.89 m in B-2 .....	159
Fig. 6.17	Uncertainty and sensitivity results for the pressure drop over the bundle in B-2 .....	160

Fig. 6.18	Uncertainty and sensitivity results for the quench front progression in B-2.....	160
Fig. 6.19	Uncertainty and sensitivity results for the liquid carryover fraction in B-2.....	161
Fig. 6.20	Uncertainty and sensitivity results for the cladding temperature at 2.69 m in B-6 .....	162
Fig. 6.21	Uncertainty and sensitivity results for the cladding temperature at 2.89 m in B-6 .....	162
Fig. 6.22	Uncertainty and sensitivity results for the pressure drop over the bundle in B-6 .....	163
Fig. 6.23	Uncertainty and sensitivity results for the quench front progression in B-6.....	163
Fig. 6.24	Uncertainty and sensitivity results for the liquid carryover fraction in B-6.....	164
Fig. 6.25	Comparison of simulated and experimental PCT data. From the middle to the outside, the dotted lines represent agreement rated as excellent (green), good (yellow) and fair (red).....	165
Fig. 6.26	Comparison of simulated and experimental quench time at PCT height. From the middle to the outside, the dotted lines represent excellent, good and fair agreement.....	166
Fig. 6.27	Comparison of simulated and experimental liquid carryover at quench time of the PCT height. From the middle to the outside, the dotted lines represent excellent, good and fair agreement.....	167
Fig. 7.1	Conceptual scheme of Gitlab-CI pipeline .....	175
Fig. 7.2	Pipeline application to ROSA-III test: Coolant temperature at core outlet, and hot rod fuel temperature .....	177
Fig. 7.3	Pipeline application to ROSA-III test: $\Delta P$ at recirculating pump heads, and numerical indexes, e.g., Jacobian updates and time step number ..	178
Fig. 7.4	Layout of new AC <sup>2</sup> user area, based on Drupal .....	188



## List of tables

Tab. 3.1	Initial and boundary conditions of COSMEA 2020 experiment .....	49
Tab. 3.2	Parameter scaling for LOTUS calculations.....	59
Tab. 3.3	Experimental and calculated values of LOTUS experiment.....	60
Tab. 3.4	Initial and boundary conditions for PERSEO Test 7 Part 1.....	63
Tab. 4.1	Boundary conditions of investigated KIT T-junction experiment .....	82
Tab. 5.1	Components of cladding inner radius displacement: .....	92
Tab. 5.2	Specifications for rods 1 and 3 of the IFA-432 .....	97
Tab. 6.1	List of RBHT uncertain input parameters .....	150



## Abbreviations

1M	one momentum equation (5-equation model)
2M	two momentum equation (6-equation model)
BMUV	Bundesministerium für Umwelt, Naturschutz, Nukleare Sicherheit und Verbraucherschutz (Federal Ministry for the Environment, Nature Conservation, Nuclear Safety and Consumer Protection)
BWR	boiling water reactor
CV	control volume
CW	control word
HCO	heat conduction object
HTC	heat transfer coefficient
KW	keyword
LOFT	loss-of-fluid test
LSTF	large-scale test facility
MF	momentum flux
ML	mixture level
PCT	peak cladding temperature
PK	point kinetic
PW	pseudo keyword
PWR	pressurized water reactor
RBHT	Rod Bundle Heat Transfer
SMR	Small Modular Reactor
SW	sub-keyword
TDV	time-dependent volume (pressure-enthalpy boundary condition)
TFD	thermo-fluid dynamic
TFO	thermo fluid object
TSO	Technical Safety Organisation
TM	thermo-mechanical

## Nomenclature

### Symbols

A	flow area, m <sup>2</sup>
C	interfacial shear coefficient, N/m <sup>3</sup>
C <sub>0</sub>	phase distribution parameter
C <sub>i</sub>	friction factor coefficient for liquid phase, -
D, d	diameter, m
E <sub>d</sub>	entrained liquid factor, -
f	interfacial shear factor, N/m <sup>2</sup>
g	gravitational acceleration, m/s <sup>2</sup>
h	height
l	length
m	mass, kg
N <sub>f</sub>	viscosity number, -
p	perimeter, m
$\vec{p}$	vector holding the overall path rates of the various flow regimes
Pr	Prandtl number, -
R, r	radius, m
Re	Reynolds number, -
S	arc length, chord length, m
t	time, s
u <sub>T</sub>	terminal velocity for spherical droplet, m/s
V	volume, m <sup>3</sup>
v, u	velocity, m/s
w	percentage in the path constructing $\vec{p}$
w <sub>v,e</sub>	minimum gas velocity required to suspend a droplet, m/s
We	Weber number, -
$\alpha$	void fraction, -
$\gamma$	inclination angle, °
$\mu$	dynamic viscosity, Pa · s
$\nu$	kinematic viscosity, m <sup>2</sup> /s
$\rho$	density, kg/m <sup>3</sup>
$\sigma$	surface tension, N/m

### **Subscripts and superscripts**

ann	annular
b	single bubble
crit	critical
d	single droplet
F	film
g	gaseous
h	hydraulic
i	interface
$\varphi, k$	phase index
l	liquid
loc	local
max	maximum
r	relative
s	superficial
v	vapor
w	wall



## Literature

- /AHN 15/ Ahn, S. H., Aksan, N., Austregesilo, H., Bestion, D., Chung, B. D., D'Auria, F., Emonot, P., Gandrille, J. L., Hanninen, M., Horvatović, I., Kim, K. D., Kovtonyuk, A., Petruzzi, A.: FONESYS: The FORum & NETwork of SYStem Thermal-Hydraulic Codes in Nuclear Reactor Thermal-Hydraulics. Nuclear Engineering and Design, Bd. 281, S. 103–113, DOI 10.1016/j.nuceng-des.2014.12.001, 2015.
- /AND 87/ Andritsos, N., Hanratty, T. J.: Influence of Interfacial Waves in Stratified Gas-Liquid Flows. AIChE Journal, Bd. 33, Nr. 3, S. 444–454, 1987.
- /AUS 21/ Austregesilo, H., Schöffel, P. J., von der Cron, D., Weyermann, F., Wielenberg, A., Wong, K. W.: ATHLET 3.3 User's Manual. Gesellschaft für Anlagen- und Reaktorsicherheit (GRS) gGmbH, GRS-P-1/Vol. 1 Rev. 9, November 2021.
- /AUS 22/ Austregesilo, H., Schöffel, P. J., von der Cron, D., Weyermann, F., Wielenberg, A., Wong, K. W.: ATHLET 3.3.1 User's Manual, GRS-P-1/Vol. 1 Rev. 10. Gesellschaft für Anlagen- und Reaktorsicherheit (GRS) gGmbH, Oktober 2022.
- /BAL 88/ Ballyk, J. D., Shoukri, M., Chan, A. M. C.: Steam-Water Annular Flow in a Horizontal Dividing T-Junction. Int. J. Multiphase flow. International Journal of Multiphase Flow, Bd. 14, Nr. 3, S. 265–285, 1988.
- /BEA 82/ Beattie, D. R. H., Whalley, P. B.: A simple two-phase frictional pressure drop calculation method. International Journal of Multiphase Flow, Bd. 8, Nr. 1, S. 83–87, 1982.
- /BIA 03/ Bianchi, F., Meloni, P., Ferri, R., Achilli, A.: In-Pool Energy Removal System for Emergency Operation: Experiment and Analytical Assessment. In: Ravnik, M. (Hrsg.): Proceedings / International Conference Nuclear Energy for New Europe 2003. European Nuclear Society (ENS), International Conference Nuclear Energy for New Europe (NENE), NENE 2003, Portorož, Slovenia, 8. - 11. September 2003, S. 308, ISBN 961-6207-21-0, Nuclear Society of Slovenia: Ljubljana, 2003.

- /BIE 20/ Bieberle, A., Moonesi Shabestary, A., Geissler, T., Boden, S., Beyer, M., Hampel, U.: Flow morphology and heat transfer analysis during high-pressure steam condensation in an inclined tube part I: Experimental investigations. Nuclear Engineering and Design, Bd. 361, S. 110553, DOI 10.1016/j.nucengdes.2020.110553, 2020.
- /BOD 24/ Boden, S., Hampel, U., Pietruske, H., Bieberle, A.: Investigation on flow morphology and heat transfer for high-pressure steam condensation in an inclined tube at low inlet steam qualities. Nuclear Engineering and Design, Bd. 419, S. 112954, DOI 10.1016/j.nucengdes.2024.112954, 2024.
- /BOU 85/ Bourteele, J. B., Boileau, M.: ECTHOR Program, PWS 2.3: Small Size Break, Final Report. Centre d'Etudes Nucléaires de Grenoble, 1985.
- /BUE 94/ Buell, J. R., Soliman, H. M., Sims, H. E.: Two-Phase Pressure Drop and Phase Distribution at a Horizontal Tee Junction. International Journal of Multiphase Flow, Bd. 20, Nr. 5, S. 819–836, 1994.
- /CHI 67/ Chisholm, D.: Flow of Incompressible Two-phase mixtures through Sharp-edged Orifices. Journal of Mechanical Engineering Science, Bd. 9, Nr. 1, S. 72–78, DOI 10.1243/jmes\_jour\_1967\_009\_011\_02, 1967.
- /CRO 23/ Cron, D. von der: Konzept für das Überblenden von Strömungsbildkarten in ATHLET. Technische Notiz, TN-VDC-23/01, 16 S., Dezember 2023.
- /DI 23/ Di Nora, V. A.: Extended ATHLET Fuel Rod Model: A New Gap Conductance Model For ATHLET. Präsentation, Gesellschaft für Anlagen- und Reaktorsicherheit (GRS) gGmbH, AC<sup>2</sup> User Meeting 2023: Garching, Germany, 28. November 2023.
- /DIN 24/ Di Nora, V. A., Schöffel, P. J., Hollands, T.: A New Gap Conductance Model for the ATHLET System Code. In: Canadian Nuclear Society (CNS) (Hrsg.): The 14th Topical Meeting on Nuclear Reactor Thermal-Hydraulics, Operation, and Safety. NUTHOS-14, Vancouver, Canada, 25. - 28. August 2024, 2024.

- /DIT 30/ Dittus, F. W., Boelter, L. M. K.: Heat transfer in automobile radiators of the tubular type. University of California publications in engineering, Vol. 2, No. 13, University of California press: Berkeley, Oktober 1930.
- /DOB 98/ Dobson, M. K., Chato, J. C.: Condensation in Smooth Horizontal Tubes. Journal of Heat Transfer, Bd. 120, Nr. 1, S. 193–213, DOI 10.1115/1.2830043, 1998.
- /DÜN 22a/ Dünne, N., Skorek, T., Schöffel, P. J.: Simulation and uncertainty analysis of the RBHT blind tests with ATHLET 3.3. In: Chung-Hwa Nuclear Society (CHNS), National Tsing Hua University (Hrsg.): NUTHOS-13 2022 Proceeding Book, 13th International Topical Meeting on Nuclear Reactor Thermal-Hydraulics, Operation and Safety. NUTHOS-13, Hsinchu, Taiwan, 5. - 10. September 2022, 2022.
- /DÜN 22b/ Dünne, N., Skorek, T., Schöffel, P.: Simulation of the open tests of the RBHT benchmark with ATHLET. In: American Nuclear Society (ANS) (Hrsg.): 19th International Topical Meeting on Nuclear Reactor Thermal Hydraulics (NURETH-19). NURETH-19, Brussels, Belgium (virtual), 6. - 11. März 2022, ISBN 9789076971261, 2022.
- /EMO 11/ Emonot, P., Souyri, A., Gandrille, J. L., Barré, F.: CATHARE-3: A new system code for thermal-hydraulics in the context of the NEPTUNE project. Nuclear Engineering and Design, DOI 10.1016/j.nucengdes.2011.04.049, 2011.
- /GEE 15a/ Geelhood, K. J., Luscher, W. G., Raynaud, P. A., Porter, I. E.: FRAPCON-4.0, A Computer Code for the Calculation of Steady-State, Thermal-Mechanical Behavior of Oxide Fuel Rods for High Burnup. Pacific Northwest National Laboratory (PNNL), 2015.
- /GEE 15b/ Geelhood, K. J., Luscher, W. G.: FRAPCON-4.0: Integral Assessment. Pacific Northwest National Laboratory (PNNL): Richland WA (United States), 2015.

- /GOT 85/ Gottula, R. C., Condie, K. G., Sundaram, R. K., Neti, S., Chen, J. C., Nelson, R. A.: Forced convective, non-equilibrium, post-CHF heat transfer experiment data and correlations comparison report. EG&G Idaho, Inc., NUREG, CR-3193, März 1985.
- /HAJ 03/ Hajal, J. E., Thome, J. R., Cavallini, A.: Condensation in horizontal tubes, part 1: two-phase flow pattern map. International Journal of Heat and Mass Transfer, Bd. 46, Nr. 18, 2003.
- /HAN 78/ Hann, C. R., Bradley, E. R., Cunningham, M. E., Lanning, D. D., Marshall, R. K., Williford, R. E.: Data Report for NRC/PNL Halden Assembly IFA-432. PNL, 1978.
- /HEW 87/ Hewitt, G. F., Owen, D. G.: EXPERIMENTAL DATA SET NO. 1: PRESSURE DROP AND ENTRAINMENT FRACTION IN FULLY DEVELOPED FLOW. Multiphase Science and Technology, Bd. 3, Nr. 1-4, S. 145–154, DOI 10.1615/MultScienTechn.v3.i1-4.60, 1987.
- /HOL 23/ Hollands, T., Buchholz, S., Di Nora, V. A., Dünne, N., Eckert, D., Junk, M., Krüssenberg, A., Rezhikova, A., Schöffel, P. J., Wielenberg, A.: ATHLET 3.4.0 Validation. GRS-P-1/Vol. 3 Rev. 8, November 2023.
- /IDE 86/ Idelčik, I. E.: Handbook of hydraulic resistance. 2. Aufl., XIX, 640 S, ISBN 0891162844, Hemisphere Publishing Corp; Springer: Washington, New York, London, Berlin, Heidelberg, New York, Tokyo, 1986.
- /IDE 08/ Idelčik, I. E.: Handbook of Hydraulic Resistance. 4. Aufl., Begell House, Inc.: New York, 2008.
- /ISH 79/ Ishii, M., Chawla, T. C.: Local drag laws in dispersed two-phase flow. Argonne National Laboratory (ANL), NUREG/CR-1230, Dezember 1979.
- /JAC 21/ Jacht, V., Junk, M.: batchplot - A new tool for plotting the HDF5 output format. Präsentation, Gesellschaft für Anlagen- und Reaktorsicherheit (GRS) gGmbH, AC<sup>2</sup> User Meeting 2021: Garching, Germany, 8. Dezember 2021.

- /JOB 24/ Jobst, M., Schäfer, F., Kliem, S.: Numerical investigation on steam condensation and heat transfer in an emergency condenser tube with the thermo-hydraulic system code ATHLET. Nuclear Engineering and Design, Bd. 421, S. 113059, DOI 10.1016/j.nucengdes.2024.113059, 2024.
- /JU 19/ Ju, P., Liu, Y., Brooks, C. S., Ishii, M.: Prediction of interfacial shear stress of vertical upward adiabatic annular flow in pipes. International Journal of Heat and Mass Transfer, Bd. 133, S. 500–509, DOI 10.1016/j.ijheatmasstransfer.2018.12.057, 2019.
- /JU 20/ Ju, P., Pan, L.-M., Yan, Y., Zhu, Q., He, H., Yang, X., Ishii, M.: Prediction of wall shear stress of vertical upward co-current adiabatic air-water annular flow in pipes. Nuclear Engineering and Design, Bd. 368, S. 110797, DOI 10.1016/j.nucengdes.2020.110797, 2020.
- /JUN 23/ Junk, M., Jacht, V., Küntzel, M.: HDF5 and batchplot - Status, Tools, and Future Prospects. Präsentation, Gesellschaft für Anlagen- und Reaktorsicherheit (GRS) gGmbH, AC<sup>2</sup> User Meeting 2023: Garching, Germany, 28. November 2023.
- /KAN 03/ Kandlikar, S. G., Grande, W. J.: Evolution of Microchannel Flow Passages--Thermohydraulic Performance and Fabrication Technology. Heat Transfer Engineering, Bd. 24, DOI 10.1080/01457630304040, 2003.
- /KAT 98/ Kattan, N., Thome, J. R., Favrat, D.: Flow Boiling in Horizontal Tubes: Part 1—Development of a Diabatic Two-Phase Flow Pattern Map. Journal of Heat Transfer, Bd. 120, Nr. 1, S. 140–147, DOI 10.1115/1.2830037, 1998.
- /KLO 19/ Kloos, M.: SUSAs Version 4.2, User's Guide and Tutorial. GRS-P-5 Vol. 1 Rev. 5, Juni 2019.
- /KLO 20/ Kloos, M.: SUSAs Version 4.2, User's Guide and Tutorial. GRS-P-5, Vol. 1, Rev. 6, Oktober 2020.
- /KOR 06/ Korea Atomic Energy Research Institute: Draft: MARS CODE MANUAL VOLUME I: Code Structure, System Models, and Solution Methods. 2006.

- /KRI 22/ Krieger, J., Bratfisch, C., Koch, M. K.: Simulation der OSU-MASLWR Versuchsanlage mit dem Systemcode AC<sup>2</sup>. In: KernD, KTG, INFORUM (Hrsg.): Kerntechnik 2022. Kerntechnik, Hyperion Hotel Leipzig, 21. - 22. Juni 2022, 2022.
- /KRI 23/ Krieger, J., Bratfisch, C., Koch, M. K.: Simulation of the Experiment OSU-002 regarding the Behavior of a Helically Coiled Steam Generator Using AC<sup>2</sup>-ATHLET. In: ICON30. Kyoto, Japan, 21. - 26. Mai 2023, 2023.
- /LAH 87/ Lahey, R. T.: Dividing Flow in a Tee Junction. In: Hewitt, G. F., Delhaye, J. M., Zuber, N. (Hrsg.): Multiphase science and technology. Bd. 3, S. 316–347, ISBN 978-3540177913, Hemisphere Publ: Washington, 1987.
- /LAN 22a/ Lanfredini, M., Bestion, D., D’Auria, F., Aydemir, N., Carnevali, S., Fillion, P., Gaillard, P., Jeong, J. J., Karppinen, I., Kim, K. D., Kurki, J., Lee, J. H., Schoeffel, P., Sha, H., et al.: Stratification criteria of 8 system codes and direct confrontation to TPTF and Mantilla data,. In: American Nuclear Society (ANS), SCK-CEN (Hrsg.): 19th International Topical Meeting on Nuclear Reactor Thermal Hydraulics. NURETH 19, virtual, 6. - 11. März 2022, 2022.
- /LAN 22b/ Lanfredini, M., Bestion, D., D’Auria, F., Aydemir, N., Carnevali, S., Fillion, P., Gaillard, P., Jeong, J. J., Junk, M., Karppinen, I., Kim, K. D., Kurki, J., Lee, J. H., Schöffel, P. J., et al.: TPTF horizontal flow prediction by SYS-TH codes - recent analyses made within the FONESYS network. In: American Nuclear Society (ANS), SCK-CEN (Hrsg.): 19th International Topical Meeting on Nuclear Reactor Thermal Hydraulics. NURETH 19, virtual, 6. - 11. März 2022, 2022.
- /LAN 22c/ Lanfredini, M., Bestion, D., D’Auria, F., Aydemir, N., Carnevali, S., Fillion, P., Gaillard, P., Jeong, J. J., Karppinen, I., Kim, K. D., Kurki, J., Lee, J. H., Lee, J., Schöffel, P. J., et al.: Droplet entrainment prediction in horizontal flow by Sys-TH codes – Mantilla experiments - recent analyses made within the FONESYS network. In: American Nuclear Society (ANS), SCK-CEN (Hrsg.): 19th International Topical Meeting on Nuclear Reactor Thermal Hydraulics. NURETH 19, virtual, 6. - 11. März 2022, 2022.

- /LEE 22a/ Lee, J., Junk, M., Skorek, T., Schöffel, P. J.: Improvement of entrainment model for horizontal flow in ATHLET and application to Mantilla experiment and TPTF. Nuclear Engineering and Design, Nr. 400, 2022.
- /LEE 22b/ Lee, J., Junk, M., Skorek, T., Schöffel, P. J.: Improvement of entrainment model for horizontal flow in ATHLET and application to Mantilla experiment and TPTF. In: American Nuclear Society (ANS), SCK-CEN (Hrsg.): 19th International Topical Meeting on Nuclear Reactor Thermal Hydraulics. NURETH 19, virtual, 6. - 11. März 2022, 2022.
- /LIL 88/ Liles, D. R., Spore, J. W., Knight, T. D., Nelson, R. A., Cappiello, M. W., Pasamehmetoglu, K. O., Mahaffy, J. H., Guffee, L. A., Stumpf, H. J., Dotson, P. J.: TRAC-PF1/MOD1 Correlations and Models. Los Alamos National Laboratory (LANL), NUREG/CR-, Nr. 5069: United States, 1988.
- /LOC 49/ Lockhart, R. W., Martinelli, R. C.: Proposed Correlation of Data for Isothermal Two-phase, Two-component Flow in Pipes. Chemical Engineering Progress, Bd. 45, Nr. 1, 1949.
- /MAR 48/ Martinelli, R. C., Nelson, D. B.: Prediction of Pressure Drop During Forced Circulation Boiling of Water. Transactions of the American Society of Mechanical Engineers, Bd. 70, S. 695, 1948.
- /MOR 67/ Mori, Y., Nakayama, W.: Study on Forced Convective Heat Transfer in Curved Pipes (2nd Report, Turbulent Region). International Journal of Heat and Mass Transfer, Nr. 10, S. 37–59, 1967.
- /NIJ 80/ Nijhawan, S., Chen, J. C., Sundaram, R. K., London, E. J.: Measurement of Vapor Superheat in Post-Critical-Heat-Flux Boiling. Journal of Heat Transfer, Bd. 102, Nr. 3, S. 465–470, DOI 10.1115/1.3244324, 1980.
- /NRC 12/ U.S. Nuclear Regulatory Commission (NRC): TRACE V5.0 Theory Manual. 2012.
- /PAL 79/ PALEN, J. W., BREBER, G., TABOREK, J.: Prediction of Flow Regimes in Horizontal Tube-Side Condensation. Heat Transfer Engineering, Bd. 1, Nr. 2, S. 47–57, DOI 10.1080/01457637908939558, 1979.

- /PAP 10/ Papini, D., Cammi, A.: Modelling of Heat Transfer Phenomena for Vertical and Horizontal Configurations of In-Pool Condensers and Comparison with Experimental Findings. Science and Technology of Nuclear Installations, Bd. 2010, DOI 10.1155/2010/815754, 2010.
- /REI 86/ Reimann, J., Seeger, W.: Two-phase flow in a T-junction with a horizontal inlet, Part II: Pressure differences. International Journal of Multiphase Flow, Bd. 12, Nr. 4, S. 587–608, 1986.
- /REI 88/ Reimann, J., Brinkmann, H. J., Domański, R.: Gas-Liquid Flow in Dividing Tee-Junctions with a Horizontal Inlet and Different Branch Orientations and Diameters. Kernforschungszentrum Karlsruhe (FZK), KfK 4399, Dezember 1988.
- /ROS 10/ Rosal, E., Lin, T. F., McClellan, I., Brewer, R. C.: Rod Bundle Heat Transfer Test Facility Description. Pennsylvania State University (PSU), Juli 2010.
- /SAB 84/ Saba, N., Lahey, R. T.: The Analysis of Phase Separation Phenomena in Branching Conduits. International Journal of Multiphase Flow, Bd. 10, Nr. 1, S. 1–20, 1984.
- /SAL 19/ Salko Jr, R., Avramova, M., Wysocki, A., Toptan, A., Hu, J., Porter, N., Blyth, T. S., Dances, C. A., Gomez, A., Jernigan, C., Kelly, J.: CTF 4.0 Theory Manual. Oak Ridge National Lab. (ORNL), Oak Ridge, TN (United States), DOI 10.2172/1550750: 2019-04-01, 2019.
- /SCH 21a/ Schöffel, P. J., Buchholz, S., Dünne, N., Guo, L., Jacht, V., Köllein, C., Krüssenberg, A., Lee, J., Lerchl, G., Skorek, T., Cron, D. von der, Weyermann, F., Wielenberg, A., Wong, K. W.: Weiterentwicklung des AC<sup>2</sup> Thermohydraulik-Moduls ATHLET zur Simulation komplexer, zweiphasiger Strömungsphänomene. Gesellschaft für Anlagen- und Reaktorsicherheit (GRS) gGmbH, GRS-Bericht, GRS-630, ISBN 978-3-949088-19-3, 2021.
- /SCH 21b/ Schöffel, P.: Release of AC<sup>2</sup> 2021 - Model and Program Improvements in ATHLET 3.3. Präsentation, Gesellschaft für Anlagen- und Reaktorsicherheit (GRS) gGmbH, AC<sup>2</sup> User Meeting 2021: Garching, Germany, 8. Dezember 2021.

- /SCH 23a/ Schöffel, P. J., Di Nora, V. A., Eckert, D., Junk, M., Cron, D. von der, Weyermann, F., Wielenberg, A.: ATHLET 3.4.0 Models and Methods. GRS-P-1/Vol. 4, November 2023.
- /SCH 23b/ Schöffel, P.: New Models and Features in ATHLET 3.4.0. Präsentation, Gesellschaft für Anlagen- und Reaktorsicherheit (GRS) gGmbH, AC<sup>2</sup> User Meeting 2023: Garching, Germany, 27. November 2023.
- /SCH 23c/ Schöffel, P. J., Di Nora, V. A., Eckert, D., Junk, M., Cron, D. von der, Weyermann, F., Wielenberg, A.: ATHLET 3.4.0 User's Manual. GRS-P-1/Vol 1 Rev. 11, November 2023.
- /SCH 24/ Schöffel, P. J., Di Nora, V. A., Eckert, D., Junk, M., Cron, D. von der, Weyermann, F., Wielenberg, A.: ATHLET 3.4.1 User's Manual. Gesellschaft für Anlagen- und Reaktorsicherheit (GRS) gGmbH, GRS-P-1/Vol 1 Rev. 12, Mai 2024.
- /SEE 86/ Seeger, W., Reimann, J., Müller, U.: Two-phase flow in a T-junction with a horizontal inlet, Part I: Phase separation. International Journal of Multiphase Flow, Bd. 12, Nr. 4, S. 575–585, 1986.
- /SIK 24/ Sikora, M., Anweiler, S., Meyer, J. P.: Comprehensive analysis of two-phase liquid-gas flow structures in varied channel geometries and thermal environments. International Journal of Heat and Mass Transfer, Nr. 228, DOI 10.1016/j.ijheatmasstransfer.2024.125665., 2024.
- /SKO 01/ Skorek, T.: Flooding Phenomenon and Determination of Interfacial and Wall Shear in One Dimensional Two-Fluid Model. In: World Conference on Experimental Heat Transfer, Fluid Mechanics, and Thermodynamics: 5th World Conf. on Experimental Heat Transfer, Fluid Mechanics, and Thermodynamics, Proceedings of the 5th World Conference on Experimental Heat Transfer, Fluid Mechanics and Thermodynamics. ExHFT-5, Thessaloniki, 24. - 28. September 2001, 2001.

- /SKO 04/ Spitzer, C., Schmocker, U., Dang, V. N. (Hrsg.): Probabilistic safety assessment and management, PSAM 7, ESREL '04,. International Association for Probabilistic Safety Assessment and Management, PSAM, ESREL, Probabilistic Safety Assessment and Management, PSAM 7 – ESREL'04, Berlin, 2004-06-14/20004-06-18, Bd. 4, ISBN 978-1852338275, Springer: Berlin, 2004.
- /SKO 16/ Skorek, T., Tiborcz, L.: Validation of ATHLET system code – scaling effects by simulation of reflooding experiments. In: Korean Nuclear Society (KNS): 11th International Topical Meeting on Nuclear Thermal-hydraulics, Operation and Safety, Proceedings. NUTHOS-11, Gyeongju, Korea, 9. - 13. Oktober 2016, 2016.
- /SKO 17/ Skorek, T.: Input uncertainties in uncertainty analyses of system codes: Quantification of physical model uncertainties on the basis of CET (combined effect tests). Nuclear Engineering and Design, Bd. 321, S. 301–317, DOI 10.1016/j.nucengdes.2016.10.028, 2017.
- /SON 89/ Sonnenburg, H.-G.: Full-range drift-flux model based on the combination of drift-flux theory with envelope theory. In: Müller, U. (Hrsg.): Fourth International Topical Meeting on Nuclear Reactor Thermal Hydraulics (NURETH-4), October 10 to 13, 1989, Karlsruhe, Federal Republic of Germany. Kernforschungszentrum Karlsruhe (FZK), NURETH-4, Karlsruhe, 10. - 13. Oktober 1989, S. 1003–1009, ISBN 3765011169, Braun: Karlsruhe, 1989.
- /SON 02/ Sonnenburg, H.-G., Hofer, E., Kloos, M.: Methodenentwicklung zur Analyse des Brennstabverhaltens bei erhöhtem Abbrand. Gesellschaft für Anlagen- und Reaktorsicherheit (GRS) gGmbH (GRS), GRS-A-Bericht, GRS-A-3079, 76 S., November 2002.
- /TAI 76/ Taitel, Y., Dukler, A. E.: A model for predicting flow regime transitions in horizontal and near horizontal gas-liquid flow. AIChE Journal, Bd. 22, Nr. 1, S. 47–55, DOI 10.1002/aic.690220105, 1976.
- /TAI 80/ Taitel, Y., Barnea, D., Dukler, A. E.: Modelling flow pattern transitions for steady upward gas-liquid flow in vertical tubes. AIChE Journal, Bd. 26, Nr. 3, 1980.

- /TAN 82/ Tandon, T. N., Varma, H. K., Gupta, C. P.: A New Flow Regimes Map for Condensation Inside Horizontal Tubes. *Journal of Heat Transfer*, Bd. 104, Nr. 763, 1982.
- /VAL 20/ Valgrind Development Team: Valgrind Web page. Erreichbar unter <https://www.valgrind.org/>, abgerufen am 23. Oktober 2020.
- /MIT 79/ Vitanza, C., Lostad, E., Graziani, U.: FISSION GAS RELEASE FROM UO" PELLETT FUEL AT HIGH BURN-UP, OECD Halden Reactor Project 1750 Halden, Norway. 1979.
- /VOJ 82/ Vojtek, I.: Untersuchung der Wärmeübertragungsverhältnisse in der Hochdruckphase eines Kühlmittelverluststörfalls mit mittlerem und grossem Bruchquerschnitt. Gesellschaft für Anlagen- und Reaktorsicherheit (GRS) gGmbH, GRS-A-Bericht, GRS-A-709: Garching, März 1982.
- /WAG 97/ Wagner, W.: Strömung und Druckverlust, Mit Beispielsammlung. Kamprath-Reihe, 4. Aufl., ISBN 3-8023-1720-3, Vogel, 1997.
- /WAL 70/ Wallis, G. B.: Annular Two-Phase Flow, Part 1: A Simple Theory. *Journal of Basic Engineering*, Nr. 59, 1970.
- /WEY 24/ Weyermann, F., Eschricht, D., Wielenberg, A., Steinhoff, T., Schöffel, P. J., Spengler, C., Lovasz, L.: AC<sup>2</sup> 2023.2 User Manual. Gesellschaft für Anlagen- und Reaktorsicherheit (GRS) gGmbH, GRS-P-15/Vol. 1 Rev. 2, 80 S., Mai 2024.
- /WIE 23/ Wielenberg, A.: Finding Errors and Optimizing ATHLET/CD Datasets. Präsentation, Gesellschaft für Anlagen- und Reaktorsicherheit (GRS) gGmbH, AC<sup>2</sup> User Meeting 2023: Garching, Germany, 27. November 2023.
- /ŽUK 72/ Žukauskas, A.: Heat Transfer from Tubes in Crossflow. In: *Advances in Heat Transfer Volume 8*. *Advances in Heat Transfer*, Nr. 8, S. 93–160, ISBN 9780120200085, DOI 10.1016/S0065-2717(08)70038-8, Elsevier, 1972.

**Gesellschaft für Anlagen-  
und Reaktorsicherheit  
(GRS) gGmbH**

Schwertnergasse 1  
**50667 Köln**

Telefon +49 221 2068-0

Telefax +49 221 2068-888

Boltzmannstraße 14

**85748 Garching b. München**

Telefon +49 89 32004-0

Telefax +49 89 32004-300

Kurfürstendamm 200

**10719 Berlin**

Telefon +49 30 88589-0

Telefax +49 30 88589-111

Theodor-Heuss-Straße 4

**38122 Braunschweig**

Telefon +49 531 8012-0

Telefax +49 531 8012-200

[www.grs.de](http://www.grs.de)

**ISBN 978-3-910548-88-6**